

# Determination of OH reactivity in the atmosphere by way of the Comparative Reactivity Method

---

Thesis submitted for the degree  
of Doctor of Philosophy

by

Rikesh Panchal (M. Chem)

Department of Chemistry

University of Leicester

September 2016

## **Statement of originality**

The work described in this thesis was conducted by the author in the Department of Chemistry at the University of Leicester, mainly during the period between October 2012 and September 2016. All the work in this thesis is original unless stated otherwise within the text or by references.

-----

Rikesh Panchal

29<sup>th</sup> September 2016

## **Abstract**

### **Determination of OH reactivity in the atmosphere by way of the Comparative Reactivity Method**

**Rikesh Panchal**

**September 2016**

Hydroxyl (OH) radicals play an important role in 'cleansing' the atmosphere of many pollutants such as, nitric oxides (NO<sub>x</sub>), methane (CH<sub>4</sub>) and various volatile organic compounds (VOCs). To measure the reactivity of OH, both the sinks and sources of OH need to be quantified, and currently the overall sinks of OH seem not to be fully constrained. In order to measure the total rate loss of OH in an ambient air sample, all OH reactive species must be considered and their concentrations and reaction rate coefficients with OH known.

Using the method pioneered by Sinha and Williams at the Max Plank Institute Mainz, the Comparative Reactivity Method (CRM) directly quantifies total OH reactivity in ambient air without the need to consider the concentrations of individual species within the sample that can react with OH.

The CRM measures the concentration of a reactive species that is present only in low concentrations in ambient air, in this case pyrrole, flowing through a reaction vessel and detected using Proton Transfer Reaction- Time of Flight-Mass Spectrometry (PTR-ToF-MS).

The research presented in this thesis will aim to build, develop, calibrate and validate a suitable instrument that measures total OH reactivity using the CRM technique, with the final aim of employing this technique in a number of field campaigns.

## Acknowledgments

I would like everyone who has helped me to complete the work in this thesis. Everyone in the atmospheric department for helping me, Bob, Rebecca and Iain Goodall for helping me and keeping me calm whenever there was a problem with the PTR-ToF-MS. For that I am truly grateful.

Tom Adams, Lloyd Hollis, Lewis Antil for all the laughs and the banter. You guys have made the long days I spent looking at data a lot more fun. Prof Paul Monks for his help and knowledge. Roberto for helping with data analysis and reading this thesis. I would like to thank Lara for her support and help.

The guys in the workshop need an honourable mention, Carl and Praful for their knowledge and skills and making sure the instruments run smoothly (and being there when the instruments were not running smoothly!).

And finally, I would like to thank my family for their unconditional support and encouraging me to work hard and putting up with the emotional rollercoaster that is writing a thesis.

## Table of Contents

Statement of originality .....	i
Abstract .....	ii
Acknowledgments .....	iii
Table of Contents .....	iv
List of tables .....	viii
List of figures .....	x
Chapter 1. Introduction.....	1
1.1 The structure of the atmosphere .....	1
1.2 Tropospheric Hydroxyl radical (OH) chemistry .....	4
1.2.1 OH production .....	5
1.2.2 Reactions of OH radicals .....	6
1.2.3 HO <sub>x</sub> termination pathways .....	8
1.3 Tropospheric Nitrogen Oxides (NO <sub>x</sub> ) chemistry .....	9
1.4 Calculating OH concentrations and reactivity .....	10
1.5 Techniques used to measure OH reactivity.....	13
1.5.1 The TOHLM.....	13
1.5.2 The pump- probe method .....	14
1.5.3 The Comparative Reactivity Method (CRM) .....	15
1.5.4 Comparisons of total OH reactivity measurement techniques .....	20
1.6 Previous measurements of total OH reactivity .....	24

1.7	Thesis objectives and structure.....	29
Chapter 2.	Instrument Development .....	31
2.1	Introduction .....	31
2.2	Glass Reactor .....	31
2.2.1	The configuration of the UOL-CRM and various phases of measurements.....	32
2.3	Proton Transfer Reaction- Time of Flight- Mass Spectrometry as a detection method .....	43
2.3.1	The Kore Technology Ltd PTR-ToF-MS .....	45
2.3.2	Hydronium cluster ratios within the flow drift tube.....	49
2.4	Conclusions.....	52
Chapter 3.	Calibration and Validation of the UOL-CRM.....	53
3.1	Introduction .....	53
3.2	Pyrrrole concentration calibration .....	53
3.3	Changes in sampled ambient air relative humidity between C2 and C3 modes. The effect on pyrrole sensitivity .....	56
3.3.1	The effect of C2 and C3 humidity differences on OH concentration .....	58
3.4	Deviations from pseudo- first order kinetics .....	62
3.4.1	Experimental characterisation of UOL-CRM operating conditions- deviation from pseudo first order conditions .....	63
3.5	Recycling of OH due to the presence of high NO concentrations within the reaction vessel .....	71
3.5.1	Experimental- Correction of C3 measurements owing to NO induced OH recycling.....	71

3.6	Dilution of ambient air within the UOL-CRM.....	75
3.7	Limit of detection (LOD) .....	75
3.8	Measurement uncertainties .....	76
3.9	Conclusions.....	76
Chapter 4. Deployment of the UOL-CRM. Measurements conducted at Weybourne Atmospheric Observatory (WAO).....		
4.1	Introduction .....	78
4.1.1	Campaign objectives .....	78
4.1.2	Measurement Location .....	79
4.2	Instrument set up .....	81
4.3	Calibrations .....	81
4.4	Measurements of VOC concentrations made by the UOL-CRM .....	83
4.5	Hydronium instability within the mass spectrometer.....	84
4.6	Data work up procedure- applications of calibrations and corrections to campaign measurements.....	94
4.7	Results .....	100
4.1	Conclusions.....	106
Chapter 5. Comparisons of UOL-CRM measurements with calculated reactivity and measurements made by the UL-LIF .....		
5.1	Introduction .....	107
5.1	Concentration measurements of VOCs and inorganic species .....	107
5.2	Calculated total OH reactivity .....	122
5.3	The UL-LIF Instrument .....	128

5.3.1	LIF determination of OH reactivity .....	130
5.4	UL- LIF measurements during the ICOZA campaign .....	132
5.5	Comparing calculated total OH reactivity and UOL-CRM measured reactivity. An overview of the campaign .....	134
5.5.1	Period 1 04/07/15 to 05/07/15 .....	143
5.5.2	Periods 2 13/07/15 to 16/07/15.....	144
5.5.3	Period 3 19/07/15 to 20/07/15 .....	146
5.5.4	Period 4 23/07/15 to 27/07/15 .....	149
5.6	Comparisons between UOL-CRM and UL-LIF measurements .....	149
5.7	Possible calibration and instrumentation errors.....	154
5.8	Conclusions.....	159
Chapter 6.	Conclusions and future work .....	161
6.1	The UOL-CRM and the PTR-ToF-MS .....	163
6.2	Interferences .....	164
6.3	Instability and noise within the UOL-CRM measurements .....	164
6.4	Discrepancies between measured and calculated OH reactivity .....	165
6.5	Future work .....	166
References	.....	170

## List of tables

Table 1:1 The main components of dry air .....	2
Table 1:2 estimated global emission rates of various trace gases (Tg) including the percentage and absolute amounts of each trace gas removed by removed during their respective reactions with OH. According to H. Ehhalt (1999), the average concentration of OH was taken as $1 \times 10^{-6}$ molecules $\text{cm}^{-3}$ ( $1 \text{Tg} = 10^{12}$ g). Adapted from Prinn (2003).....	4
Table 1:3 Comparisons of total OH reactivity measurement techniques. Adapted from Yang et al. (2016).....	21
Table 1:4 Summary of OH reactivity instruments. Adapted from Hansen et al. (2015).....	23
Table 1:5 Previous OH reactivity field campaign measurements. Adapted from Hansen et al. (2015) and Yang et al. (2016). .....	27
Table 3:1 Calculated and measured OH reactivity at a pyrrole to OH ratio of 3.51 for a mix of hydrocarbons.....	66
Table 3:2 All pyrrole OH ratios from propyne and hydrocarbon kinetics calibrations and their corresponding OH reactivity correction factors.....	69
Table 3:3 Error budget table listing the components used to derive measured OH reactivity using the UOL-CRM and their corresponding uncertainty.....	76
Table 4:1 Summary of data shown in Figure 4:19 Measurements made by the UOL-CRM during the ICOZA campaign .....	102
Table 5:1 A list of instruments provided by the University of Birmingham, Leicester, East Anglia, Leeds and York and the corresponding species detected by each instrument for the campaign .....	108
Table 5:2 concentrations of VOCs throughout the ICOZA campaign, along with the respective minimum, maximum and average concentration of each VOC (ppb).....	110

Table 5:3 Summary of ancillary measurements made during the ICOZA campaign. Used for OH reactivity calculations .....	114
Table 5:4 Average total OH reactivity calculated for the ICOZA campaign and the percentage of total OH reactivity separated by functional group .....	124
Table 5:5 Calculated average total OH reactivity after the removal of NO and NO <sub>2</sub> measurements, and the percentage contribution to total OH reactivity by functional group.....	125
Table 5:6 Statistics from the box and whisker plot shown in Figure 5:14. Comparing data from the UOL-CRM and calculated OH reactivity for the duration of the field campaign. Shading in grey and blue represent days of the campaign when the agreement between measured and calculated reactivity was high and low respectively. These periods are discussed in the following sections .....	138
Table 5:7 summary of the statistics collected from the box and whisker plot comparing the data collected by the UOL-CRM and the UL-LIF .....	151
Table 5:8 Summary of measurements comparing the average UOL-CRM/ calculated R, UOL-CRM/ UL-LIF ratios for periods 1, 2 and 3, along with the percentage difference between measurements and calculated reactivity for the three periods .....	153
Table 6:1 A list of problems determined during the development and deployment of the UOL-CRM and recommended improvements .....	167

## List of figures

Figure 1:1 The vertical structure of the atmosphere. Vertical changes in temperature can be used as an indicator of different atmospheric layer. Adapted from Brasseur and Solomon (2005) .....	3
Figure 1:2 Calculated rates of OH production through the photolysis of HONO, O <sub>3</sub> and HCHO. Adapted from Winer and Biermann (1994) and Finlayson-Pitts and Pitts Jr (2000c) .....	6
Figure 1:3 Systematic diagram representing the OH production and destruction pathways within the troposphere (Tuck, 1992) .....	9
Figure 1:4 A schematic of the instrument employed by the TOHLM technique. From Kovacs and Brune (2001) .....	14
Figure 1:5 A schematic of the CRM glass reaction vessel adapted from (Sinha et al., 2008) .....	15
Figure 1:6 A representation of the CRM measurement principle depicting the changes in pyrrole concentration during various measurement periods, (Sinha et al., 2008) .....	17
Figure 2:1 Schematic of University of Leicester CRM reaction vessel .....	31
Figure 2:2 A magnified diagram of the Wood's horn depicting the principles of its operation. Adapted from Moore and Coplan. (2009).....	32
Figure 2:3 A schematic representation of the CRM set up developed at The University of Leicester .....	36
Figure 2:4 C0 wet measurements are conducted with pyrrole, zero air and nitrogen and water vapour. No UV light enters the reaction vessel at this time .....	37
Figure 2:5 C0 dry measurements are conducted with pyrrole, zero air and dry nitrogen with no UV light entering the reaction vessel at this time .....	37

Figure 2:6 An illustration of the C1 measurement configuration. C1 has the same flow regime as C0 dry, however during C1, UV light enters the reaction vessel .....	38
Figure 2:7 An illustration of C2 measurement mode. In this case, the reaction vessel is under humid conditions and OH radicals are produced through the UV lamp. Scrubbed ambient air is also introduced .....	40
Figure 2:8 C3 is the final mode of measurements. In comparison to C2, ambient air is introduced into the reaction vessel to induce a reaction of VOCs with OH radicals .....	41
Figure 2:9 A representation of all pyrrole measurement modes and the associated changes in concentration over time. Adapted from a poster created by the John Williams group at the University of Mainz .....	42
Figure 2:10 A schematic of a PTR-ToF-MS depicting the hollow cathode (HC) ion source, source drift (SD) tube, flow drift tube (FDT), into a MCP detector.	45
Figure 2:11 Schematic of the PTR-ToF-MS hollow cathode region and PTR reaction cell(Kore-Technology-Ltd, 2010). .....	46
Figure 2:12 A depiction of passing through the time of flight region of a ToF-MS (Blake. R. S et al., 2009, 2009) .....	48
Figure 2:13 Measured distributions of hydronium and hydronium water clusters as an effect of changing E/N .....	50
Figure 3:1 PTR-ToF-MS pyrrole calibration curves measured over a period of approximately one year .....	56
Figure 3:2 Measurements of PTR-MS pyrrole sensitivity conducted in dry and humid air by Sinha et al. (2009).....	57
Figure 3:3 Measured hydronium $m/z$ 37 ion counts (ncps) and the corresponding pyrrole concentrations when switching from modes C2 to C3 and back to C2	59

Figure 3:4 Time series of pyrrole concentrations C1, C2 and C3. C2 measured with a dilution of zero air, and C3 measured with a dilution of ambient air. C2 measurements are highlighted in grey. ....60

Figure 3:5 Experimentally determined humidity calibrations measured at relative humidity ranging from 20 to 70% (22°C). Error bars are measured at one standard deviation of each pyrrole concentration. Calibrations conducted on 20/04/16, 24/03/16, 14/12/15, 23/01/15, 20/01/15 and 27/01/15 .....62

Figure 3:6 Measured pyrrole concentrations during C1 and C2. Increasing amounts of propyne introduced into the reaction vessel to induce higher rates of OH reactivity. Shaded grey areas indicate the measurement mode and the concentration of propyne introduced into the UOL-CRM.....64

Figure 3:7 Experimentally determined OH reactivity and its deviation from calculated OH reactivity using propyne gas standard at pyrrole to OH ratios of 1.37, 1.4 and 3.9 .....65

Figure 3:8 Measured and calculated OH reactivity of a hydrocarbon mix (methane, ethane, propane and n-butane). At pyrrole to OH ratios of 2.0, 3.51 and 3.53. As a function of the summed rate coefficients and concentrations of all hydrocarbons .....67

Figure 3:9 The relationship between the correction factor at measured pyrrole to OH ratios. The ratios are obtained from kinetics studies of propyne and a mix of hydrocarbons (Figure 3:7 Figure 3:8). Adapted from (Michoud et al., 2015). The area highlighted in grey indicate the pyrrole OH ratios measured during the Weybourne campaign. Error bars are calculated from one standard deviation of measured correction factor.....68

Figure 3:10 CRM pyrrole concentration measurements. Areas highlighted in grey show measurements of C1, C2 and baseline C3 measurement obtained with the addition of propyne. Further addition of 20, 30, 50, 70 and 120 ppb of NO results in the decrease of pyrrole signal.....72

Figure 3:11 Observed changes in pyrrole concentration when switching from C2 to C3 followed by the addition of increasing concentrations of NO into the

reaction vessel. NO concentrations of 30, 40, 50, 60 and 70ppb at a pyrrole to OH ratio of 1.29 and 3.97. 20, 30, 50, 70 and 120 ppb at pyrrole/ OH ratio 3.55. 27, 36, 44, 52, 59 and 66ppb pyrrole/ OH ratio 3.7 .....	72
Figure 3:12 Experimental characterisation of the degree at which C3 differs from a baseline measurement with the addition of NO at pyrrole to OH ratios of 2.46, 3.55, 3.7 and 3.97. Error bars are calculated from the standard deviation in $\Delta C3$ .....	73
Figure 3:13 Gradients calculated from the correction experiments shown in Figure 3:12 at their corresponding pyrrole to OH ratios.....	74
Figure 4:1 Google Maps image of the measurement location for the ICOZA field campaign.....	80
Figure 4:2 A picture of the University of Leicester shipping container housing the UOL-CRM .....	80
Figure 4:3 Pyrrole calibration conducted during the ICOZA campaign to determine instrument sensitivity towards pyrrole.....	82
Figure 4:4 Concentrations of VOCs measured by the UOL-CRM PTR-ToF-MS from 19th July to 20th July .....	84
Figure 4:5 Temperature recordings measured by a temperature humidity probe located within the reaction vessel from 20th to 21st July and from 28th to 21st July, in comparison to temperature recorded using a data logger next to the mass spectrometers ion source for the same time period .....	85
Figure 4:6 Relative humidity (%) measured within the reaction vessel from 20th to 21st July and from 28th to 29th July.....	86
Figure 4:7 a. and b. hydronium along with the corresponding pyrrole signal (c. and d.) measured on 20th through to 21st July with measurements carried out from 28 <sup>th</sup> July to 29 <sup>th</sup> July .....	89

Figure 4:8 a. and c. m/z 21 hydronium isotope count rate measured alongside b. and d. temperature within the reaction vessel measured on 20th through to 21st July and 28th through to 29th July respectively .....	89
Figure 4:9 a. and d. raw pyrrole signal measured from 20th to 21st July and 28th to 29th July along with the corresponding normalised pyrrole signals (b. and c.) .....	90
Figure 4:10 a. measured total OH reactivity and b. the corresponding pyrrole concentrations from 20th to 21st July and the same measurements c. and d. for 28th to 29th July .....	91
Figure 4:11 Calculations of E/N during periods of temperature fluctuations within the mass spectrometer from 20th July to 21st July and from 28th to 29th July .....	93
Figure 4:12 A flow diagram representing the data processing sequence from measured pyrrole signals to final OH reactivity data. Adapted from (Kesel et al., 2014) .....	97
Figure 4:13 Raw data collected from 04/07/15 to 05/07/15. a. m/z 21 hydronium isotope signal. b. pyrrole signal. Measurements conducted during C1 (highlighted in grey), C2 (highlighted in white), C3 (highlighted in green) and VOC ambient air measurement mode highlighted in blue .....	98
Figure 4:14 a. Background subtracted pyrrole signal. b. pyrrole concentration (ppb). Measurements made from 04/07/15 to 05/07/15. C1 highlighted in grey, C2 highlighted in white, C3 highlighted in green and ambient air VOC mode highlighted in blue .....	98
Figure 4:15 Total OH reactivity measurements from 04/07/15 corrected for: a. C2 C3 humidity variations (red markers), b. humidity variations and deviation from pseudo- first order kinetics (black markers) and c. humidity variations, deviation from pseudo- first order kinetics and dilution of ambient air .....	99
Figure 4:16 Measurements made by the UOL-CRM from 13/07/15 to 14/07/15 during periods of high NO events. Red dots show measurements before the	

application of the NO concentration derived correction factor, blue dots show measurements made after correction due to NO based OH recycling .....	101
Figure 4:17 Measurements made by the UOL-CRM from 04/07/15 to 05/07/15 before (red dots) and after (blue dots) the application of the NO concentration derived correction factor .....	101
Figure 4:18 Total OH reactivity measured during ICOZA campaign.....	104
Figure 4:19 Box and whisker plot depicting the measurements made by the UOL-CRM during the ICOZA campaign .....	105
Figure 5:1 Diagram of a quadrupole mass analyser adapted from Ellis and Mayhew (2014a).....	109
Figure 5:2 a. and b. measured concentrations of NMHCs and OVOCs throughout the ICOZA campaign. Measurements made via the UEA PTR-QMS and the UEA GC-FID.....	113
Figure 5:3 Measurements of OVOCs NMHCs NO <sub>x</sub> CO, ozone and wind direction measured during the field campaign .....	116
Figure 5:4 Total NMHC, OVOC and inorganic species measured during the field campaign, including calculated total OH reactivity. And their sources depending on wind direction .....	117
Figure 5:5 One day back trajectory showing the origin of air travelling to the measurement site.....	118
Figure 5:6 One day trajectories of air masses arriving at the measurement site .....	119
Figure 5:7 SO <sub>2</sub> concentrations measured during the ICOZA campaign and the corresponding wind direction.....	120
Figure 5:8 One day back trajectory depicting air travelling to the campaign site during the high ozone production regime .....	121

Figure 5:9 Calculated OH reactivity based on the concentrations of VOCs and inorganic species measured during the ICOZA campaign .....	127
Figure 5:10 A schematic of the University of Leeds LIF instrument. From (Stone et al., 2016) .....	128
Figure 5:11 (a) OH decay profile measured during a polluted period of the Clean Air for London (ClearfLO) campaign (2012), and (b) measurements made during a cleaner period of the campaign. Measurements made are shown with black point and red lines show the fits using E 5:1. Adapted from Stone et al. (2016). .....	131
Figure 5:12 Measurements of OH reactivity made by the University of Leeds using LIF instrument during the ICOZA campaign.....	133
Figure 5:13 Time series of measurements made using the UOL-CRM and the UL-LIF along with calculated total OH reactivity .....	136
Figure 5:14 Box and whisker plot comparing UOL-CRM measurement and calculated total OH reactivity .....	137
Figure 5:15 Box and whisker plot showing UOL-CRM data measured during the ICOZA campaign and the corresponding error within the mean.....	139
Figure 5:16 Measurements made of VOC concentrations throughout the ICOZA campaign (a.) (total OVOC, total NMHC), NO <sub>x</sub> (b.) along with total OH reactivity measured using both the UL-LIF and UOL-CRM and calculated total OH reactivity (c. and d.). Areas shaded in grey are regions of high instrument and calculated agreement and regions in blue are periods where there is little agreement, discussed, (the same regions are also highlighted in the figures below).....	140
Figure 5:17 (a). Calculated ratios of total OH reactivity measurements and calculations, UOL-CRM/Calculated reactivity, UOL-CRM/UL-LIF reactivity. (b). Ratio of UL-LIF/ calculated OH reactivity. Colour scale applied to both a. and b. show the concentrations of NO during the field campaign And (c). Ratios of UOL-CRM/UL-LIF reactivity, colour scales show the ratio of the VOC and inorganic	

species contribution to OH reactivity to the contribution of NO <sub>x</sub> to total reactivity .....	141
Figure 5:18 Magnification of Period 1 shown in Figure 5:17 .....	144
Figure 5:19 Magnified view of Period 2 from Figure 5:17 .....	145
Figure 5:20 Magnified view of Period 3 .....	147
Figure 5:21 Box and whisker plot of the OH reactivity measurements made by the UL-LIF and the UOL-CRM during the ICOZA campaign .....	150
Figure 5:22 Scatter plot comparing the UL-LIF measured OH reactivity to the calculated reactivity. Red line shows a 1:1 ratio between calculated and measured reactivity. The colour scale shows concentrations of NO measured during the campaign.....	152
Figure 5:23 a. and b. Correlations of the total OH reactivity measured by the UOL-CRM to the calculated total OH reactivity for periods 1 and 2. Colour scales depict concentrations of OVOCs and NMHCs. Lines in black show a 1:1 ratio .....	156

## **Chapter 1. Introduction**

The primary aim of this thesis is to quantify the rates of Hydroxyl radical (OH) loss through the use of the Comparative Reactivity Method (CRM). The CRM explores comparative reactions of OH with pyrrole and with atmospheric Volatile Organic Compounds (VOCs) in order to determine OH loss rate.

The CRM was first employed by Sinha et al. (2008), and the development of the CRM for use by the University of Leicester (UOL-CRM) is discussed within this thesis. Particular focus is paid to characterising the UOL-CRM, the determination of interferences and the procedures used to correct for these interferences.

A Proton Transfer Reaction- Time of Flight- Mass Spectrometer (PTR-ToF-MS) is coupled to the UOL-CRM. The feasibility of using a PTR-ToF-MS to simultaneously detect VOC concentrations and measure total OH reactivity through to the CRM technique is also discussed within this thesis.

The final chapters of this thesis discuss the use of the UOL-CRM during a field campaign. The stability of the instrument is explored and measurements are compared to both calculated total OH reactivity and a second instrument used to measure total OH reactivity (a pump- probe instrument). These comparisons aim to validate the UOL-CRM as any variables and interferences during periods of disagreement between the calculated OH reactivity and measurements made by the pump- probe method are characterised.

### **1.1 The structure of the atmosphere**

The atmosphere is a thin gaseous envelope surrounding the earth and is composed predominantly of nitrogen (78%), followed by oxygen at 20% and argon at 0.9%, (Table 1:1) (Harrison, 2007). It can be divided into a number of

layers depending on the temperature and pressure at a specific altitude (Figure 1:1).

Constituent	Molecular mass (g mol <sup>-1</sup> )	(% amount fraction)	
		(a)	(b)
Nitrogen (N <sub>2</sub> )	28.01	78.08 ± 0.004	78.09
Oxygen (O <sub>2</sub> )	32.00	20.94 ± 0.002	20.936
Argon (Ar)	39.95	0.93 ± 0.001	0.93
Carbon dioxide (CO <sub>2</sub> )	44.01	0.03 ± 0.001	0.040*

**Table 1:1 The main components of dry air**

Table adapted from Derwent (2001) and contains data from Glueckauf (1951). The CO<sub>2</sub> content was extrapolated from data collected from Callendar (1940).

\* recalculated for a CO<sub>2</sub> content of 400 ppm and oxygen consumption due to combustion of fossil fuels, assuming 48% of CO<sub>2</sub> have remained in the atmosphere. CO<sub>2</sub> concentrations from August 2016, from (Trans and Keeling)

These layers include:

1. The troposphere from the surface of the earth to an approximate height of 10- 15 km. Temperature within the troposphere ranges from -50°C during wintertime at the poles to a maximum of 40°C over the continents close to the equator (Webb and Coe, 2007).
2. The stratosphere lies above the troposphere (10-50 km). The ozone layer exists within the stratosphere which plays a key role in absorbing solar ultraviolet radiation thus reducing the amount of harmful UV rays entering the troposphere. At a height of approximately 50 km is the stratopause, in which the temperature of the stratosphere reaches a maximum (due to ozone UV absorption), thus marking the boundary of the stratosphere and the mesosphere as the atmospheric temperature within the mesosphere is cooler than the stratosphere
3. Above 50 km is the mesosphere. Atmospheric temperatures decrease in comparison to the stratosphere within the mesosphere and there are

large regions of turbulent motion. The mesosphere extends to 90 km in height where it reaches a temperature minimum at the mesopause.

4. Finally, above the mesosphere is the thermosphere. At this altitude, there is a large inversion in temperature in comparison to the mesosphere, and atmospheric pressure is significantly lower than at lower altitudes. So low that, species such as molecular oxygen and nitrogen dissociate as molecular collisions occur less often, (Webb and Coe (2007), Harrison (2007)).

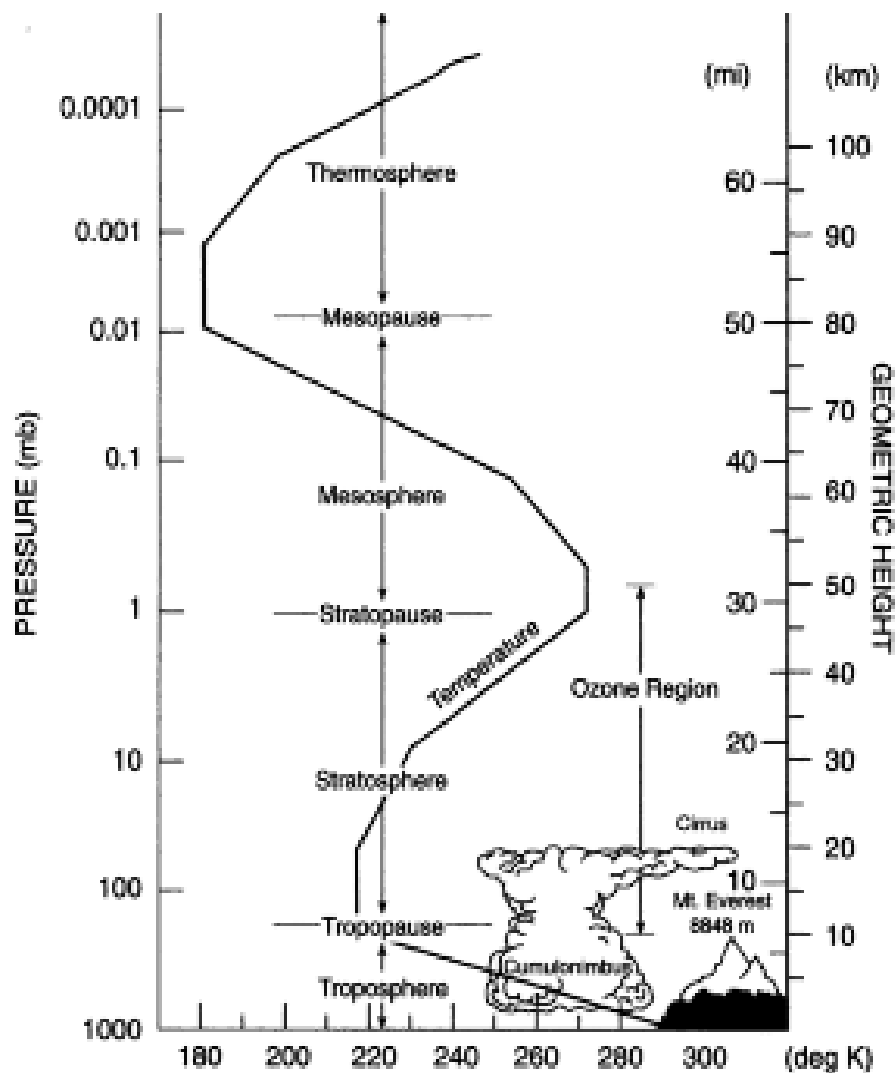


Figure 1:1 The vertical structure of the atmosphere. Vertical changes in temperature can be used as an indicator of different atmospheric layer. Adapted from Brasseur and Solomon (2005)

## 1.2 Tropospheric Hydroxyl radical (OH) chemistry

The hydroxyl radical, is a key molecule within that atmosphere dictates the pathways of many chemical reactions. It is capable of oxidising many VOCs, greenhouse gases and is able to initiate chain reactions in an oxygen containing atmosphere (Prinn (2003) H. Ehhalt (1999)) owing to its unpaired electron resulting in highly energetic molecules. This feature of the radical, plus its presence in high concentrations (up to  $10^7 \text{ cm}^{-3}$  (H. Ehhalt, 1999)) ensures its importance to the chemistry of the troposphere (Monks, 2007).

For example, less than 15% of tropospheric carbon CO is removed through the processes of soil microorganisms and bacteria, whereas approximately 85% is removed through the reaction with OH, a similar removal proportion pertains for methane ( $\text{CH}_4$ ), alkanes and biologically emitted VOCs (BVOCs) such as isoprene, all present within the troposphere (H. Ehhalt, 1999).

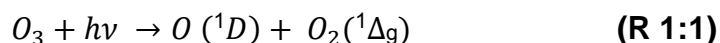
The importance of OH radicals in the removal of trace gases is summarised in Table 1:2, depicting the estimated emissions of various trace gasses per year and the percentage removed through their respective reactions with OH radicals.

	Global emission rate (Tg/ yr)	Removal by OH (%)	Removal by OH (Tg/ yr)
CO	2800	85	2380
$\text{CH}_4$	530	90	477
$\text{C}_2\text{H}_6$	20	90	18
Isoprene	570	90	513
Terpene	140	50	70
$\text{NO}_2$	150	50	75
$\text{SO}_2$	300	30	90
$(\text{CH}_3)_2\text{S}$	30	90	27

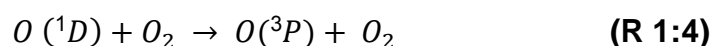
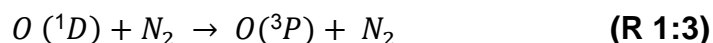
Table 1:2 estimated global emission rates of various trace gases (Tg) including the percentage and absolute amounts of each trace gas removed during their respective reactions with OH. According to H. Ehhalt (1999), the average concentration of OH was taken as  $1 \times 10^{-6}$  molecules  $\text{cm}^{-3}$  ( $1 \text{ Tg} = 10^{12} \text{ g}$ ). Adapted from Prinn (2003).

### 1.2.1 OH production

The major source of OH radicals is through the photolysis of ozone by UV light in the presence of water (Harrison, 2007) (R 1:1 and 1:2):



In the presence of molecular nitrogen and oxygen, most excited O(<sup>1</sup>D) atoms are quenched back to their ground state (R 1:3 1:4):



Other, secondary OH production pathways include the photolysis of: nitrous acid (HONO) in polluted regions (Lee et al., 2016), formaldehyde (HCHO), hydrogen peroxide (H<sub>2</sub>O<sub>2</sub>), and acetone (C<sub>3</sub>H<sub>6</sub>O). The reaction of O(<sup>1</sup>D) with methane is also considered a secondary source of OH (Harrison, 2007). OH can also be formed via reaction 1:9, as HO<sub>2</sub> formed in R 1:6 reacts with ozone.

The photolysis of HONO can be a major source of OH radicals in polluted regions and is of particular importance at sunrise. During early periods of the morning, the frequency of sunlight entering the troposphere has sufficient energy to dissociate HONO. As concentrations of HONO generally reach a maximum before or at sunrise, the rate of OH production then reaches a maximum at the same time (Alicke et al., 2003).

As HONO is rapidly photolysed, the primary source of OH production then shifts HCHO and ozone photolysis as seen in Figure 1:2.

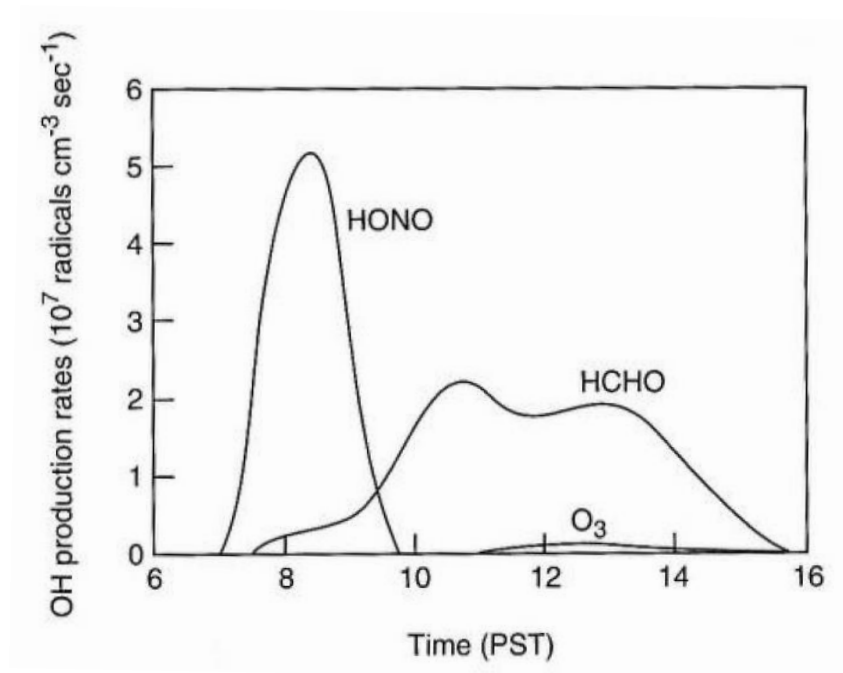
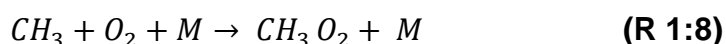
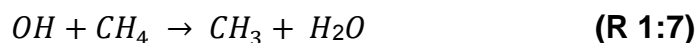


Figure 1:2 Calculated rates of OH production through the photolysis of HONO, O<sub>3</sub> and HCHO. Adapted from Winer and Biermann (1994) and Finlayson-Pitts and Pitts Jr (2000c)

## 1.2.2 Reactions of OH radicals

In areas where the concentration of NO<sub>x</sub> (NO and NO<sub>2</sub>) is low, OH radicals will primarily react with either carbon monoxide (CO) or methane (CH<sub>4</sub>). R 1:5 generates a hydrogen atom, which can further react with oxygen to produce a hydroperoxy radical HO<sub>2</sub> (R 1:6).



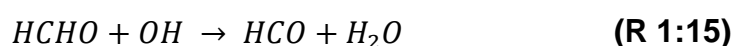
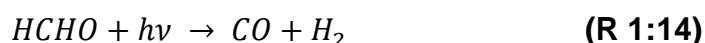
However, the reaction of OH with methane produces a CH<sub>3</sub> radical which then reacts with oxygen generating a methylperoxy radical (R 1:7 and 1:8).

When the concentration of NO is high (larger than approximately 10ppt) (Finlayson-Pitts and Pitts Jr, 2000b), the HO<sub>2</sub> radical formed in R 1:6 can react with NO to form NO<sub>2</sub> thereby recycling OH (R 1:10). This is because, the HO<sub>2</sub> radical is highly reactive, more so than O<sub>2</sub> as the addition of a hydrogen atom to an oxygen molecule weakens the bond between oxygen atoms within the radical, (H. Ehhalt (1999), Monks (2005)).

Whereas the methylperoxy radical generated in R 1:8 reacts with NO to form a methoxy radical that proceeds to generate formaldehyde as it reacts with molecular oxygen (R 1:10, 1:12)



Formaldehyde is then removed by photolysis (R 1:13), however, it can also react with OH forming a formyl radical (HCO). HCHO can then further react with oxygen to regenerate HO<sub>2</sub>, (R 1:13 to 1:16).

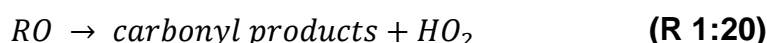
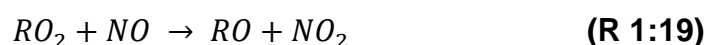


The reaction of OH with methane (R 1:7) illustrates the typical pathway for the reaction of OH with alkanes (R 1:17). As OH abstracts a hydrogen from the alkane forming a radical species and water as a by-product.

OH reacts with alkenes via the addition onto the alkene double bond to form an adduct or intermediate that can either decompose or be stabilised. The rate of reaction of OH radicals with hydrocarbons increases with increasing size and the number of branches within the hydrocarbon. This also depends upon the

number of primary, secondary and tertiary bonds within the hydrocarbon, as tertiary carbon hydrogen bonds react faster with OH than secondary bonds which in turn react faster with OH than primary bonds (Finlayson-Pitts and Pitts Jr, 2000b).

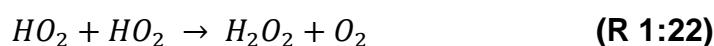
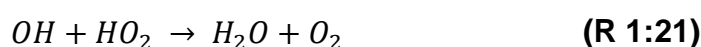
When the concentrations of non-methane hydrocarbons (NMHCs) along with NO<sub>x</sub> (the summation of NO and NO<sub>2</sub>) are elevated, the reactions of OH with hydrocarbons proceeds in a similar way to that seen in R 1:7. In which a radical of the alkyl chain is formed (R 1:17), the radical then proceeds to react with oxygen to form a peroxy- radical (RO<sub>2</sub>), (R 1:18), and following the reaction of the peroxy- radical with NO, oxy- radicals (RO) are formed (R 1:19) (Monks, 2005).



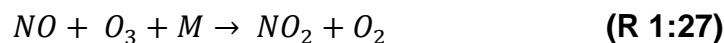
Finally, the peroxy- radicals formed in R 1:18 can either be photolysed (similarly to R 1:13 and 1:14) or will be further oxidised in thermal reactions, (Tuck (1992), Atkinson (1986), Atkinson (2007)).

### 1.2.3 HO<sub>x</sub> termination pathways

The reactions discussed above show that the OH radical has the ability to initiate chain reactions whilst maintaining a cycle where there is no net loss in OH. In order to terminate the cycle, (thus ensuring a net loss in HO<sub>x</sub> radicals), both OH and HO<sub>2</sub> radicals have to react with other radicals (R 1:21 to 1:23):

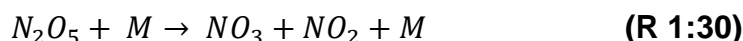
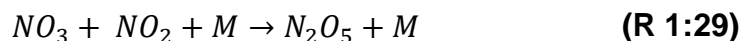
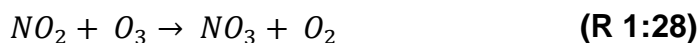






In addition to NO reacting with ozone, NO<sub>2</sub>, can also react with ozone to form a nitrate radical (NO<sub>3</sub>) (R 1:28) at night.

The nitrate radical can react with NO<sub>2</sub> to produce N<sub>2</sub>O<sub>5</sub> (R 1:29), which exists in equilibrium with NO<sub>2</sub> and NO<sub>3</sub> (R 1:29 and 1:30).



Reactions 1:5 and 1:6 leading to the formation of HO<sub>2</sub>, can ultimately result in the formation of ozone through reaction 1:10, and following this, reactions 1:25, and 1:26 within the troposphere. Therefore illuminating the fact that OH reactions with trace gases such as CO (in high NO environments) can produce ozone or other species that can be particularly harmful (H. Ehhalt, 1999).

## 1.4 Calculating OH concentrations and reactivity

OH radicals play a major role in tropospheric chemistry as they are to react with a wide range of compounds whilst possessing a short atmospheric lifetime (~1 s). Although OH radicals possess a short lifetime, large concentrations have been measured within the troposphere, (on the order of 2 x 10<sup>6</sup> molecules cm<sup>-3</sup>) (Monks, 2005).

As stated previously, the major source of OH production is through the photolysis of ozone, resulting in the production of excited oxygen atoms (R 1:1), and the subsequent reaction of the excited oxygen atoms with water vapour (R 1:2).

The rate of OH production can therefore be expressed as:

$$P(OH) = 2f[O_3] \times j(^1D) \quad (\text{E 1:1})$$

$$f = \frac{k_{1:2}[H_2O]}{k_{1:2}[H_2O] + k_{1:3}[N_2] + k_{1:4}[O_2]} \quad (\text{E 1:2})$$

Where  $k_{1:2}$ ,  $k_{1:3}$  and  $k_{1:4}$  are the rates at which oxygen atoms are quenched by water, oxygen and nitrogen.

The overall rate of change in OH concentration is expressed as:

$$-\frac{\delta[OH]}{dt} = P(OH) + k_{1:9}[HO_2][O_3] + k_{1:10}[HO_2][NO] + \sum_i v_i J_i [i] + P' - \sum_n k_{OH+L_n} [L_n][OH] \quad (\text{E 1:3})$$

Where  $v_i$  and  $J_i$  are the stoichiometric coefficients and the photolysis rates of any species ( $i$ ) that will generate OH after photolysis, (as mentioned in section 1.2.1, photolysis of HONO, formaldehyde and hydrogen peroxide).  $P'$  represents the rate of OH production from any other chemical reaction, such as the ozonolysis of alkenes, and  $L_n$  is the total loss rate of OH with all of its sinks.  $k_{OH+L_n}$  is the rate coefficient for the reaction of  $L_n$  with OH.

When the rate of OH production is equal to the rate of OH loss, a steady- state is established and the concentration of OH can be calculated (Stone et al., 2012) as:

$$[OH] = \frac{P(OH) + k_{1:9}[HO_2][O_3] + k_{1:10}[HO_2][NO] + \sum_i v_i J_i [i] + P'}{\sum_n k_{OH+L_n} [L_n]} \quad (\text{E 1:4})$$

Equation 1:4 derives OH concentration, by considering the rates of OH production and loss. However, in order to calculate OH loss (OH reactivity) due to a chemical, one must consider the concentration of the species reacting with OH and the respective OH reaction rate coefficient (E 1:5). In order to calculate total OH reactivity however, the concentration of all species (and their respective rate coefficient) that can react with OH must be considered, this includes: all NMHCs, all oxygenated volatile organic compounds (OVOCS), NO<sub>x</sub>, ozone and other inorganic species.

$$R(s^{-1}) = \sum k_{(x+OH)}[x] \quad \text{(E 1:5)}$$

By taking the inverse of E 1:5, the lifetime of the species that reacts with OH can be calculated, (Bell et al. (2003), Finlayson-Pitts and Pitts Jr (2000a)):

$$\tau = \frac{1}{k_{(x+OH)}[OH]} \quad \text{(E 1:6)}$$

Measurements of total OH reactivity act to help improve the understanding of tropospheric chemistry in a number of ways. For example:

1. Measurement of total OH reactivity and OH concentrations can be used to calculate OH production rates, assuming steady state conditions where the rate of production is equal to the rate of loss.
2. The accuracy of photochemical models can be better constrained using total OH reactivity measurements. Photochemical models must accurately consider all atmospheric species that can react with OH radicals, whereas OH reactivity measurements can be made using various instruments without the need to measure the concentrations of all atmospheric VOCs. These measurements can act to improve the accuracy of photochemical models.

3. Using Equation 1:5, total OH reactivity can be calculated based on the measured concentration of OH reactive species. This calculated total OH reactivity can be compared to measurements in order to determine any OH reactivity that can be considered as 'missing'. Where there is a significant difference between the measured and calculated total OH reactivity which can be attributed by unmeasured or unidentified VOCs (Michoud et al. (2015), Sinha et al. (2008)) .

## **1.5 Techniques used to measure OH reactivity**

A number of instruments have been developed for the specific purpose of measuring total OH reactivity (Heard and Pilling, 2003).

These techniques include: The Total OH Loss Method (TOHLM) (Kovacs and Brune, 2001), the pump- probe method (Sadanaga et al., 2004b) and the Comparative Reactivity Method (CRM) (Sinha et al., 2008). These measurement techniques synthetically generate OH radicals, a sample of ambient air then reacts with OH and a change in concentration is measured. By directly measuring the rate of OH decay using the TOHLM and pump- probe (indirect measurements of the changes in OH concentration and kinetics is measured by the CRM technique) methods, there is no need to measure the individual concentrations of all OH sinks within a certain environment (Sinha et al., 2008).

### **1.5.1 The TOHLM**

The TOHLM uses a flow tube to generate OH radicals through the photolysis of water vapour (184 nm UV light) (R 1:31). OH generated within the instrument is then injected into a larger flow tube where the radicals mix with trace gases from an ambient air sample (Figure 1:4).

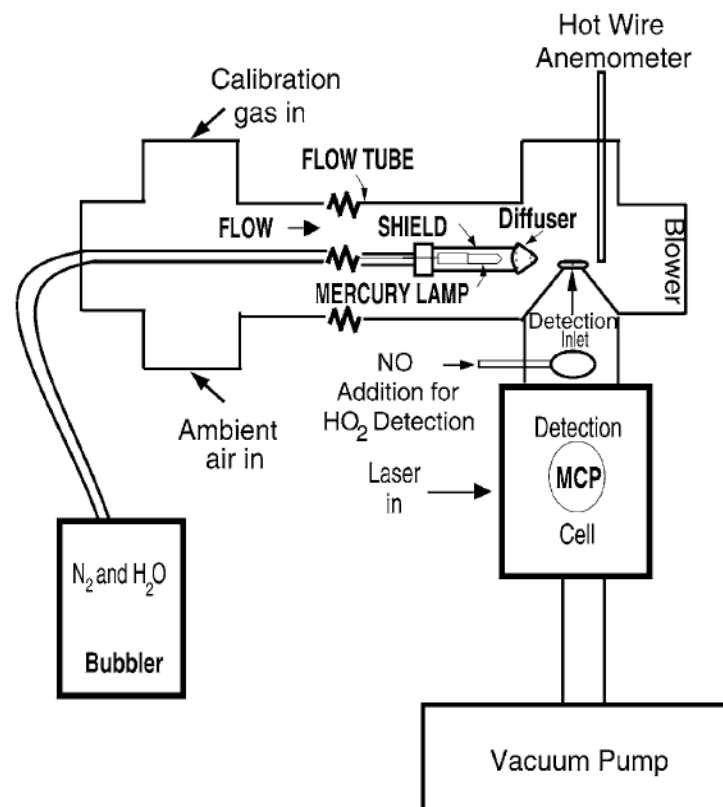


Figure 1:4 A schematic of the instrument employed by the TOHLM technique. From Kovacs and Brune (2001)

The sample is then detected using Fluorescence Assay with Gas Expansion (FAGE) (described within section 5.3). After a period of time, the injector is then pulled backwards, increasing the reaction time within the flow tube. Measurements are then made at different reaction times in order to measure a OH decay signal (Kovacs and Brune, 2001).

### 1.5.2 The pump- probe method

The second technique is the so- called pump- probe method (Sadanaga et al., 2004b). Ozone photolysis is used as a source of OH radicals inside a photolysis cell. OH radicals then react with trace gases within an ambient air sample. Using a FAGE laser, the OH radicals are then probed in order to measure OH decays. In contrast to the TOHLM, (in which a steady state of OH concentration is

needed for each position of the sample injector), the use of a laser to generate OH radicals enables OH decays to be recorded in real time, (Sadanaga et al. (2004b), Hansen et al. (2015), Stone et al. (2012)). A detailed description of the pump-probe method is discussed in section 5.3 and a schematic is shown in Figure 5:10.

### 1.5.3 The Comparative Reactivity Method (CRM)

A third technique used to measure total OH is the Comparative Reactivity Method (CRM). The CRM is a technique designed to measure OH reactivity. Initially developed by the Max Planck Institute, Mainz (Sinha et al., 2008). CRM involves the examination of competing OH radical reactions, the first with a specific reagent, the second with a sample of ambient air within a glass reaction vessel. A schematic of the glass CRM reaction vessel is shown in Figure 1:5.

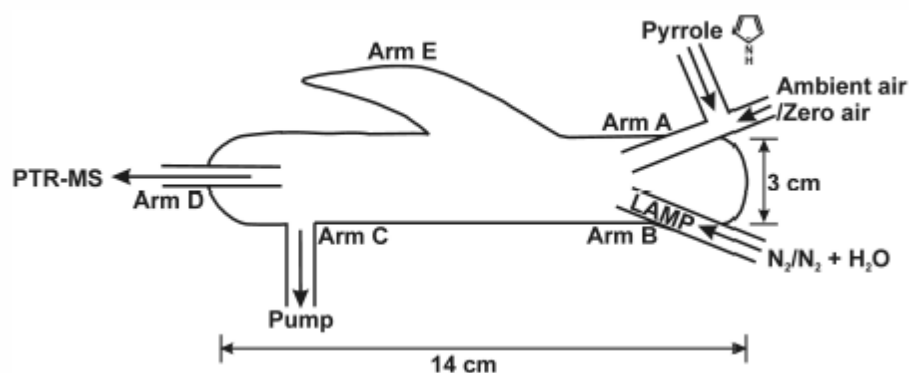


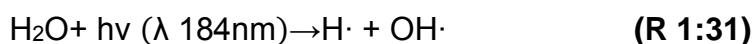
Figure 1:5 A schematic of the CRM glass reaction vessel adapted from (Sinha et al., 2008)

The methodology used by the CRM is as follows:

1. A reactant, pyrrole ( $C_4H_5N$ ) along with dry zero air (ZA) is introduced into the reaction vessel, and its concentration is determined by Proton Transfer Reaction - Time of Flight - Mass Spectrometry (PTR-

ToF-MS), (Rennie et al. (1999), Taipale et al. (2008)). The PTR-ToF-MS used in this thesis is discussed in further detail in section 2.3. Derivation of pyrrole concentrations from a PTR-ToF-MS signal is discussed in section 3.2. This phase of measurement is designated as C0 mode

2. A mercury UV lamp positioned within the glass reaction vessel is switched on, and the concentration of pyrrole is then determined, this is because the use of the UV lamp results in some photolysis of pyrrole, (the need for the UV lamp is discussed within step 3), this phase of measurement is labelled as C1 mode
3. Humidified nitrogen (nitrogen gas in the presence of water vapour) is then introduced into the reaction vessel and with the mercury UV lamp still switched on, OH radicals are produced through the photolysis of water vapour, according to reaction 1:31 (Creasey et al., 2000). Clean ambient air also flows through the reaction vessel at this time, this ensures that the humidity within the reaction vessel during this mode of measurement is the same as C3 mode (discussed below and in further detail in section 3.2). As OH within the reaction vessel reacts with pyrrole, the monitored concentration of pyrrole decreases (C2 measurement phase).



4. The final phase of measurement is C3. During this mode, ambient air is introduced into the reaction vessel along with pyrrole and the synthetically generated OH radicals. Any VOCs present within the ambient air will compete with pyrrole for the reaction with OH. This results in the increase in pyrrole concentration in comparison to C2 (Sinha et al., 2008).

An illustration of the changes in pyrrole concentration during each measurement phase is illustrated in Figure 1:6. Chapter 2 discusses each measurement phase in more detail and how phase is implemented, with the aid of a practical example of each measurement phase.

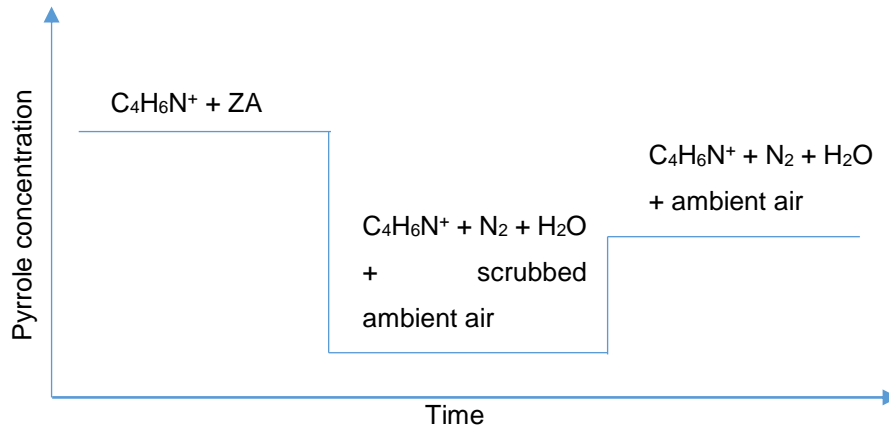


Figure 1:6 A representation of the CRM measurement principle depicting the changes in pyrrole concentration during various measurement periods, (Sinha et al., 2008)

OH loss occurs during C2 and C3, by comparing the concentration of pyrrole during C2 to the concentration during C3 (and the difference in kinetics for both modes of measurements), the loss of OH during both modes is given as:



The rate equations for both reactions are therefore:

$$-\frac{\delta[\text{OH}]}{dt} = k_p [\text{OH}] [\text{pyrrole}] \quad (\text{E 1:7})$$

$$-\frac{\delta[\text{OH}]}{dt} = k_{\text{OH}+\text{VOC}} [\text{OH}] [\text{VOC}] \quad (\text{E 1:8})$$

And a combined rate equation of:

$$-\frac{\delta[OH]}{dt} = k_p[OH][pyrrole] + k_{OH+VOC}[OH][VOC] \quad (\text{E 1:9})$$

Where  $k_p$  ( $\text{cm}^3 \text{ molecule}^{-1} \text{ s}^{-1}$ ) is considered the rate coefficient for the reaction of OH with pyrrole ( $\text{molecules cm}^{-3}$ ), and  $k_{OH+VOC}$  ( $\text{cm}^3 \text{ molecule}^{-1} \text{ s}^{-1}$ ) is the rate coefficient for the reaction of OH with the summed concentrations of VOCs within the ambient air sample. The rate coefficient  $k_p$  at  $25^\circ\text{C}$  is  $1.2 \times 10^{-10} \text{ cm}^3 \text{ molecule}^{-1} \text{ s}^{-1}$  (Dillon et al. (2012), Atkinson et al. (1984)).

If  $R_p$  is considered the first order rate loss of OH with respect to pyrrole, and  $R_{VOC}$ , the rate loss of OH with respect to VOCs within the air sample, then the change in pyrrole concentration (C1-C3) is given as:

$$(C1 - C3) = \frac{R_p}{R_p + R_{VOC}} \times [OH] \quad (\text{E 1:10})$$

As stated previously, the concentration of pyrrole is determined during C1 (during which, no OH is present within the reaction vessel), introducing OH radicals into the reaction vessel (during C2) results in the decrease in pyrrole concentration. Therefore, as pyrrole reacts completely with OH, the concentration of OH ( $\text{molecules cm}^{-3}$ ) is given as:

$$(C1 - C3) = \frac{R_p}{R_p + R_{VOC}} \times (C1 - C2) \quad (\text{E 1:11})$$

Rearranging E 1:11 gives:

$$R_{air} = \left( \frac{(C1 - C2)}{(C1 - C3)} - 1 \right) \times R_p \quad \text{(E 1:12)}$$

Considering the concentration of pyrrole is given as C1:

$$R_{VOC} = \left( \frac{(C1 - C2)}{(C1 - C3)} - 1 \right) \times k_p C1 \quad \text{(E 1:13)}$$

Finally, the calculation of total OH reactivity is given as: (Sinha et al., 2008)

$$R_{VOC}(s^{-1}) = \frac{(C3 - C2)}{(C1 - C3)} \times k_p C1 \quad \text{(E 1:14)}$$

The technique however, is prone to a number of interferences which need correcting (Michoud et al., 2015):

1. Differences in humidity within the sampled air results in different concentrations of OH within the reaction vessel during C2 and C3, (Sinha et al. (2008), Nölscher et al. (2012a), Sinha et al. (2009)).
2. The equations above assume that the CRM operates under a pseudo- first kinetics regime (the concentration of pyrrole is in excess of the OH). However, this is not the case and the UOL-CRM operates in conditions in which the concentration of pyrrole is at a maximum twice as high as the OH concentration, (Sinha et al., 2008).
3. An influx of high NO concentrations within the ambient air sample into the CRM reaction vessel results in the recycling of OH (Dolgorouky et al. (2012), Hansen et al. (2015), Michoud et al. (2015)).

4. The use of pyrrole and nitrogen during C3 results in the dilution of sampled VOCs during C3, this needs to be corrected for during the final calculations of total OH reactivity (Zannoni et al., 2015).

The determination into the degree at which these interferences need to be corrected are discussed in detail in chapter 3, and the implementation of these corrections to data collected during a field campaign is discussed in chapter 4 and 5.

#### **1.5.4 Comparisons of total OH reactivity measurement techniques**

All of the measurement technique mentioned above have their advantages and disadvantages. Table 1:3 compares the measurement principles, uncertainties and interferences between the TOLHM, pump- probe method and the CRM (adapted from Yang et al. (2016)). The TOHLM and the CRM are susceptible to interferences from high NO concentrations as photolysis of OH radicals will also generate HO<sub>2</sub> radicals (R 1:31 and 1:6). HO<sub>2</sub> radicals, will then react with NO to regenerate OH within the instrument (R 1:10) (Sadanaga et al. (2004b), Stone et al. (2016), Michoud et al. (2015), Shirley et al. (2006)). This artefact results in a deviation from the true OH reactivity and needs to be calibrated and corrected for. Corrections due to NO based OH recycling within the CRM is discussed in chapter 3.

As stated previously, in order to establish a series of reaction times in the TOHLM technique, the position of the OH injector needs to be varied, this requires time to establish a steady state concentration of OH. However, the use of a laser allows the pump- probe technique to generate a constant, stable concentration of OH radicals, (Hansen et al. (2015), Stone et al. (2016), Sadanaga et al. (2004b)). OH radicals are also generated within the CRM at a constant concentration, however this also depends upon the humidity of the ambient air entering the reaction vessel, if the humidity of the air sampled during the C2 measurement phase is significantly different to that during C3, there will

be a discrepancy in the concentration of OH when comparing both phases of measurement. This will ultimately result in different C2 and C3 reaction rates as the concentration of OH changes (E 1:7 and 1:8). However, any difference in C2 and C3 humidity is compensated for with the use of a catalyst and a humidity calibration.

Other interferences that result in deviations from a true measurement of OH reactivity with the CRM technique are stated above and discussed in more detail in chapter 3.

Method	TOLHM	Pump-probe	CRM
OH radical production	Photolysis of water	Photolysis of ozone	Photolysis of water
Measurement principal	Direct measurement of OH decay	Direct measurement of OH decay	Measurement of reference species concentration
Detector	FAGE	FAGE	PTR-MS/ GC-PID
Main interference	NO recycling		Humidity, NO recycling, temperature
Uncertainty	10-15%	10-20%	43% <sup>b</sup> 15-20% <sup>c</sup>

**Table 1:3 Comparisons of total OH reactivity measurement techniques. Adapted from Yang et al. (2016).**

<sup>a</sup>. CRM interferences and corrections are described in chapter 3. Within this work the effect of temperature fluctuations on CRM data are discussed within section 4.5. <sup>b</sup>. An uncertainty of 43% was calculated for this work and is described in further detail in section 3.8. <sup>c</sup>. Uncertainties determined within previous work.

A third interference was also determined within the frame of the University of Leicester CRM, in which temperature fluctuations within the shipping container that housed the University of Leicester CRM resulted in variations of the detected PTR-MS signal. This interference is not described in other CRM work

by Sinha et al. (2008), Michoud et al. (2015), as the detector used in previous work was not subject to this interference, it was however determined that the Kore Technology PTR-ToF-MS used here is. The effect of temperature on the detected PTR-ToF-MS signal and overcoming this issue is discussed in section 4.5.

Comparing total OH reactivity measurement techniques, the CRM shows similar uncertainty to both the TOHLM and the pump-probe method. However, the CRM used within this work has a higher uncertainty due to errors within techniques used to correct reactivity data, (described within section 3.8).

The CRM is able to measure a wide range of total OH reactivity, ranging from the Limit of Detection (LOD) to a maximum of  $130 \text{ s}^{-1}$  measured by Dolgorouky et al. (2012). However, in comparison, the CRM measures at a lower limit of detection in comparison to the TOHLM and pump- probe method. The LODs and time resolutions for each OH reactivity measurement technique is shown in Table 1:4.

Technique	Reference	LOD (s <sup>-1</sup> ) <sup>a</sup> / time resolution (min)	Institution	Comments
TOHLM	Kovacs and Brune (2001)	2.4/4	Penn State University, USA	Laminar- flow reactor
	Ingham et al. (2009)	2.0/5	University of Leeds, UK	Turbulent- flow reactor
	Hansen et al. (2014b)	2.1/2.5	Indiana University, USA	Turbulent- flow reactor
Pump-probe	Sadanaga et al. (2004b)	<sup>-b/</sup> 3 <sup>c</sup>	Tokyo, Metropolitan University, Japan	-
	Lou et al. (2010)	0.9 <sup>d</sup> /1-3	Forschungszentrum Julich, Germany	-
	Michoud et al. (2015), Amedro et al. (2012)	3.6-0.9/ 1-3	University of Lille-PC2A, France	-
	Stone et al. (2016)	1-1.5/ 1-3	University of Leeds, UK	-
CRM	Sinha et al. (2008)	3.5-6 <sup>e</sup> /1	Max Planck Institute Mainz, Germany	PTR-QMS <sup>f</sup>
	Kim et al. (2011)	15/ <sup>-b-</sup>	NCAR, USA	PTR-QMS branch enclosure measurements
	Nölscher et al. (2012b)	3-6 <sup>h</sup> / 1	Max Planck Institute Mainz, Germany	GC-PID
	Dolgorouky et al. (2012)	3.0/2 <sup>i</sup>	LSCR, France	PTR-QMS
	Kumar and Sinha (2014)	4/1	IISER Mohali, India	PTR-QMS
	Hansen et al. (2015)	3.4/5	Mines Douai, France	PTR-ToF- MS
	This Work	5/1	University of Leicester, UK	PTR-ToF- MS

**Table 1:4 Summary of OH reactivity instruments. Adapted from Hansen et al. (2015).**

<sup>a</sup> Limit of detection:  $3\sigma$  unless otherwise stated, <sup>b</sup> value not reported, <sup>c</sup> value reported by Yoshino et al. (2006), <sup>d</sup>LOD determined from  $3\sigma$  in zero air reported by Lou et al. (2010), <sup>e</sup> LOD of  $6\text{ s}^{-1}$  reported by Sinha et al. (2008), LOD of  $3.5\text{ s}^{-1}$  reported by Sinha et al. (2010), <sup>f</sup> Proton Transfer Reaction-Quadrupole Mass Spectrometry, <sup>g</sup> values taken from Table 2 of Nölscher et al. (2012a), <sup>h</sup> value reported for  $2\sigma$  relative to C<sub>2</sub>, <sup>i</sup> based on frequency of measurements made in Figure 8 of Dolgorouky et al. (2012).

## 1.6 Previous measurements of total OH reactivity

The first set of OH reactivity measurements utilising the CRM technique was made by Sinha et al. (2008) at the Max Planck Institute, Germany.

However the CRM technique described in this thesis has changed slightly in comparison to that described in Sinha et al. (2008). The method discussed in Sinha et al. (2008) had no heated catalyst attached to the glass reaction vessel (whereas the CRM used within this thesis does utilise a heated catalyst). The lack of a catalyst results in large differences in humidity during the C2 mode of measurement in comparison to C3. As, C2 consisted of sampling pyrrole along with, synthetically generated OH and dry zero air, whereas during C3, zero air is replaced with ambient air of higher humidity.

Other OH reactivity measurements using the CRM have employed a PTR-QMS as a pyrrole detector, (Sinha et al. (2008), Kim et al. (2011), Dolgorouky et al. (2012) and Kumar and Sinha (2014)) (Tables 1:4 and 1:5). However, Nölscher et al. (2012a) have explored the use of a Gas- Chromatography- Photo Ionisation Detector (GC-PID), rather than a PTR-Mass Spectrometer. This alternative to a mass spectrometer however has a number of disadvantages, for example: the GC-PID results in a higher total OH reactivity limit of detection ( $3 - 6 \text{ s}^{-1}$ ) compared to  $3 - 4 \text{ s}^{-1}$  measured with a PTR-MS, and a higher degree of uncertainty (25 - 46 %) compared to 16 - 20% uncertainty in PTR-MS measurements,

More recently, Michoud et al. (2015), have moved away from using a PTR-QMS as a detector to a PTR-ToF-MS, this type of detector has its advantages and disadvantages over a PTR-QMS. The disadvantage is that the PTR-QMS is ion selective, as the use of a quadrupole allow many unwanted ions to be filtered out. Therefore the quadrupole is tuned to only detect a signal of pyrrole thus generating higher detection sensitivities in comparison to a PTR-ToF-MS, (Ellis and Mayhew, 2014a). However, this can also provide an advantage for the PTR-ToF-MS over the PTR-QMS, as the ability to monitor multiple ions in a single scan means that VOCs can be detected in ambient air samples whilst at the same time measuring changes in pyrrole concentrations for the CRM.

Kumar and Sinha (2014), have in fact adapted the CRM sampling strategy to accommodate for VOC measurements, in which ambient air is sampled in between C2 and C3 measurement modes. Within this thesis, the same method is used as concentrations of a number of VOCs are measured simultaneously to total OH reactivity.

Table 1:5 shows that the CRM has been utilised for OH reactivity measurements in a number of environments, from the Amazon rainforest (Nolscher et al., 2016), to a European megacity such as Paris, France (Dolgorouky et al., 2012) in which a wide range of total OH reactivity has been measured.

For example, Nolscher et al. (2016) have measured total OH reactivity during a dry and wet season within the Amazon at  $62.4 \text{ s}^{-1}$  and  $9.9 \text{ s}^{-1}$  respectively. Whereas a range in total OH reactivity is measured in Paris by Dolgorouky et al. (2012) depending on the trajectory of the air mass passing over the city. One period at which the OH reactivity measured was at  $130 \text{ s}^{-1}$  a second at  $20 \text{ s}^{-1}$  and a third at  $110 \text{ s}^{-1}$  as air masses from Germany, from the Atlantic Ocean and from Germany again passed over the sampling location.

In contrast, measurements made using the pump- probe method by Lee et al. (2009) at a coastal location (Weybourne Atmospheric Observatory, Norfolk), show a significant difference in total OH reactivity to the measurements discussed above (the Amazon rainforest and Paris). As an average total OH reactivity of  $4.85 \text{ s}^{-1}$  was recorded. This measurement however is higher than that calculated based on measured concentrations of VOCs ( $1.9 \text{ s}^{-1}$ ) (calculated using E 1:5). This difference is observed during other field campaigns (Table 1:5).

The difference between calculated and measured total OH reactivity is evidence for unknown species that contribute to total OH reactivity. Discrepancies between measured and calculated total OH reactivity arise because E 1:5 considers all species that act as a sink for OH.

During some field campaigns however, ancillary measurements are sometimes unable to determine the entire contribution of all OH sinks to total OH reactivity for a variety of unmeasured and unidentified species, (Yang et al., 2016). Di

Carlo et al. (2004) have determined that some missing reactivity is temperature dependant, and monoterpene emissions respond to fluctuations in temperature, Yoshino et al. (2006) in contrast, have observed that secondary oxidation products by photochemical reactions are responsible for missing reactivity.

Campaign	Site	Dates	Environment	Technique	Collected Measurements <sup>a</sup>	Missing OH reactivity fraction <sup>b</sup>	k <sub>OH</sub> (measured) (s <sup>-1</sup> )	Reference
SOS	Nashville, TN, USA	Jun- Jul 99	Urban	TOHLM	HICOF	1.4	11.3	Kovacs et al. (2003)
PROPHET 2000	Michigan, USA	Jul- Aug 00	Forest (mixed)	TOHLM	HIC <sup>c</sup>	~1.5	1-12	Di Carlo et al. (2004)
TexAQS 2000	Houston, TX, USA	Aug- Sept 00	Urban	TOHLM	HICOFB <sup>d</sup>	~1	7-12	(Mao et al., 2010)
PMTACS-NY	New York City, USA	Jun- Aug 01	Megacity	TOHLM	HICOF	~1	15-25	Ren et al. (2003)
-	Pennsylvania, USA	May- Jun 02	Rural	TOHLM	HI <sup>e</sup>	-	6.1	Ren et al. (2005)
PMTACS	Whiteface Mountain, USA	Jul- Aug 02	Forest (mixed)	TOHLM	HICOF	~1	5.6	Ren et al. (2006)
CareBeijing-2006	Yufa, China	Summer, 2006	Suburban	Pump- probe	I	-	10-30	Lu et al. (2010), Lu et al. (2013)
MCMA 2003/ MILAGRO	Mexico City, Mexico	Apr-03	Megacity	TOHLM	HICF <sup>e</sup>	-	10-120	Shirley et al. (2006)
-	Tokyo, Japan	Jul- Aug 03	Megacity	Pump- probe	ICOFB	1.4-1.5	10-100	Sadanaga et al. (2004a)
PMTACS	New York City, USA	Jan- Feb 04	Megacity	TOHLM	HICF	<1.5	18-35	Ren et al. (2006)

**Table 1:5 Previous OH reactivity field campaign measurements. Adapted from Hansen et al. (2015) and Yang et al. (2016).**

<sup>a</sup> Measurements made at the same location. Key: H= HO<sub>2</sub>, I= inorganics (including CO), C= anthropogenic NMHCs (including isoprene), O= OVOCs (excluding formaldehyde), F= formaldehyde, B= biogenic VOCs (BVOCs). <sup>b</sup> Missing OH reactivity, expressed as a ratio of measured total OH reactivity to total OH reactivity (Lou et al., 2010). <sup>c</sup> OVOCs, formaldehyde and BVOCs estimated from 1998 PROPHET campaign for OH reactivity calculation. <sup>d</sup> Based on description from (Mao et al., 2010). <sup>e</sup> Ancillary measurements not used to calculate total OH reactivity during this campaign. <sup>f</sup> Measurements of isoprene oxidation products not used in OH reactivity calculations. <sup>g</sup> Branch enclosure measurements. <sup>h</sup> Ambient measurement. <sup>i</sup> No measurements of CO, limited coverage of OVOCs and formaldehyde. <sup>j</sup> Data collected by the University of Leeds and presented within this work.

TORCH-2	Weybourne Norfolk, UK	May, 04	Costal marine	TOHLM	HICOF	1.6	4.85	Lee et al. (2009)
-	Tokyo, Japan	Nov-04	Megacity	Pump- probe	ICOFB	1.3	10-100	Yoshino et al. (2006)
-	Mainz, Germany	Aug-04	Urban	CRM	-	-	10.4	Sinha et al. (2008)
HO <sub>x</sub> Comp	Julich, Germany	Summer, 2005	Suburban	Pump- probe	-	-	6-20	Elshorbany et al. (2012)
-	Brownsburg, Suriname	Oct-05	Forest (tropical)	CRM	CO	~3.5	53	Sinha et al. (2008)
PRIDE-PRD	Backgarden, China	Summer, 2006	Suburban	Pump- probe	I	-	10-120	Lou et al. (2010)
INTEX-B	Pacific Ocean	Apr- May 06	Marine	TOHLM	HICOF	2.5	4.0	Mao et al. (2009)
PRIDE-PRD2006	Pearl River Delta, China	Jul-06	Rural	Pump- probe	HIC	~2	10-120	Lou et al. (2010)
TRAMP2006	Houston, TX, USA	Aug- Sept 06	Urban	TOHLM	HICOFB	~1	9-22	Mao et al. (2010)
-	Tokyo, Japan	Aug- Sept 07	Megacity	Pump- probe	ICOFB	~1.4	10-55	Chatani et al. (2009)
OP-3	Borneo, Malaysia	Apr- May 08	Forest (tropical)	TOHLM	HICOFB <sup>f</sup>	~2	83	Edwards et al. (2013)
SMEAR-BFORM	Hyytiala, Finland	Aug-08	Forest (boreal)	CRM	ICOB	~2	3.5-60	Sinha et al. (2010)
BEACHON-SRM08	Colorado, USA	Aug-08	Forest (conifer)	Pump- probe	ICOB	1.4	6.7	Nakashima et al. (2014)
DOMINO	El Arensillo, Spain	Nov- Dec 08	Costal marine	CRM	HIF <sup>e</sup>	-	6.3-85	Sinha et al. (2012)
BEARPEX09	California, USA	Jun- Jul 09	Forest (conifer)	TOHLM	HICOFB	~1.5	24	Mao et al. (2012)
CABINEX	Michigan, USA	Jul- Aug 09	Forest (mixed)	CRM	COB	~1		Kim et al. (2011)
CABINEX	Michigan, USA	Jul- Aug 09	Forest (mixed)	TOHLM	HICOFB	~2	3-33	Hansen et al. (2014a)
MEGAPOLI	Paris, France	Jan- Feb 10	Megacity	CRM	ICO	~2	10-130	Dolgorouky et al. (2012)
CalNex--SJV	California, USA	May- Jun 10	Rural	TOHLM	HICO	-	2.1	Pusede et al. (2014)
HUMPPA-COPEC	Hyytiala, Finland	Jul- Aug 10	Forest (boreal)	CRM	ICOFB	3-9	3-76	Nölscher et al. (2012b)
CleafLO	London, UK	Jul- Aug 12	Megacity	Pump- probe	HIOFB	-	15-116	Whalley et al. (2016)

Table 1:5 continued

-	Lille, France	Oct-12	Urban	CRM, Pump-probe	ICOF <sup>i</sup>	~1	~70	Hansen et al. (2015)
	Dunkirk, France	Summer, 2014	Urban	CRM	IOC	-	10-130	Michoud et al. (2015)
ATTO	Amazon Rainforest, Brazil	Oct-12-Sept- 13	Forest (tropical)	CRM	IOCB	79% (dry season), 49% (wet season)	62.4 dry season, 9.9 wet season	Nolscher et al. (2016)
-	Beijing, China Amazon Rainforest, Brazil	Aug- 13 Sept- 13	Megacity Forest (tropical)	CRM	ICO	-	19.98	Williams et al. (2016)
CANOPEE	Haute Provence, France	Summer, 2014	Forest	CRM	IFOB	Daytime match, possible night time missing	3-70	Zannoni et al. (2016)
ICOZA	Weybourne Norfolk, UK	Jul- Aug 15	Costal marine	CRM, Pump-probe <sup>*</sup>	HIOCF	5.2	14.4	This work

Table 1:5 continued

## 1.7 Thesis objectives and structure

OH reactivity measurement techniques have increasingly become a standard measurement parameter during field campaigns, with the use of the TOHLM and pump-probe techniques along with the CRM. They provide insight into the extent to which OH sinks, during pollution regimes contribute to the loss of OH.

The research presented in this thesis will aim to build, develop, calibrate and validate a suitable instrument that measures total OH reactivity using the CRM technique, with the final aim of employing this technique in a number of field campaigns. The innovation was to explore the application and insights that could be added using a PTR-ToF-MS detector with the capability to simultaneously measure OH reactivity and VOC concentrations.

Chapter two discusses the CRM instrument built at the University of Leicester, the fundamentals of how each measurement mode (C1, C2 and C3) are employed by the UOL-CRM and a background discussion on the PTR-ToF-MS that is coupled to the UOL-CRM.

Chapter three then moves on to characterise and calibrate for the interferences which result in deviations of measured total OH reactivity from a true measurement of OH reactivity. These interferences and artefacts are briefly stated above, (section 1.5.3), variations in C2 and C3 relative humidity, NO driven recycling of OH and deviations from pseudo- first order kinetics.

The calibrations conducted above are then applied to field campaign measurements made by the UOL-CRM at a coastal location of the UK. The results of these measurements, the performance and stability of the UOL-CRM and PTR-ToF-Ms are then discussed in chapter four.

Following from this, the measurements that are shown in chapter four are then compared to measurements made by a pump- probe, the University of Leeds Laser Induced Fluorescence instrument (UL-LIF), and also compared to calculations of total OH reactivity. This acts to validate the UOL-CRM by comparing measurements to an established technique. Any variations in measurements errors and interferences are then explored.

Finally, chapter six concludes this thesis and discusses future work.

## Chapter 2. Instrument Development

### 2.1 Introduction

The University of Leicester CRM (UOL-CRM) consists of a Pyrex reaction vessel that is used to mix pyrrole, zero air, ambient air, OH radicals and a gas standard (propyne) coupled to a PTR-ToF MS acting to detect changes in pyrrole concentrations.

### 2.2 Glass Reactor

Figure 2:1 shows a diagram of the reaction vessel used in the UOL-CRM instrument. The 14 cm x 10 cm x 2 cm Pyrex vessel is internally coated with Teflon and has three inlet arms attached, along with two output arms. The reaction vessel was crafted and Teflon coated by the John Williams group at the Max Planck Institute Mainz, and delivered to the University of Leicester for use as a standard reaction vessel in CRM measurements.

The caveat in using a mercury UV lamp to generate OH radicals via the photolysis of water (R 1:31) is the potential photolysis of trace gases and pyrrole within the reactor. In order to minimise the interference that can occur if pyrrole and VOCs within the sampled ambient air are photolysed, a tapered Wood's horn exists on the vessel.

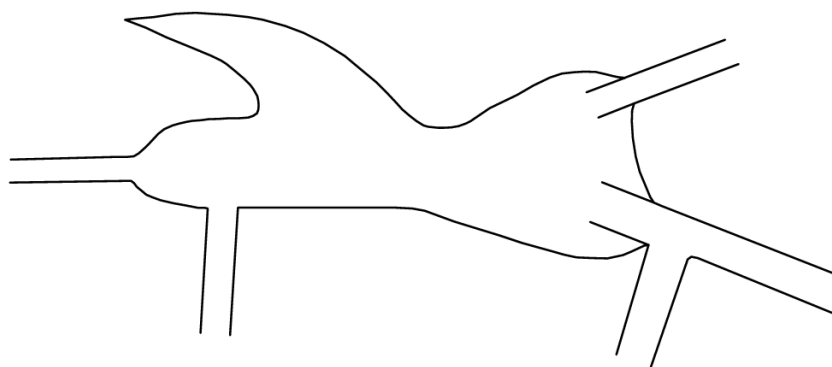


Figure 2:1 Schematic of University of Leicester CRM reaction vessel

The Wood's horn is a curved surface that acts to attenuate a beam of UV light entering the reaction vessel by reflecting off each side of the horn, acting to reduce the degree of photolysis of gases flowing into the reactor (Moore and Coplan., 2009). It is important to note that, in comparison to the Wood's horn shown in Figure 2:2, the UOL-CRM reaction vessel is not blackened on both the inside and outside of the reaction vessel.

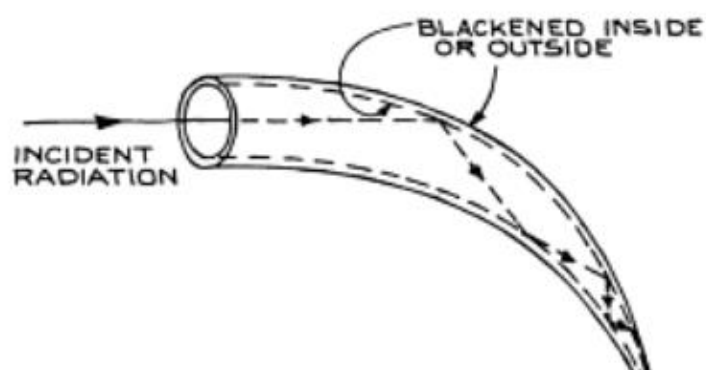


Figure 2:2 A magnified diagram of the Wood's horn depicting the principles of its operation. Adapted from Moore and Coplan. (2009)

### 2.2.1 The configuration of the UOL-CRM and various phases of measurements

The UOL-CRM consists of seven Tylan mass flow controllers (MFCs) used to regulate the flows of pyrrole (BOC, 10 ppm in nitrogen), nitrogen (BOC) and zero air (BOC) into the reaction vessel through quarter inch Teflon tubing, (Figure 2:3). The same configuration shown in Figure 2:3 is used in laboratory calibrations, testing and on field campaigns, shown in chapters three, four and five.

Owing to the design of the reaction vessel (two inlet arms and two output arms), pyrrole is mixed with either: ambient air, zero air, or propyne (test gas) before it is introduced into the reaction vessel, and a separate arm is used for an inlet flow of nitrogen (Figure 2:3).

For calibration purposes, propyne can be used to test the reactivity and response of the system (controlled by a 100 sccm MFC). The OH reactivity is measured with respect to propyne in order to validate the instrument and determine, if there is a large discrepancy between the measured reactivity and calculated reactivity (section 3.4).

Two water bubblers generate water vapour and, along with a UVP mercury pen ray lamp, one bubbler creates the OH radicals necessary for the CRM technique by passing humidified nitrogen over a UV lamp, the second bubbler is used for amplifying the humidity levels within the reaction vessel (via the flow of humidified zero air) during the experimentation discussed within section 3.3. During OH reactivity measurements, this flow of zero air is not used.

Like the bubbler designed to deliver humidified nitrogen, zero air is split through a 500 sccm MFC for dry air, and a 100 sccm MFC for humid air in order to quickly and accurately adjust the humidity levels within the UOL-CRM reaction vessel.

One Solenoid valve is used to direct a flow of ambient air after it has been drawn through a Teflon diaphragm pump into either, a heated catalyst for C2 mode or the catalyst is bypassed so ambient air flows directly into the reaction vessel for C3 mode.

A second Solenoid valve is used to divert the flow of ambient air from the reaction vessel completely, this allows the PTR-ToF-MS to sample ambient air directly.

The MFCs used vary depending on which mode the instrument is in at the time. The flow of nitrogen is split through two MFCs (one 100 sccm MFC used for dry air, and another 100 sccm used for humid air). For C0 dry (section 2.2.1.1) and C1 (section 2.2.1.2), nitrogen flows through a 100 sccm dry MFC, along with pyrrole through a 50 sccm MFC, and zero air through a 500 sccm MFC into the glass reactor (Figure 2:3).

Included with an explanation of each measurement phase below is, a detailed representation of the flow changes along with the corresponding pyrrole concentration changes (for each measurement mode) in Figure 2:9. This

example is taken from a series of measurements taken on the 22<sup>nd</sup> of July during a field campaign at a site in Weybourne, Norfolk, (see Chapter 4 and Chapter 5).

Some degree of scatter is observed within Figure 2:9, this is owing to noise within the PTR-ToF-MS reagent ion signal. This noise signal propagates into the measured pyrrole signal. Any large variations within the mass spectrometers signal when making measurements are corrected through normalisation, (described in section 3.2).

### **2.2.1.1 C0 wet and C0 dry modes**

The first mode in the UOL-CRM measurement cycle is C0 wet and is used as a starting point for measurements in combination with C0 dry. C0 wet (Figure 2:4) is a measurement of pyrrole concentration diluted with zero air and in humid nitrogen with no UV light. Whereas, C0 dry (Figure 2:5) is measured in the same conditions, however dry nitrogen is used instead of humid nitrogen.

A ratio of C0 dry to C0 wet needs to be calculated, and multiplied by the pyrrole concentrations in modes C2 and C3. This is because the sensitivity of pyrrole within the mass spectrometer is humidity dependant (see section 3.3 for further details). C2 and C3 are measured in humid conditions, whereas the PTR-MS pyrrole sensitivity, (used to convert from the detector ion count rate to a concentration during all measurement modes) (section 3.2) is calculated through a calibrations completed in dry conditions. However, discrepancies in pyrrole sensitivities are observed when calibrating in dry air, in comparison to humid air, (Sinha et al., 2009). In order to correct for this, a ratio of C0 wet to C0 dry is calculated in order to obtain an accurate pyrrole concentration for C2 and C3 measurement modes.

For C0 wet, humid air is introduced into the vessel through a water bubbler. This is done by switching a dry 100 sccm nitrogen MFC off, and a second 100 sccm MFC on, allowing a flow of nitrogen into the bubbler, (Figure 2:3). The flow rates of gases entering the reaction vessel is the same during C0 dry mode as it is in

C0 wet mode, thus ensuring that the concentration of pyrrole is always diluted to the same degree during both measurement modes.

When switching between C0 wet and C0 dry, the reaction vessel needs to be dried completely in order to avoid any humid air within the vessel introducing a bias altering the measured ratio of C0 wet/ C0 dry. This is done by flushing the vessel with dry nitrogen and zero air. The MFCs regulating the flow of these gases are increased to their maximum to ensure that the time taken to dry out the reaction vessel is kept to a minimum, (approximately 10 minutes). A temperature, pressure and humidity sensor (Hygrosens CON-HYTE-LOG humidity and temperature probe) connected to the exhaust flow of the vessel is used to monitor humidity changes between C2 and C3, it is also used to determine if the vessel is completely dry before C1 measurements, (Figure 2:3).

In Figure 2:9, the average concentration during C0 wet is 600 ppb, as the mode of measurement is changed to C0 dry, the average pyrrole concentration decreases to 590 ppb. This is due to the changes in the PTR-ToF-MS sensitivity that occur when sampling in dry air and humid air, (Sinha et al., 2009), this is discussed in greater detail in section 2.3.2 and in 3.3.

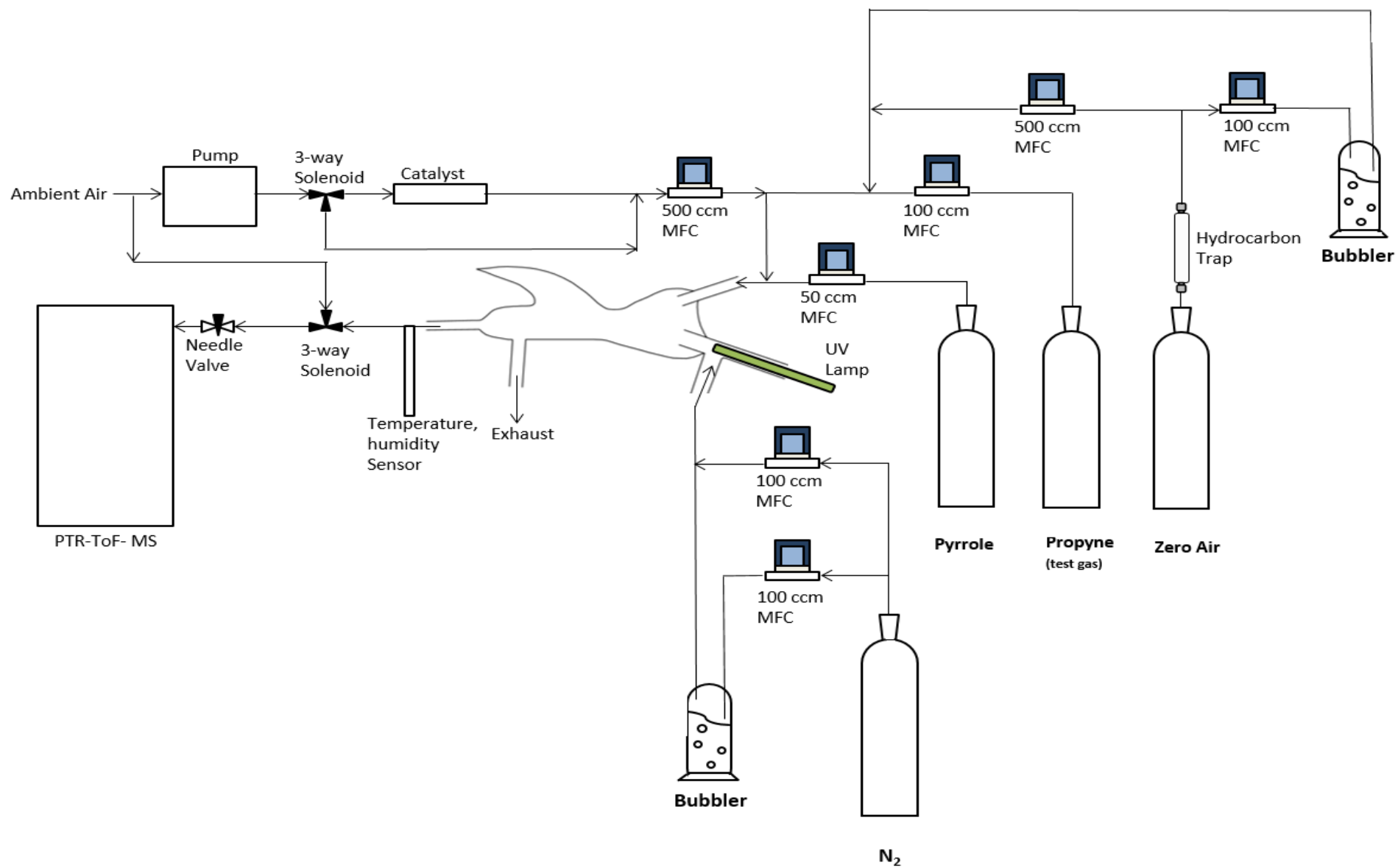


Figure 2:3 A schematic representation of the CRM set up developed at The University of Leicester

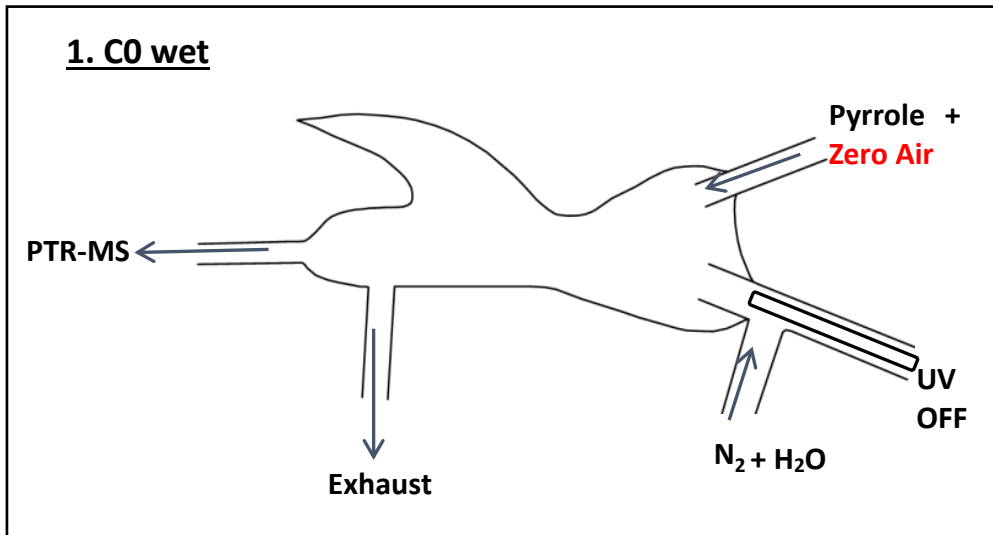


Figure 2:4 C0 wet measurements are conducted with pyrrole, zero air and nitrogen and water vapour. No UV light enters the reaction vessel at this time

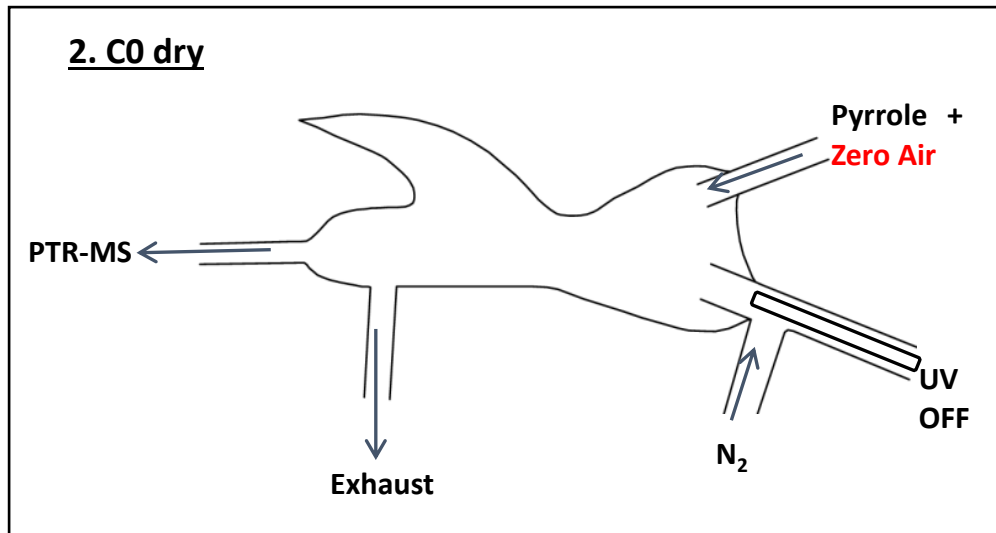


Figure 2:5 C0 dry measurements are conducted with pyrrole, zero air and dry nitrogen with no UV light entering the reaction vessel at this time

### 2.2.1.2 C1 mode

During C1, (Figure 2:6) the mercury UV lamp is switched on. As the reaction vessel is dry during this period, no OH radicals are produced. Therefore, C1 is used to determine the initial concentration of pyrrole within the vessel.

The same mass flow controllers used to regulate the flow of nitrogen and zero air into the reaction vessel during C0 dry are used in C1, (Figure 2:3).

As the UV light is switched on (C1 mode), a degree of pyrrole photolysis does occur within the reaction vessel, pyrrole decreases in concentration from C0 dry to C1. This is due to the angle at which the UV lamp is positioned in comparison to the pyrrole inlet as some UV light does shine onto the pyrrole flow.

The degree of pyrrole photolysis is calculated by determining the percentage loss of pyrrole between C0 dry and C1.

In the case shown in Figure 2:9, there is 6% pyrrole photolysis between C0 dry and C1. As the concentration of pyrrole decreases from 590 ppb to 554 ppb.

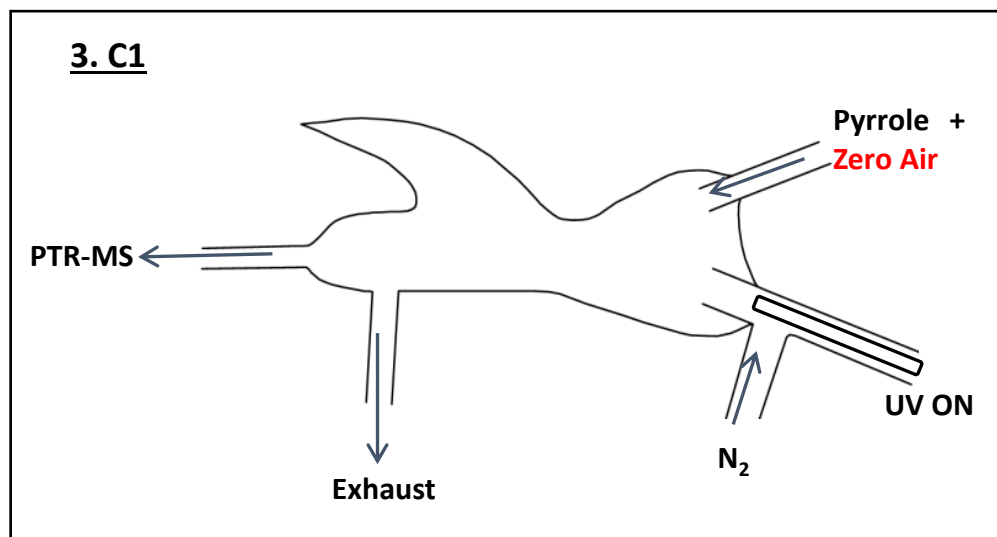


Figure 2:6 An illustration of the C1 measurement configuration. C1 has the same flow regime as C0 dry, however during C1, UV light enters the reaction vessel

### 2.2.1.3 C2 mode

As the reaction vessel is switched from dry air measurement mode to humid measurements by passing humidified nitrogen over the UV lamp (from C1 to C2), OH radicals are produced through the photolysis of water using the 184 nm emission line of the lamp (Figure 2:7) (R 1:31).

During C2 mode, ambient air is drawn through a Teflon (KNF) pump into catalyst consisting of platinum pellets heated to 350 °C, (Figure 2:3) generating clean air free of any VOCs with the same relative humidity as the ambient air used during

C3 mode. Differences in ambient air humidity when sampling during C2 and C3 results in fluctuations in OH concentration. Any large fluctuation in humidity is negated with the use of a heated catalyst. The resulting effects of C2 and C3 humidity differences are discussed in chapter 3. The flow of ambient air in these steps is controlled by a 500 sccm MFC.

The concentration of OH can be calculated from the difference between C1 and C2 pyrrole concentrations (E 2:1) (E 1:11). As stated previously, the PTR-MS sensitivity towards pyrrole varies depending on the humidity of the air entering the PTR- MS. As C1 is a measurement of pyrrole concentration in dry air, and C2 is a measurement in humid air, the sensitivity towards pyrrole is different for C1 and C2. Therefore C2 measurement of pyrrole concentration is multiplied by the ratio of C0 dry and C0 wet, in order to correct for the differences in pyrrole sensitivity as humidity changes.

$$[OH]ppb = C1 - \left( C2 \cdot \frac{C0\ dry}{C0\ wet} \right) \quad \text{(E 2:1)}$$

For the example shown in Figure 2:9, the concentration of OH calculated as 164 ppb. As the Weybourne Atmospheric Observatory is located on the Norfolk coast, the humid coastal air acts to increase the concentration of OH generated within the reaction vessel as ambient air is sampled during C0 wet, C2 and C3.

When changing from C1 mode to C2 mode, the concentration of pyrrole decreases to 390 ppb. These changes in pyrrole concentration are then used to calculate a value of total OH reactivity (E 1:14).

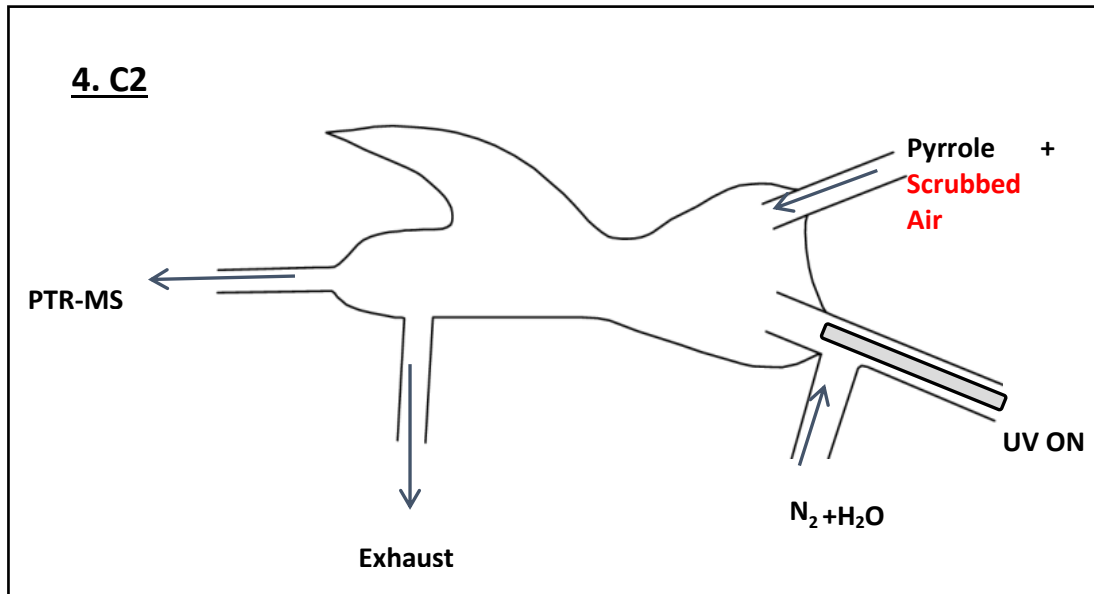


Figure 2:7 An illustration of C2 measurement mode. In this case, the reaction vessel is under humid conditions and OH radicals are produced through the UV lamp. Scrubbed ambient air is also introduced

#### 2.2.1.4 C3 mode

In the final mode of the cycle, C3 (Figure 2:8) ambient air is introduced into the reaction vessel, bypassing the catalyst. In this step, any VOCs present in the ambient air flow react with OH radicals within the vessel. The same mass flow controller used to regulate the flow of ambient air into the reaction vessel during C2 is used during C3, (Figure 2:3). Just as the concentration of pyrrole is multiplied by the ratio of C0 dry to C0 wet pyrrole concentrations during C2 mode, the measurement made during C3 mode is also multiplied by this ratio.

When switching from C2 to C3, the pyrrole concentration increases from 390 ppb to 410 ppb as ambient air flows into the vessel. These changes in pyrrole concentration are seen in Figure 2:9, when switching from C2 to C3, during which time any VOCs present within the ambient air sample during C3 consume OH.

C0 wet/ dry and C1 are measured manually by setting the flow rates for each mode of measurement. C2 C3 and ambient air measurement modes however, are measured by switching automatically between each flow regime. This is

done by using software developed by Dan Spence at the University of Leicester to switch the two, 3-way Solenoid valves (engineered at the University of Leicester electrical workshop) on and off at pre- determined times.

The pyrrole dilution factor is maintained at a constant level during all measurement modes as the use of mass flow controllers maintains a constant, stable flow of pyrrole, nitrogen and either zero air (for C0 wet, C0 dry and C1 modes), or ambient air for C2 and C3 modes. Therefore any changes in pyrrole concentration should occur owing to the production of OH during C2 and the introduction of VOCs into the UOL-CRM during C3.

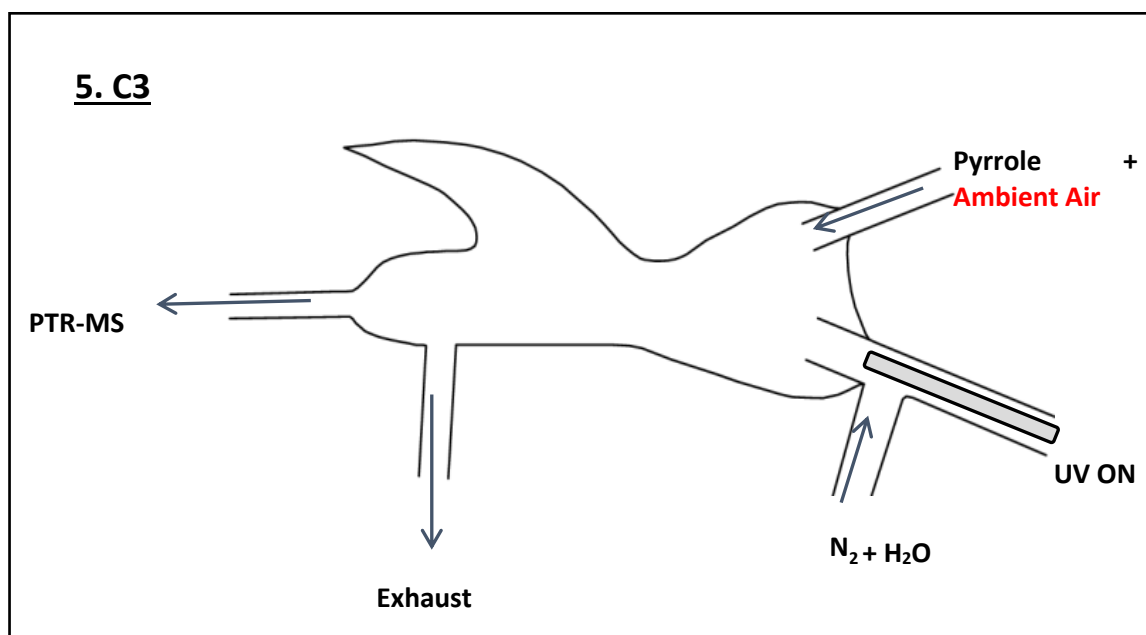


Figure 2:8 C3 is the final mode of measurements. In comparison to C2, ambient air is introduced into the reaction vessel to induce a reaction of VOCs with OH radicals

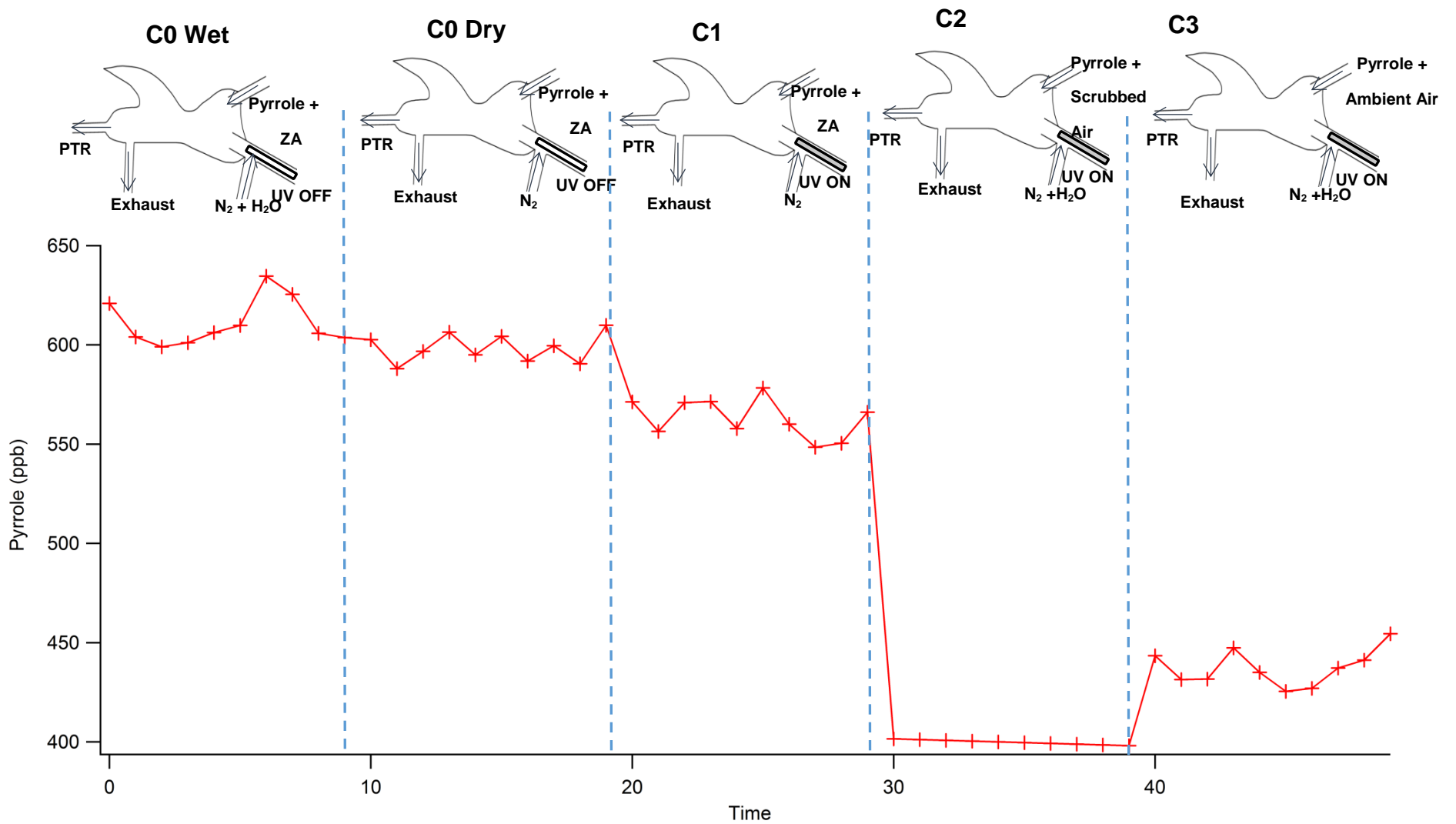


Figure 2:9 A representation of all pyrrole measurement modes and the associated changes in concentration over time. Adapted from a poster created by the John Williams group at the University of Mainz

## 2.3 Proton Transfer Reaction- Time of Flight- Mass Spectrometry as a detection method

There are a number of advantages with regards to the use of pyrrole as a reagent for the UOL-CRM and PTR-ToF-MS as a detector:

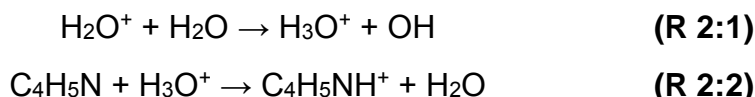
1. For a VOC (and pyrrole) to be detected using the PTR-ToF-MS, a proton transfer reaction must occur from a hydronium ion ( $\text{H}_3\text{O}^+$ ) to a pyrrole molecule ( $\text{R} 2:2$ ) which then generates a detectable protonated ion. In comparison to other ionisation techniques such as electron impact (Ellis and Mayhew, 2014c), using a proton transfer method, there is little to no fragmentation of the detected pyrrole parent ion ( $\text{C}_4\text{H}_6\text{N}^+$   $m/z$  68).
2. Aside from nitrile molecules with the same molecular formula as pyrrole, there are no known species in ambient air with the same protonated mass as pyrrole that could interfere with the pyrrole ion signal. For example, whilst 3-butenitrile and (z)-2-butenitrile are BVOCs that have been found within natural oils (Sghaier et al., 2016) and have the same molecular formula, and therefore the same molecular weight as the protonated pyrrole ion ( $\text{C}_4\text{H}_6\text{N}^+$   $m/z$  68). They can interfere with the detected pyrrole signal during C3 mode, but this cannot be accounted for as there is no way to differentiate between different ions with the same mass when using the PTR-ToF-MS. The resolution of the PTR-ToF-MS used within this work is 1 atomic mass unit and it cannot distinguish between different molecules with the same mass.
3. Common atmospheric VOCs when protonated have odd mass to charge ratios, for example: methanol ( $\text{CH}_4\text{OH}^+$   $m/z$  33), methyl vinyl ketone ( $\text{C}_4\text{H}_7\text{O}^+$   $m/z$  71), acetone ( $\text{C}_3\text{H}_7\text{O}^+$   $m/z$  59) and isoprene ( $\text{C}_5\text{H}_9^+$   $m/z$  69). Whereas, the protonated pyrrole ion has an even mass to charge ratio (due to the presence of a nitrogen atom within its structure) ( $m/z$  68). This helps to differentiate pyrrole from other species that could be detected by PTR-ToF-MS.

4. Pyrrole is present in low concentrations in the ambient environment and has only been detected during biomass burning events, (Karl et al. (2007), Yokelson et al. (2007), Sinha et al. (2008)).

In order to generate the necessary ions to be detected, proton transfer reactions are employed in which a reagent ion (in the case of the UOL-CRM, hydronium  $\text{H}_3\text{O}^+$  is the reagent ion), transfers a proton to the analyte creating an ionised sample of the analyte.

Hydronium ions are produced in a hollow cathode region of the PTR-ToF-MS via R 2:1, (Blake. R. S et al., 2009), (Lindinger et al., 1998) and is discussed in greater detail in section 2.3.1.

In relation to the UOL-CRM, a hydronium proton is transferred to pyrrole, thus generating a pyrrole ion, (R 2:2). This reaction proceeds because pyrrole has a higher proton affinity ( $875 \text{ kJmol}^{-1}$ ) than water ( $619 \text{ kJmol}^{-1}$ ), (used to generate  $\text{H}_3\text{O}^+$  hydronium ions (R 2:1)), allowing for a proton transfer reaction to occur between hydronium ions ( $\text{H}_3\text{O}^+$   $m/z$ 19) within the mass spectrometer and pyrrole (R 2:2).



If the proton affinity of pyrrole was lower than water, it could not abstract a proton from the hydronium ion and, therefore it would not be detectable (Ellis and Mayhew, 2014c).

Once the relevant ions are generated, they are directed to a time of flight mass analyser where they are separated depending on their mass finally reaching a detector, where a signal is measured and a mass spectrum is collected. The entire process, including its relation to the UOL-CRM, and the PTR-ToF-MS used alongside the UOL-CRM is discussed in further detail in section 2.3.1.

A diagram of a mass spectrometer similar to that used in this thesis can be seen in Figure 2:10, (Ennis et al., 2005) illustrating: a Hollow Cathode (HC) in which hydronium ions are produced (described below), a Flow Drift Tube (FDT) where proton transfer reactions occur, a transfer and flight tube region where a beam of ions are focused and travel to the detector and a mass analyser region consisting of a Reflectron and Detector, where, as stated above, ions are separated according to their masses.

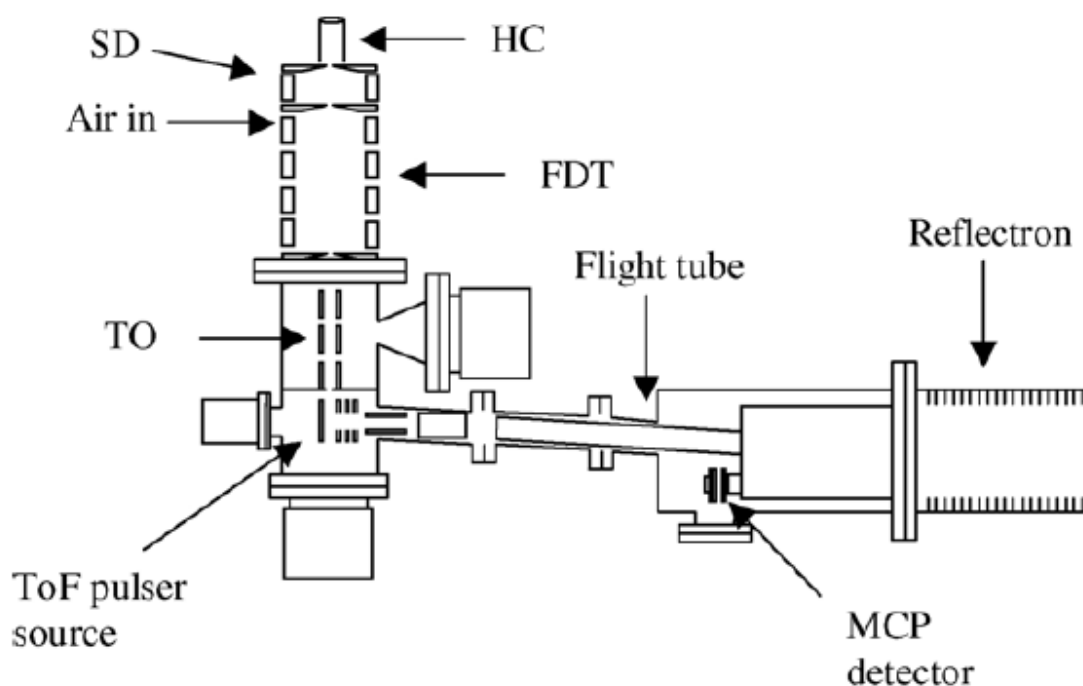


Figure 2:10 A schematic of a PTR-ToF-MS depicting the hollow cathode (HC) ion source, source drift (SD) tube, flow drift tube (FDT), into a MCP detector

### 2.3.1 The Kore Technology Ltd PTR-ToF-MS

A Kore Technology Ltd (2010) Proton Transfer Reaction- Time of Flight- Mass Spectrometer was utilised with the UOL-CRM. The Kore Technology PTR-ToF-MS consists of a hollow cathode glow discharge reaction cell coupled to a time of flight mass analyser and multi-channel plate detector.

Detailing the ion source and PTR region of the mass spectrometer is Figure 2:11 (Kore-Technology-Ltd). Plasma is generated in the HC region as a voltage is passed between an anode and a cathode, ionising a flow of water vapour

(reagent gas) to  $\text{H}_2\text{O}^+$  ions. In order to produce the necessary hydronium ions needed for proton transfer reactions, an excess of water is required to react with the ions produced (R 2:1), (Ellis and Mayhew, 2014c). Typical operating conditions used in the Hollow Cathode region are approximately 1.5 mbar to 2.0 mbar, 380 V.

The glow discharge region of the mass spectrometer produces hydronium ions with a purity of approximately 99.5%, however some side reactions within the hollow cathode do occur generating ions such as  $\text{N}_2^+$  and  $\text{N}^+$ . The source drift region can compensate for this, by converting these secondary ions into  $\text{H}_3\text{O}^+$  through reactions with water (Lindinger et al., 2001).

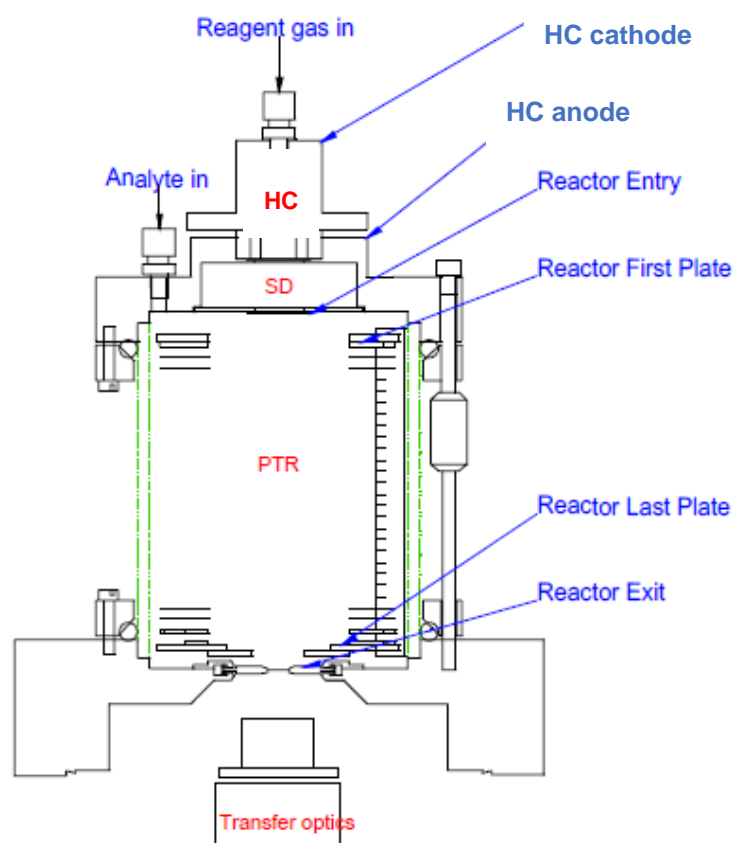


Figure 2:11 Schematic of the PTR-ToF-MS hollow cathode region and PTR reaction cell(Kore-Technology-Ltd, 2010).

From the hollow cathode, hydronium ions pass into a flow drift tube (shown as PTR in Figure 2:11) where proton transfer reactions with pyrrole or VOCs occur,

(in the case of the UOL-CRM, R 2:2). The typical pressure used within the PTR region is 1.3 mbar.

Within the flow drift tube, a series of electrodes provide an electric field to facilitate the transport of ions towards the transfer optics and flight tube. The electric field also acts to reduce any water clusters that could form within the PTR region changing the kinetics and thermodynamics of the PTR reaction (section 2.3.2).

As the series of ions then flow into the transfer optics section of the mass spectrometer, a beam of ions is extracted, accelerated (or decelerated), focused and steered. In a similar fashion to the electrodes used to facilitate the transition of ions from the flow drift tube to the transfer optics, the same occurs within the transfer optics region, in order to transfer the ions towards the pulsar. (Ellis and Mayhew, 2014d).

At this point, a continuous stream of ions reaches the mass spectrometers pulsar. The pulsar unit is a series of electrodes that receives the stream of ions, and using a timed mechanism (controlled by the Time- to Digital- Converter (TDC) acting as a trigger), generates a voltage (300- 400 V) at regular intervals, converting the continuous stream into a series of ion packets. In order for the ion beam to reach the detector, the direction at which the beam transverses the spectrometer needs to be changed. This is done with the use of a pulsar unit in combination with the TDC.

The electrodes are positioned so that, when fired, the ions change direction and travel orthogonally towards a flight tube and reflectron (Kore-Technology-Ltd, 2010).

Whilst travelling through the flight tube of the mass spectrometer, there is an option to steer the ion beam in order to maximise the ion count number upon the detector, this is done by adjusting the voltage output of two electrodes within the flight tube. This acts to steer the beam along its x and y axes.

As the ions enter the time of flight region (reflectron) (Figure 2:12), they are separated by their mass to charge ratio ( $m/z$ ) and heavier ions now travel slower

than the lighter mass ions (all ions are assumed to have a single positive charge).

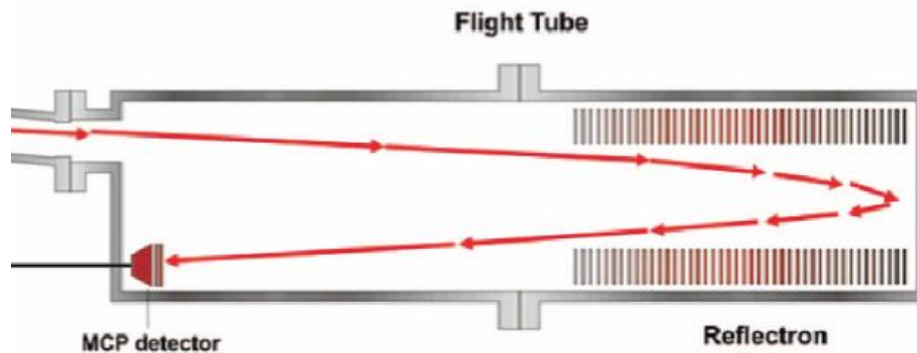


Figure 2:12 A depiction of passing through the time of flight region of a ToF-MS (Blake, R. S et al., 2009, 2009)

Within the reflectron exists a number of electrodes, these electrodes are employed to slow down and reflect the ion beam in the opposite direction using a sequence of electrodes of increasing potential within the flight tube. Ions travelling at faster speeds will penetrate further into the reflectron than those moving at a slower pace. This acts to increase the mass resolution of the instrument (Ellis and Mayhew, 2014d).

Once the ions are reflected back through the flight tube, they reach the detector. The detector used in this instrument is a microchannel plate (MCP). The MCP is a disc of lead consisting of a number of cylindrical channels. Electrons are emitted from the walls of each channel as the ions travelling through the spectrometer impact upon the MCP. The electrons that are emitted from the plate are accelerated by an electric field towards a higher potential. Following this, secondary electrons are generated through a cascade within each channel (Braham et al., 1995).

Data collection software working alongside the MCP then acts to count the number of ions passing through the instrument within a designated period of time.

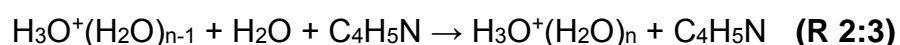
The mass spectrometer is operated under a vacuum at all times, using a series of turbo molecular pumps and a rotary pump. The GD, PTR and flight tube are sustained at pressures of: 1.7 - 2.0 mbar, 1.3 mbar and  $1.6 \times 10^{-6}$  mbar respectively. The vacuum needed is essential for various reasons: to prevent collisions of ions with background gas molecules within the time of flight region, and to protect the sensitive MCP.

By manipulating the pressure within the flow drift tube, the formation of water clusters can be controlled; for instance, at higher pressures, there would be multiple collisions between the reagent ion and the sample analyte, sufficient for protonation (Ellis and Mayhew, 2014d).

### 2.3.2 Hydronium cluster ratios within the flow drift tube

Hydronium should be the only reagent ion within the hollow cathode to act as a proton donor to pyrrole or VOCs, however a high pressure (or low electric field) within this region could result in high concentrations of water, leading to the formation of hydrated hydronium clusters (R 2:3).

High concentrations of water clusters can greatly affect the ability to transfer a proton from hydronium to the reagent ion due to the fact that water clusters possess higher proton affinities than water molecules. The  $m/z$  37 hydronium cluster for example,  $(\text{H}_3\text{O}^+(\text{H}_2\text{O}))$  has a proton affinity  $808 \text{ kJ mol}^{-1}$  whereas the lone hydronium molecule has a proton affinity of  $691 \text{ kJ mol}^{-1}$ . As a result of this, in scenarios when there is a higher concentrations of the  $m/z$  37 hydronium cluster in comparison to the  $m/z$  19, and if analyte ion has a higher proton affinity than  $808 \text{ kJ mol}^{-1}$ , protonation from the water cluster, rather than the hydronium ion can occur (Ellis and Mayhew, 2014c). As pyrrole has a higher proton affinity than both the water and the  $m/z$  37 water cluster ( $875 \text{ kJ mol}^{-1}$ ), this is likely the case if the signal for the hydronium clusters is higher than the hydronium ion signal.



This can result in variation in CRM measurements because, the  $m/z$  37 ion is an indicator of sample humidity, (discussed further in 3.3), therefore any variability in sample humidity, during C2 and C3 modes, will result in variability in the measured pyrrole signal, and so the  $m/z$  37 is reduced as much as possible.

To reduce the cluster ratios within the PTR region of the mass spectrometer, the reduced electric field ( $E/N$ ) of the instrument needs to be altered. The  $E/N$  is a measurement of the ratio of the electric field strength ( $E$ ) ( $V\ cm^{-1}$ ) to the gas number density ( $N$ ) ( $cm^{-3}$ ) within the flow drift tube. Where, the gas density and electric field within the FDT are altered by changing the pressure of the water reservoir used to generate the necessary hydronium ions and voltage output of various electrodes.

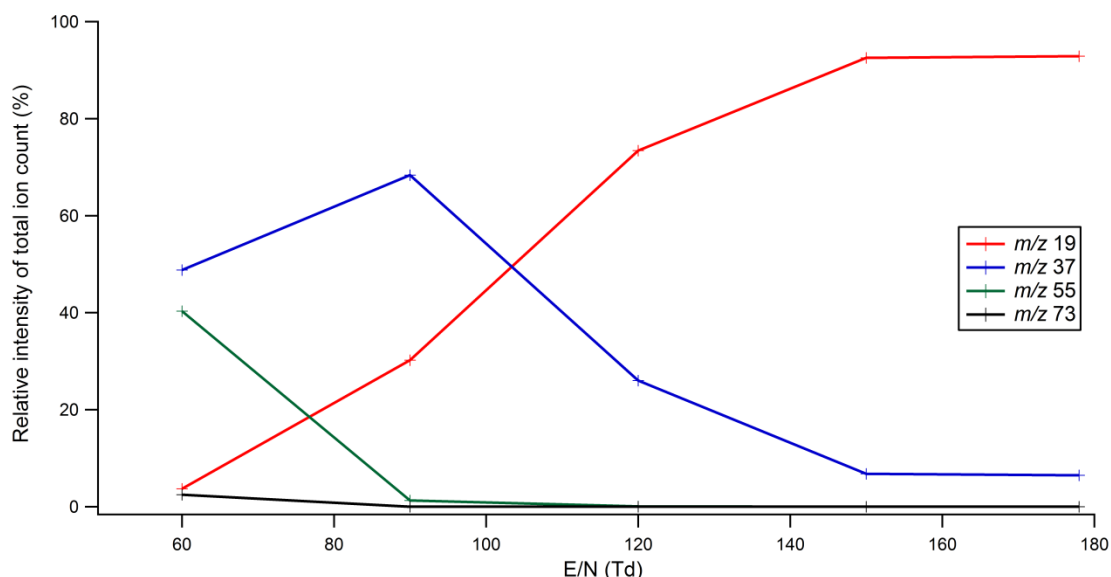


**Figure 2:13 Measured distributions of hydronium and hydronium water clusters as an effect of changing  $E/N$**

Figure 2:13 shows the effect of changing the reduced field on the proportion of hydronium clusters as a percentage of the total ion count, measured on the Kore PTR-ToF-MS to determine the ideal  $E/N$  to be used with the UOL-CRM system. Above 110 Td ( $1\ Td = 1\ Townsend = 1 \times 10^{-17}\ V\ cm^2$ ) the total ion count is dominated by the hydronium ion. Over 90% of the total ions produced are hydronium ions, this therefore results in proton transfer solely occurring through

the  $m/z$  19 hydronium ion. Throughout this work, the PTR-ToF-MS operated at 178 Td over the entire drift tube. This E/N values was determined by changing the electric field strength across the flow drift tube whilst maintaining a constant pressure. Changing the E/N over the PTR region requires a balance, between breaking water clusters at a high E/N whilst also reducing the risk of fragmentation of the pyrrole ion.

178 Td, is above the threshold at which there is a shift between  $m/z$  19 ions and  $m/z$  37 hydronium clusters causing proton transfer. The  $m/z$  37 hydronium cluster produces only 6%, of the total ion count (in comparison to the  $m/z$  19 producing 92% of the total ion count), as a result, at this E/N, proton transfer will only occur from the hydronium ion to pyrrole, and not from the hydronium water cluster. Also at this E/N there is also no fragmentation of the pyrrole ion. As no other ion is observed in the mass spectrum, only the  $m/z$  19, 37 and 68 ions.

The E/N for the mass spectrometer was calculated using a derivation of the ideal gas equation to calculate the gas number density (N) (E 2:2).

$$N = \frac{(N_A \times T_0 \times P_d)}{(V_M \times T_d \times P_0)} \quad (\text{E 2:2})$$

Where:  $N_A$  is Avogadro's constant ( $6.022 \times 10^{23} \text{ mol}^{-1}$ ),  $V_M$  is the molecular volume of an ideal gas ( $22414 \text{ cm}^3 \text{ mol}^{-1}$ ),  $P_0$  is the pressure (in kPa) at 1 atmosphere (101.325),  $T_0$  is the temperature at 1 atmosphere (273.15 K),  $T_d$  and  $P_d$  are the temperatures (in Kelvin) and pressures (in kPa) within the drift tube respectively (Ellis and Mayhew, 2014d).

Finally, the E/N is calculated by measuring the voltages at a number of electrodes within the drift tube, and then dividing this number by the gas number density above.

A value for the E/N can be calculated for the majority of the drift tube component, (measured from the reactor entry and the reactor first plate electrodes), the collision cell (from the reactor entry and the reactor last plate electrode) and an

average for the entire drift tube (reactor entry to the reactor exit electrodes) (Figure 2:11)

The E/N that is measured above and in Figure 2:13 is a measurement of the average E/N through the drift tube.

## **2.4 Conclusions**

The CRM designed at the Max Planck Institute, Mainz has been adapted and implemented into a system at the University of Leicester (UOL-CRM).

The UOL-CRM consists of a glass Teflon coated reaction vessel, in which a flow of pyrrole is introduced into the reaction vessel. Additional flows of nitrogen and zero air introduced into the reaction vessel (C1), and along with the use of a UV lamp, humidified nitrogen is used to generate OH radicals (C2). Ambient air enters the reaction vessel during C3 mode and the presence of VOCs within the ambient air sample causes the concentration of pyrrole to increase. The UOL-CRM is coupled to a PTR-ToF-MS, this is used to monitor the changes in pyrrole concentration during each mode of measurement.

It has been tuned, and optimised to monitor pyrrole concentrations when measuring total OH reactivity.

## Chapter 3. Calibration and Validation of the UOL-CRM

### 3.1 Introduction

A number of interferences can affect the total OH reactivity measurements by the CRM technique by causing deviations of pyrrole concentrations during C2 and C3 modes. The interferences reported by: Michoud et al. (2015), Zannoni et al. (2015) and Dolgorouky et al. (2012) include:

1. Changes in sampled ambient air relative humidity between C2 and C3 modes
2. Deviations from pseudo- first order kinetics
3. Recycling of OH due to the presence of high NO concentrations within the reaction vessel
4. Dilution of ambient air within the UOL-CRM

This chapter presents the calibration used in order to convert the measured PTR-ToF-MS signal into an absolute measurement of pyrrole concentrations and experiments performed in order to characterise the UOL-CRM, and the interferences which can cause a deviations in measured OH reactivity. This is done through several tests initially developed in the references above. Once these calibrations have been carried out, the results are then applied to atmospheric measurements.

### 3.2 Pyrrole concentration calibration

In order to convert the pyrrole signal measured by the PTR-ToF-MS into a concentration, the PTR-ToF-MS must be calibrated in order to determine its sensitivity towards pyrrole.

This calibration is conducted by mixing the desired concentrations of pyrrole with nitrogen. The corresponding signal is then detected by the PTR-ToF-MS and a

calibration curve is then plotted. An example of this is shown in Figure 3:1.

The vertical scale in Figure 3:1 is plotted in units of normalised counts per second (ncps). Normalisation is the process of scaling the ion count of an analyte signal relative to the hydronium ion ( $m/z$  19  $\text{H}_3\text{O}^+$ ), more specifically the isotope of hydronium of the hydronium ion ( $m/z$  21). As the mass spectrometer is commonly used continuously during the day, the ion count rate of the hydronium isotope could change significantly during the day. Normalising the pyrrole ion count ensures that the pyrrole concentration detected, is a measurement of the actual concentration of pyrrole exiting the UOL-CRM reaction vessel, and is not affected by any fluctuations within the hydronium signal.

Normalisation is carried out by applying the following equation to the measured pyrrole signal:

$$\text{ncps} = 1 \times 10^6 \times \frac{i(\text{MH}^+)}{i(m/z\ 19)} \quad (\text{E 3:1})$$

Where  $i(\text{MH}^+)$  is the ion count rate of the analyte and  $i(m/z\ 19)$  is the ion count rate of hydronium ions. The ratio of the analyte count rate to hydronium is multiplied by one million because the PTR-ToF-MS generates an  $\text{H}_3\text{O}^+$  ion count rate of close to one million.

However, large concentrations of hydronium ( $m/z$  19) have the capacity to overwhelm and saturate the detector, possibly damaging the MCP detector. To account for this, the measured pyrrole signal is normalised to the  $^{18}\text{O}$  isotope of hydronium ion, ( $\text{H}_3^{18}\text{O}^+$   $m/z$  21) instead of the  $\text{H}_3^{16}\text{O}^+$  ( $m/z$  19) hydronium signal as seen in equation (E 3:2) (Ellis and Mayhew, 2014e).

$$\text{ncps} = \frac{1 \times 10^6}{500 \times i(m/z\ 21) \times i(\text{MH}^+)} \quad (\text{E 3:2})$$

The naturally occurring  $^{16}\text{O}$  to  $^{18}\text{O}$  ratio is close to 500:1, so multiplying the  $m/z$  21 signal by five hundred, allows the abundance of  $\text{H}_3\text{O}^+$  to be deduced. Dividing this by the  $\text{H}_3\text{O}^+$  ion count rate (assumed to be one million) and multiplying by the analyte count rate normalises the analyte signal to the  $m/z$  21 signal (Ellis and Mayhew, 2014b).

The sensitivity of the PTR-ToF-MS towards pyrrole is then calculated from the gradient from the calibration curve (Figure 3:1) and is expressed in units of normalised counts per second per  $\text{ppb}^{-1}$  ( $\text{ncps ppb}^{-1}$ ) (de Gouw et al., 2003). A decrease in sensitivity can occur however if there are changes in the E/N of the instrument. de Gouw et al. (2003), have observed that reducing the pressure within the flow drift tube of the PTR-MS (thereby changing the E/N of the mass spectrometer) will reduce the sensitivity of the PTR-ToF-MS. Due to this effect, all measurements throughout this work have been made at the same E/N.

The determination of the sensitivity towards pyrrole allows the calculation of pyrrole concentrations by dividing the measured normalised counts per second of pyrrole by the sensitivity factor (E 3:3).

$$\text{pyrrole (ppbV}^{-1}\text{)} = \frac{m/z \text{ 68 (ncps)}}{m \text{ (ncps}^{-1} \text{ ppbV}^{-1}\text{)}} \quad \text{(E 3:3)}$$

The variation in the mass spectrometers sensitivity towards pyrrole is shown in Figure 3:1, as calibrations are conducted over a period of approximately one year. A precision of 38% within the PTR-ToF-MS sensitivity was caudated using E 3:4. Using the average standard deviation and average sensitivity for all of the calibrations shown within Figure 3:1.

$$\text{precision (\%)} = \frac{\text{standatd deviation (1}\sigma\text{) of sensitivity}}{\text{average sensitivity}} \quad \text{(E 3:4)}$$

With a maximum and minimum sensitivity of 0.213 and 0.061 ncps<sup>-1</sup> ppb<sup>-1</sup> respectively, a large variation in sensitivity is seen in period of time. Based on this instability and variation in sensitivity, it is concluded that the sensitivity needs to be measured frequently. As a result, before the characterisation of each correction (C2, C3 relative humidity deviations, kinetics corrections and NO artefact corrections), the pyrrole sensitivity is measured.

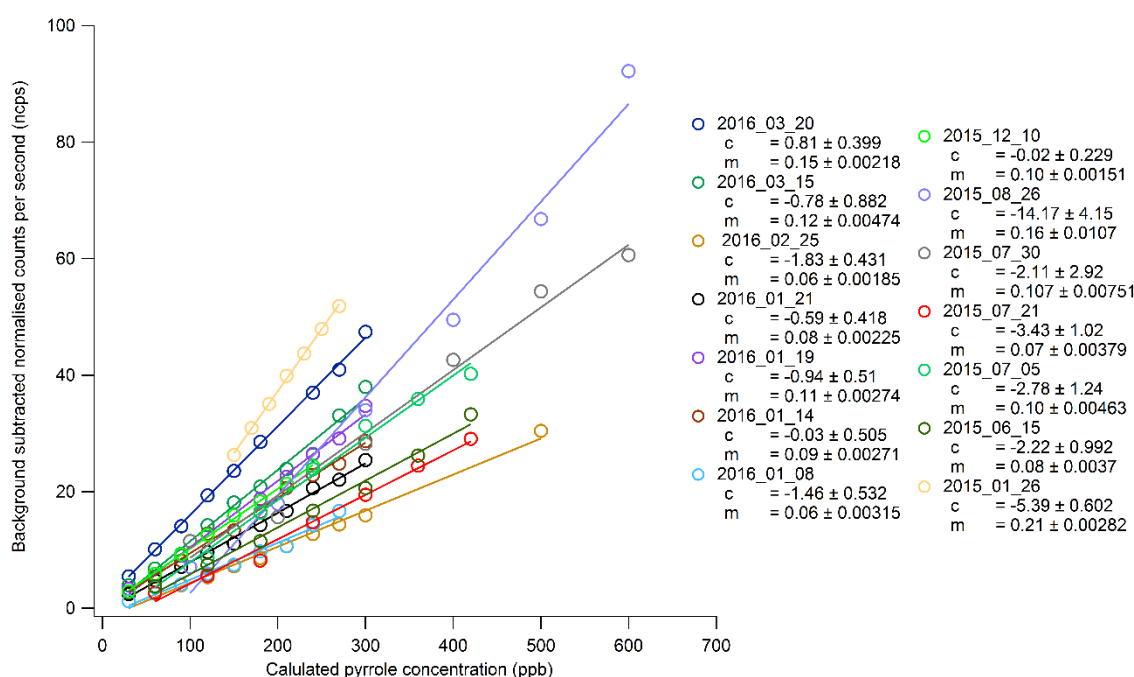


Figure 3:1 PTR-ToF-MS pyrrole calibration curves measured over a period of approximately one year

### 3.3 Changes in sampled ambient air relative humidity between C2 and C3 modes. The effect on pyrrole sensitivity

As stated in section 2.2.1.1, the ratio of  $m/z$  19 to hydrated water clusters can affect the thermodynamics and kinetics of proton transfer between pyrrole and hydronium, this can result in a different pyrrole sensitivity when sampling humid air, in comparison to dry air measurements.

In a study by Sinha et al. (2009) the influence of humid air on pyrrole sensitivity was investigated. The sensitivity was measured in dry air approximately 0% relative humidity and in humid air of approximately 70% relative humidity. It was

concluded that the sensitivity changes by as much as 16% between dry air and humid air (Figure 3:2).

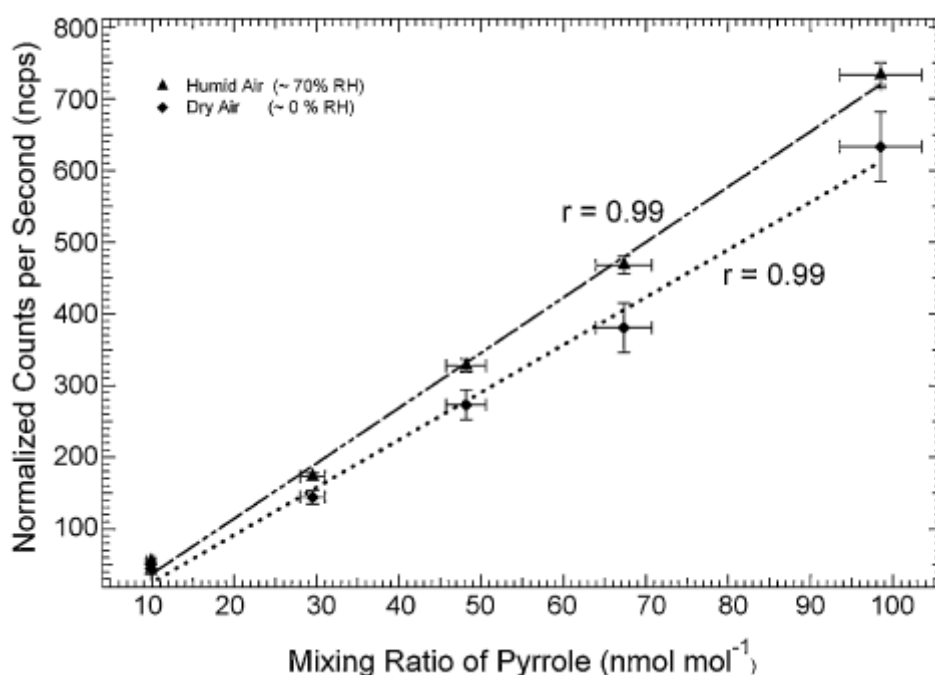


Figure 3:2 Measurements of PTR-MS pyrrole sensitivity conducted in dry and humid air by Sinha et al. (2009)

The calibration to determine sensitivity of the PTR-ToF-MS towards pyrrole is conducted under dry conditions (the calibrations discussed within section 3.2, and shown in Figure 3:1), at a relative humidity ranging from approximately 1 - 2%. However, C2 and C3 modes (sections 2.2.1.3 and 2.2.1.4) are measured under humid air conditions (relative humidifies ranging from approximate (30-40%)), due to the differences in humidity between the dry air and humid measurements modes, there is also an inherent difference in sensitivity, this difference in sensitivity will result in variations of the measured pyrrole concentrations between dry air and humid air modes.

Figure 2:9 shows that when the concentration of pyrrole is determined in dry and humid conditions, the concentration of pyrrole in humid air is 10 ppb higher than in dry air, (as shown by the C0 dry and C0 wet measurements within the figure). This difference is solely due to the differences in sensitivity, as no OH is produced within these modes. Therefore a correction factor is needed to account

for differences in humidity dependant sensitivity, this is done by multiplying C2 and C3 pyrrole concentrations by the ratio of C0 dry to C0 wet.

### **3.3.1 The effect of C2 and C3 humidity differences on OH concentration**

Humid air is introduced into UOL-CRM reaction vessel is during C2 and C3 modes because the photolysis of humidified nitrogen is used to generate OH radicals. However, measurements of C2 and C3 modes requires the influx of ambient air into the reaction vessel, the caveat of using ambient air during C2 and C3 modes is that any fluctuations in ambient air relative humidity results in fluctuations in OH concentrations. This needs to be accounted for and measurements of pyrrole concentration during C2 mode are corrected by determining the degree at which the measured pyrrole concentration changes (owing to changes in OH concentrations) with relative humidity.

For this correction, the ratio of the hydronium water cluster ( $\text{H}_2\text{O}\cdot\text{H}_3\text{O}^+$   $m/z$  37) to the hydronium isotope ( $m/z$  21) ion is used as an indicator of humidity within the mass spectrometer (Inomata et al., 2008) and UOL-CRM reaction vessel. Michoud et al. (2015), have determined that there is a linear relationship between relative humidity and the ratio of  $m/z$  37 to  $m/z$  19 ions (Figure 3:3). This ratio can therefore be used when examining the effect of humidity on the pyrrole ion signal. In the case of the corrections conducted here, the hydronium isotope ( $m/z$  21) ion is used in place of the  $m/z$  19 ion.

As stated within section 2.3.2, the E/N of the PTR-ToF-MS has been altered to reduce the degree of hydronium clustering within the PTR-ToF-MS ion source as the  $m/z$  37 hydronium cluster contributes to 6% of the total ion count. However, the  $m/z$  37 signal will naturally increase with humidity, regardless of the E/N, (in the case of the UOL-CRM, the water cluster signal will increase with increasing humidity of ambient air). This does not prove a problem with measurements made by the UOL-CRM because the  $m/z$  19 signal is always higher (90% higher) than the  $m/z$  37 signal, therefore the kinetics of proton

transfer between the hydronium ion and pyrrole molecule is not affected when increasing humidity and  $m/z$  37 clusters (only the concentration of OH is affected).

As a starting point, an experiment was carried out to determine the degree at which the concentration of pyrrole changes during conditions when the relative humidity within the UOL-CRM reaction vessel during C2 mode is lower than that measured during C3 mode. In order to generate these conditions, zero air was used to dilute pyrrole during C2 rather than ambient air. The results of this experiment is seen in Figures 3:3 and 3:4

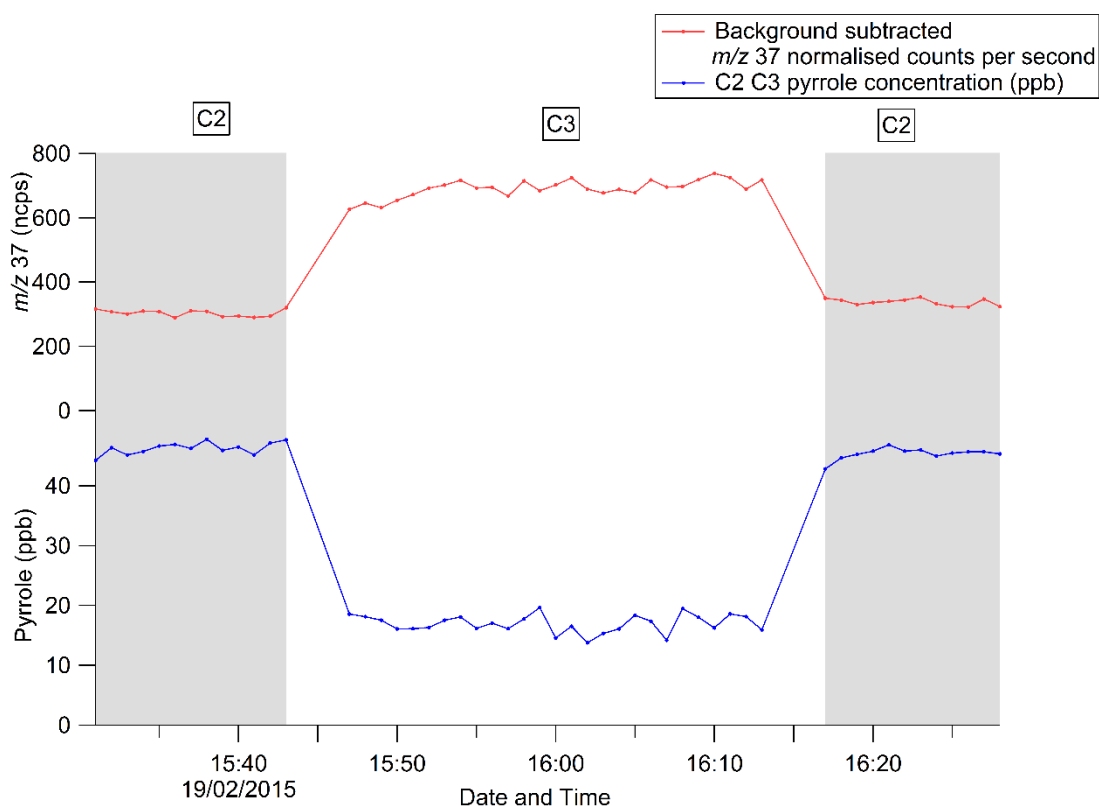


**Figure 3:3 Measured hydronium  $m/z$  37 ion counts (ncps) and the corresponding pyrrole concentrations when switching from modes C2 to C3 and back to C2**

During C2 measurements, due to the use of dry zero air to dilute pyrrole, a  $m/z$  37 count rate of approximately 300 ncps is detected (25% relative humidity), this then increases to approximately 700 ncps when switching to C3 (40% relative humidity), using ambient air to dilute pyrrole. As the flow regime switches back to C2 from C3, the  $m/z$  37 water cluster then returns to a base line. This

change in the hydronium cluster signal when changing from C2 to C3 and back to C2 mode is confirmed by the changes in relative humidity measured using a sensor, located on the output flow of the reaction vessel (Figure 2:3).

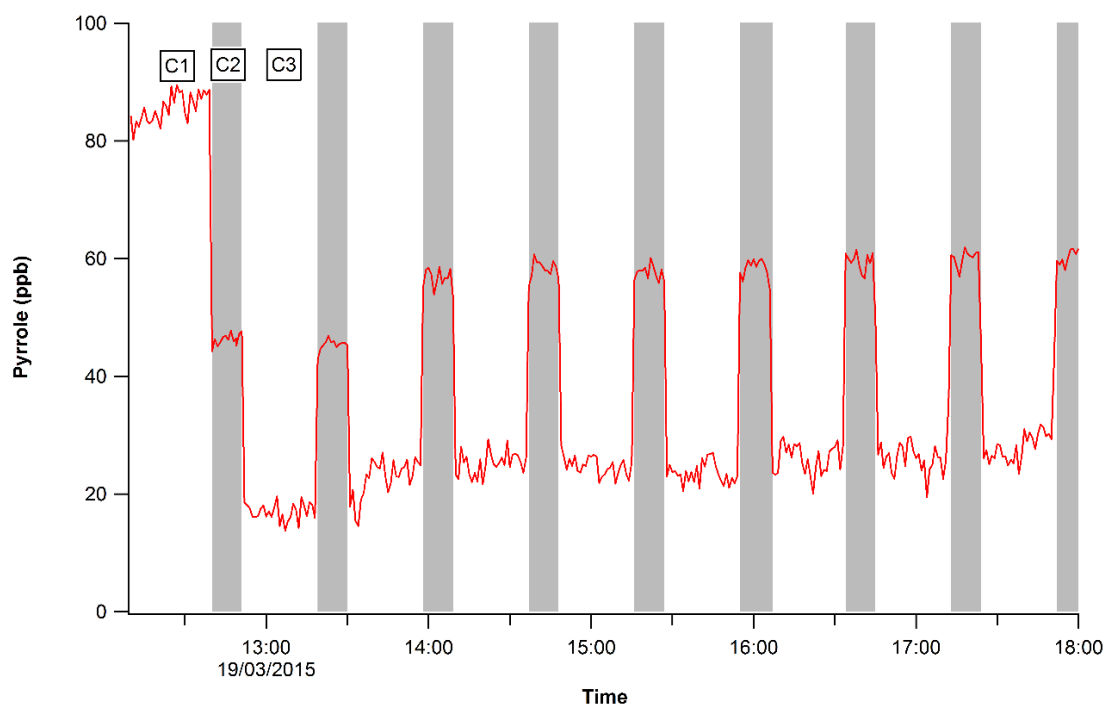


**Figure 3:4 Time series of pyrrole concentrations C1, C2 and C3. C2 measured with a dilution of zero air, and C3 measured with a dilution of ambient air. C2 measurements are highlighted in grey.**

As can be seen from the measurements (Figure 3:4), C3 mode pyrrole concentrations are now lower than that measured during C2 mode. This occurs because there is now a higher concentration of OH during C3 mode than there is for C2 mode (due to the relative humidity during C3 mode being higher than in C2 mode) as more OH available to react with pyrrole during C3 than C2 mode.

This is not ideal scenario because in order to calculate total OH reactivity using the CRM equation, the concentration of pyrrole measured during C3 needs to be higher than that during C2 mode, (E 1:14).

In order overcome this problem, ambient air is sampled during both C2 and C3 modes, thereby resulting relatively in small changes relative humidity in comparison to that observed within Figure 3:3 (and therefore small changes in

OH concentrations). Clean air free of VOCs is generated during C2 mode by drawing ambient air through a heated catalyst. (Figure 2:3).

However, slight variations in relative humidity are still observed between C2 and C3 modes even with the use of a catalyst. To compensate and correct for variations in humidity and  $m/z$  37 normalised counts, a correction factor is applied to C2 mode, determined through calibration measurements.

### **3.3.1.1 Experimental- Correcting for changes in relative humidity between C2 and C3 modes**

With the mercury pen ray lamp switched on, a constant flow of humid nitrogen, pyrrole and zero air is introduced into the reaction vessel. In this case, a second bubbler is used to increase the humidity within the reaction vessel. In the same way that a flow of nitrogen is split to allow a flow of dry and humid nitrogen into the reaction vessel (for C1 and C2), a flow of zero air is also split through two MFC's (500 sccm directly into the reaction vessel, and 100 sccm through a water bubbler Figure 2:3).

By changing the ratio of dry air flow to humid air flow through both MFC's, the humidity within the reaction vessel is increased whilst maintaining the same pyrrole dilution factor.

The results of numerous humidity calibrations are shown in Figure 3:5, in which a linear decrease in pyrrole concentration is observed as the  $m/z$  37 to  $m/z$  21 ratio (and therefore the relative humidity within the reaction vessel) increases. Using the linear regression from the experiments, a corrected value of C2 pyrrole concentration is calculated based on the pyrrole concentration during measured C mode, and the difference in the  $m/z$  37 to  $m/z$  21 ratio monitored during C2 and C3 modes. This leads to equation 3:5 where  $m$  is the slope of the linear regression and  $(m/z\ 37/ m/z\ 21)$  is calculated from ambient air measurements during C2 and C3 modes, (Dolgorouky et al. (2012) Michoud et al. (2015)).

$$C2_{\text{corrected}} = C2 + m \left[ \left( \frac{m/z\ 37}{m/z\ 21} \right)_{C3} - \left( \frac{m/z\ 37}{m/z\ 21} \right)_{C2} \right] \quad (\text{E 3:5})$$

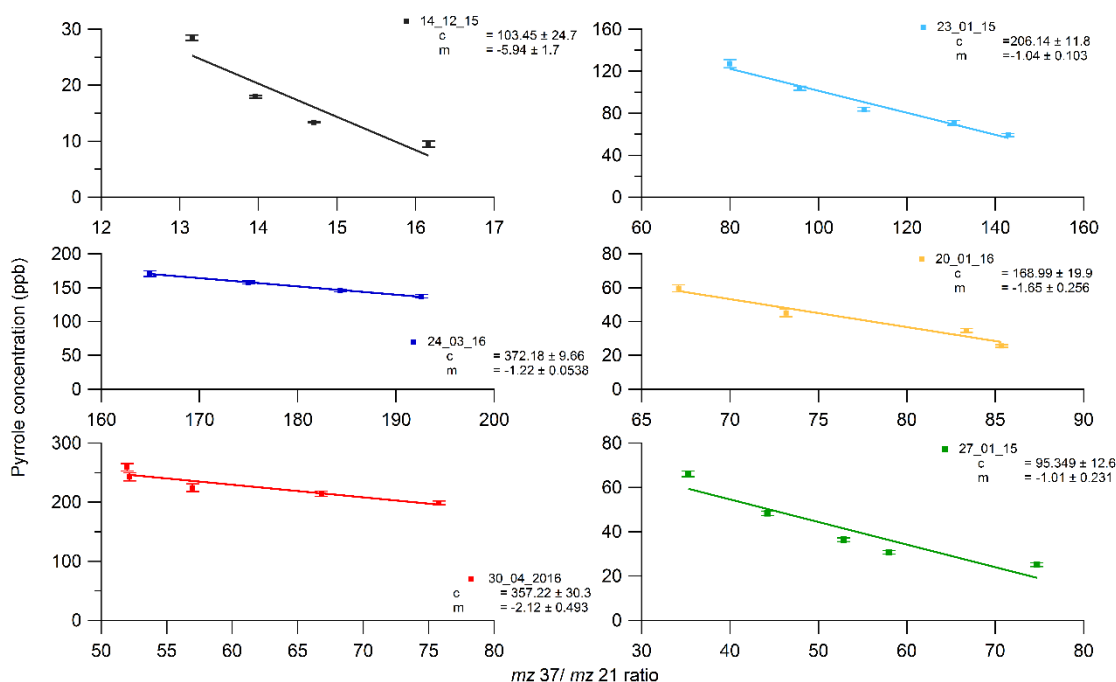


Figure 3:5 Experimentally determined humidity calibrations measured at relative humidity ranging from 20 to 70% (22°C). Error bars are measured at one standard deviation of each pyrrole concentration. Calibrations conducted on 20/04/16, 24/03/16, 14/12/15, 23/01/15, 20/01/15 and 27/01/15

### 3.4 Deviations from pseudo- first order kinetics

Throughout all of the OH reactivity measurements, the CRM equation (E 1:14), assumes that the system is under pseudo- first order kinetics regime and that the concentration of pyrrole is at least several orders of magnitude higher than the concentration of OH radicals.

However, the UOL-CRM does not usually operate under these conditions, as the concentration of pyrrole used can be on the same order of magnitude as the OH generated. This is due to a need to create a concentration balance, if the concentration of pyrrole is too high, then the amount of OH generated will not be large enough to cause a significant decrease in the pyrrole signal when

switching from C1 mode to C2 mode. Whereas due to the relatively low sensitivity of the PTR-ToF-MS toward pyrrole, a high concentration is needed to observe a detectable change in pyrrole when switching between measurement modes.

The ratio of pyrrole to OH is an indicator of whether the system is under pseudo-first order conditions and is calculated using E 3:6. Where, as stated within section 1.5.3, the difference between C1 and C2 is a calculation of the OH concentration within the reaction vessel. The higher the ratio of pyrrole to OH, the closer the system is to pseudo- first order conditions.

$$\text{Pyrrole : OH} = \frac{C1}{C1 - C2} \quad (\text{E 3:6})$$

Owing to this need for a concentration balance between pyrrole and OH, an overestimation of OH reactivity is determined through measurements with a gas standard. Which can be corrected for by calibrations.

### **3.4.1 Experimental characterisation of UOL-CRM operating conditions- deviation from pseudo first order conditions**

Using a test gas (propyne, BOC 500 ppb in nitrogen, 200 bar), the degree at which the measured OH reactivity deviates from the theoretical, calculated OH reactivity under a pseudo- first order kinetics regime (based on a specific concentration of propyne introduced into the UOL-CRM reaction vessel and its rate of reaction with OH) can be determined.

After measuring C0 dry, C0 wet, C1 and C2, increasing concentrations of propyne are introduced into the reaction vessel to induce increasing rates of OH reactivity, (from 7 s<sup>-1</sup> to 239 s<sup>-1</sup>) a measurement of OH reactivity is determined using the CRM equation (E 1:14) for each concentration of propyne.

When conducting these experiments, ambient air flows through the catalyst to generate air free of VOCs which could cause interferences with this calibration. The flow of ambient air is also used to dilute propyne whilst providing a stable constant humidity. Using zero air to dilute propyne has the disadvantage altering humidity levels within the reaction vessel as the concentration of propyne is changed.

By only changing the ratio of propyne to VOC- free ambient air (at a total flow rate of 150 sccm), the concentration of can be propyne changed, whilst ensuring a constant concentration of pyrrole.

The changes in pyrrole concentration that occur when adding propyne into the reaction vessel are shown in Figure 3:6. As usual, the concentration of pyrrole decreases when changing from modes C1 to C2 as OH radicals are generated. When propyne is introduced along with OH, the concentration of pyrrole increases as propyne competes with pyrrole over the reaction with OH (as seen in (Figure 1:6). As more propyne is introduced, the concentration of pyrrole increases further.

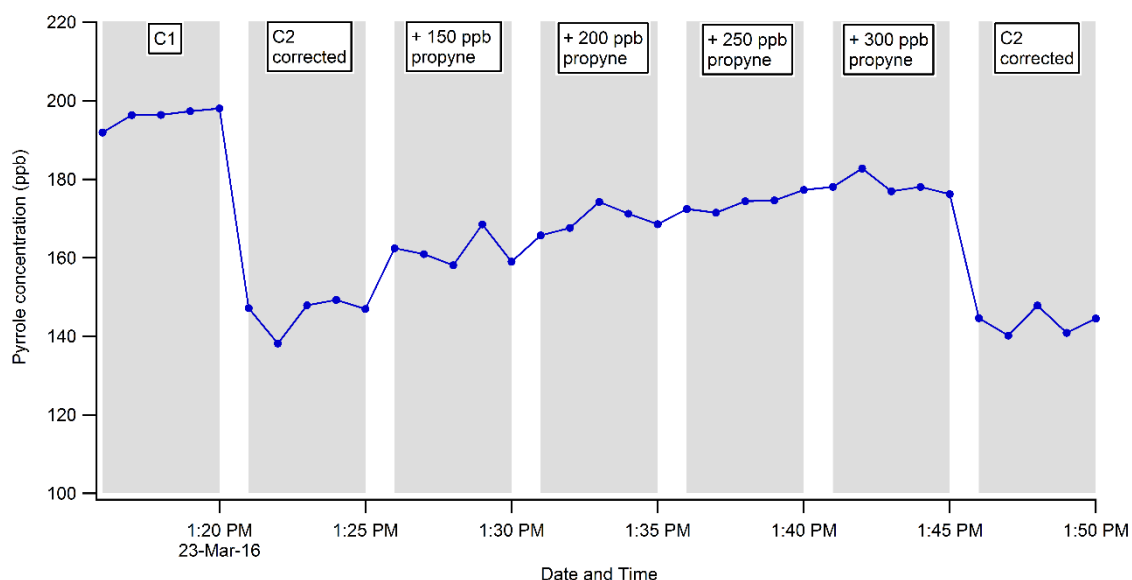


**Figure 3:6 Measured pyrrole concentrations during C1 and C2. Increasing amounts of propyne introduced into the reaction vessel to induce higher rates of OH reactivity. Shaded grey areas indicate the measurement mode and the concentration of propyne introduced into the UOL-CRM**

When calculating OH reactivity for each C3 modulation, any deviation in humidity that occurs between C2 and C3 have been accounted for by applying the correction factor from determined from Equation 3:5. After calculating OH reactivity, based on the rate coefficient for the reaction of OH with propyne ( $6.21 \times 10^{-12} \text{ cm}^3 \text{ molecule}^{-1} \text{ s}^{-1}$  at 298 K and 1 bar), (Lockhart et al., 2013) and the concentration of propyne introduced during each C3 step (E 1:5), the degree at which the measured OH reactivity differs from the calculated reactivity is determined (Figure 3:7).

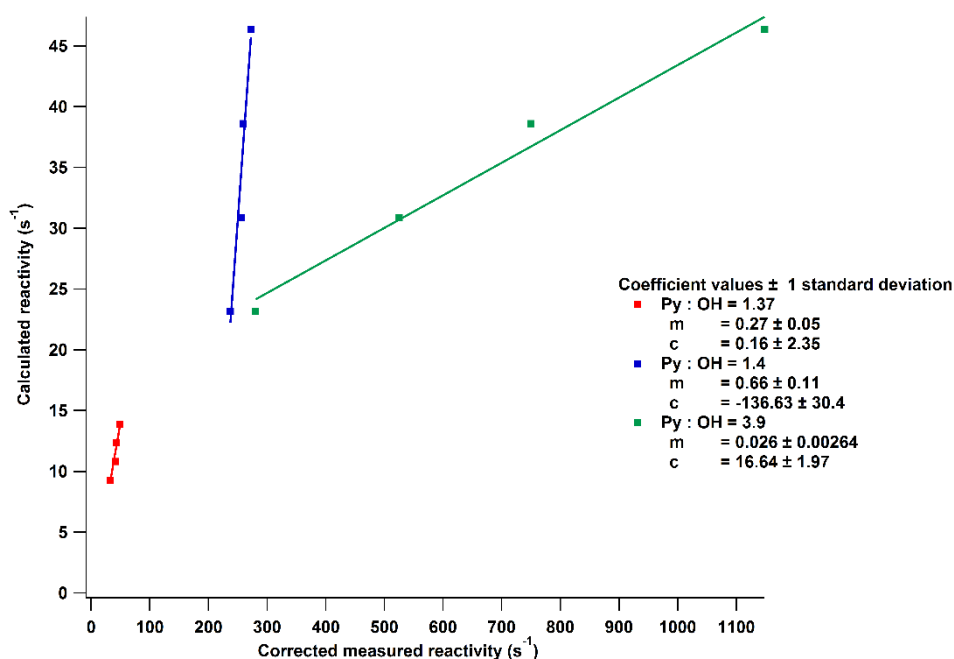


**Figure 3:7 Experimentally determined OH reactivity and its deviation from calculated OH reactivity using propyne gas standard at pyrrole to OH ratios of 1.37, 1.4 and 3.9**

This experiment is repeated at a series of pyrrole to OH ratios, (controlled by either changing the concentration of pyrrole or changing the humidity within the reaction vessel) (Figure 3:7).

The results of these experiments show that a linear relationship is observed between the theoretical calculated OH reactivity, and measured OH reactivity of the UOL-CRM system. As a result, the gradient of the linear regression (F) can be used as a factor to correct the measured OH reactivity using Equation 3:7.

Where  $R(OH)_{\text{true}}$  is the calculated OH reactivity (based on the concentration of the gas standard flowing through the reaction vessel and its OH reaction rate coefficient), and  $R(OH)_{\text{measured}}$  is the OH reactivity measured through the UOL-CRM, corrected for deviations in humidity between C2 and C3. For ambient air measurements,  $R(OH)_{\text{true}}$  is the measured OH reactivity corrected for deviations from pseudo- first order kinetics.

$$R(OH)(s^{-1})_{\text{true}} = F \times R(OH) (s^{-1})_{\text{measured}} \quad (\text{E 3:7})$$

The relationship between corrected and measured OH reactivity was also investigated with the use of a mix of hydrocarbons (200 bar BOC 20 ppm methane, 20.1 ppm ethane, 19.9 ppm propane and 20 ppm n-butane in nitrogen). This test is conducted in the same manner as the propyne test described above, using a similar range of concentrations to induce a range of OH reactivity from:  $13 \text{ s}^{-1}$  to  $36 \text{ s}^{-1}$  at pyrrole to OH ratios of 3.5, 3.51 and 2.0.

Concentration (ppb)	Total rate coefficient ( $\text{cm}^3 \text{ molecule}^{-1} \text{ s}^{-1}$ ) <sup>a</sup>	Calculated reactivity ( $\text{s}^{-1}$ )	Measured reactivity ( $\text{s}^{-1}$ )
150	$3.70 \times 10^{-12}$	13.8	122.1
200		18.4	233.9
250		23.0	205.6
300		27.6	259.2
350		32.2	301.0
400		36.8	421.6

**Table 3:1** Calculated and measured OH reactivity at a pyrrole to OH ratio of 3.51 for a mix of hydrocarbons

<sup>a</sup> Total rate coefficient calculated through the summation of OH + hydrocarbon rate coefficients for all hydrocarbons tested

Rate coefficients of  $6.4 \times 10^{-15} \text{ cm}^3 \text{ molecules}^{-1} \text{ s}^{-1}$ ,  $2.48 \times 10^{-13} \text{ cm}^3 \text{ molecules}^{-1} \text{ s}^{-1}$ ,  $1.09 \times 10^{-12} \text{ cm}^3 \text{ molecule}^{-1} \text{ s}^{-1}$  and  $2.36 \times 10^{-12} \text{ cm}^3 \text{ molecules}^{-1} \text{ s}^{-1}$  for the reactions of OH with methane, ethane, propane and n-butane respectively (298K and 1 bar) (Atkinson, 2003) are used to calculate the OH reactivity with these hydrocarbon mixture (Table 3:1, pyrrole to OH ratio of 3.51).

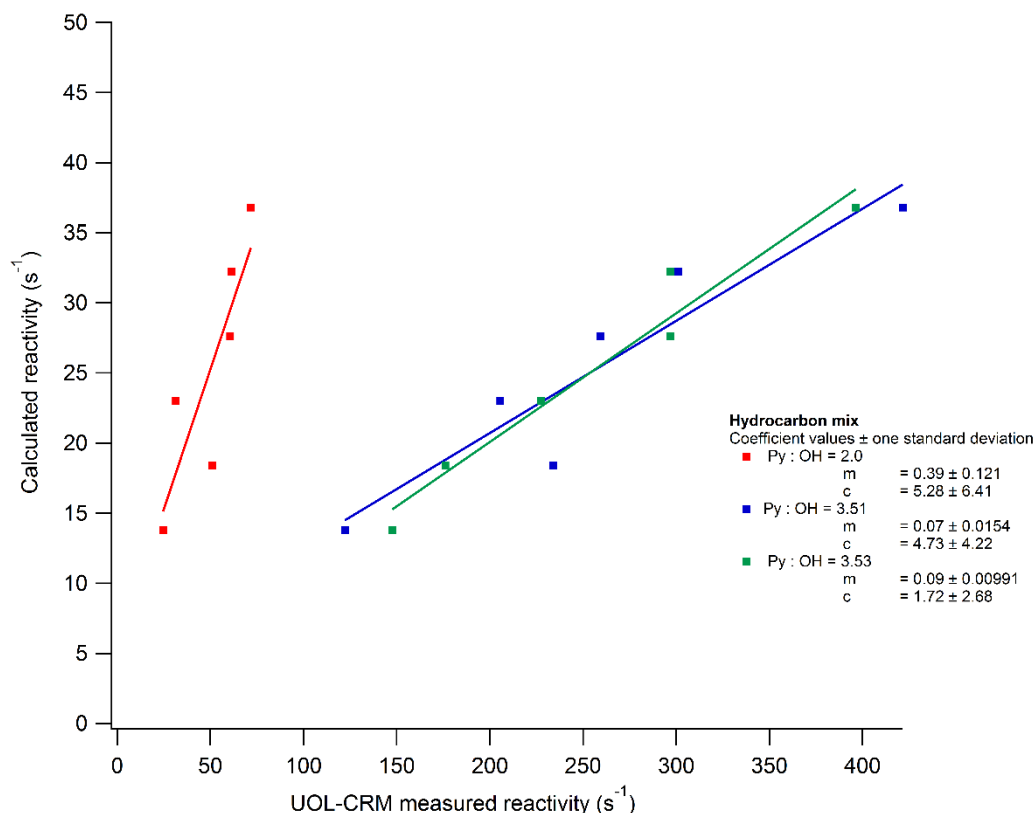


**Figure 3:8 Measured and calculated OH reactivity of a hydrocarbon mix (methane, ethane, propane and n-butane). At pyrrole to OH ratios of 2.0, 3.51 and 3.53. As a function of the summed rate coefficients and concentrations of all hydrocarbons**

In the same fashion as the propyne experiments, tests were conducted at various pyrrole- to- OH ratios, and a linear relationship is also observed between the calculated and measured reactivity, which can be used to correct the measurements made by the UOL-CRM (Figure 3:8).

Using Equation 1:5, the rate coefficients of all the hydrocarbons tested, (along with their respective concentrations) can be summed to obtain an average the total OH reactivity.

It is worth noting that, reactivity measurements conducted at pyrrole to OH ratio of 3.53 was conducted on a different PTR-ToF-MS to that at ratios of 3.51 and 2.0, but produces a correction factor that follows the trend.

The results of these experiments show a relationship between the pyrrole-to-OH ratio and the correction factor (shown in Figure 3:9). As the ratio of pyrrole-to-OH increases, the correction factor  $F$ , derived from the gradients within Figures 3:7 and 3:8 decreases, where the largest pyrrole-to-OH ratio at 3.9, has a correction factor of 0.02, and the lowest pyrrole-to-OH ratio generates the highest correction factor. As seen in Table 3:2 summarising the correction factors obtained and their respective pyrrole-to-OH ratios.

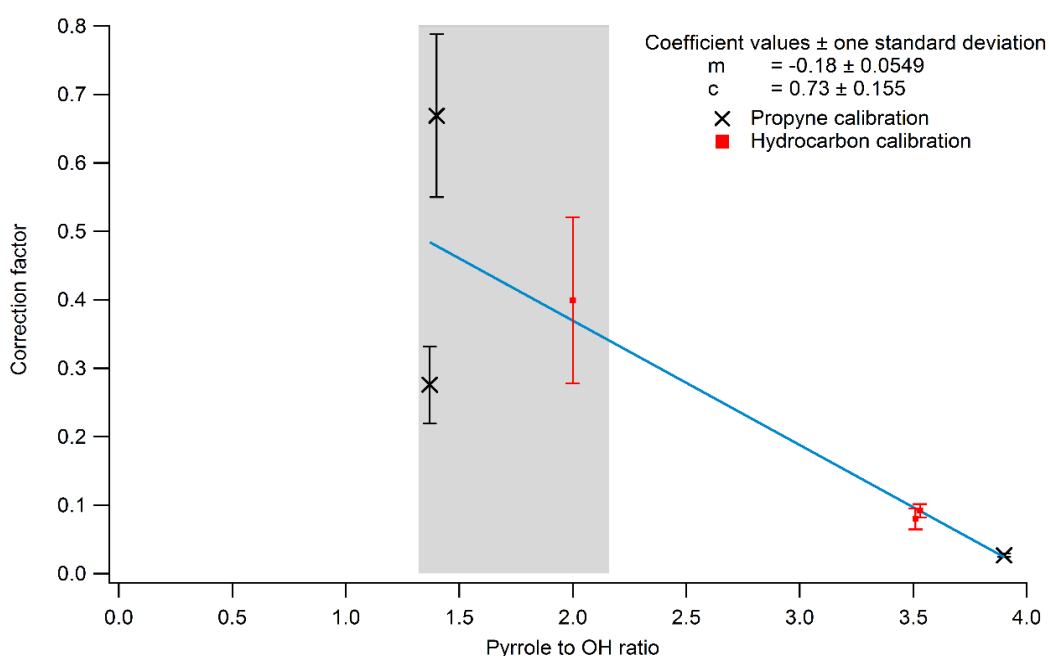


**Figure 3:9** The relationship between the correction factor at measured pyrrole to OH ratios. The ratios are obtained from kinetics studies of propyne and a mix of hydrocarbons (Figure 3:7 Figure 3:8). Adapted from (Michoud et al., 2015). The area highlighted in grey indicate the pyrrole OH ratios measured during the Weybourne campaign. Error bars are calculated from one standard deviation of measured correction factor

This trend is consistent with the kinetics of the system verging on a regime that is closer to pseudo-first-order. In which, at higher pyrrole-to-OH ratios the concentration of pyrrole is higher and in excess of the OH concentration, the difference between measured and calculated OH reactivity is minimal and the correction factor  $F$  is also small.

<b>Pyrrole / OH ratio</b>	<b>Correction factor <sup>a</sup></b>	
	1.37 <sup>b</sup>	0.27
	1.4 <sup>b</sup>	0.66
	2.0 <sup>c</sup>	0.39
	3.51 <sup>c</sup>	0.07
	3.53 <sup>c</sup>	0.09
	3.9 <sup>b</sup>	0.02

**Table 3:2 All pyrrole OH ratios from propyne and hydrocarbon kinetics calibrations and their corresponding OH reactivity correction factors**

<sup>a</sup> slope from hydrocarbon and propyne kinetics calibrations

<sup>b</sup> Pyrrole to OH ratio from propyne calibrations

<sup>c</sup> Pyrrole to OH ratio from hydrocarbon calibrations

Therefore in order to correct UOL-CRM based measured OH reactivity the pyrrole-to-OH ratio of the system must be known in order to derive the correction factor.

Using Table 3:2, and Figure 3:9, the relationship between the correction factor and the pyrrole-to-OH ratio is determined (E 3:8). During the time of measurement, the pyrrole-to-OH ratio is calculated and used within Equation 3:8 to determine the factor needed to correct the UOL-CRM measurements. This factor is then substituted into Equation 3:7 (along with the measured OH reactivity) in order to determine a true value of UOL-CRM based OH reactivity.

$$F = -0.18 \times \left( \frac{\text{Pyrrole}}{\text{OH}} \right) + 0.733 \quad \text{(E 3:8)}$$

The experiment conducted using propyne at a pyrrole to OH ratio of 1.4 showed a large degree of error within the intercept ( $-136.63 \pm 30.4 \ 1\sigma$ ), this was conducted during the ICOZA field campaign (campaign discussed within chapter 4), the source of this error is owing to variations within the measured C1 mode pyrrole signal as a standard deviation of 2.2 was calculated during C1 mode, however for C2 mode, and the addition of propyne (C3), the standard deviation ranged from 0.09 to 0.7 ( $1\sigma$ ). This was because the hydronium isotope signal measured during C1 mode was 22% lower than during C2 modes.

A test using the mix of hydrocarbons also showed a large degree of error within the measurements, as the test conducted at a pyrrole-to-OH ratio of 2.0 has a calculated intercept of 5.28 and an error of  $\pm 6.41$  ( $1\sigma$ ).

It is likely that this error within the measurements is also owing to short experiment times, and a lack of time allowed for the instrument to stabilise in between adjustment of the gas standards concentration resulting in long response time for the instrument. From Figure 3:6, it can be seen that whilst the concentration of propyne increases in between each C3 mode, it may also be increasing during C3. This is likely owing to a short residence time and low flow rates of the introduced gas standard.

All of the raw measurements in the following chapters have been corrected using the factor determined in Equation 3:8, after the correction factor is determined from the pyrrole to OH ratio, it is then substituted in Equation 3:7 in order to generate a measurement of total OH reactivity.

Owing to the fact the ambient air flowing into the reaction vessel contains a mixture of VOCs, it is best to correct the measured reactivity of the UOL-CRM by an average correction factor determined at a specific pyrrole to OH ratio at the time of sampling. This leads to the use of equation (E 3:7) (Michoud et al., 2015)

Using a similar calibration method, Michoud et al. (2015) have observed that higher correction factors are determined for more reactive species at the same pyrrole to OH ratios. At pyrrole to OH ratios of 1.4, they have determined that the correction factor based isoprene experiments is 7.6% higher than for propene, which is 50.6% higher than for ethane. However, at a lower pyrrole to OH ratio (2.3), the correction factor derived for isoprene was only 1% different than for isoprene. The consequence of this is that the CRM method needs to be fully characterised at numerous pyrrole to OH ratios with a number of fast and slow reacting species.

### **3.5 Recycling of OH due to the presence of high NO concentrations within the reaction vessel**

Hydrogen atoms generated through Reaction 1:31, will proceed to react with oxygen present within the reaction vessel to form HO<sub>2</sub> molecules (R 1:6). HO<sub>2</sub> can then react with NO present in ambient air to form excess OH along with NO<sub>2</sub> (R 1:10). The process of generating OH within the UOL-CRM reaction vessel (photolysis of water vapour) can generate a stable concentration of OH, however, high concentration of NO within the ambient air can cause the concentration of NO to fluctuate.

In some circumstances, high concentrations of NO within ambient air will regenerate so much OH that C3 pyrrole concentrations establish a level similar or lower than C2.

#### **3.5.1 Experimental- Correction of C3 measurements owing to NO induced OH recycling**

This effect can be accounted through experimentation in order to determine the degree at which NO regenerates OH. This experiment involves the injection of a gas standard to in order to obtain a measurement of a baseline C3 level (termed: C3<sub>expected</sub>). Increasing concentrations of NO are then added to the reaction vessel, as more and more NO is added to the vessel, the measured C3 pyrrole concentration deviated further away from the baseline pyrrole C3<sub>expected</sub> signal. The degree at which the measured C3 level decreases with each addition of NO is then characterised and used to corrected pyrrole concentrations measured during C3 mode when NO is present within the sampled ambient air (Michoud et al., 2015, Hansen et al., 2015).

Figure 3:10 shows the results of a particular experiment in which five minute measurements are recorded of C1, C2, C3 modes, followed by a final measurement of C2 mode, (propyne in the absence of ambient air flows into the reaction vessel during C3 mode). As higher concentrations of NO flows into the

reaction vessel, more OH is generated within the reaction vessel and the pyrrole C3 level decreases further from the baseline.

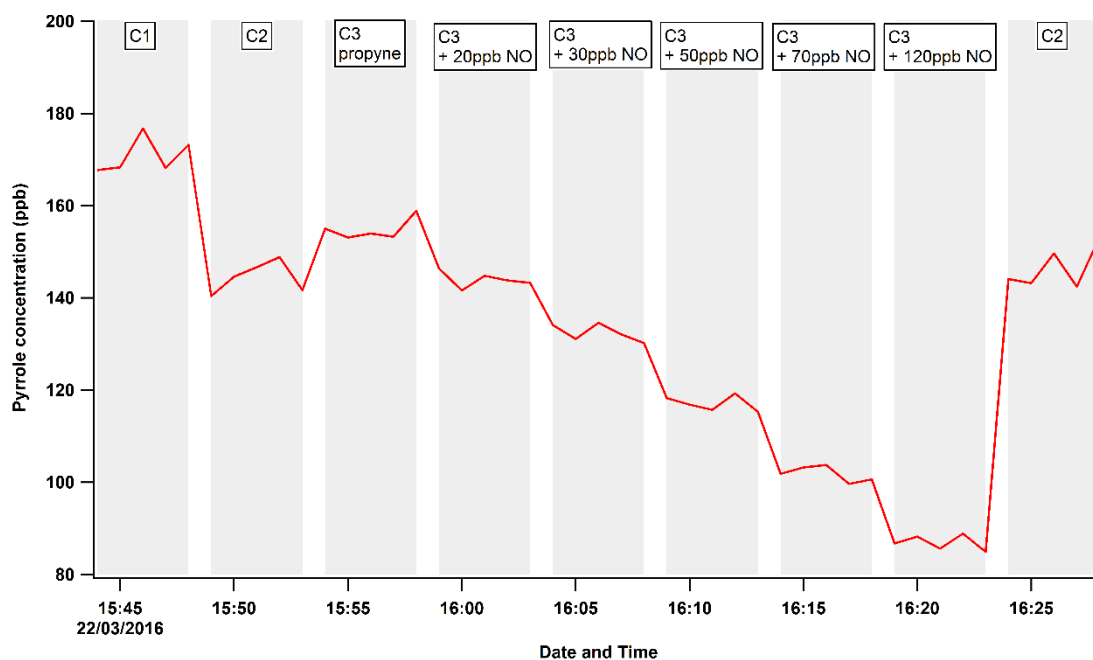


Figure 3:10 CRM pyrrole concentration measurements. Areas highlighted in grey show measurements of C1, C2 and baseline C3 measurement obtained with the addition of propyne. Further addition of 20, 30, 50, 70 and 120 ppb of NO results in the decrease of pyrrole signal

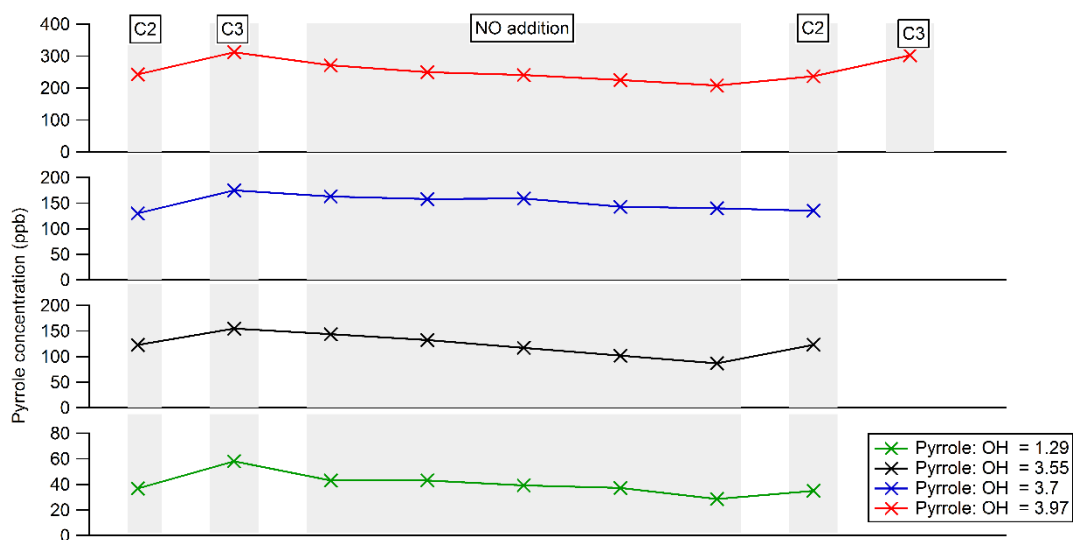
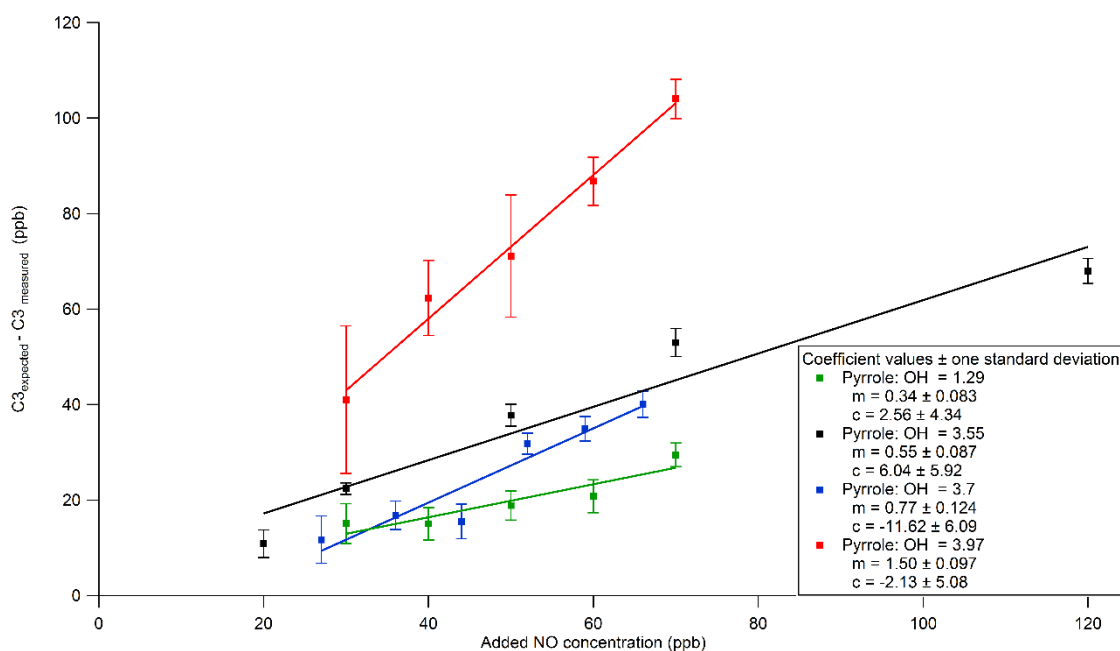


Figure 3:11 Observed changes in pyrrole concentration when switching from C2 to C3 followed by the addition of increasing concentrations of NO into the reaction vessel. NO concentrations of 30, 40, 50, 60 and 70ppb at a pyrrole to OH ratio of 1.29 and 3.97. 20, 30, 50, 70 and 120 ppb at pyrrole/OH ratio 3.55. 27, 36, 44, 52, 59 and 66ppb pyrrole/ OH ratio 3.7



**Figure 3:12 Experimental characterisation of the degree at which C3 differs from a baseline measurement with the addition of NO at pyrrole to OH ratios of 2.46, 3.55, 3.7 and 3.97. Error bars are calculated from the standard deviation in  $\Delta C3$**

The experiment was repeated at various pyrrole to OH ratios (Figure 3:11). As expected, when injecting higher concentrations of NO into the UOL-CRM, the difference between the baseline,  $C3_{\text{expected}}$  and the actual measured concentration of pyrrole (termed  $C3_{\text{measured}}$ ) increases.

For each experiment it was observed that levels of approximately 50-66 ppb of NO within the reaction vessel is enough to cause a drop in the pyrrole signal to a concentration similar to that of C2.

In order to determine the degree at which C3 pyrrole concentrations diverge from the baseline the difference between  $C3_{\text{expected}}$  and  $C3_{\text{measured}}$  ( $\Delta C3$ ) is then calculated and a linear fit is applied to the variables;  $\Delta C3$  and the concentration of NO added (ppb) generating coefficient values that can be used to correct C3, based on the concentration of NO measured at a specific time, through the use of equations 3:9 and 3:10. (Michoud et al., 2015).

$$C3_{\text{corrected}} = C3_{\text{measured}} + \Delta C3 \quad (\text{E 3:9})$$

$$\Delta C3 = m [\text{NO}](ppb) + c \quad (\text{E 3:10})$$

The results show that the change in C3 pyrrole concentration is dependent on the ratio of pyrrole to OH. Therefore the pyrrole- to- OH ratio at the time of measurement can be substituted into equation 3:10 and then used to correct C3 mode pyrrole concentrations (E 3:11). Where m and c is the gradient and intercept shown in Figure 3:13.

$$\Delta C3 = m \left( \frac{\text{Pyrrole}}{\text{OH}} \right) [\text{NO}] + c \quad (\text{E 3:11})$$

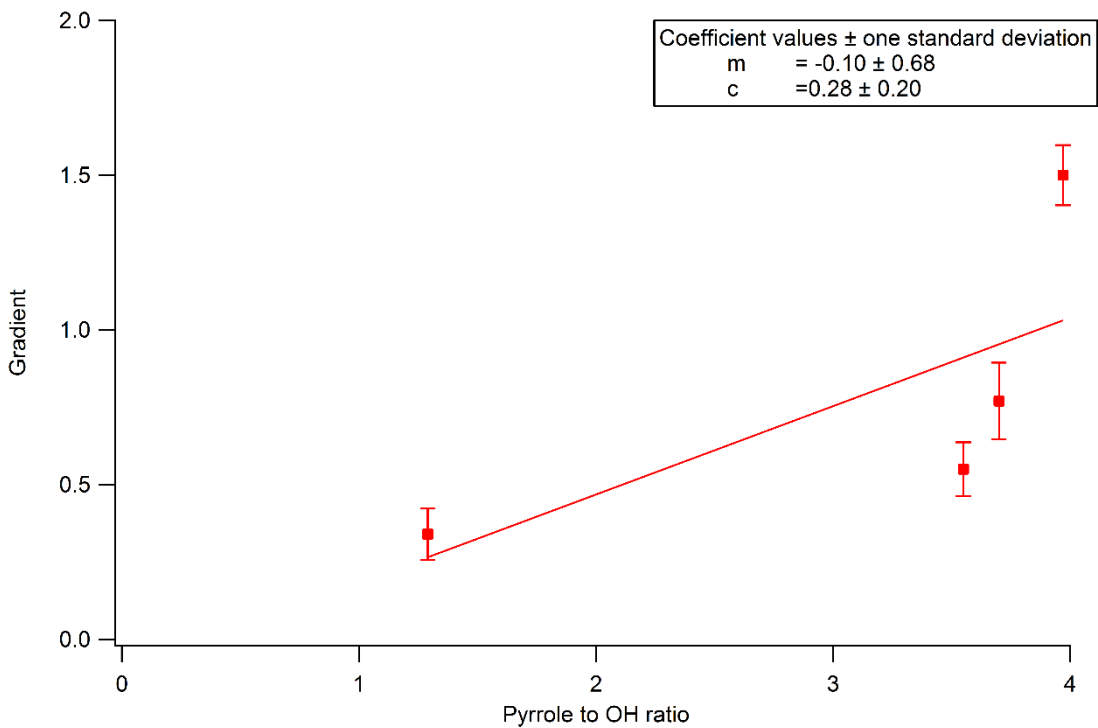


**Figure 3:13 Gradients calculated from the correction experiments shown in Figure 3:12 at their corresponding pyrrole to OH ratios**

### 3.6 Dilution of ambient air within the UOL-CRM

During C3 mode, as nitrogen and pyrrole flow into the UOL-CRM reaction vessel along with ambient air, any VOCs present within the sampled ambient air are therefore diluted with nitrogen and pyrrole resulting in an underestimation of OH reactivity. By calculating the dilution factor based on the flow rates ambient air, pyrrole and nitrogen, a final corrected value of OH reactivity can be determined, (E 3:12 and 3:13) (Zannoni et al., 2015).

$$\begin{aligned} & \text{Dilution factor} \\ & = \frac{\text{ambient air (sccm)} + \text{pyrrole (sccm)} + \text{nitrogen (sccm)}}{\text{ambient air (sccm)}} \end{aligned} \quad \text{(E 3:12)}$$

$$\text{R OH (s}^{-1}\text{)}_{\text{final}} = \text{R OH (s}^{-1}\text{)}_{\text{measured}} \times \text{Dilution factor} \quad \text{(E 3:13)}$$

### 3.7 Limit of detection (LOD)

The UOL-CRM LOD is defined as the minimal detectable difference between C2 and C3 mode pyrrole concentrations. The UOL-CRM LOD was calculated using measurements of C1 and C2 mode, in a similar method to that described within Michoud et al. (2015). Measurements were conducted in the same manner as that discussed within sections 2.2.1.2 and 2.2.1.3, however C2 measurements were conducted for 24 hours and separated into five minute section.

The standard deviation within the measured pyrrole concentration for each five minute C2 section was calculated ( $\sigma_{C2}$ ) ( $1\sigma$ ), along with the average standard deviation for the entire period (average  $\sigma_{C2}$ ) and the average pyrrole C2 signal for the whole period (average  $C2_{[\text{pyrrole}]}$ ).

C3 pyrrole concentrations are calculated by summing three times the average standard deviation in C2, with the average pyrrole signal ( $C3 = 3(\text{average } \sigma_{C2}) + \text{average } C2_{[\text{pyrrole}]}$ ). Following this, the total OH reactivity was calculated using the CRM equation (E 1:14).

At an average pyrrole to OH ratio of 1.5, the LOD was therefore calculated as  $5 \text{ s}^{-1}$  (corrected for deviations in pseudo first order kinetics).

### 3.8 Measurement uncertainties

The uncertainty of the field campaign measurements shown in chapters 4 and 5 are calculated through the propagation of errors using the uncertainties shown within Table 3:3 which contribute to the error within the final measurement of total OH reactivity, the rate coefficient between pyrrole and OH, the calculated sensitivity pyrrole (Figure 4:3). These errors include: the correction due to deviations from pseudo first order kinetics (Figure 3:9) and the correction owing to differences in humidity between modes C2 and C3 (Figure 3:5) an overall systematic uncertainty of ~43% is calculated. The error associated the correction owing to NO derived OH recycling is not included within this calculation as the data within chapters 4 and 5 has not been corrected for NO based OH recycling.

<b>Error Source</b>	<b>Error (%)</b>
Uncertainty of OH+ pyrrole rate coefficient	8
Calculated pyrrole sensitivity	7
Deviations in pseudo- first order kinetics	30
Corrected differences in C2 and C3 humidity	28
<b>Total Error</b>	<b>43</b>

Table 3:3 Error budget table listing the components used to derive measured OH reactivity using the UOL-CRM and their corresponding uncertainty

### 3.9 Conclusions

The Comparative Reactivity Method is subject to a number of interferences that need to be corrected:

1. Deviations in ambient air humidity within C2 and C3 modes results in variations of OH concentrations. The influence of relative humidity on C2 pyrrole concentration is determined by performing experiments in which the pyrrole concentration is measured at increasing relative humidity, (Figure 3:5). Using equation 3:5 derived from the experiment, the humidity measured during C3 mode is then used to correct C2 pyrrole concentrations.
2. The CRM equation used to calculate total OH reactivity assumes that the system is under pseudo first order conditions (the pyrrole concentration is in excess of the OH concentration). However this is not the case as a balance of flow rates is needed in order to produce a stable pyrrole concentration and ensure that a suitable dataable change is observed when switching from C2 to C3 modes. In order to correct for this deviation from pseudo first order kinetics, a series of experiments were conducted in which a gas standard (propyne and a mixture of hydrocarbons) is injected into the UOL- CRM. The OH reactivity is the measured by the UOL-CRM, and compared to an expected reactivity (calculated based on the concentrations of gas standard injected into the UOL-CRM reaction vessel). A linear relationship between the measured and calculated reactivity, and a dependence on pyrrole to OH ratio is observed. This dependence is then used to derive a correction factor based on the pyrrole to OH ratio. Ambient air measurements are then corrected based on this correction factor and the calculated pyrrole OH ratios (E 3:8).
3. A correction also needs to be applied to measured reactivity as NO present within the UOL-CRM can recycle OH. Increasing concentrations of NO within with UOL-CRM will linearly decrease the measured C3 signal. This effect has been characterised within section 3.5.1
4. Finally, VOC within the ambient air sampled during C3 mode are diluted by the presence of pyrrole and humidified nitrogen present within the UOL-CRM reaction vessel. A dilution factor is therefore calculated based on the flow rates of nitrogen, ambient air and pyrrole at the time of sampling to correct for this dilution.

## **Chapter 4. Deployment of the UOL-CRM. Measurements conducted at Weybourne Atmospheric Observatory (WAO)**

### **4.1 Introduction**

Chapters 2 and 3 discussed the instrumentation used for the UOL-CRM, its development, calibrations and validation. Following this, the UOL-CRM was deployed during the Integrated Chemistry of Ozone in the Atmosphere (ICOZA) field campaign throughout July 2015.

#### **4.1.1 Campaign objectives**

ICOZA was a National Environmental Research Council (NERC) funded field campaign throughout July 2015. Led by the University of Birmingham, along with the University of East Anglia (UEA), Leeds, York and Leicester.

The purpose and objectives of this campaign was to measure and understand ozone transport and formation, by studying aged pollution regimes from London in comparison to cleaner air approaching from the North Sea. During the field campaign, local chemical ozone production rates were measured. Included with this are measurements in response to ozone production with respect to measurements of  $\text{NO}_x$  and VOC levels.

Measurements of ozone concentration can act to constrain act to constrain OH concentration and OH loss measurements. For example, during periods of the campaign when  $\text{NO}_x$  concentrations are high, the capacity for ozone production is high, this could result in high degrees of OH reactivity if the contribution to OH reactivity is dominated by  $\text{NO}_x$  rather than VOCs. OH reactivity measurement could thereby act as an indicator of varying pollution regimes, by measuring total OH reactivity when a specific contributor to total OH reactivity such as ozone is

high or low. Once the UOL- CRM had been tested in laboratory conditions through calibrations and validations. The next aim is to test the system during a field campaign. The objective was to measure total OH reactivity profiles and regimes which be attributed to air masses from local megacities upwind of the site.

A final objective is to in order to test the capability of the UOL- CRM set up for field measurements. With the aid of total OH reactivity measurement made by the UL-LIF, and measurements of VOC, NO<sub>x</sub>, ozone and CO concentrations (used to calculate total OH reactivity), measurements made by the UOL-CRM can be easily understood. Any variations in measurements made by the UOL-CRM in comparison to that made by the UL-LIF and calculated total OH reactivity can be identified and used to improve the UOL-CRM. Supporting measurements are also used to correlate any trends in OH reactivity to changes in VOC, NO<sub>x</sub> and ozone concentration.

#### **4.1.2 Measurement Location**

The Weybourne Atmospheric Observatory is a site located on the North Norfolk Coast (52°N52'02"N, 1°07'19"E) (Figure 4:1), established by the University of East Anglia in order to measure various components of atmospheric gases such as: carbon monoxide, methane and oxygen (Brooks, 2016).

At the location, a converted shipping container (Figure 4:2) (was used to host the PTR-ToF-MS and the UOL-CRM, along with the other instruments provided by the University of Leicester, such as a Chemical Ionisation Mass Spectrometer (CIMS), and a Broadband Enhanced Cavity Enhanced Spectrometer (BBCEAS).

The shipping container is situated approximately 200 m from the North Sea, owing to this, the location of the site is susceptible to clean air sea salt and aerosols from the North Sea. Including long range transport of polluted air passing from Europe. Polluted air from London can also pass over the measurement site. Trajectories of air masses during various periods of the

campaign and the corresponding total OH reactivity for each period are shown in chapter 5.

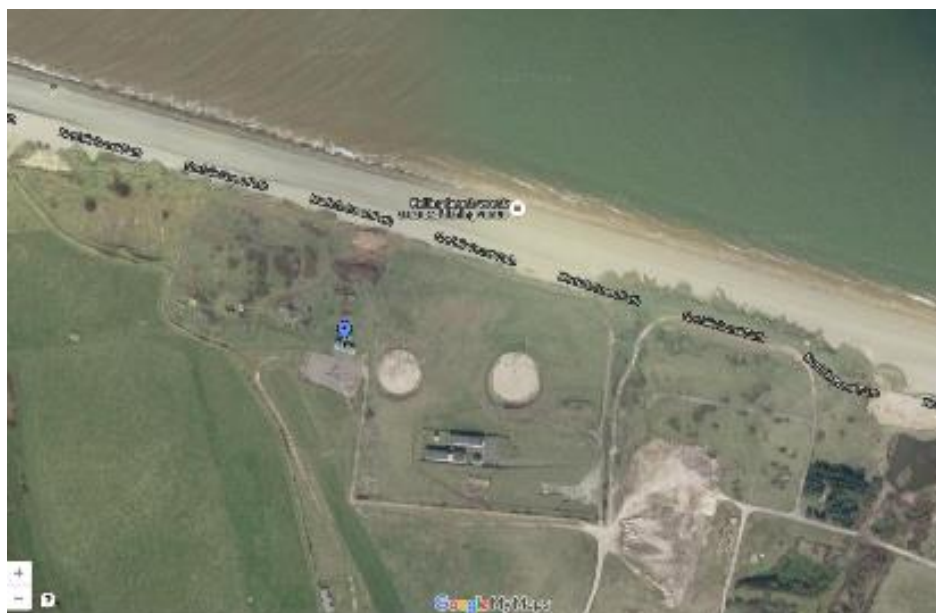


**Figure 4:1** Google Maps image of the measurement location for the ICOZA field campaign



**Figure 4:2** A picture of the University of Leicester shipping container housing the UOL-CRM

## 4.2 Instrument set up

The UOL-CRM is configured the same manner as that described in chapter 2 and shown in Figure 2:3. The exhaust line from the reaction vessel was directed to flow out of the shipping container and positioned downwind (10 m) from a 3 m Teflon, quarter inch diameter sample inlet. Typically, the wind direction throughout the field originated from a south to south-west direction (Figure 5:3).

An air conditioning unit regulated the temperature within the shipping container, ranging from a maximum of 36°C to a minimum 19°C, and averaging 22°C for the duration of the campaign. Through the regulation of the temperature within the shipping container, a stable kinetics regime within the UOL-CRM reaction vessel should be observed, whilst also maintaining a stable hydronium production rates within the mass spectrometer. However small temperature fluctuations within the container were observed and resulted in variations in hydronium production within the mass spectrometer. The effects of these variations on UOL-CRM measured total OH reactivity are discussed in further detail in section 4.4

## 4.3 Calibrations

A pyrrole calibration was conducted at the start of the campaign (in the same manner as that discussed within section 3.2) in order to determine the sensitivity of the mass spectrometer towards pyrrole (calculated as 0.100 ncps/ppb) as seen in Figure 4:3. This sensitivity is used throughout the whole campaign period and it is used to determine the OH reactivity as discussed below.

The raw data was corrected for deviations from pseudo first order kinetics (section 3.4) by calculated the pyrrole to OH ratio for each measurement and applying equations 3:7 and 3:9 to the data.

Calibrations for the recycling of OH due to the presence of NO, and a humidity calibration were also conducted, but these were unsuccessful due to instability of hydronium counts within the mass spectrometer. These calibrations were

repeated in the laboratory post- campaign, at the same sensitivity and E/N observed during the campaign. And applied to the data collected during the period of the campaign. The results of these calibrations are seen along with others in chapter 3.

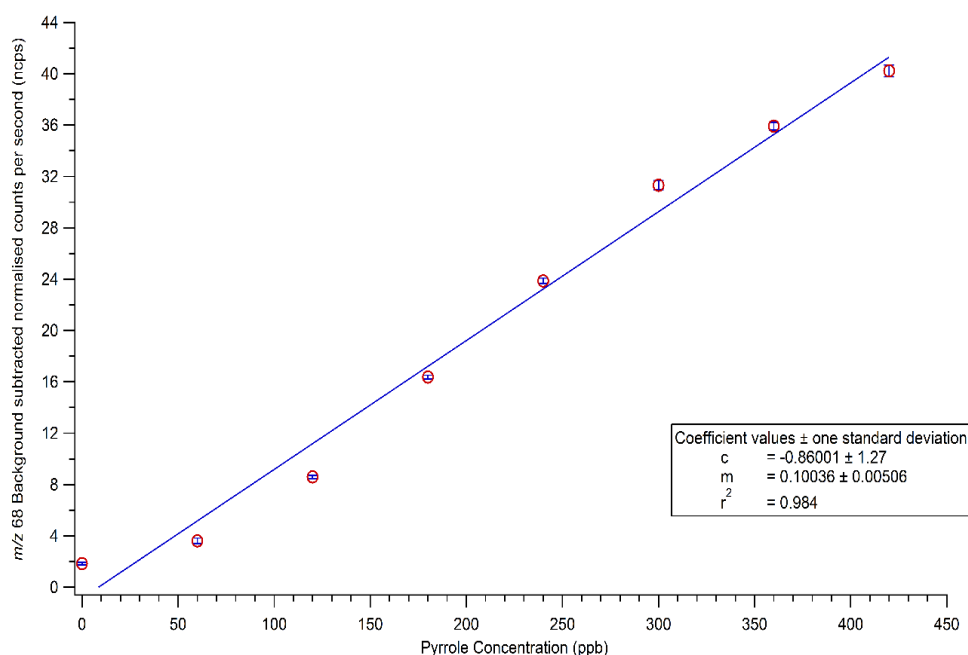


**Figure 4.3 Pyrrole calibration conducted during the ICOZA campaign to determine instrument sensitivity towards pyrrole**

C0 wet, C0 dry and C1 is measured at the start of every measurement cycle. Measurements of C2 and C3 were conducted continuously throughout the campaign via sequential cycling between C2 and C3. At the start of each day, the reaction vessel is dried by flowing propyne into the reaction vessel, this acts to scavenge any residual OH present within the reaction vessel, generating a true C1 signal that is in dry conditions (Zannoni et al., 2015). Days in which calibrations were conducted are seen within the time series as gaps within the data, gaps are also present due to a power cut on the morning of 04/07/15 and in the evening on 06/07/15.

## 4.4 Measurements of VOC concentrations made by the UOL-CRM

Chapter 1 discussed the objectives that this research will work towards, one objective was to utilise extra functionality provided by the PTR-ToF-MS to simultaneously measure total OH reactivity and VOC concentrations.

Kumar and Sinha (2014), have explored a method in which the PTR-ToF-MS, samples ambient air in between C2 and C3 measurement modes. This approach was employed during the field campaign, as concentrations of numerous VOCs were measured by bypassing the UOL-CRM reaction vessel as ambient air is directed into the PTR-ToF-MS (Figure 2:3).

However, this method proved unsuccessful as a caveat with regards to PTR-ToF-MS measurements are exposed. The PTR-ToF-MS is tuned and optimised for the sole detection of pyrrole as the E/N (178 Td) is adapted to reduce the formation of hydronium clusters, whilst reducing the probability of pyrrole fragmentation.

At this E/N, whilst no fragmentation of pyrrole occurs, it is likely that ambient VOCs could fragment. For example, at an E/N of 106 Td, de Gouw and Warneke (2007) have observed the fragmentation of alkyl benzenes, therefore changing the E/N to accommodate for pyrrole measurements will increase the sensitivity of the PTR-ToF-MS towards pyrrole but also at the detriment of the PTR-ToF-MS sensitivity towards VOCs. Baasandorj et al. (2015), for example have observed that at an E/N of 125 Td, the PTR-MS sensitivity towards ethanol is 5 – 20 times lower than that of formic acid.

Figure 4:4 shows a series of VOC (methanol, acetonitrile, acetaldehyde, acetone, toluene, isoprene, MVK and MEK) concentration measurements made from 19<sup>th</sup> July to 20<sup>th</sup> July. A large degree of noise can be seen within these measurements, and all of the VOCs measured follow the same trends. Whilst daily changes in VOC concentrations are observed, no individual variation between VOC time profiles were observed, as seen within Figure 4:4. This is attributed to the poor sensitivity of the PTR-ToF-MS towards these VOCs.

Measurements of VOC concentrations made by the UOL-CRM were therefore not used when examining OH reactivity measurements due to the high amount of noise and unreliability within these measurements.

As a result, UOL-CRM OH reactivity data was compared to instruments specifically designed to monitor VOC concentrations, a Proton Transfer Reaction- Quadrupole Mass Spectrometer (PTR-QMS) and a Gas Chromatography- Flame Ionisation Detector (GC- FID), (Table 5:1).

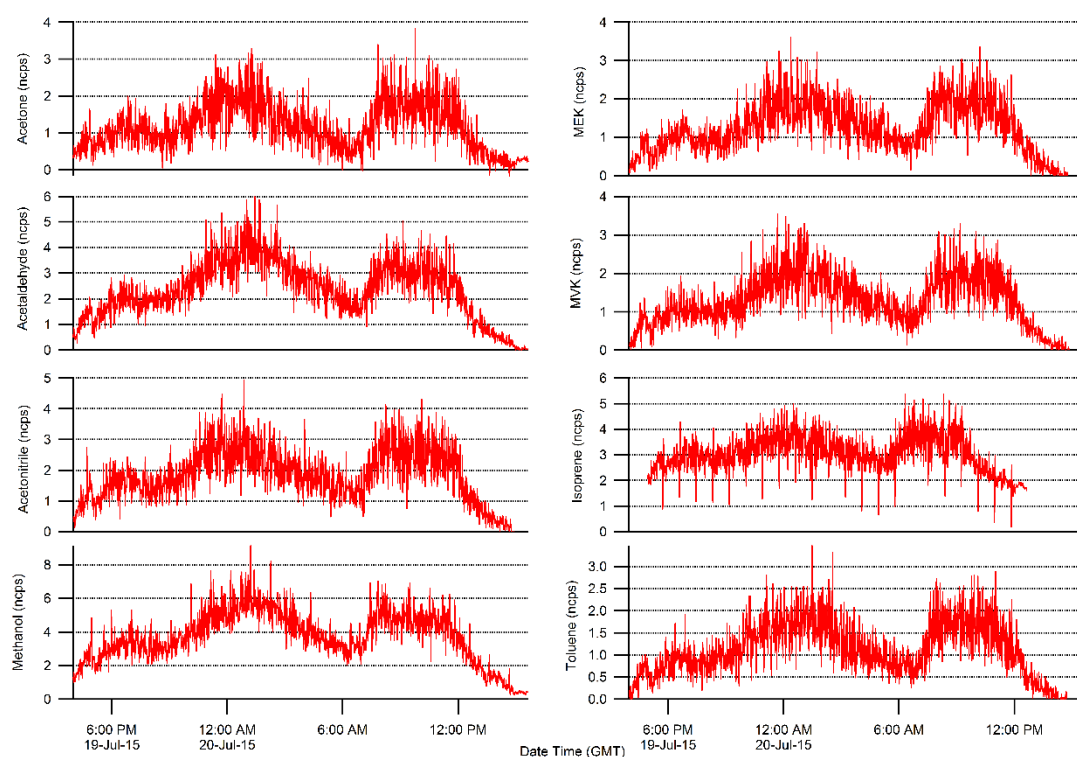
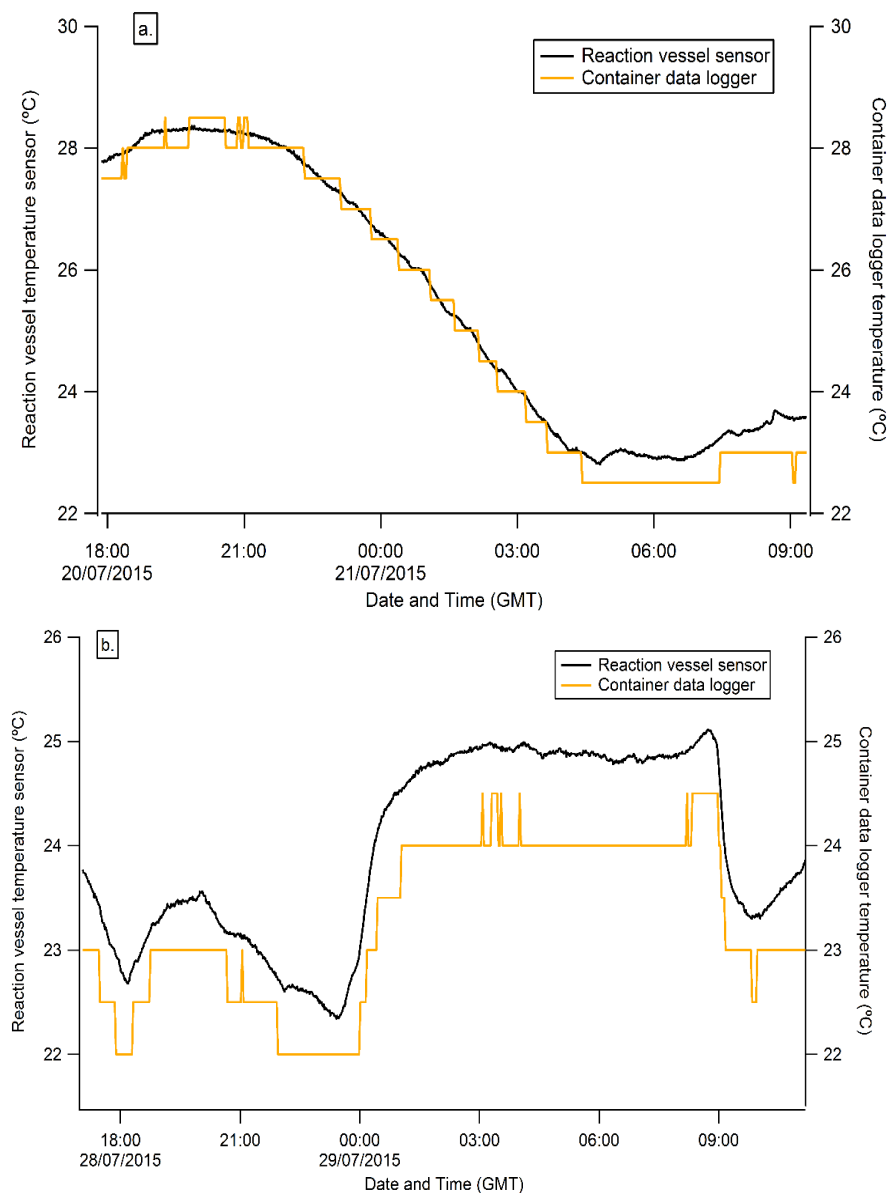


Figure 4:4 Concentrations of VOCs measured by the UOL-CRM PTR-ToF-MS from 19th July to 20th July

## 4.5 Hydronium instability within the mass spectrometer

Two sets of temperature and humidity probes were located within the shipping container, one attached to the UOL-CRM reaction vessel, and a second situated within the container next to the mass spectrometers ion source. Both sets of temperature/ humidity measurements agree with each other (Figure 4:5 a. and b.), and from this it can be concluded that any temperature fluctuations that

occur within the reaction vessel are also a representation of the same temperature fluctuations that occur within the shipping container.



**Figure 4:5** Temperature recordings measured by a temperature humidity probe located within the reaction vessel from 20th to 21st July and from 28th to 21st July, in comparison to temperature recorded using a data logger next to the mass spectrometers ion source for the same time period

These temperature fluctuations within the shipping container have the potential to influence the hydronium count rate within the mass spectrometer. Other interferences influencing the measured total OH reactivity have an effect that is

negligible during this period of measurements and throughout the campaign. For example, the relative humidity of sampled ambient air during the period of the field campaign seen within Figure 4:5 saw only variation of approximately 10% when sampling during C2 and C3. Spikes in relative humidity were only observed when the Solenoid valves used to switch between C2 and C3 modes turn on and off (Figure 4:6). Fluctuations in relative humidity on a scale of 10% within the reaction vessel should not affect the hydronium isotope count rate within the mass spectrometer as a constant supply of hydronium and humidity is provided by the mass spectrometers water bubbler. Only the  $m/z$  37 count rate is influenced by humidity. This 10% fluctuation in relative humidity is accounted for when calculating total OH reactivity as a humidity calibration is applied to C2 and C3 measurements, (section 4.4, Figure 4:12).

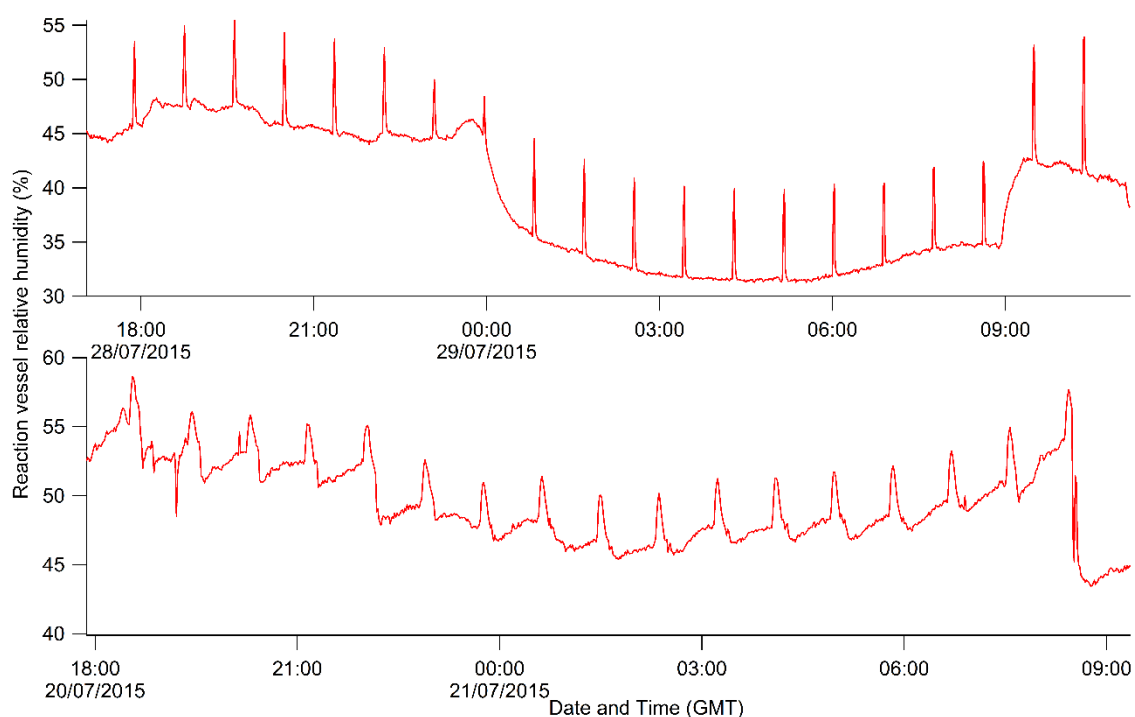


**Figure 4:6 Relative humidity (%) measured within the reaction vessel from 20th to 21st July and from 28th to 29th July**

#### **4.5.1.1 The effect of temperature on the PTR-ToF-MS hydronium signal**

Temperature fluctuations within the shipping container is the only reasonable source for the fluctuations within hydronium count rate. The shipping container is fully air conditioned, however the use of pumps, along with entering and leaving the container can cause slight fluctuations in temperature within the container. This affects the water reservoir that is used as a water vapour source for hydronium production which was not heated and insulated during the field campaign. As a result, fluctuations in temperature can change the rate of water vapour production from the bubbler with a rise in temperature increasing the kinetic energy of the water within the bubbler.

This variation in temperature introduces, variations and instability within the hydronium ( $m/z$  19) reagent ion signal within the mass spectrometer throughout the campaign. This instability is therefore propagated into the count rate of the hydronium isotope ( $m/z$  21) discussed within section 3.2.

Fluctuations within the hydronium count rates also introduces noise within the normalised pyrrole signal, this is owing to the degree at which the hydronium count rate decreases, for example during the time period at which the hydronium count rate is at its maximum on 20<sup>th</sup> July (68661 counts per minute), the standard deviation within the C2 normalised pyrrole count rate is 0.38, and a high signal to noise ratio of 310 is calculated.

As the hydronium count rate decreases, the standard deviation within the normalised pyrrole signal increases to 2.04, this is due to the count rate for the hydronium reagent ion being so low (859 cpm), that a reduced amount of pyrrole is protonated via the proton transfer reaction. At this point, the C2 signal to noise ratio is also reduced (218) in comparison to that measured at the maximum point of hydronium concentration. It is assumed that the background noise throughout the entire experiment is constant, however as the pyrrole signal decreases, so does the signal to noise ratio.

This effect is observed in Figure 4:8 a. and b. Temperature recorded using the sensor within the reaction vessel is plotted alongside the  $m/z$  21 count rate (in counts per minute) for 20<sup>th</sup> through to 21<sup>st</sup> July. During this time period, the mass spectrometer and the UPL-CRM was cycling through C2, C3 and ambient air measurement phases.

It is obvious from these measurements that temperature within the reaction shipping container, has a profound influence on the hydronium count rate. At the start of this particular measurement cycle, a maximum temperature within the reaction vessel is recorded at 28.3 °C, this then decreases to 22.8°C. This happens on the same time scale at which the hydronium isotope count rate ( $m/z$  21) fluctuates within the mass spectrometer, reaching a maximum count rate of 68661 counts per minute and a minimum of 859 counts per minute. A similar relationship can be seen on 28<sup>th</sup> to 29<sup>th</sup> of July (Figure 4:8 c. and d.) as the temperature within the reaction vessel fluctuates, so does the hydronium count rate within the mass spectrometer.

Since hydronium is used as a reagent ion for proton transfer reactions (section 2.3) any changes in hydronium concentration will result in changes in pyrrole count rate. Figure 4:7 is an example of this effect in which the raw pyrrole signal is seen to follow and track the hydronium signal.

Because the pyrrole signal follows the hydronium signal so well (Figure 4:7), any changes in the pyrrole signal that occurs through variation in the hydronium counts can be corrected through normalisation, resulting in a pyrrole time series in which any changes in concentration occur only through the switching between C2 and C3 modes.

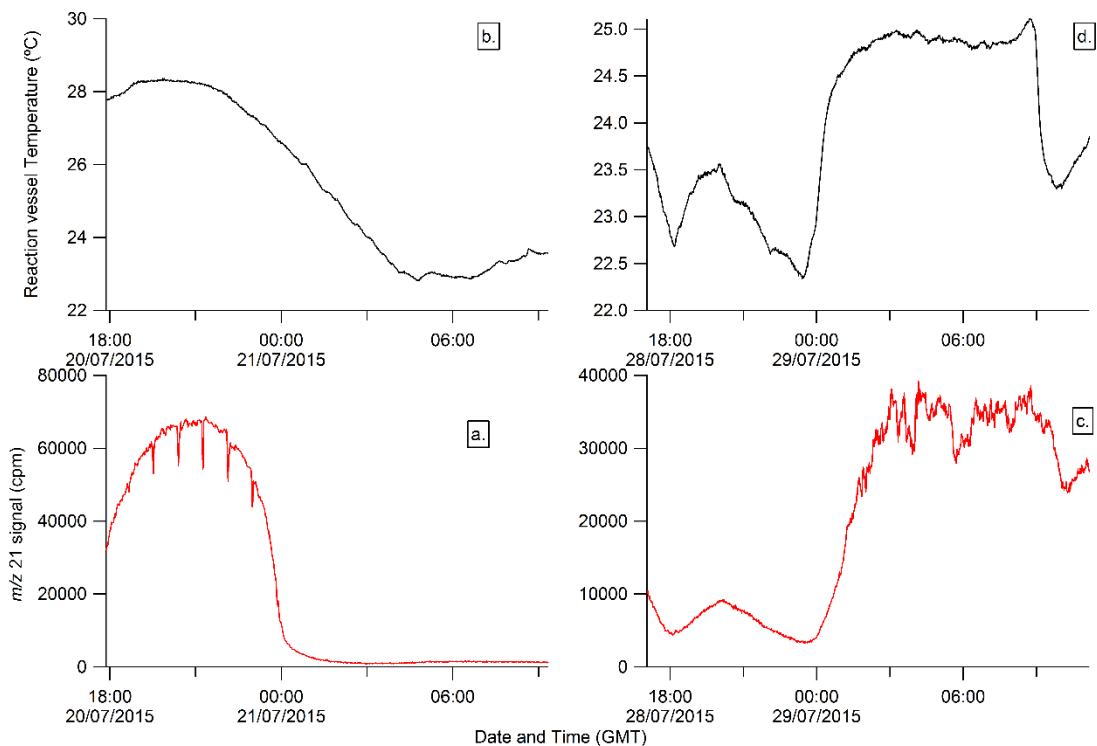


**Figure 4:8 a. and c.  $m/z$  21 hydronium isotope count rate measured alongside b. and d. temperature within the reaction vessel measured on 20th through to 21st July and 28th through to 29th July respectively**

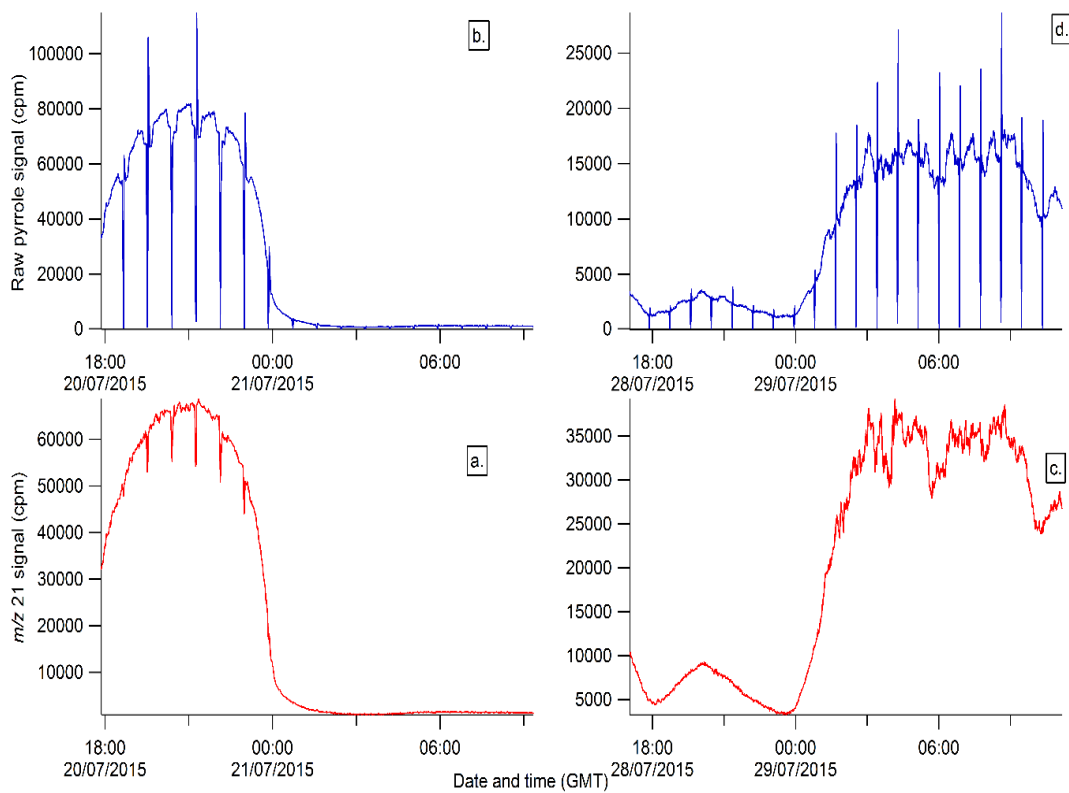


**Figure 4:7 a. and b. hydronium along with the corresponding pyrrole signal (c. and d.) measured on 20th through to 21st July with measurements carried out from 28<sup>th</sup> July to 29<sup>th</sup> July**

For example; changes in the measured pyrrole concentration when alternating between C2 and C3 modes can be seen in the raw pyrrole data (Figure 4:9 a.), however, due to the variation in hydronium signal during this period, the full degree at which the changes occur in both measurement modes in the raw data is not clarified. For example, from 11:00 pm 20/07/15 to 1:00 am 21/07/15 within Figure 4:9 a. as the hydronium ion count is fluctuating, it is impossible to differentiate between C2 and C3 when examining the raw pyrrole signal. Normalising the raw data can then correct for changes in hydronium isotope count rate and allows the true difference between C2 and C3 to be easily clarified and calculated. This effect is also seen in Figure 4:9 c. and d.

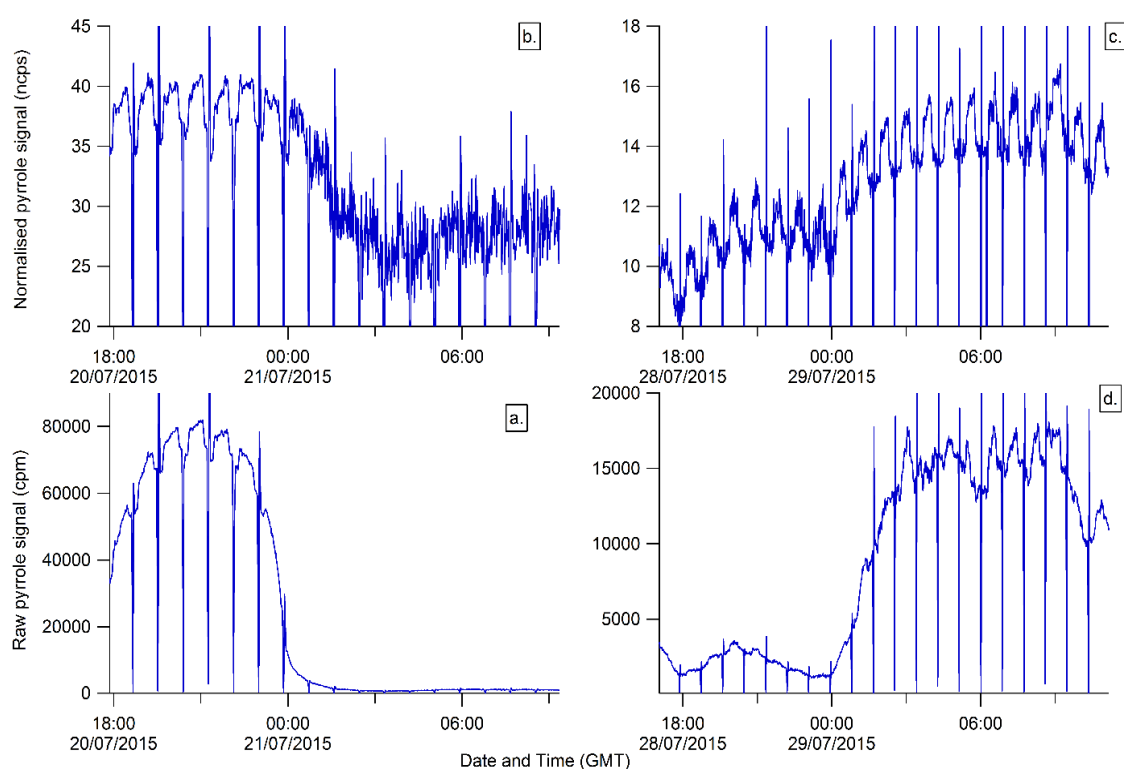


**Figure 4:9 a. and d. raw pyrrole signal measured from 20th to 21st July and 28th to 29th July along with the corresponding normalised pyrrole signals (b. and c.)**

The consequence of this variation in within the hydronium signal however, results in a variation in the measured total OH reactivity. As seen in Figure 4:10 a. and b. the variation in hydronium signal, propagates through into a normalised pyrrole signal, which finally propagates into the measured total OH reactivity.

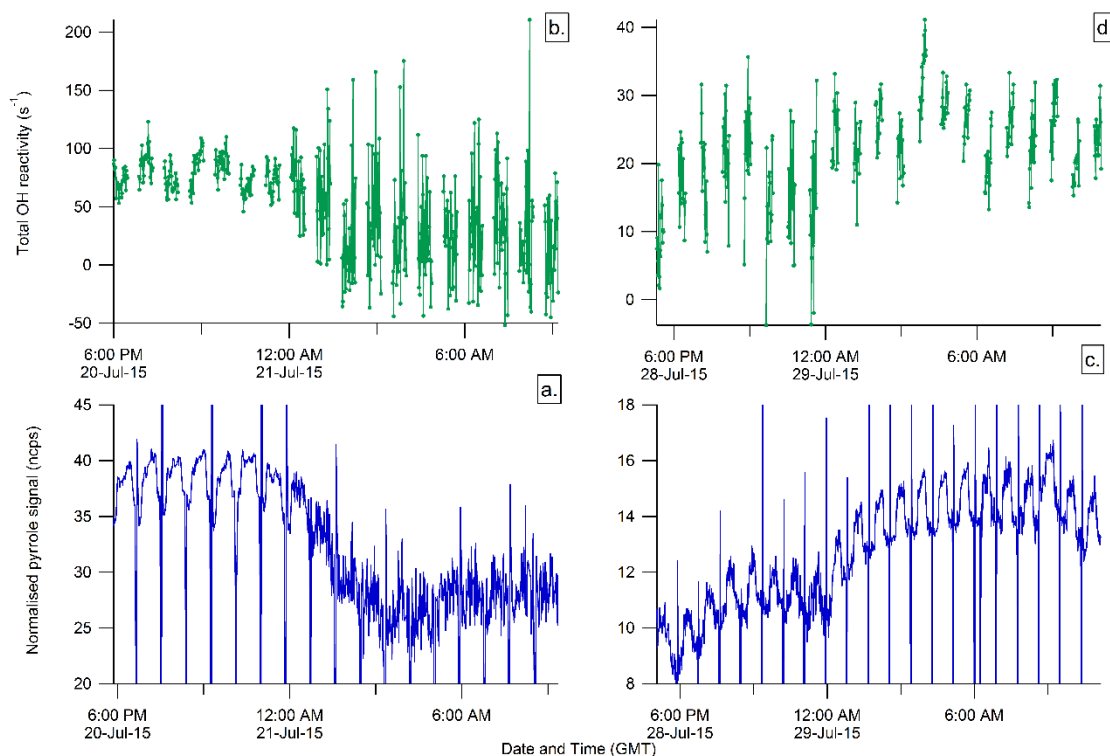


**Figure 4:10 a. measured total OH reactivity and b. the corresponding pyrrole concentrations from 20th to 21st July and the same measurements c. and d. for 28th to 29th July**

The effect can clearly be seen in Figure 4:10 for both time series, as a similar magnitude of variation in baseline C2 can be seen on the same time scales as the variation in baseline total OH reactivity. So whilst normalisation can correct for small changes within the hydronium signal, on the scale at which the fluctuation is observed within the PTR-ToF-MS within the examples show, normalisation cannot correct for large temperature based baseline changes thus resulting in large variations within the measured total OH reactivity.

Although the temperature fluctuations that occur within the shipping container are significant to cause such a large variation in hydronium ion count rates, the degree at which temperature varies within the reaction vessel varies would not be enough to cause a significant shift in the OH pyrrole rate coefficient, as throughout the campaign, only a maximum difference of 5 °C is observed on an individual day.

Using the temperature dependent OH pyrrole rate coefficient (Dillon et al., 2012):

$$k(\text{cm}^3 \text{molecule}^{-1} \text{s}^{-1}) = 1.45 \times 10^{-10} (T/298)^{1.40} \quad \text{(E 4:1)}$$

At an average temperature of 22°C measured within the shipping container, the pyrrole OH rate coefficient is calculated as  $1.05 \times 10^{-10} \text{ cm}^3 \text{ molecule}^{-1} \text{ s}^{-1}$ , the  $\pm 5^\circ\text{C}$  variation from the average temperature within the shipping container would therefore result in an error of  $\pm 2.5 \times 10^{-12} \text{ cm}^3 \text{ molecule}^{-1} \text{ s}^{-1}$ .

As the mass spectrometers ion source is not heated, it is possible that the temperature fluctuations that are observed could affect the glow discharge of the mass spectrometer and the kinetics of the proton transfer reaction. There is also the possibility that pressure issues could change ion count rates within the mass spectrometer as the E/N changes with pressure, (section 2.3.2). Pressure fluctuations can possibly occur due to blockages within the mass spectrometers inlet line, however if this were to happen, the hydronium count rate and the pyrrole count rate would fall to zero, which was not observed during the campaign. Also the use of gas cylinders and mass flow controllers ensures a constant stable flow of gasses into the mass spectrometer. Measurements of the mass spectrometers inlet flow rate however showed no change, as the mass spectrometers hollow cathode and flow drift tube pressures (Figure 2:10) are dependent on the inlet flow rate, no pressure fluctuations within these sections of the mass spectrometry are therefore observed.

#### 4.5.1.2 The effect of temperature on E/N

As stated in 2.3.2 the E/N within the drift tube of the mass spectrometer determines the partitioning of water clusters and the fragmentation of pyrrole ions. If the E/N is low, then proportionally, there will be a large number of

hydronium water clusters in comparison to bare hydronium ion. Whereas, if the E/N is too high, then fragmentation of pyrrole ion can occur.

The E/N is effected by temperature according to Equation 2:2, therefore, by manipulating this equation, the effect that temperature has on the calculated E/N can be determined. Figure 4:11 shows the temperature measured within the reaction vessel for the above time series, and the E/N calculated for the drift tube component and collision cell at each temperature.

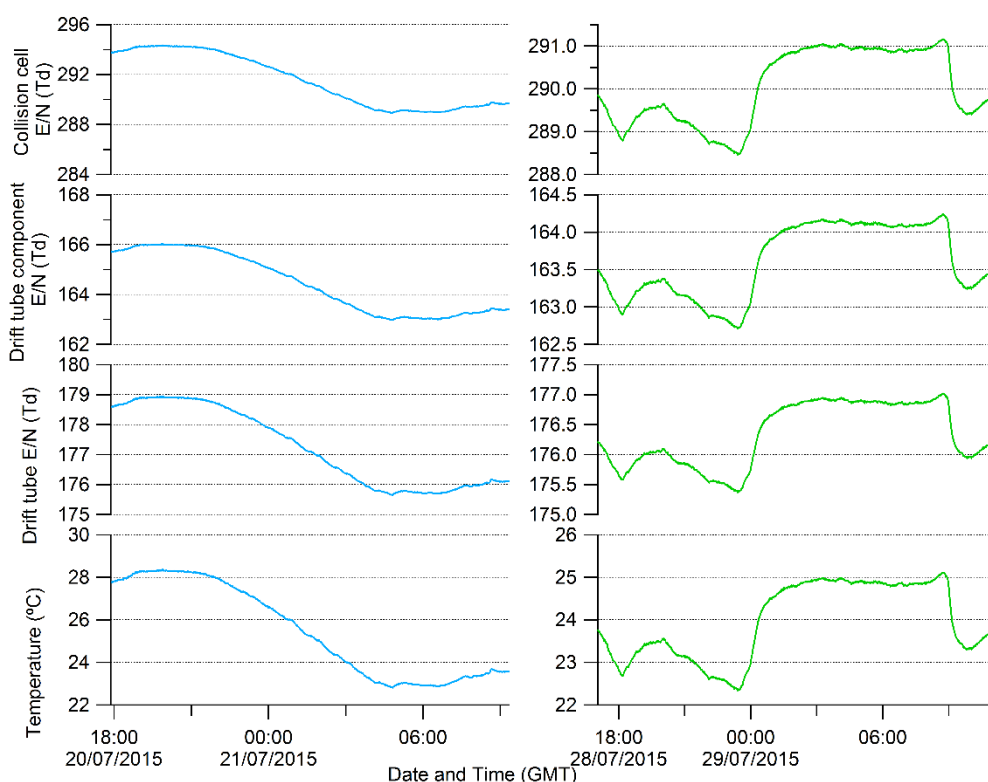


**Figure 4:11 Calculations of E/N during periods of temperature fluctuations within the mass spectrometer from 20th July to 21st July and from 28th to 29th July**

The figure above is based on E/N calculations that assume the fluctuations of temperature within the shipping container only effects the drift tube. It does not account for the influence that temperature has on water vapour production through the water bubbler.

As can be seen in Figure 4:11, only a slight variation in E/N is observed at the temperatures measured within the container, this is not enough to cause a

significant variation in hydronium water cluster ratios as the minimum average E/N calculated for the drift tube was 175 Td. Comparing to this, to the E/N measurements conducted in Figure 2:13 then at this E/N (175 Td), the concentrations of hydronium ions are significantly higher than its water clusters. Therefore, the temperature fluctuations observed within the container would not cause a shift in hydronium to hydronium cluster ratios.

It is important to note that throughout the campaign, all of the factors that could affect the instruments hydronium count rate, (the instruments sample flow rate, its pressures, and the voltages within the ion source) and therefore its E/N were not changed. Therefore all measurements were conducted at the same E/N.

Using a heater and insulated for the ion source (and bubbler) would ensure that the temperature within the drift tube and water bubbler is constant and stable. However this was not present during the campaign, it is therefore impossible to fully determine whether the temperature fluctuations within the shipping container had more of an effect on water vapour production by heating and cooling the water bubbler or by heating and cooling the drift tube.

#### **4.6 Data work up procedure- applications of calibrations and corrections to campaign measurements**

Measurements of total OH reactivity were conducted in the same manner as shown in (2.2.1 through to 2.2.1.4). Chapter 3 discussed the calibrations and corrections applied to the collected raw data, this section discusses the application of these calibrations on data collected during the first UOL-CRM measurement day of the ICOZA field campaign (04/07/15 to 05/07/15).

Once all of the measurement cycles have been completed (C0 wet and dry, C1, C2 and C3), and all of the data has been collected, total OH reactivity is then calculated via the following steps shown in the flow chart within Figure 4:12. Examples of the data analysis process are also shown within Figures 4:13 to 4:15 (one minute time resolution).

1. Raw data is normalised to the  $m/z$  21 isotope of hydronium (Figure 4:13 a. and b.). A slow decrease is seen in the hydronium isotope signal from 04/07/15 to 05/07/15 (from approximately 15000 to 5000 counts per minute), this variation in hydronium signal will result in a variation in proton transfer kinetics, this is because, as the hydronium concentrations decrease within the mass spectrometer, as less hydronium is available to protonate pyrrole, resulting in a decrease in the measured pyrrole signal. This effect can be accounted for by normalisation.
2. Normalised pyrrole counts are converted to a concentration (in ppb) (Figure 4:14 a. and b) by dividing the measured pyrrole count rate by a sensitivity factor measured via a pyrrole calibration seen within Figure 4:3 and applied to C0, C1, C2 and C3 pyrrole concentrations.
3. Spikes within the measured pyrrole concentration due to pressure spikes from the Solenoid valves switching on and off are removed when alternating between C2 and C3 modes are removed from the data series. As the Solenoid valves switch on and off, there is a sudden and rapid change in the direction of flows, this causes spikes in pressure within the reaction vessel as the dead volume of air within gas lines also start to flow when a specific mode of measurement is activated.
4. C2 and C3 modes are sequentially recorded for approximately 24 hours. Each C2-C3-C2 cycle are separated into individual data sets
5. Averages are calculated for each measurement mode
6. A ratio is calculated for C0 dry/ C0 wet, (as discussed within section 2.2.1).
7. Average C2 pyrrole concentrations are then interpolated over C3 measurement time periods. C3 is a mode of measurement in which the pyrrole concentration depends upon the concentration of OH (and therefore the humidity within the reaction vessel), and the concentration of VOCs within the ambient air sample. C2 pyrrole concentrations are also determined by OH concentrations within the reaction vessel. However, changes in ambient air humidity during sampling can result in variations of C2 pyrrole concentrations, therefore due to changes in

ambient air humidity when sampling over the duration C3 mode, the C2 concentration (and relative humidity within the reaction vessel) measured before switching to C3 may not be the same sampling C2 mode after C3. To account for this, C2 needs to be interpolated over the C3 time period. A C2 concentration is therefore calculated from a specific time period of C3. For example, in Figure 4:14 (b); one minute C3 measurements are made over a period of twenty minutes per cycle. Average C2 measured before and after C3 are interpolated to generate a C2 measurement over the entire period of C3.

8. Each C2 and C3 concentration is then multiplied by the ratio of C0 dry to C0 wet, (section 2.2.1.1).
9. Whilst calculating average pyrrole concentrations for C2 and C3, average  $m/z$  37 to  $m/z$  21 ratios are also calculated, (for C2 and C3 modes). The ratios are then used to correct interpolated C2 concentrations, due to differences in humidity between C2 and C3 according to Equation 3:5. The interpolated C2 signal is shown as dotted lines in Figure 4:14.
10. Using the corrected C2 and C3 mode measurements along with C1, a value of total OH reactivity is calculated that has been corrected for variation in C2 and C3 humidity using the CRM equation (E 1:14) (Figure 4:15 red dots uncorrected data) (Sinha et al., 2008).
11. Depending on the ambient concentrations of NO measured alongside the UOL-CRM (and the pyrrole to OH ratio), Equations 3:9 and 3:11 are applied to C3 concentrations to for the recycling of OH. The pyrrole to OH ratio is calculated for the average of C1 and each interpolated C2 (E 3:6).
12. The raw total OH reactivity is then corrected for deviations from pseudo-first order kinetics using E 3:8 based on the same pyrrole to OH ratio calculated in step 11, (Figure 4:15 black dots).
13. Finally, the corrected reactivity is multiplied by a dilution factor. The dilution factor is calculated based on the flow rates of pyrrole, nitrogen and ambient air entering the reaction vessel, (E 3:12 and 3:13) (Figure 4:15 blue dots).

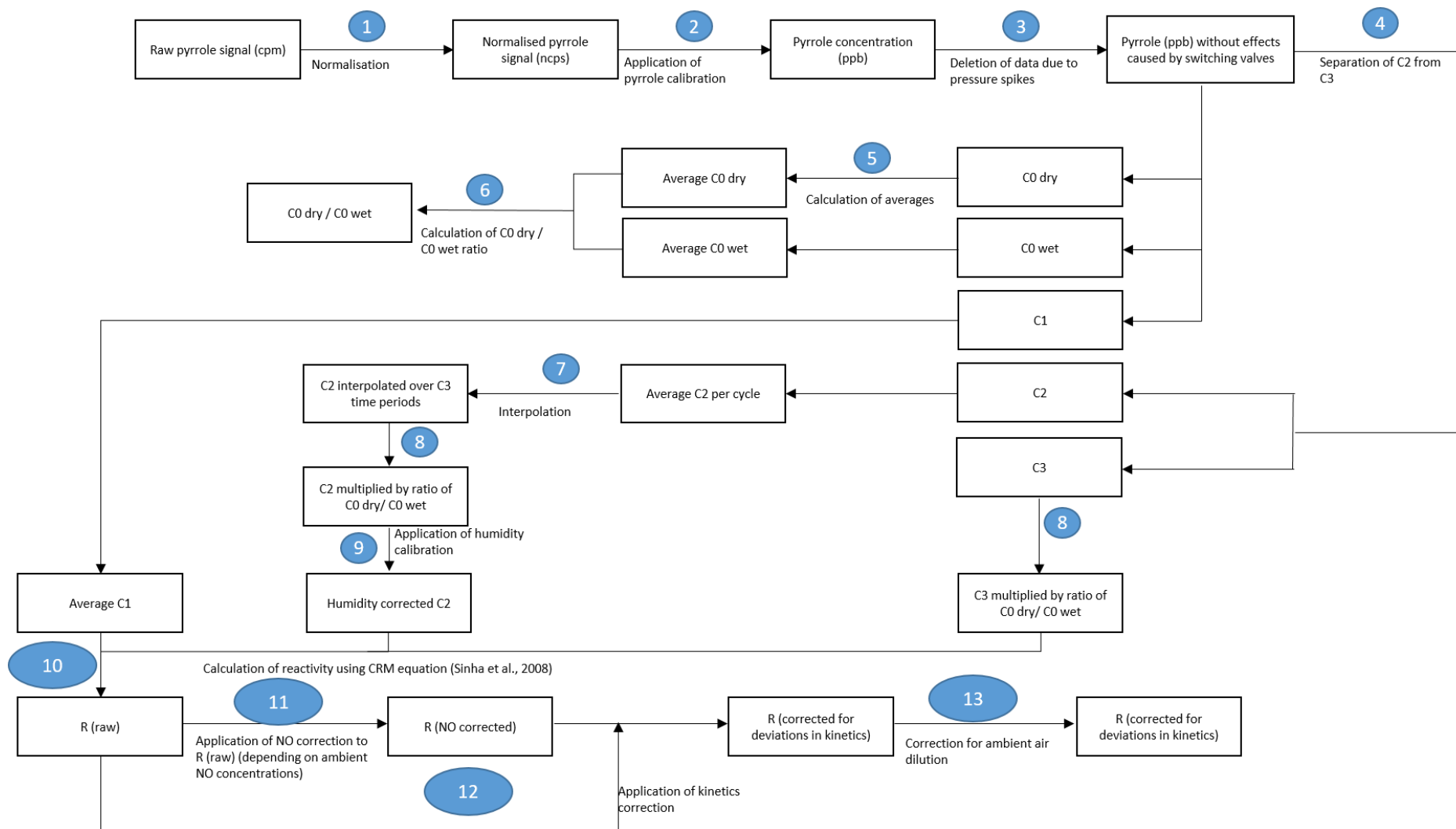


**Figure 4:12** A flow diagram representing the data processing sequence from measured pyrrole signals to final OH reactivity data. Adapted from (Kesel et al., 2014)

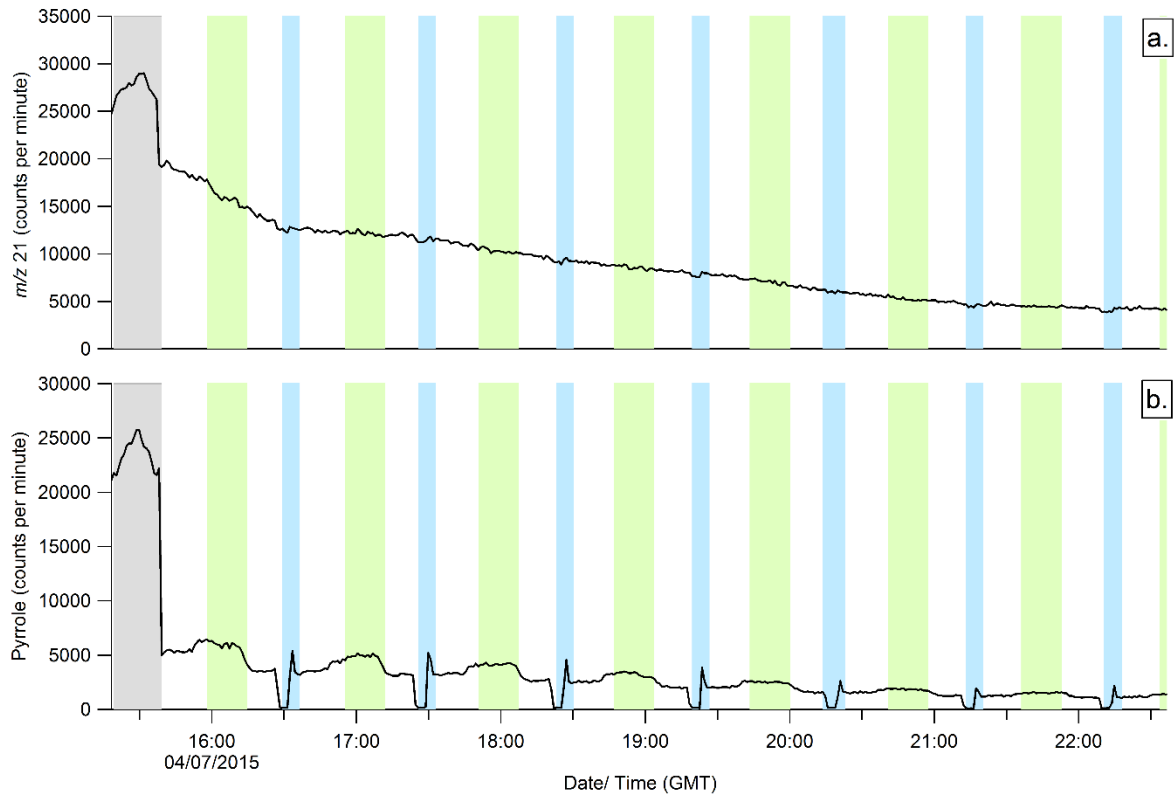


**Figure 4:13** Raw data collected from 04/07/15 to 05/07/15. a. m/z 21 hydronium isotope signal. b. pyrrole signal. Measurements conducted during C1 (highlighted in grey), C2 (highlighted in white), C3 (highlighted in green) and VOC ambient air measurement mode highlighted in blue

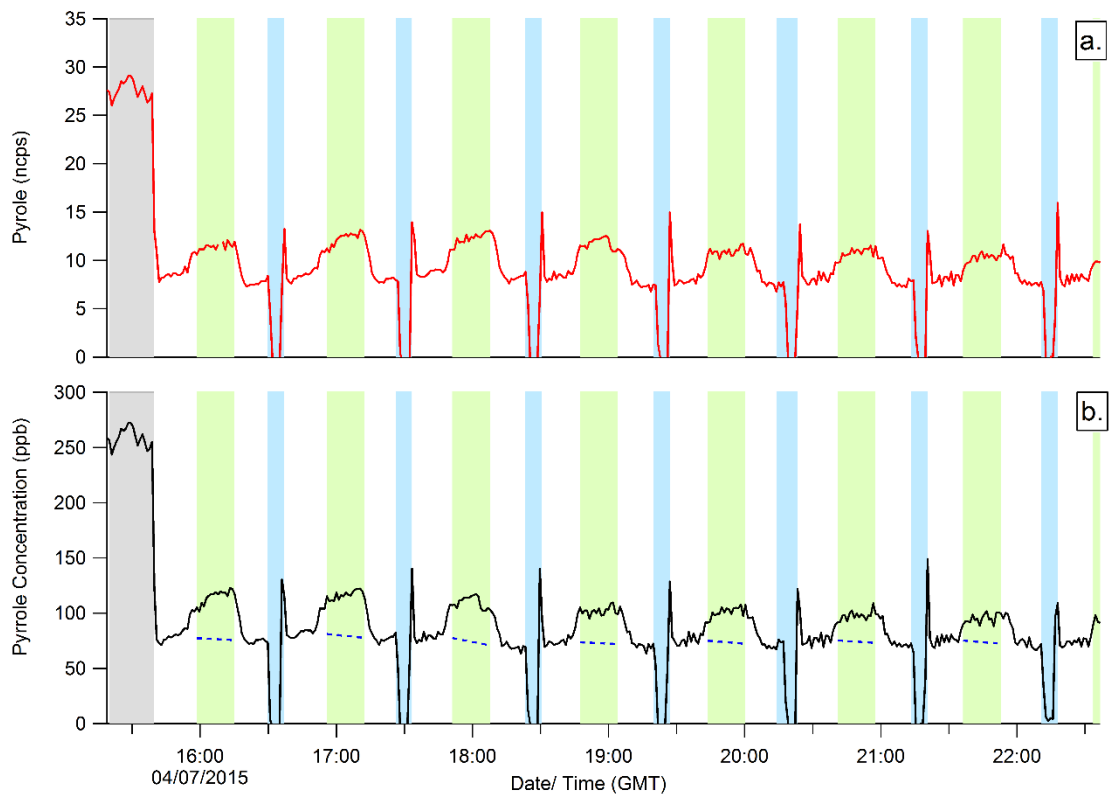


**Figure 4:14** a. Background subtracted pyrrole signal. b. pyrrole concentration (ppb). Measurements made from 04/07/15 to 05/07/15. C1 highlighted in grey, C2 highlighted in white, C3 highlighted in green and ambient air VOC mode highlighted in blue

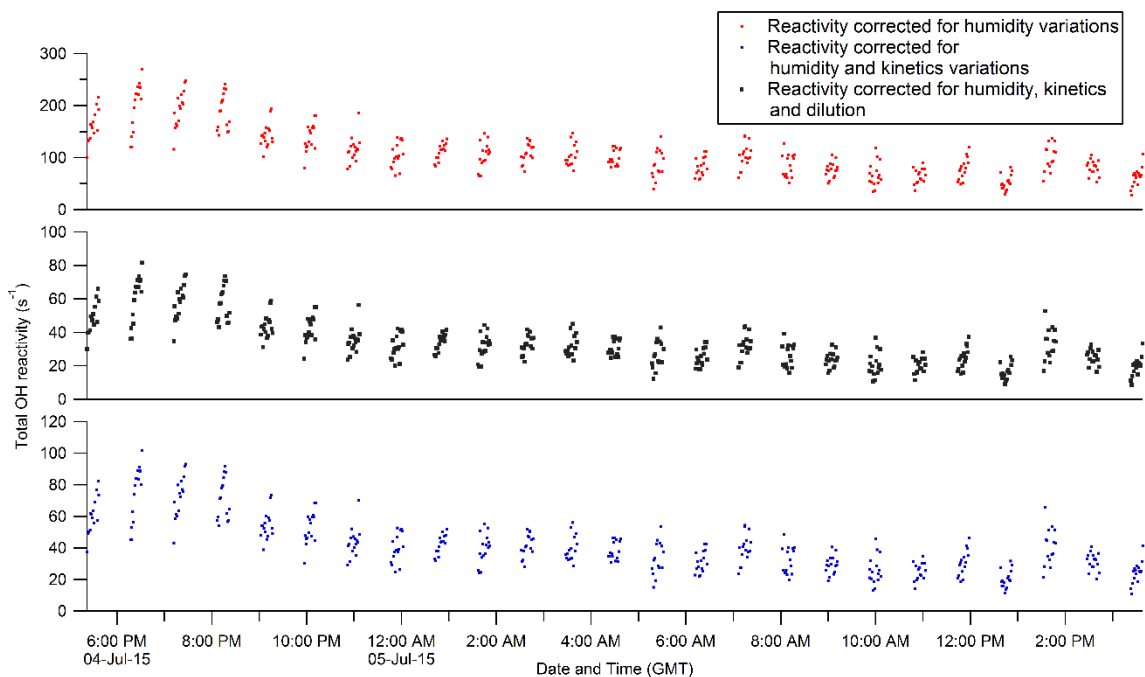


**Figure 4:15 Total OH reactivity measurements from 04/07/15 corrected for: a. C2 C3 humidity variations (red markers), b. humidity variations and deviation from pseudo- first order kinetics (black markers) and c. humidity variations, deviation from pseudo- first order kinetics and dilution of ambient air**

Figure 4:15 shows the final results of measurements from 04/07/15 to 05/07/15 after steps one through to eleven have been completed and all calibrations and correction factors have been applied to data as an example of the work up procedure.

Although a humidity correction is applied to the uncorrected data in Figure 4:15, the difference in relative humidity between C2 and C3 was determined at approximately 2-3%, this results in correction of 0.5 ppb in C2. Therefore, whilst the final measurements of OH reactivity was corrected for differences between C2 and C3 humidity, the humidity correction of the raw data, (before the correction due to dilution) is not displayed on Figure 4:15 due to the small difference in calculated OH reactivity before and after this correction is applied.

During this period, the average concentration of NO was measured at 0.6 ppb, with maximum and minimum concentrations of 0.1 and 2.5 ppb respectively. This range of NO concentration is not large enough to cause a significant

artefact within the UOL-CRM by recycling OH and reducing the C3 pyrrole concentration as seen in Figure 4:17. The average pyrrole to OH ratio during this period was 1.34, using equation 3:11 and the average NO concentration for this time, it was determined that C3 pyrrole concentration would reduce by 0.7 ppb, as a result, the NO correction determined within chapter 3 was not applied to the data in Figure 4:15, (the application of the NO concentration based correction to all of the measured data during the field campaign is discussed within section 4.7).

Gaps within the time series appear because the measured reactivity is plotted over the time period for C3 measurements. As ambient air enters the reaction vessel only during periods of C3 measurement mode, total OH reactivity is measured and calculated based only on each period of C3. Therefore, gaps will appear within the data because C2 is measured in between each C3 cycle.

## 4.7 Results

All measurements were corrected based on the factors discussed within sections 3.3 and 3.4, however the measurements were not corrected for NO based OH recycling, as the concentrations of NO measured during the field campaign were not large enough to cause significant differences in C3 pyrrole concentrations.

This is demonstrated within Figures 4:16 and 4:17, in which the measurements made by the UOL-CRM are corrected based on the concentrations of ambient NO measured by the University of Birmingham for two periods of the field campaign. Both figures show data that has been corrected for deviations in sample humidity and shifts in the kinetics regime, however, the two sets of data in each figure show minimal difference in the measured OH reactivity when applying the NO correction ( $\pm 0.3 \text{ s}^{-1}$  from 04/07/15 to 05/07/15 and  $\pm 0.1 \text{ s}^{-1}$  from 13/07/15 to 14/07/15).

As this data is taken from two periods of the field campaign when the measured concentrations of NO are at a minimum and maximum (Figure 5:3) and no

difference in measured OH reactivity is observed, the correction was not applied to the field campaign data.

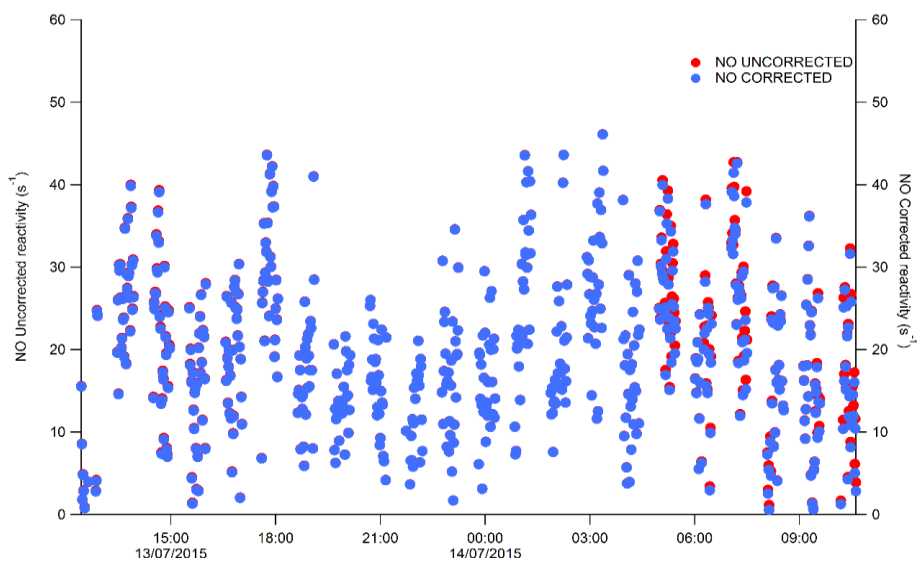


**Figure 4:16** Measurements made by the UOL-CRM from 13/07/15 to 14/07/15 during periods of high NO events. Red dots show measurements before the application of the NO concentration derived correction factor, blue dots show measurements made after correction due to NO based OH recycling

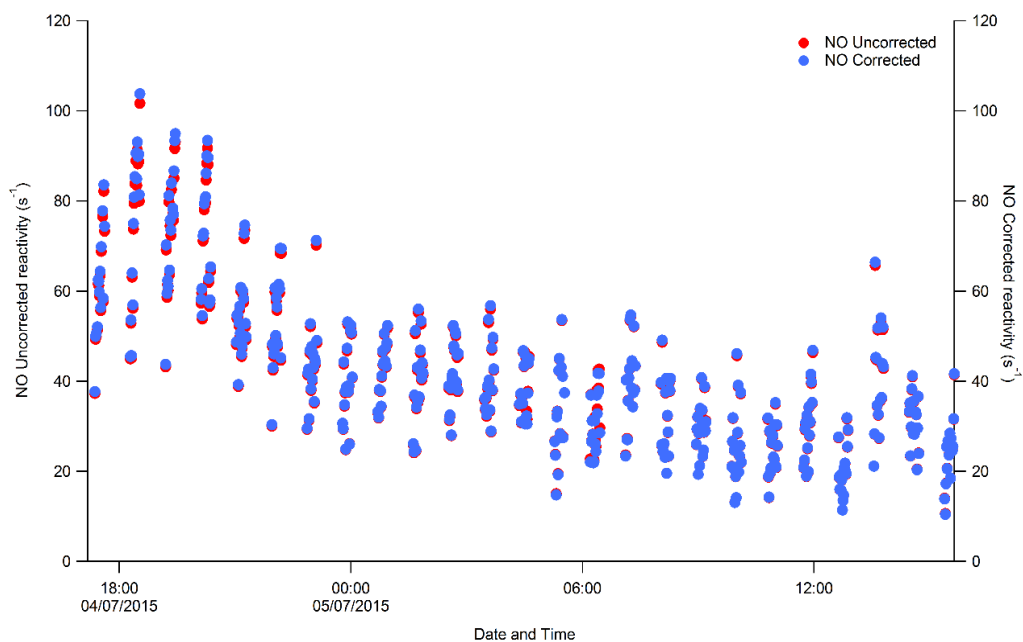


**Figure 4:17** Measurements made by the UOL-CRM from 04/07/15 to 05/07/15 before (red dots) and after (blue dots) the application of the NO concentration derived correction factor

	<b>Minimum</b>	<b>Mean</b>	<b>Maximum</b>	<b>25% Percentile</b>	<b>75% Percentile</b>	<b>Standard deviation</b>
04/07	24.77	57.3	101.7	45.58	72.57	17.41
05/07	10.59	32.79	65.69	25.6	40.73	10.22
06/07	32.6	50.35	69.74	44.65	54.75	7.456
08/07	12.91	12.91	151.4	44.59	78.74	26.29
09/07	39.59	39.59	125.4	62.94	93.67	22.31
11/07	24.45	24.45	131	54.23	87.18	22.15
12/07	25.44	25.44	140.7	64.69	95.29	21.06
13/07	5.22	5.22	43.63	13.58	25.08	8.21
14/07	5.02	5.02	55.36	12.18	25.07	9.25
15/07	5.13	5.13	69.73	11.38	25.85	12.59
16/07	5.32	5.32	57.1	8.88	19.1	9
18/07	5.32	5.32	25.38	8.53	16.1	4.63
19/07	5.01	5.01	131.8	14.55	49.63	27.05
20/07	5.16	5.16	226.7	44.5	83.41	28.53
21/07/	5.39	5.39	210.7	25.02	69.97	35.38
23/07	7.37	7.37	38.01	16.4	25.49	6.66
24/07	5.47	5.47	56.34	13.52	26.44	10.67
25/07	5.55	5.55	31.87	12.51	19.45	5.98
26/07	5.74	5.74	56.4	14.12	29.52	10.55
27/07	6.12	6.12	36.08	12.24	19.79	6.68
28/07	5.32	5.32	54.6	14.14	33.04	11.82
29/07	10.98	10.9	36.68	20.71	28.57	5.6
30/07	3.34	3.34	49.16	26.83	37.31	8.02
31/07	12.47	12.47	45.66	28.67	34.84	5.19
<b>Average</b>	<b>11.43</b>	<b>14.45</b>	<b>83.78</b>	<b>26.66</b>	<b>45.48</b>	<b>13.86</b>

Table 4:1 Summary of data shown in Figure 4:19 Measurements made by the UOL-CRM during the ICOZA campaign

One minute averaged measurements of total OH reactivity for the whole campaign are seen in Figure 4:18. Daily average measurements are shown in Figure 4:19 box and whisker plots (summary of daily measurements in Table 4:1).

To summarise: an average total OH reactivity of  $30.1 \text{ s}^{-1}$  is measured through the campaign, with a maximum of  $226.6 \text{ s}^{-1}$  on 22/07/15 at 12:40 am. Negative reactivity is also measured, this is attributed to the large degree of noise within the UOL-CRM measurements.

During periods of the campaign when pyrrole concentrations during C3 mode are as low as C2 mode, the measured total OH reactivity is low (as the concentration of VOCs within the ambient air sample are at a minimum), however, due to the large degree of noise within the hydronium isotope and pyrrole signals, there are occasions when C3 pyrrole concentrations are lower than C2 concentrations. This ultimately results in negative measurements of total OH reactivity, (as C3 has to be subtracted from C2 when calculating total OH reactivity). These periods are removed from Figure 4:19, Table 5:1 and the measurements discussed within chapter 5.

Owing to the high degree of noise within the measurements made by the UOL-CRM, there are periods of the campaign in which the measurements made are lower than the limit of detection ( $5 \text{ s}^{-1}$ ), the periods are also removed from the box and whisker plot shown in Figure 4:19 and Table 4:1. Further discussions of the measurements made by the UOL-CRM are made in chapter 5, when comparing to UL-LIF and VOC measurements.

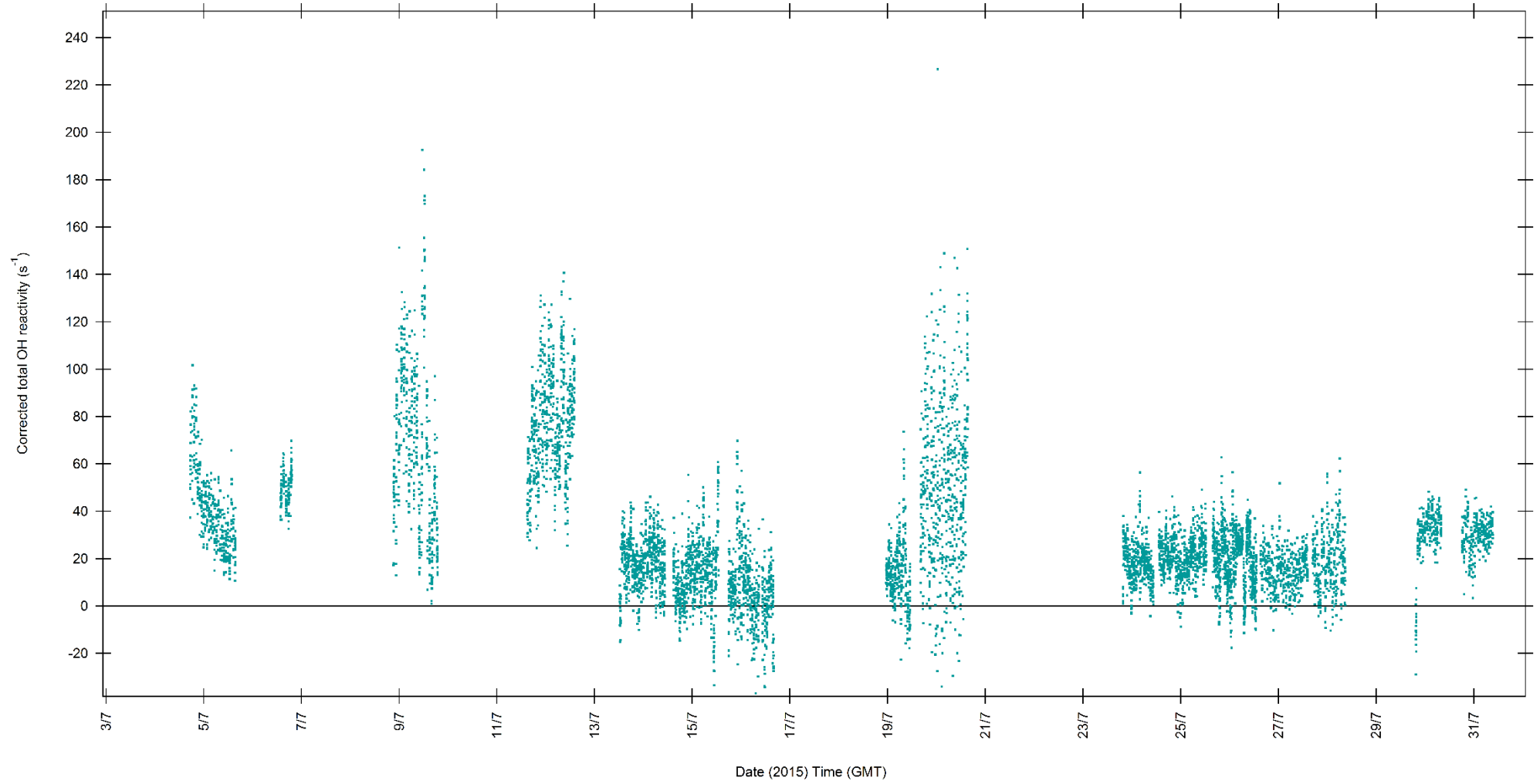


Figure 4:18 Total OH reactivity measured during ICOZA campaign

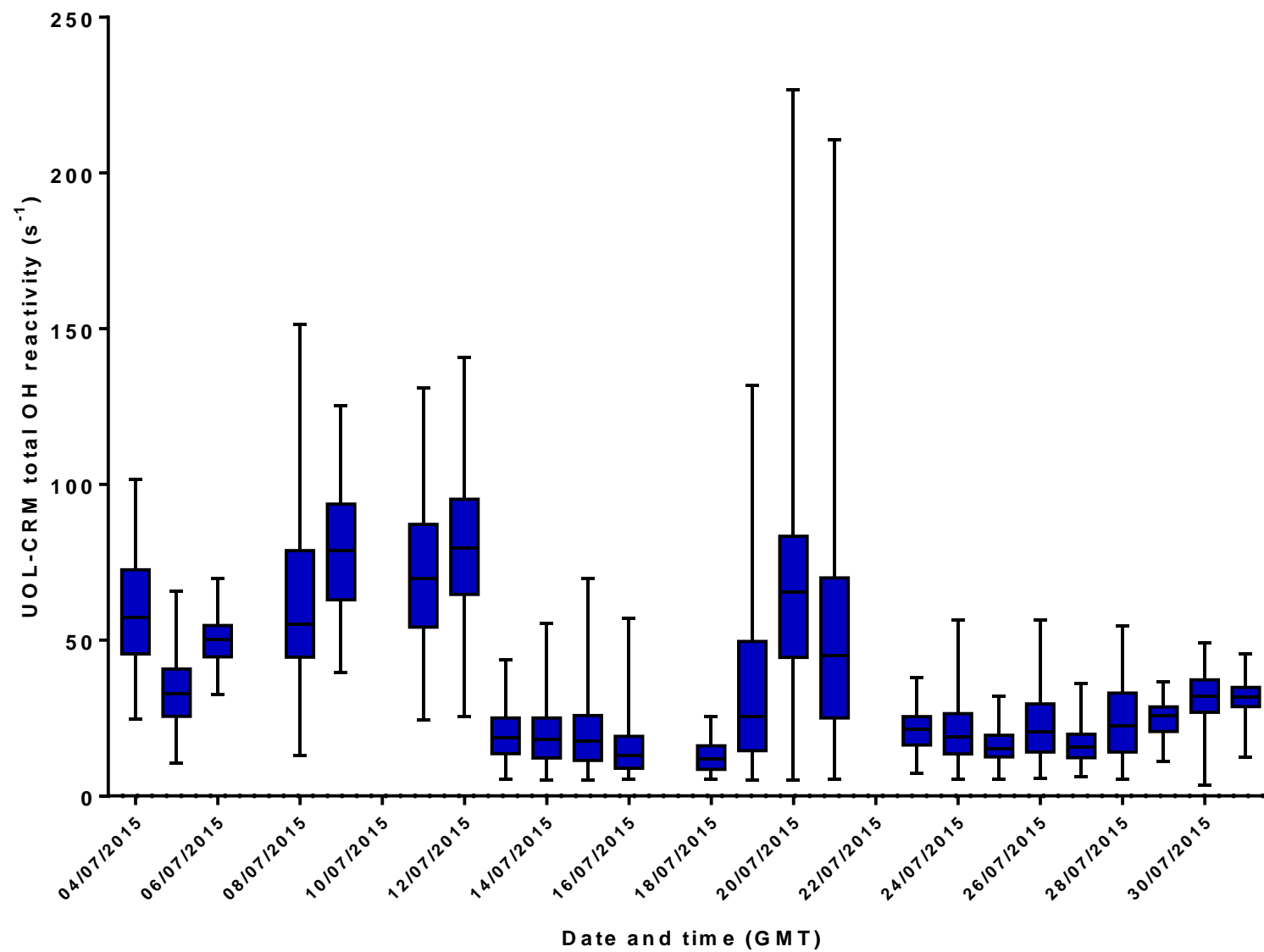


Figure 4:19 Box and whisker plot depicting the measurements made by the UOL-CRM during the ICOZA campaign

## 4.1 Conclusions

The UOL-CRM was deployed during the ICOZA field campaign in Weybourne Norfolk (July 2015).

Measurements of total OH reactivity were conducted during the field campaign with the addition of VOC measurements made by the UOL-CRM between C2 and C3 modes. These VOC measurements proved unsuccessful as the PTR-ToF-MS is optimised specifically for pyrrole detection, as a result, there were not used when examining total OH reactivity measurements.

Fluctuations in temperature within the shipping container are observed throughout the field campaign (as much as 5°C variation from the average) within a day. This variation is enough to cause fluctuations in hydronium  $m/z$  19 count rate. This variation propagates into the measured pyrrole signal and therefore the measured total OH reactivity. Small variation in pyrrole signal are corrected by normalising this signal to the hydronium isotope.

The same fluctuations in temperature as seen within the shipping container are also observed within the measured E/N of the PTR-ToF-MS drift tube, this degree of temperature variation is not large enough to cause a shift in hydronium cluster ratios.

Periods of the campaign in which there are large fluctuations in hydronium signal have been removed from the final UOL-CRM total OH reactivity data set. The result of this is that the average measured total OH reactivity for the campaign was 30 s<sup>-1</sup>. Full examination of UOL-CRM based total OH reactivity are discussed in the next chapter.

## **Chapter 5. Comparisons of UOL-CRM measurements with calculated reactivity and measurements made by the UL-LIF**

### **5.1 Introduction**

Chapter 4 discussed the deployment of the UOL-CRM at the ICOZA field campaign throughout July 2015 with the aim of discussing how the calibrations conducted in chapter 3 are applied to measurements.

Chapter 4 also discussed the stability of the PTR-ToF-MS and problems that occurred. The measurements shown in chapter 4 were then compared to total OH reactivity calculated through measurements of VOC, NO<sub>x</sub>, O<sub>3</sub> and CO concentrations.

Any fluctuations in calculated total OH reactivity, (including measurements made by the UL-LIF), are compared to measurements made by UOL-CRM. Periods during the campaign when total OH reactivity is high, the species contributing to that particular period of high reactivity is determined, and compared with the response from the UOL-CRM measurements.

Correlations between UOL-CRM, calculated reactivity and UL-LIF measurements are then determined. The factors responsible for agreement or disagreement between the measured and calculated reactivity is determined, whether this is owing to an atmospheric factor (i.e. when the wind speed is particularly high, when wind is flowing in a particular direction or when the concentration of a measured species is high), or an instrumental issue.

### **5.1 Concentration measurements of VOCs and inorganic species**

A number of ancillary measurements were made during the field campaign, those that are used to calculate total OH reactivity are shown in Table 5:1. NMHCs and OVOCs were made using a GC-FID and a PTR-QMS respectively.

<b>Institute</b>	<b>Instrument</b>	<b>Parameters</b>
Birmingham	Thermo Fisher 42i-TL NO <sub>x</sub> analyser	NO <sub>x</sub>
	Thermo Fisher 49i Ozone analyser	O <sub>3</sub>
Leicester	UOL-CRM	OH reactivity
UEA	RGA3, Trace Analytical, Inc.	CO, H <sub>2</sub>
	Aero Laser AL4021 Formaldehyde monitor	HCHO
	Thermo Scientific 43i sulphur dioxide analyser	SO <sub>2</sub>
	GC FID	NMHCs
	PTR-QMS	OVOCs
Leeds	UL-LIF	OH reactivity

**Table 5:1 A list of instruments provided by the University of Birmingham, Leicester, East Anglia, Leeds and York and the corresponding species detected by each instrument for the campaign**

The GC-FID used by UEA is a PerkinElmer On-line Ozone Precursor Monitoring system that consists of a thermal desorption GC coupled to a flame ionisation detector. In order to sample ambient air, analytes are cooled onto an absorbent trap. Following this, the analytes are thermally desorbed and transported via a carrier gas into the GC separating column, the analytes are then separated depending on their volatility and transported to a flame ionisation detector (Seeley et al.).

The PTR-QMS is an Ionicone, Analytik Proton Transfer Reaction- Quadrupole-Mass Spectrometer adapted from the one described by Lindinger et al. (1998) and Murphy et al. (2010).

Dynamic calibrations for the PTR-QMS were conducted with an Apel- Riemer multi-component gas mixture in order to determine a sensitivity for all VOCs

within the gas mixture. This method is similar to that used to calibrate the PTR- ToF- MS used with the UOL-CRM, (section 3.2).

The UOL-CRM employs a proton transfer reaction mass spectrometer with a Time of Flight mass analyser in order to separate ions, (described in further detail in section 2.3). A quadrupole mass analyser consists of a series of four cylindrical electrodes positioned perpendicular from each other (Figure 5:1). The quadrupole mass analyser has an advantage over the use of a Time of Flight mass analyser in that it provides better sensitivity signals towards compounds. However the ToF-MS has the ability to detect a wider range of mass channels in comparison to a quadrupole mass spectrometer.



**Figure 5:1** Diagram of a quadrupole mass analyser adapted from Ellis and Mayhew (2014a)

Concentration measurements from made by both the PTR-QMS and GC-FID are shown in Figures 5:2 a. and b. Owing to the large range of concentrations measured, a number colour scales have to be used in order to plot the time series for each for each VOC, (Figure 5:2). The extent to which the range of VOC concentrations vary is shown in Table 5:2 summarising the measurements made by the PTR-QMS and GC-FID depicting the minimum, average and maximum concentration of each VOC respectively.

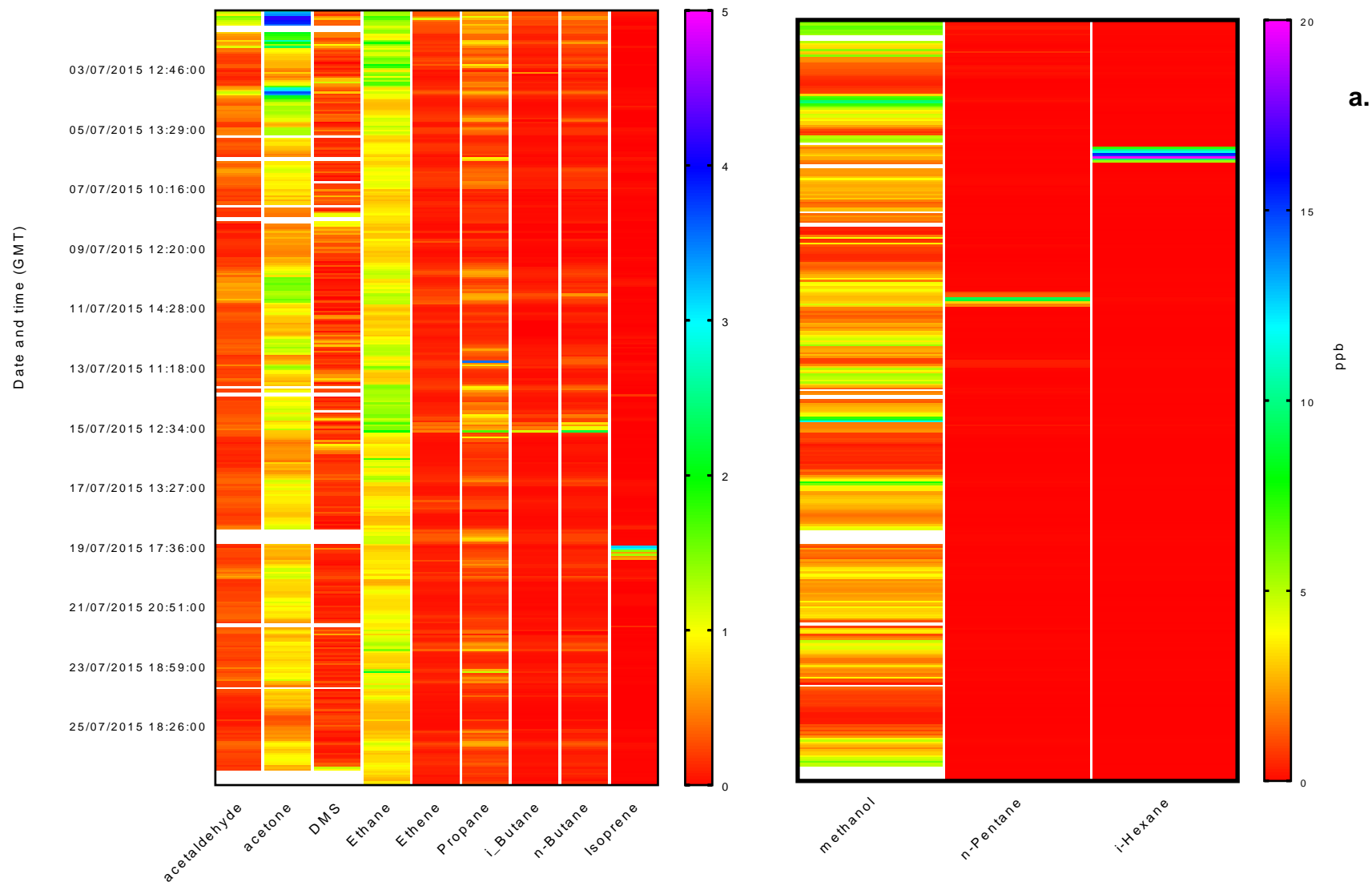
It is important to note that whilst pinenes and terpenes have been detected using the PTR- MS at  $m/z$  137 and 121 respectively, unfortunately; the PTR-MS is unable to differentiate between isomers of compounds, such as terpenes,  $\alpha$ -pinene,  $\beta$ - pinene, and isomers of Trimethylbenzene (TMB).

Instrument	Species Detected		Measured concentrations (ppb)		
	Functional group	VOC	Minimum	Average	Maximum
PTR-QMS	Alcohol	methanol	0.33	2.7	12.04
	Nitrile	acetonitrile	0.03	0.08	0.2
	Aldehyde	acetaldehyde	0.05	0.33	1.53
	Sulphide	dimethyl sulphide (DMS)	0	0.27	1.19
		methylvinyl Ketone	0	0.08	0.64
	Ketone	methylethyl ketone	0.02	0.1	0.54
		Acetone	0	0.71	4.16

**Table 5:2 concentrations of VOCs throughout the ICOZA campaign, along with the respective minimum, maximum and average concentration of each VOC (ppb)**

Instrument	Species Detected		Measured concentrations (ppb)		
	Functional group	VOC	Minimum	Average	Maximum
GC-FID	Terpene	$\alpha$ -pinene	0	0.01	0.08
		$\beta$ -pinene			
		isoprene	0	0.12	1.19
		ethane	0.67	1.02	2.15
		propane	0	0.34	3.56
	Alkane	2-methylpropane	0	0.08	1.15
		butane	0	0.16	2.24
		2-methylbutane	0	0.13	1
		n-pentane	0	0.13	9.3
		n-hexane	0	0.01	0.11
	Alkene	i-hexane	0	0.27	19.81
		ethene	0.03	0.15	1.12
		propene	0	0.14	0.63
		trans-2-butene	0	0	0.01
		cis-2-butene	0	0.01	0.04
		1-butene	0	0.01	0.08
1,3-butadiene		0	0.02	0.15	
PTR-QMS	Aromatic	benzene	0	0.04	0.24
		toluene	0	0.04	0.33
		Trimethyl benzene (TMB)	0	0.02	0.10
	Terpene	isoprene	0	0.04	3.18

Table 5:2 continued



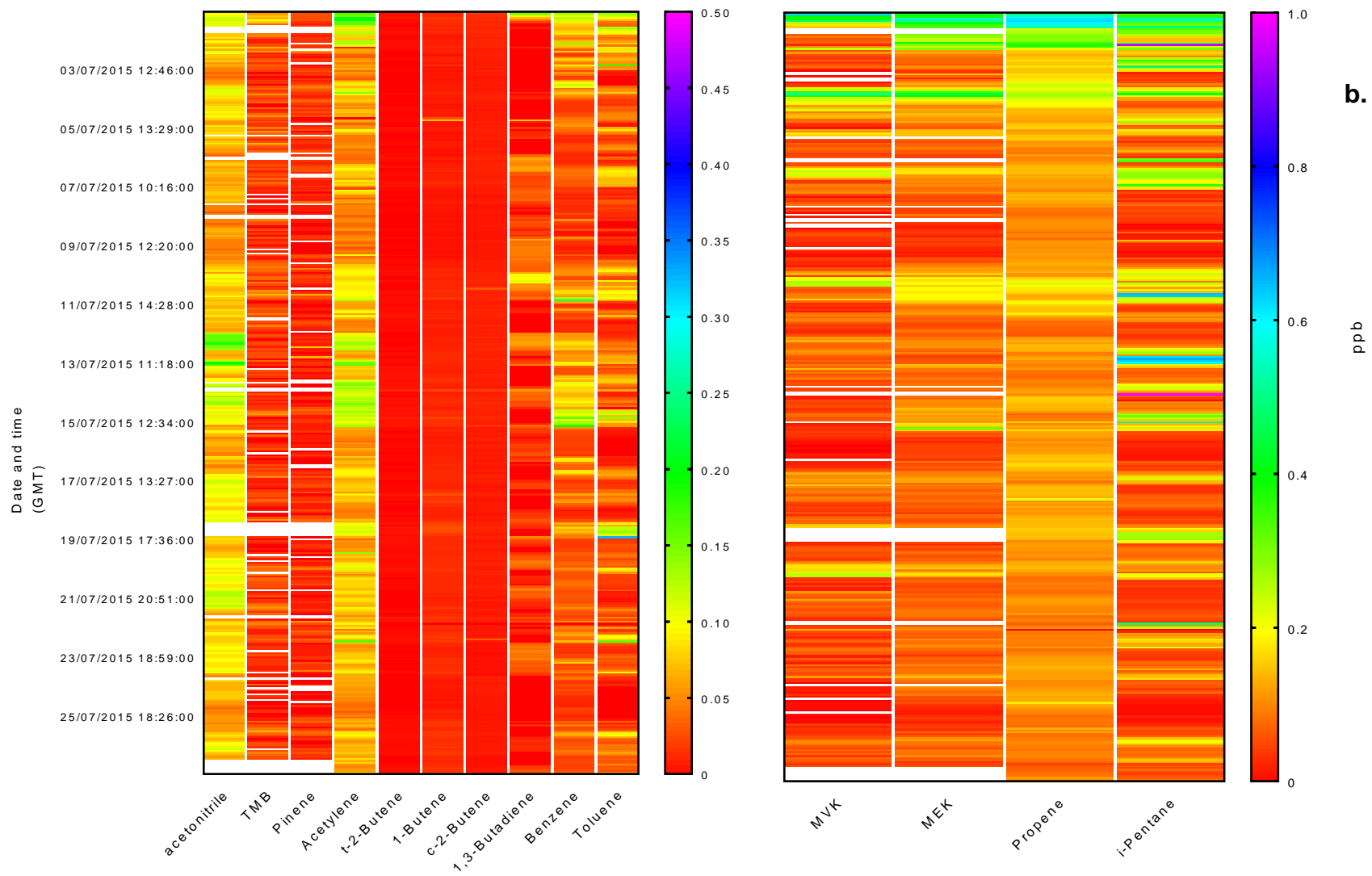


Figure 5:2 a. and b. measured concentrations of NMHCs and OVOCs throughout the ICOZA campaign. Measurements made via the UEA PTR-QMS and the UEA GC-FID

Species	Concentrations (ppb)		
	Minimum	Average	Maximum
NMHC (non-methane hydrocarbons)	1.2	3.0	22.1
OVOC (oxygenated VOCs)	0	7.2	44.5
NO	0	0.5	8.3
NO <sub>2</sub>	0	3.3	12.0
CO	81.1	111.7	188.2
O <sub>3</sub>	10.3	35.0	113.5
SO <sub>2</sub>	0.02	0.1	0.6

**Table 5:3 Summary of ancillary measurements made during the ICOZA campaign. Used for OH reactivity calculations**

Table 5:3 shows a summary of measurements made during the campaign by summing together the concentrations of all species detected by the PTR-QMS and the GC-FID, (OVOCs and NMHCs respectively). Table 5:3 also includes measurements of inorganic species made by instruments stated in Table 5:1.

A time series of all measurements is also shown in Figure 5:3, and their dependence on wind direction in Figure 5:4.

NO<sub>2</sub> was observed within air masses arriving from a south to westerly direction (local wind direction 170 to 270°), from the 1st to 2nd July with concentrations ranging from 7 - 10 ppb. The same is observed until the 14th July as large spike in NO<sub>2</sub> occurred whenever the wind was arriving from the same direction (Figures 5:3 and 5:4). This is indicative of air masses travelling from London and other large cities that are south/ south west of the measurement site. One day back trajectories shown in Figure 5:5 (created by Zoe Flemming, University of Leicester), from 2nd July and 13th July confirm this, as air is observed as passing over the Atlantic, and then through large cities such as Birmingham and London.

Added to this, Figures 5:3 and 5:4 also shows that large spikes in OVOC and NMHC concentrations (maximum 24 - 44 ppb and 14 to 22 ppb respectively)

were observed in polluted air arriving at the measurement location from the same direction and over the same time periods as that observed when examining changes in NO<sub>2</sub> concentrations (south/ west 170 to 270°).

However, whilst NO<sub>2</sub> arrives predominantly from a south to south west location, whenever the wind direction changed to northerly (23 to 53°), large increases in NO concentration is observed, (Figure 5:3 and 5:4 ). This is particularly obvious on 3rd, 9th and 14th July when NO concentrations spiked at 4 ppb, 3.9 ppb and 8.33 ppb (the average concentration of NO for the duration of the campaign was 0.5 ppb, (Table 5:3).

The one day trajectories in Figure 5:6 show air travelling from a northern location during the periods discussed above, when spikes in measured NO are observed. These trajectories indicate that the spikes in NO concentration are owing to air arriving from North Sea, most likely due the emissions from ship plumes, as SO<sub>2</sub> which is observed within ship plumes (McLaren et al., 2012) are also high during this period measured (Figure 5:7).

No CO dependence on wind direction was observed during the campaign, however, large concentrations of ozone was measured at the start of the campaign (1st July), owing to high temperatures measured at the location and large concentrations of NO<sub>2</sub>, resulting in the formation of ozone according to reactions 1:25 and 1:26, with air masses travelling to the measurement site from mainland (and coastal) Europe (Figure 5:8) at which point total large concentrations of OVOCs are also observed due to a period of intense pollution.

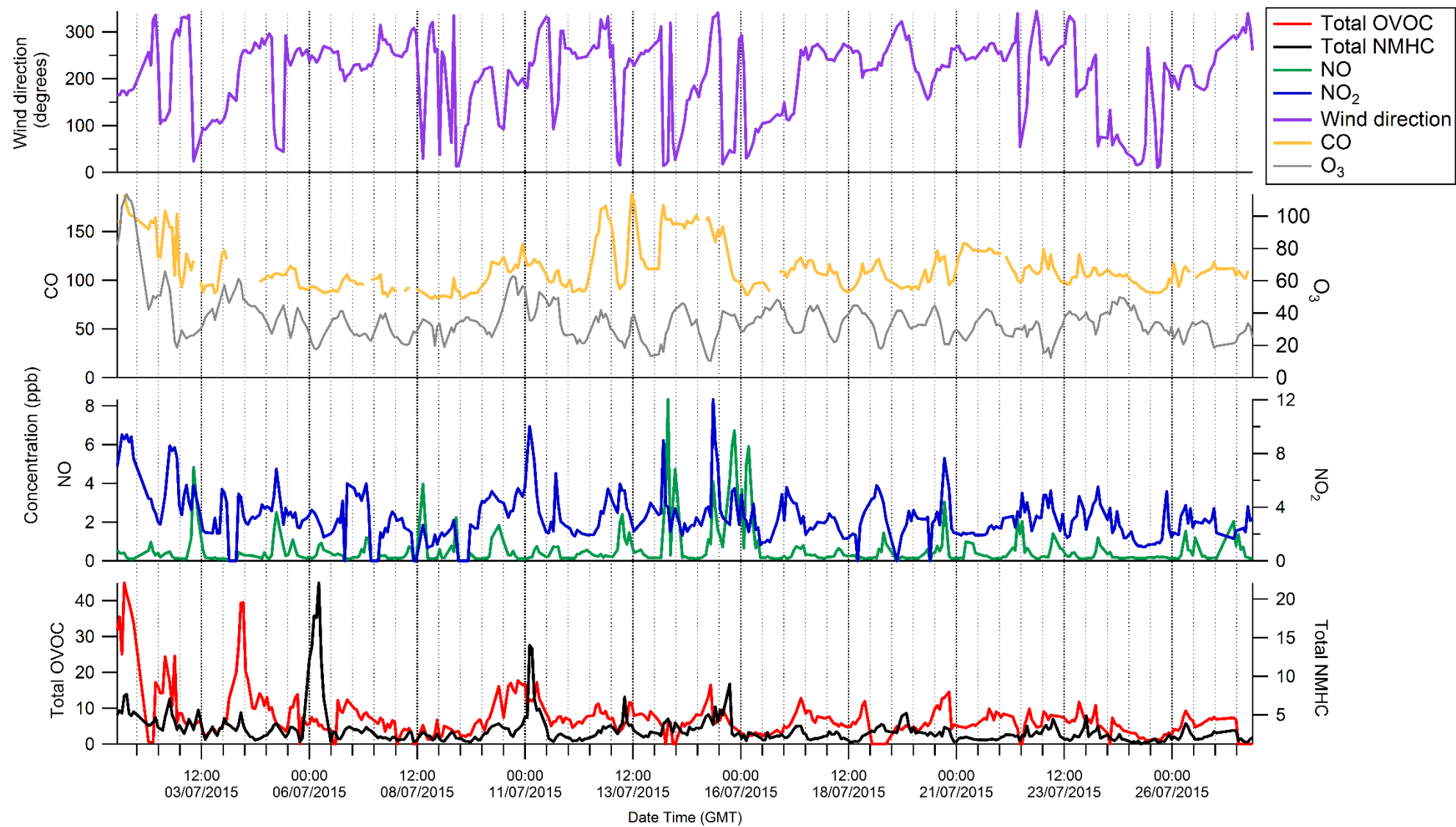
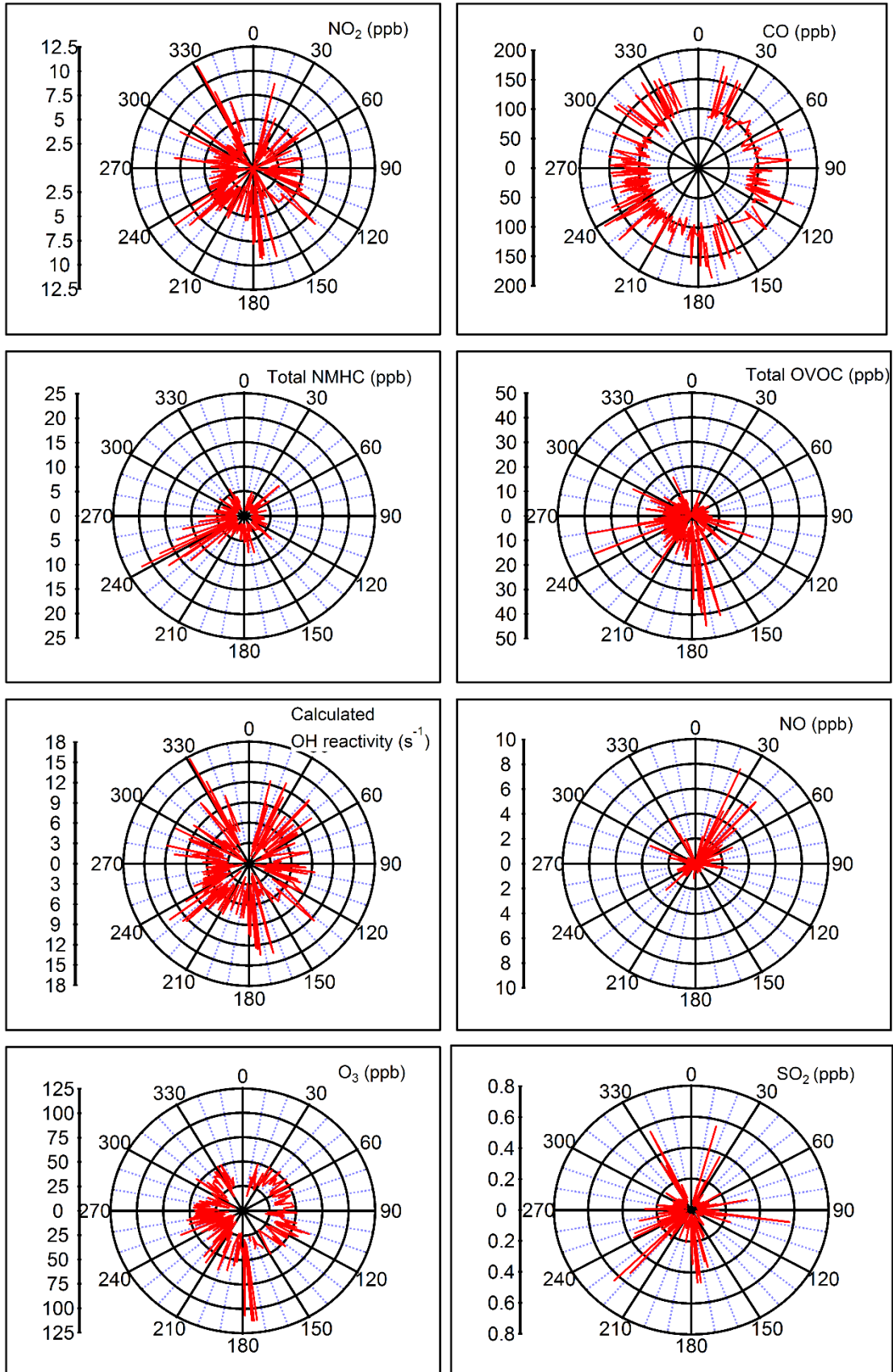
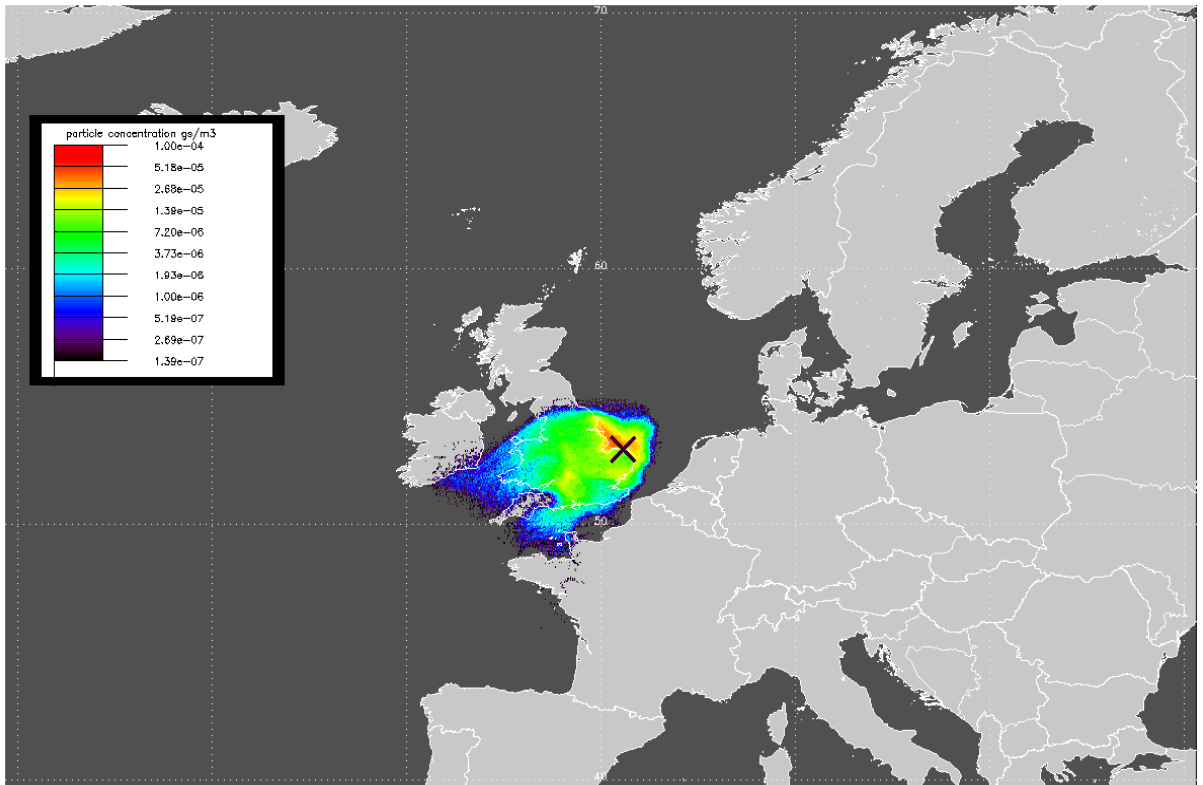


Figure 5:3 Measurements of OVOCs NMHCs NO<sub>x</sub> CO, ozone and wind direction measured during the field campaign



**Figure 5:4** Total NMHC, OVOC and inorganic species measured during the field campaign, including calculated total OH reactivity. And their sources depending on wind direction

1 day (0–100m) arriving at Weybourne 3 Hourly release from: 20150702\_2100



1 day (0–100m) arriving at Weybourne 3 Hourly release from: 20150713\_600

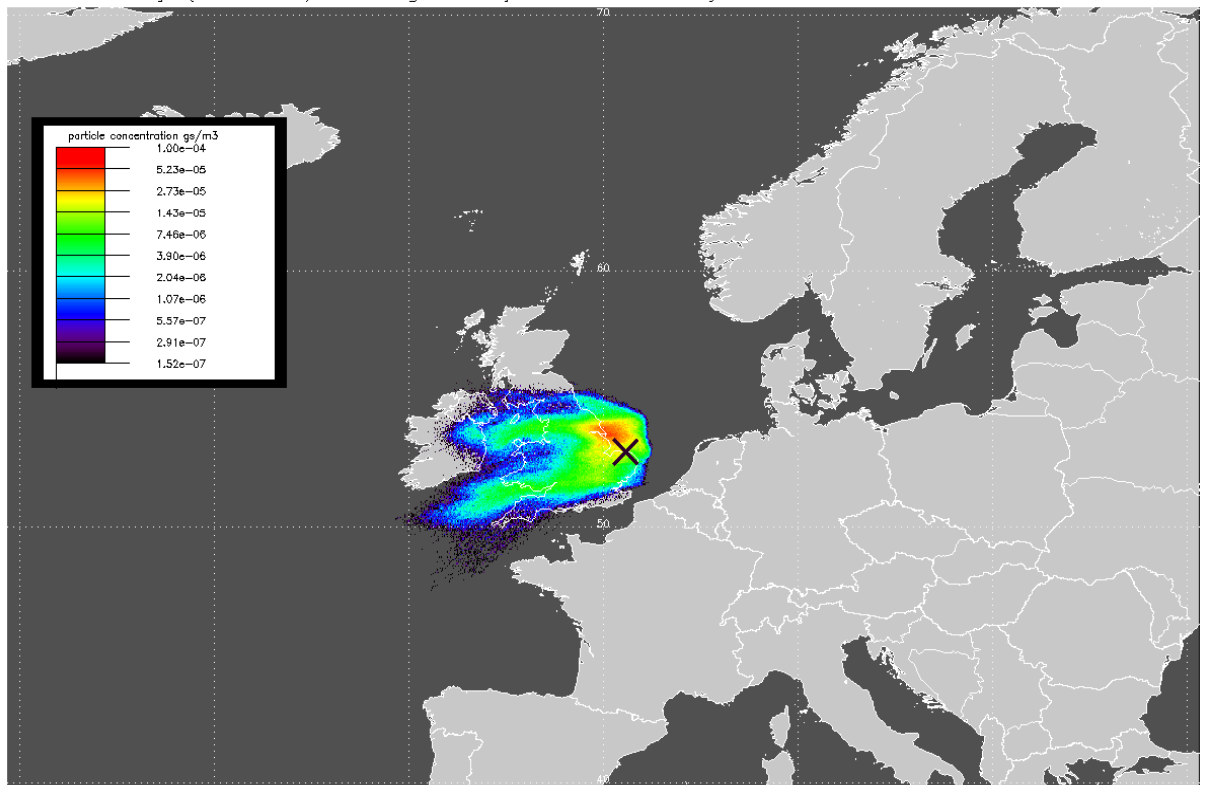
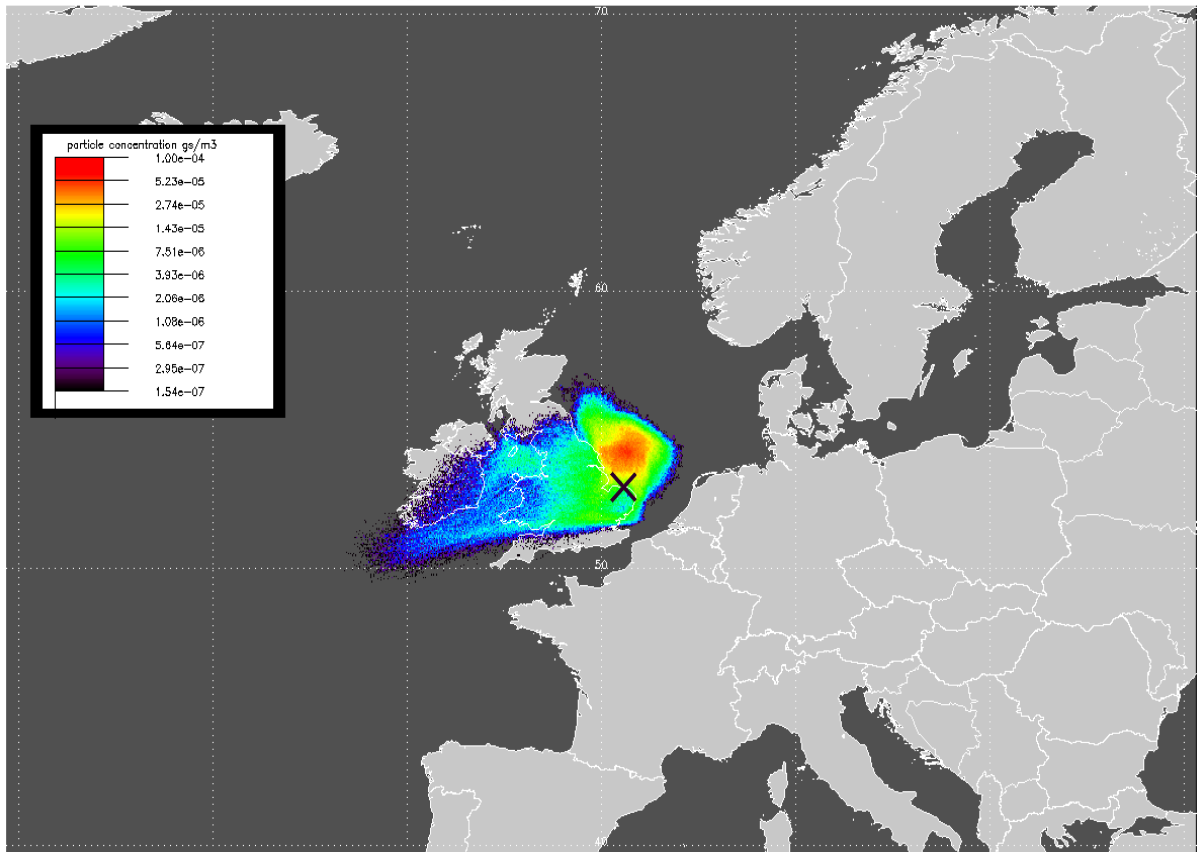


**Figure 5:5** One day back trajectory showing the origin of air travelling to the measurement site

1 day (0–100m) arriving at Weybourne 3 Hourly release from: 20150714\_900



1 day (0–100m) arriving at Weybourne 3 Hourly release from: 20150703\_900

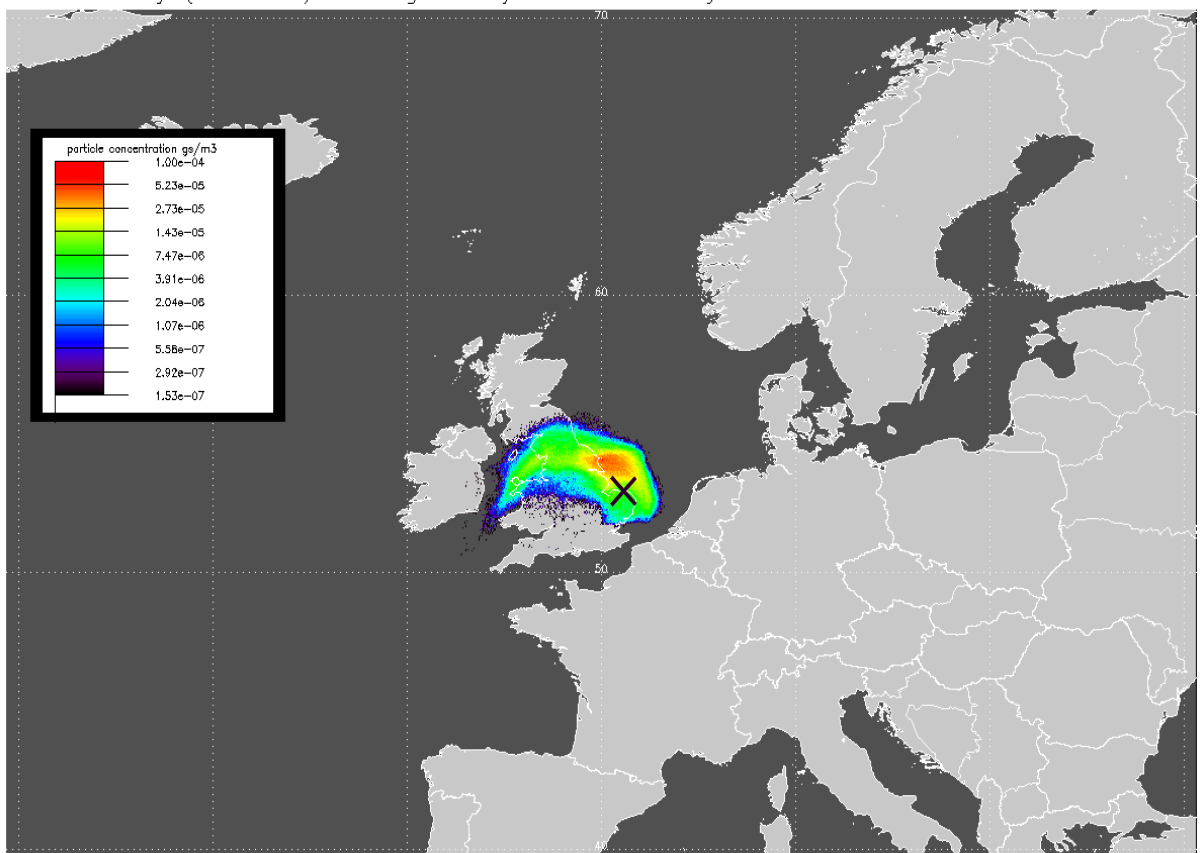
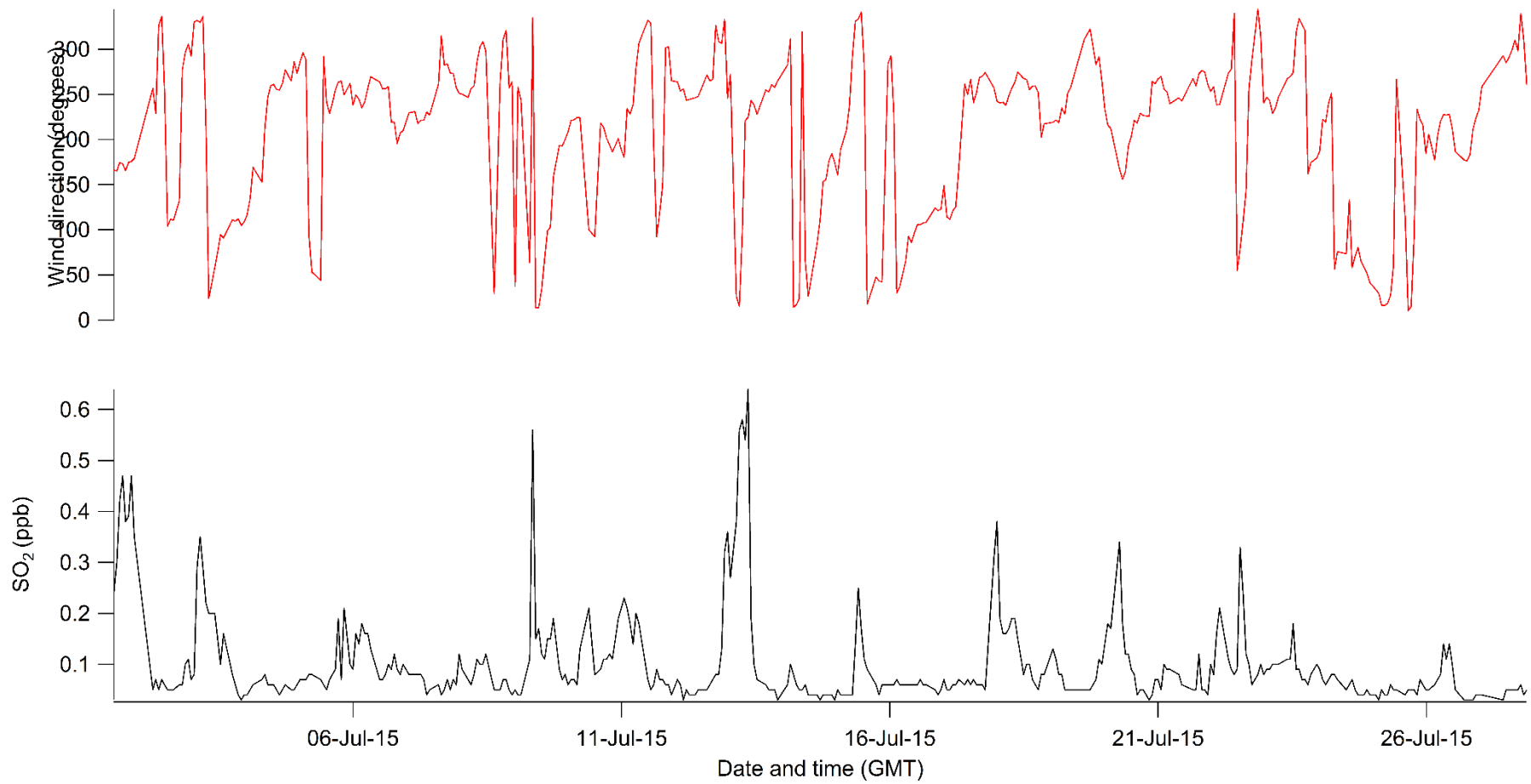
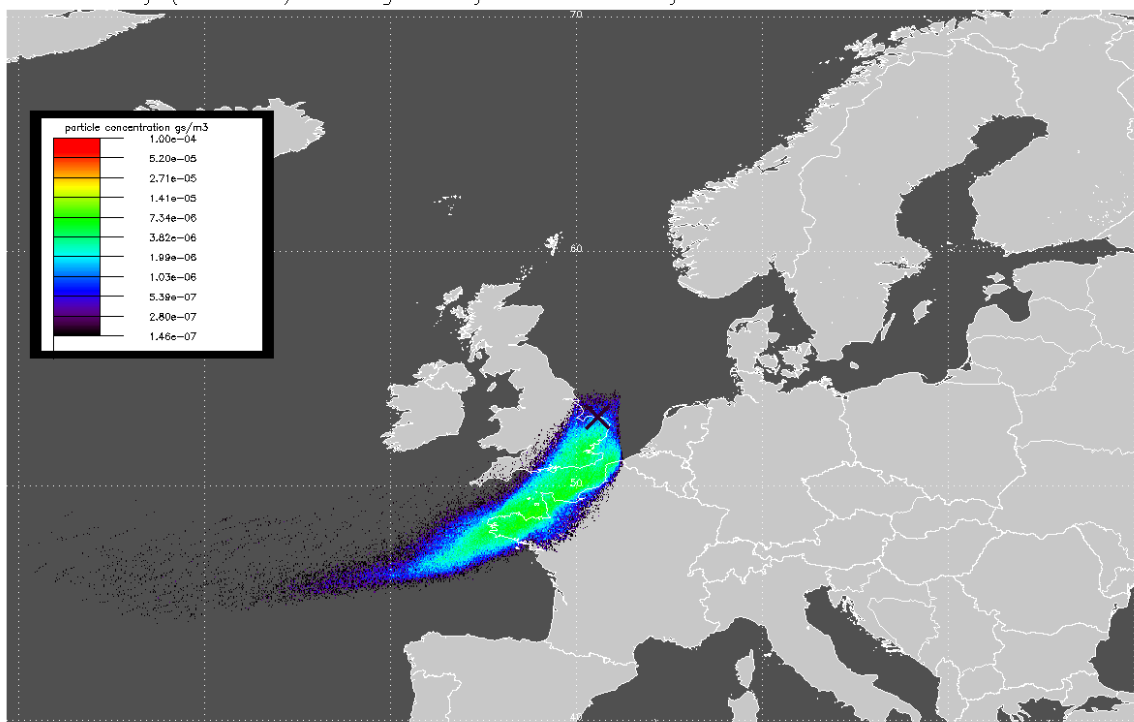


Figure 5:6 One day trajectories of air masses arriving at the measurement site



**Figure 5:7 SO<sub>2</sub> concentrations measured during the ICOZA campaign and the corresponding wind direction**

1 day (0–100m) arriving at Weybourne 3 Hourly release from: 20150601\_2100



**Figure 5:8 One day back trajectory depicting air travelling to the campaign site during the high ozone production regime**

With the use of a PTR-QMS, PTR-ToF-MS and GC-FID, quantitative measurements of VOC concentrations are limited. One disadvantage to the PTR technique stated in section 2.3, is that only VOCs that have a high enough proton affinity to abstract a proton from a hydronium ion can be detected, therefore certain hydrocarbons especially hydrocarbons emitted from diesel engines cannot be detected. Chin and Batterman (2012), for example have detected multiple alkanes such as: n-Heptane, n-Decane and Cyclohexane that would not be detected by the PTR-MS due to their low proton affinity. A further disadvantage with the use of a QMS is a decrease in sensitivity towards ions with a mass to charge ratio above 150 owing to increased losses of heavier ions in the quadrupole filter (Müller et al., 2014).

In order to use Gas Chromatography to detect atmospheric VOCs, the stationary phase of the separating column needs to be considered, as only certain functional groups present within a molecule can be separated depending on the phase and type of separating column. For example, the use of a non-polar

stationary phase within the separating column will only efficiently separate non-polar hydrocarbons. Whereas a polar column is used for the separation of polar compounds such as OVOCs from a sample. Therefore the species of VOC detected using a GC during a field campaign depends solely on the type of separating column, it may not be possible to detect a full suite of VOCs if only a certain type of separating column is available (Ellis and Mayhew, 2014a).

In order to overcome this issue, two dimensional Gas Chromatography (GC x GC) can be used to further separate VOCs from an ambient air sample. This technique utilises two separation columns. This can be a primary column in one dimension used to separate polar compounds from a sample and a non-polar column in the second dimension used to separate non-polar compounds.

A chiral stationary phase can also be employed within this method in order to separate chiral molecules from a sample such as the enantiomers of pinene which may otherwise not be detected using a non-polar separating column.

This leads to the conclusion that, it is possible some species that can react with OH can go undetected when calculating OH reactivity based solely on the measured concentrations of VOCs using these techniques. In order to measure the concentrations of all the individual VOCs that can react with OH radicals within an environment, a multitude of techniques must be employed, as no single technique has the ability to measure the concentrations of all VOCs within an environment. Whereas, with the use of total OH reactivity measurement techniques there is no need to measure the concentrations of VOCs.

## **5.2 Calculated total OH reactivity**

For each VOC and inorganic species measured during the campaign, (Tables Table 5:2 and 5:3), their respective temperature dependant OH reaction rate coefficients were calculated, based on the atmospheric temperature recorded during the campaign. The resulting rate coefficients were then used with their measured concentrations, to calculate total OH reactivity using E1:5.

The results of these calculations are shown in Figure 5:9, which shows total OH and the contributions of different classes of compounds to the total for the whole of the ICOZA campaign.

By segregating the calculated total OH reactivity, individual functional group related contributions to total reactivity can be determined. Table 5:4 shows the average total OH reactivity measured throughout the whole of the campaign, along with calculations of the percentage of the total reactivity by functional group. As can be seen from both Figure 5:9 and Table 5:4, OH reactivity throughout the campaign is dominated by NO<sub>2</sub>, contributing up to 64% of the total OH reactivity.

NO at 8.85%, is the second most dominant species that contributes to total OH reactivity. Although the majority of total OH reactivity is provided by NO<sub>2</sub>, the effect of NO<sub>2</sub> on OH production and pyrrole concentration within the UOL-CRM reaction vessel is negligible. As Hansen et al. (2015) and Michoud et al. (2015) have observed, NO<sub>2</sub> within the reaction vessel has the potential to be converted to NO, this however, does not proceed through photolysis, but rather by heterogeneous reactions on stainless steel surfaces upstream and downstream of the reaction vessel. However, for the UOL-CRM, the presence of NO<sub>2</sub> within the ambient air should not prove a problem with the UOL-CRM as there are no stainless steel components within the entire system.

In Table 5:5, the average total OH reactivity for the entire field campaign has been calculated once the contribution from NO<sub>x</sub> to OH reactivity has been subtracted) and the percentage contribution by species has also been calculated.

As discussed within section 1.2.3, the reactions of OH radicals with both NO and NO<sub>2</sub> act as HO<sub>x</sub> termination pathways (R 1:23 and R 1:24) in which there is no re-generation of OH radicals once these reactions take place. Therefore, once the contribution of NO<sub>x</sub> to the calculated reactivity has been subtracted, the contribution of other OH reactive species and ozone can be determined. Therefore, from this analysis it was determined that alkenes are the primary contributors to total OH reactivity at 27.9% followed by CO.

Average total OH reactivity (s <sup>-1</sup> )	Functional group	% of total OH reactivity
5.38	NO <sub>2</sub>	64.6
	NO	8.85
	Alkene	7.43
	CO	4.39
	Alkanes	3.83
	Terpene	2.87
	Aldehyde	2.32
	Carboxylic acids	1.37
	Ozone	1.06
	Alcohol	1.05
	Ketone	0.87
	Aromatic	0.611
	Sulphide	0.51
	SO <sub>2</sub>	0.06
	Alkyne	0.03
Nitrile	0.0007	

**Table 5:4 Average total OH reactivity calculated for the ICOZA campaign and the percentage of total OH reactivity separated by functional group**

Average total OH reactivity (s <sup>-1</sup> )	Functional group	% of total OH reactivity
1.48	Alkene	27.9
	CO	16.50
	Alkanes	14.42
	Terpene	10.79
	Aldehyde	8.71
	Carboxylic acids	5.17
	Ozone	3.93
	Alcohol	3.92
	Ketone	3.30
	Aromatic	2.29
	Sulphide	1.95
	SO <sub>2</sub>	0.22
	Alkyne	0.13
	Nitrile	0.0028

**Table 5:5** Calculated average total OH reactivity after the removal of NO and NO<sub>2</sub> measurements, and the percentage contribution to total OH reactivity by functional group

However, whilst alkenes were determined as the primary contributors to total OH reactivity, spikes in alkane and terpene related OH reactivity are observed at certain periods of the field campaign, more specifically, from 05/07/15 at 23:59 to 06/07/15 at 06:37 at which point, alkane based OH reactivity reaches a maximum of 2.7 s<sup>-1</sup> and from 19/07/15 at 17:36 to 20/7/15 at 02:48 when terpene based OH reactivity reaches a maximum of 8.1 s<sup>-1</sup> (Figure 5:9).

The increase in alkane based OH reactivity can be attributed to an increase in isohexane concentration (diesel emissions are a source of isohexane), which rapidly rises from approximately 0.01 ppb to 19.8 ppb and then proceeds to fall to a concentration of 0.0054 ppb. Isohexane is the only alkene observed to have such a rapid change in concentration during this time period. The concentrations

of the other alkanes measured during this time do not rise above 1 ppb as shown in Figure 5:2 a. and b.

The terpene responsible for the increase in OH reactivity from 19<sup>th</sup> July to 20<sup>th</sup> July can be ascribed to an increase in isoprene concentration. During this time period, the concentration of isoprene quickly increases from a baseline of approximately 0.05 ppb to 3.1 ppb and then decreases back to the average baseline concentration as isoprene based OH reactivity increases from;  $0.2 \text{ s}^{-1}$  to  $8.1 \text{ s}^{-1}$  and then decreases back to  $0.2 \text{ s}^{-1}$ . As with the increases in alkane based OH reactivity described above, only an increase in isoprene concentration can be responsible for this spike in total OH reactivity, as the concentration of other VOCs and terpenes during this time does not change. Although, the measured concentration of isoprene was low during this period, (and the increase in isoprene concentration is small), the rate of reaction between OH and isoprene is so fast that a large increase in OH reactivity is seen ( $1.0 \times 10^{-10} \text{ cm}^3 \text{ molecule}^{-1} \text{ s}^{-1}$  at 298 K 1 bar (Atkinson et al., 2004)). For example, whilst 3.1 ppb of isoprene is measured, at the same time, a higher concentration of ozone is measured (41.29 ppb). However, as the rate coefficient of OH + isoprene is a factor of 100 times faster than the rate coefficient of OH + ozone ( $7.3 \times 10^{-14} \text{ cm}^3 \text{ molecule}^{-1} \text{ s}^{-1}$  (Atkinson et al., 2004)), a large OH reactivity is calculated with respect to isoprene in comparison to the reaction of OH + ozone ( $8.1 \text{ s}^{-1}$  and  $0.06 \text{ s}^{-1}$  respectively).

Relating the calculated total OH reactivity to wind direction measurements and the dependence of VOCs and inorganic species on wind direction (Figures 5:3 and 5:4), it is clear that calculated reactivity is at its highest in air masses arriving from either a south to south westerly or northern direction, (Figure 5:4). This also corresponds to periods at the start of the when concentrations of  $\text{NO}_2$  are at its highest (and therefore based on the trajectories shown in Figures 5:5 and 5:6 periods during the campaign when polluted air arrived at the measurement site), as shown in the calculations of OH reactivity.

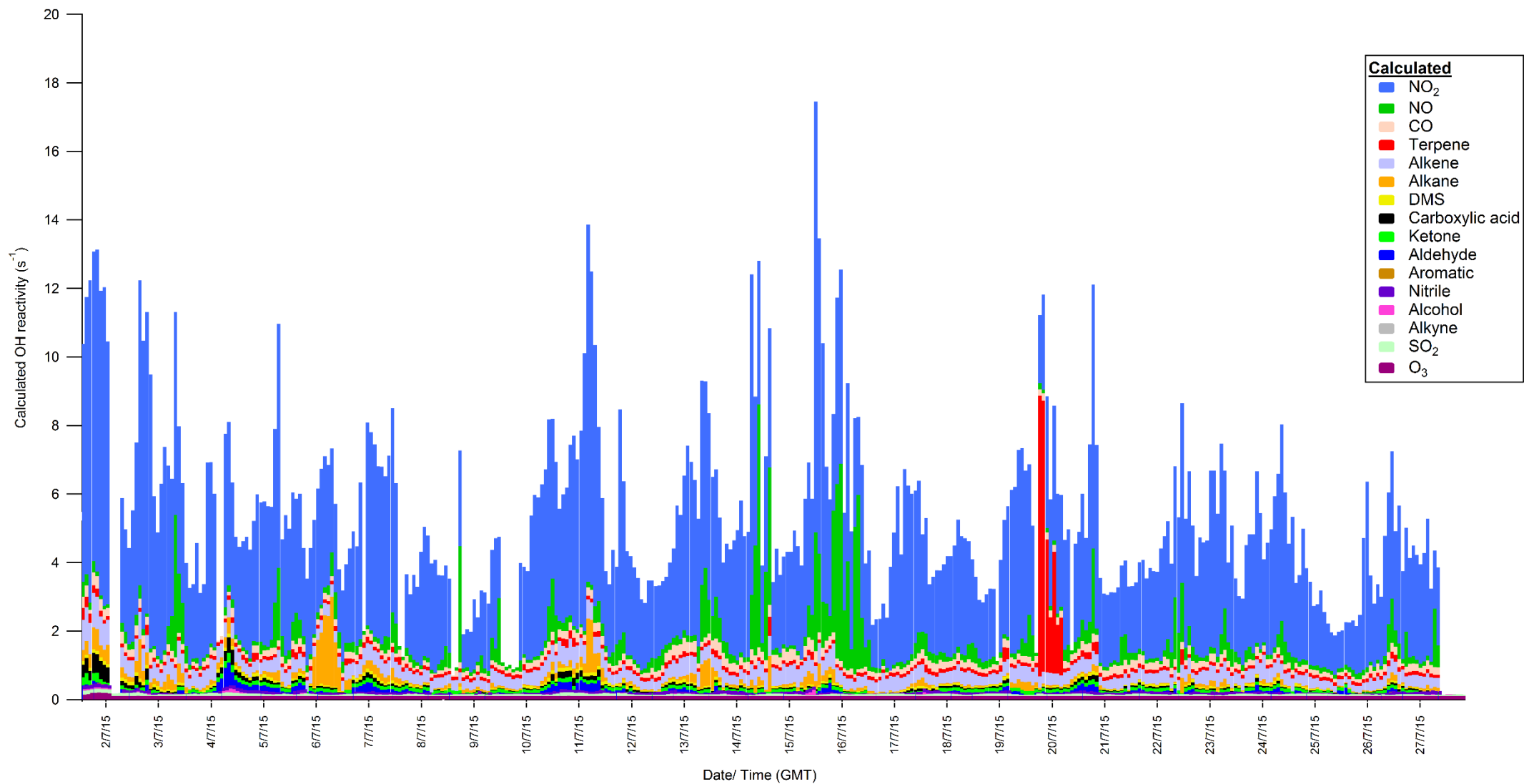


Figure 5:9 Calculated OH reactivity based on the concentrations of VOCs and inorganic species measured during the ICOZA campaign

### 5.3 The UL-LIF Instrument

As discussed in section 1.5, along with the Comparative Reactivity Method, total OH reactivity can be measured via the TOHLM method (Ingham et al. (2009), Kovacs and Brune (2001)) and Laser Induced Flash Photolysis (LIF) (Whalley et al. (2016), Sadanaga et al. (2004a)).

The instrument used by the University of Leeds employs Laser Induced Flash Photolysis, a schematic of which is shown in Figure 5:10, and is described in more detail in Stone et al. (2016).

The LIF instrument has the capacity to monitor ambient OH concentrations and to measure OH reactivity, (Hansen et al., 2015).

The instrument consists of a reaction cell where OH radicals are formed and react with VOCs within an ambient air sample, and a detection cell where the decay signals of OH is measured (Sadanaga et al. (2004a), Ingham et al. (2009)).

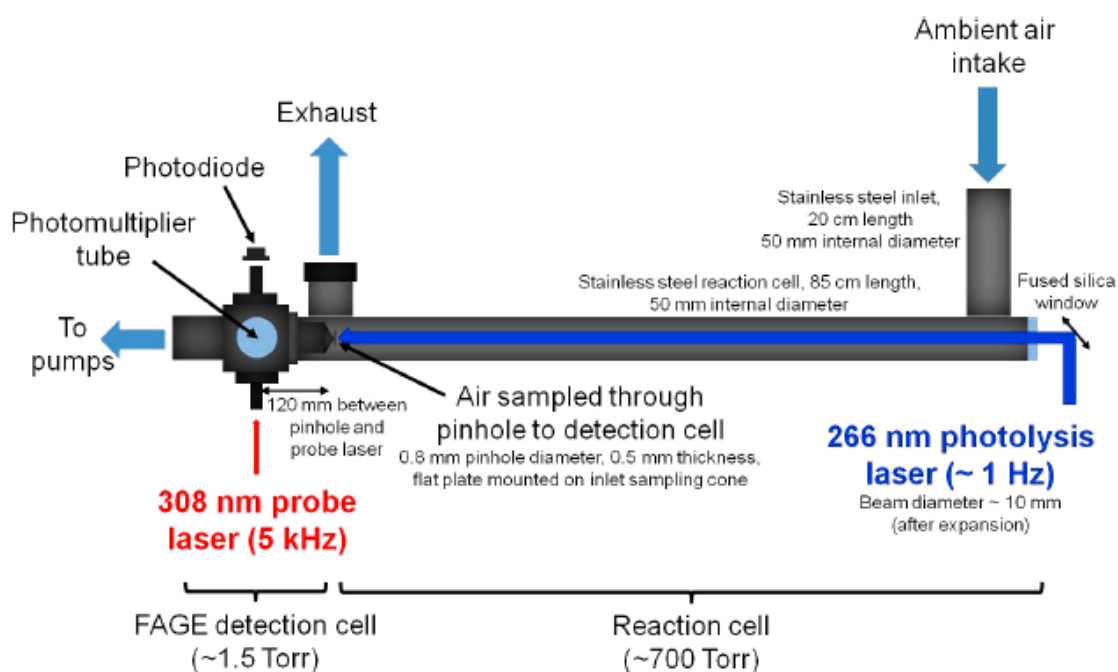
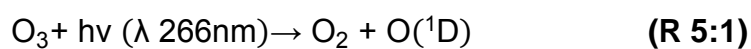


Figure 5:10 A schematic of the University of Leeds LIF instrument. From (Stone et al., 2016)

The reaction cell is a stainless steel tube that draws in ambient air via an extractor fan. Situated adjacent to the reaction cell is a flashlamp pumped Nd:YAG laser which, via a series of mirrors allows light from the laser to enter the reaction cell. After which, the laser is used to generate OH radicals through the photolysis of ozone in the presence of water vapour at ambient concentrations (R 5:1 and 5:2).



However, at concentrations of less than 10 ppb of ozone, a makeup flow of high purity air can be used to increase the concentration of ozone, and therefore OH within the reaction cell (Stone et al., 2016).

Once the OH radicals have reacted with any VOCs within the ambient air sample, the flow of gas from the reaction cell enters the detection cell where OH radicals are detected through Laser Induced Fluorescence using the Fluorescence Assay by Gas Expansion (FAGE) technique (Ingham et al., 2009).

The FAGE detection cell consists of a pumped sapphire laser (Bloss et al., 2003) that produces light at a wavelength of 308 nm. Pulsing of the laser within the detection cell causes the OH radicals within the detection cell to fluoresce as electronic transitions occurs within OH radicals from the ground state to a higher state (Ingham et al., 2009).

The light generated as the electronically excited OH radicals relax back down to the ground state is focused onto a photomultiplier tube (PMT) (Sadanaga et al., 2004a).

A short time after the OH fluorescence has been detected (10  $\mu\text{s}$ ), the instrument background is measured by collecting solar radiation entering the reaction cell through the sampling pinhole. The background signal is then subtracted from the signal measured from the sample.

LIF measurements of OH concentration and reactivity are made during a number of cycles. An online period during which, the 308 nm laser is tuned to electronically excite OH radicals. And an offline period at which point, the emission lines of the laser is changed from 308 nm to a wavelength that doesn't result in electronic transitions within OH radicals when excited. The purpose of this change in wavelength is to allow background ambient concentrations of OH to be measured (Whalley et al., 2010). Following this, the emission wavelength of the laser is then shifted back to 308 nm and used to excite OH within a reference cell. The reference cell is used for calibration purposes and to determine the linearity of the LIF. During the cycling of the instrument, the LIF is used to determine reactivity during the online period (Stone et al., 2016).

### 5.3.1 LIF determination of OH reactivity

The measured OH reactivity is determined by monitoring the OH decay signal once OH within the reaction cell reacts with trace gases within the ambient air sample.

The rate coefficient for OH losses ( $k_{loss}$ ) is then fitted to the decay signal which has the expression:

$$S_{OH,t} = S_{OH,0} e^{(-k_{loss}t)+b} \quad (\text{E 5:1})$$

Where:  $S_{OH,t}$  is the fluorescence signal at time,  $t$  after the 266 nm laser pulse,  $S_{OH,0}$  is the fluorescence signal at time zero,  $k_{loss}$  is the rate coefficient for the loss of fluoresce signal,  $t$  is the time since the pulse of the 266 nm laser and  $b$  is the background fluorescence signal (Stone et al., 2016). OH decay is then given by the sum of a number of different OH loss pathways within the reaction cell. These losses ( $k_{loss}$ ) can occur due to chemical reactions (OH reactivity), diffusion and wall losses. Therefore, the OH reactivity due to chemical reactions ( $k_{OH,obs}$ ) can be determined from  $k_{loss}$  and  $k_{phys}$  (E 5:2). Where  $k_{phys}$  is the rate coefficients of physical OH losses within the reaction cell.

$$k_{OH,obs} = k_{loss} - k_{phys} \quad (\text{E } 5:2)$$

The physical losses of OH within the instrument ( $k_{phys}$ ) is determined through the measurement of OH decays in the absence of any VOCs within the ambient air sample. It is measured in order to improve the accuracy of the true OH reactivity, and is completed by flowing ultra-pure air into the reaction cell whilst measuring OH decay (Stone et al., 2016).

Examples of OH decay profiles are shown in Figure 5:11. Equation 5:1 is fit to the OH decay signal shown in Figure 5:11 (red line), and from the fitting function,  $k_{loss}$  is determined. Using 5:2, total OH reactivity is then determined.

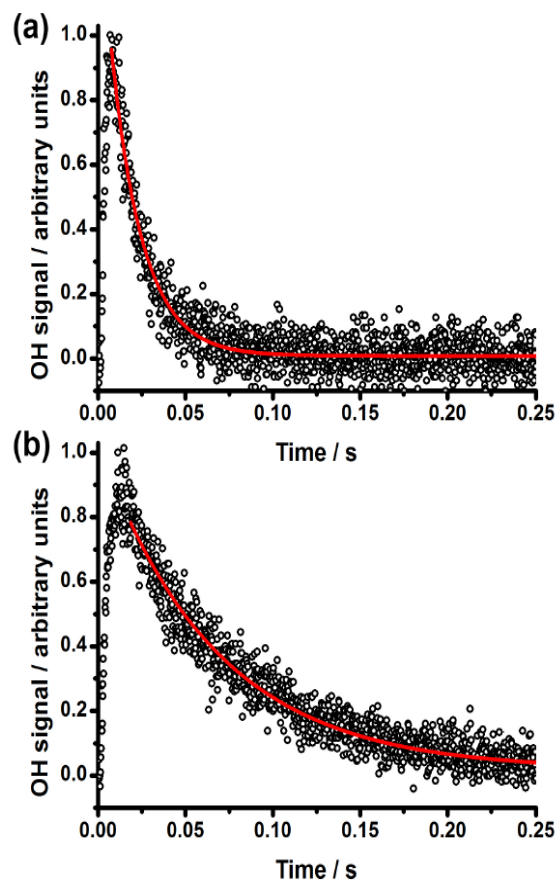


Figure 5:11 (a) OH decay profile measured during a polluted period of the Clean Air for London (ClearfLO) campaign (2012), and (b) measurements made during a cleaner period of the campaign. Measurements made are shown with black point and red lines show the fits using E 5:1. Adapted from Stone et al. (2016).

Measured in London 2012 during the Clean Air for London (ClearfLO) campaign, Figure 5:11 (a) shows a profile measured during a polluted period of the campaign, OH reactivity measured during this period was determined as  $46.6 \text{ s}^{-1}$ , (b) shows measurements made during a particularly clean period, in which reactivity was  $13.9 \text{ s}^{-1}$  (Stone et al., 2016).

#### **5.4 UL- LIF measurements during the ICOZA campaign**

The instrument was positioned within a shipping container with its sample inlet positioned directly next to the sample lines used for the UOL-CRM. The UL-LIF ran for the majority of the campaign period (from 1<sup>st</sup> July to 22<sup>nd</sup> July), with calibrations and zero measurements conducted in between sampling periods.

The measurements during ICOZA made by the UL-LIF are shown in Figure 5:12. The measurements are time averaged based upon the sampling interval of the GC-FID. To summarise: the minimum, maximum, average and standard deviation in total OH reactivity was:  $1.87 \text{ s}^{-1}$ ,  $15.57 \text{ s}^{-1}$ ,  $4.87 \text{ s}^{-1}$  and 1.91 respectively.

The box plots shown in Figure 5:21 summarises the data collected by the UL- LIF for each day of the campaign, alongside the comparable UOL-CRM measurements. Comparisons of measurements made by both instruments are discussed in the section 5.6.

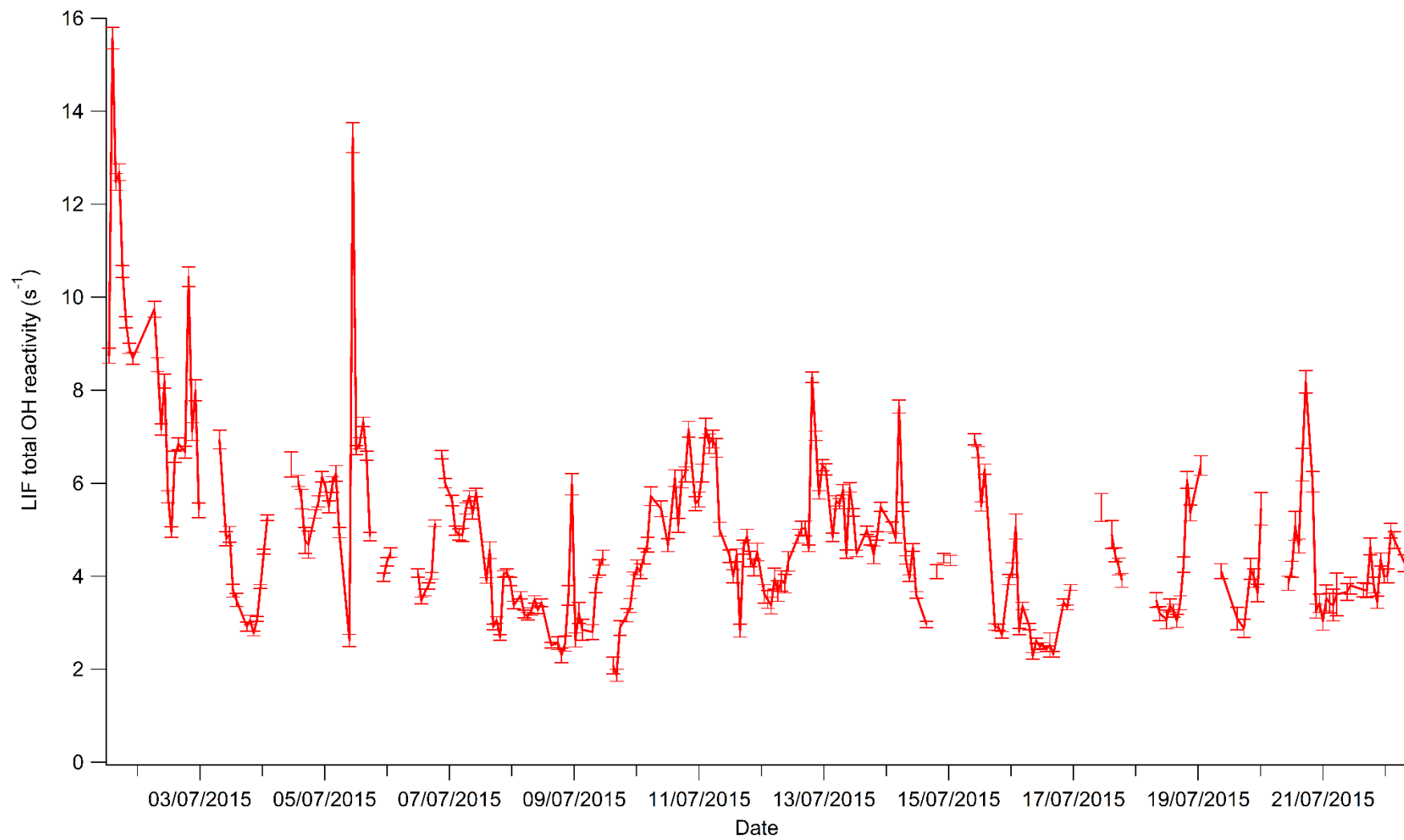


Figure 5:12 Measurements of OH reactivity made by the University of Leeds using LIF instrument during the ICOZA campaign

## 5.5 Comparing calculated total OH reactivity and UOL-CRM measured reactivity. An overview of the campaign

Figure 5:13 shows the measurements made by the UOL- CRM and the UL-LIF along with calculated total OH reactivity.

In Figure 5:13 and hereafter, the calculations and measurements of OH reactivity are averaged based on the sampling times of the GC-FID, (for comparison, the data shown in Figure 4:18 is composed of one minute measurements). The data set was averaged in order to reduce the degree of noise within the UOL-CRM measurements and facilitate the comparison between datasets. As a result, the average standard deviation ( $1\sigma$ ) in the total OH reactivity measurements was reduced from 29.09 (one minute data) to 24.6 (averaged to GC time series).

No clear correlation is observed between the measurements made by the UOL- CRM and the calculated OH reactivity. However there are periods of the field campaign when the disagreement between the measured and calculated is lower in comparison to other periods.

These areas are depicted in Figure 5:13 (and after). Areas shaded in grey, are periods when the agreement between UOL-CRM measurements and calculated reactivity is high, and areas highlighted in blue are periods of the field campaign when the agreement is low, (these periods are discussed in greater detail from section 5.5.1 onwards).

More specifically, the periods discussed are:

1. 04/07/15 (03:18) to 05/07/15 (09:33), at which point there is a large spike in total OVOC concentration which slowly decreases over time.
2. 13/07/15 (21:51) to 16/07/15 (08:23) when measured  $\text{NO}_x$  concentrations are above the average for the entire campaign.
3. 19/07/15 (06:14) to 20/07/15 (22:38) when there is a spike in total OVOC concentrations and an increase in  $\text{NO}_2$
4. 23/07/15 (18:59) to 27/07/15 (20:49) during which, the concentrations are total NMHC, OVOC and  $\text{NO}_x$  all reach a minimum.

The box and whisker plot shown in Figure 5:14, (and the corresponding data in Table 5:6) show daily UOL-CRM measurements and calculated OH reactivity, (during periods of the campaign when the UOL-CRM, PTR-QMS and GC-FID were simultaneously sampling ambient air). Both the figure and table show the extent to which the data sets disagree.

When comparing the overall campaign measurements, there was a difference of  $30 \text{ s}^{-1}$  between the UOL-CRM and calculated total OH reactivity (85% difference). On average, no overlap between the measured and calculated reactivity was observed as the measured range in OH reactivity was a lot larger ( $23 \text{ s}^{-1}$ ) in comparison to that of the calculated OH reactivity (range of  $6 \text{ s}^{-1}$ ). With the minimum ( $2.5 \text{ s}^{-1}$ ) and maximum ( $9.3 \text{ s}^{-1}$ ) calculated OH reactivity being lower than that measured by the UOL-CRM respectively ( $23 \text{ s}^{-1}$  to  $52.5 \text{ s}^{-1}$ ) on average for the entire campaign. This wide range in UOL-CRM measurements can be attributed to the higher standard deviation in measurements in comparison to the calculated OH reactivity. On average the standard deviation within the UOL-CRM measurements was 80% higher than within the calculated reactivity. The standard deviation of UOL-CRM measurements are lower during periods of the campaign when the agreement between measurements and calculations are high (Table 5:6).

Looking at all of the periods of the campaign shown in blue in Table 5:6, the standard deviation in UOL- CRM measurements was 82% higher than that of calculated reactivity. In comparison, for the periods of the campaign shown in grey in Table 5:6, the standard deviation in UOL- CRM measurements was 67% higher than that of the calculated OH reactivity.

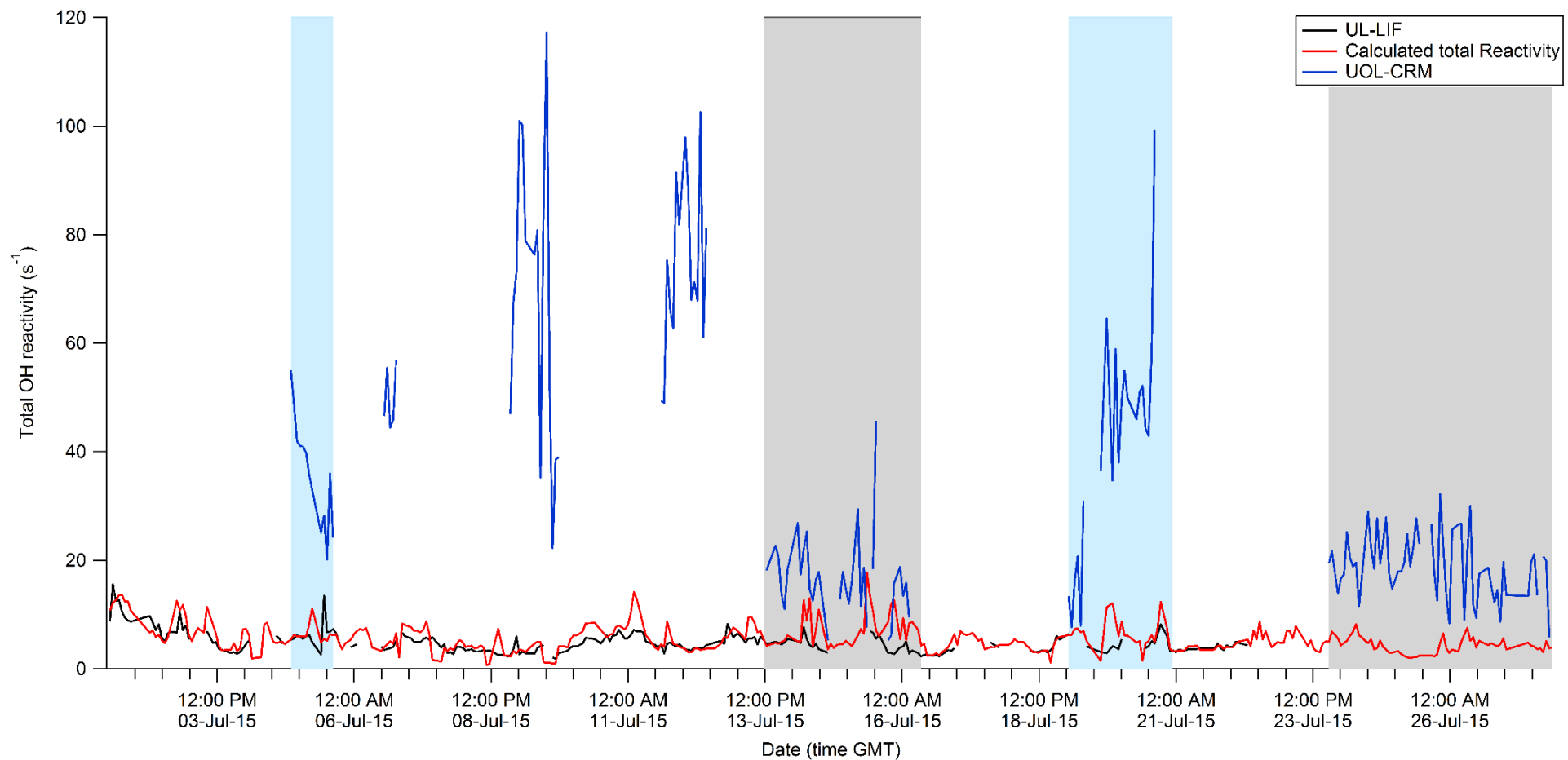


**Figure 5:13 Time series of measurements made using the UOL-CRM and the UL-LIF along with calculated total OH reactivity**

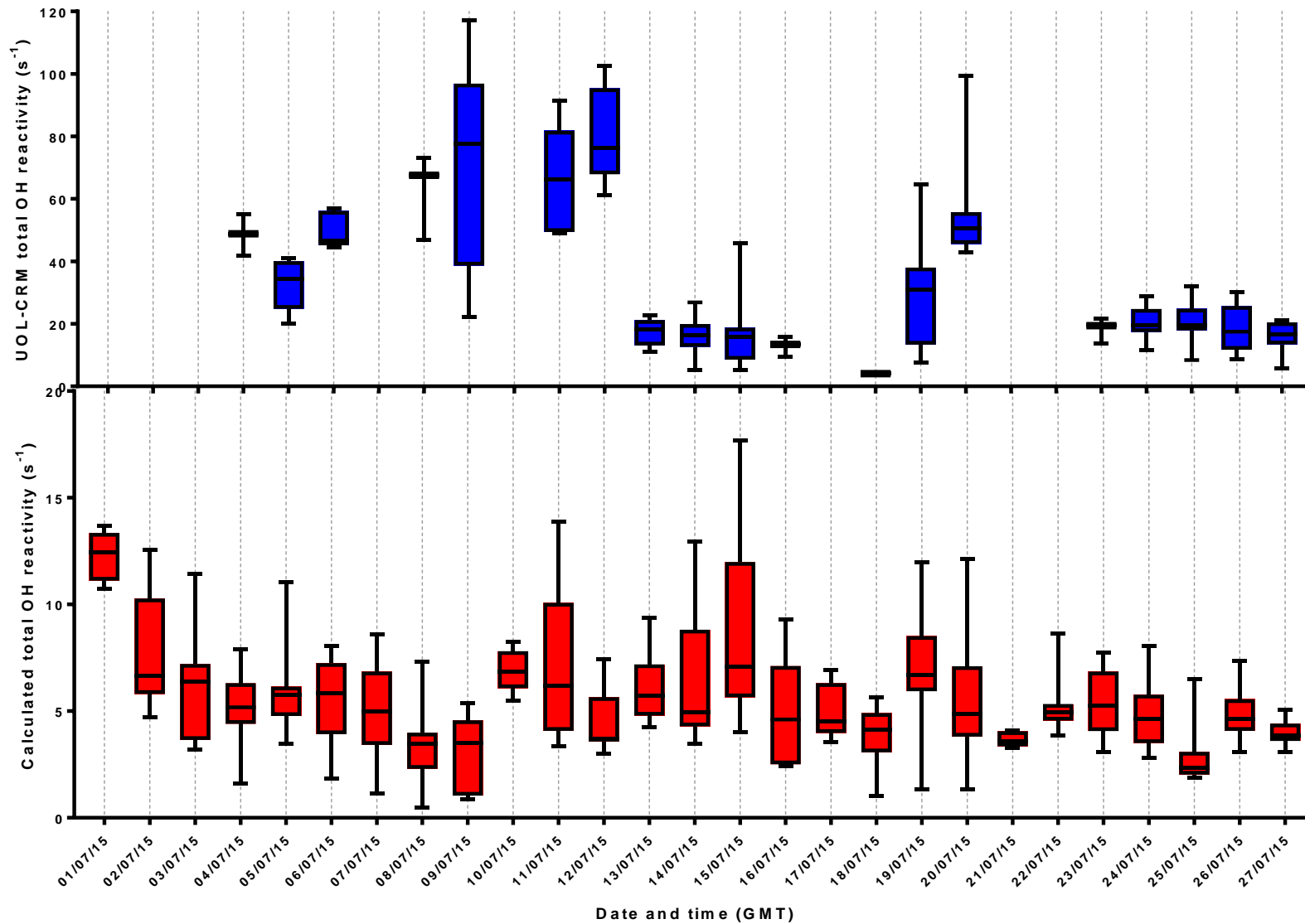


Figure 5:14 Box and whisker plot comparing UOL-CRM measurement and calculated total OH reactivity

Total OH reactivity (s <sup>-1</sup> )												
	Minimum		Mean		Maximum		25% Percentile		75% Percentile		Std. Deviation (1σ)	
	Calculated	UOL-CRM	Calculated	UOL-CRM	Calculated	UOL-CRM	Calculated	UOL-CRM	Calculated	UOL-CRM	Calculated	UOL-CRM
04/07/15	1.6	41.89	5.205	48.58	7.89	55.05	4.41	41.89	6.31	55.05	1.83	6.58
05/07/15	3.47	20.15	5.85	32.42	11.03	41.07	4.77	24.84	6.143	40.08	1.70	7.57
06/07/15	1.82	44.43	5.541	49.84	8.05	56.88	3.92	45.16	7.25	56.17	1.89	5.84
08/07/15	0.5	46.93	3.226	62.54	7.31	73.12	2.3	46.93	3.99	73.12	1.67	13.8
09/07/15	0.88	22.18	3.091	68.95	5.39	117.2	1.04	38.67	4.57	96.86	1.65	30.76
11/07/15	3.34	49.05	6.947	68	13.88	91.47	4.08	49.41	10.07	81.82	3.43	15.97
12/07/15	3	61.11	4.521	79.74	7.44	102.6	3.578	67.89	5.658	95.39	1.45	15.21
13/07/15	4.24	11.02	6.23	17.43	9.38	22.7	4.79	13.08	7.19	21.19	1.74	4.33
14/07/15	3.47	5.21	6.39	16.31	12.94	26.86	4.29	12.66	8.82	19.96	3.26	6.11
15/07/15	4.03	5.25	8.63	17.1	17.68	45.73	5.65	8.56	11.99	18.76	3.98	11.76
16/07/15	2.41	9.494	5.03	12.95	9.3	15.91	2.51	9.49	7.11	15.91	2.39	3.23
19/07/15	1.34	7.67	7.01	29.95	11.97	64.55	5.93	13.34	8.51	37.99	2.79	19.25
20/07/15	1.35	42.92	5.53	54.8	12.11	99.34	3.81	45.57	7.1	55.73	2.53	16.34
23/07/15	3.07	13.83	5.3	18.3	7.75	21.63	4.07	13.83	6.85	21.63	1.47	4.02
24/07/15	2.83	11.55	4.72	20.62	8.06	28.92	3.50	17.35	5.77	24.75	1.44	4.95
25/07/15	1.88	8.37	2.84	20.42	6.48	30.04	2.02	11.71	3.09	24.82	1.25	6.20
26/07/15	3.1	8.65	4.80	17.81	7.37	30.04	4.08	11.71	5.56	25.67	1.10	7.08
27/07/15	3.08	5.78	3.99	15.97	5.08	21.15	3.6	13.42	4.41	20.5	0.601	5.36
<b>Average</b>	<b>2.52</b>	<b>23.08</b>	<b>5.27</b>	<b>36.20</b>	<b>9.39</b>	<b>52.46</b>	<b>3.79</b>	<b>26.97</b>	<b>6.68</b>	<b>43.63</b>	<b>2.01</b>	<b>10.24</b>

Table 5:6 Statistics from the box and whisker plot shown in Figure 5:14. Comparing data from the UOL-CRM and calculated OH reactivity for the duration of the field campaign. Shading in grey and blue represent days of the campaign when the agreement between measured and calculated reactivity was high and low respectively. These periods are discussed in the following sections

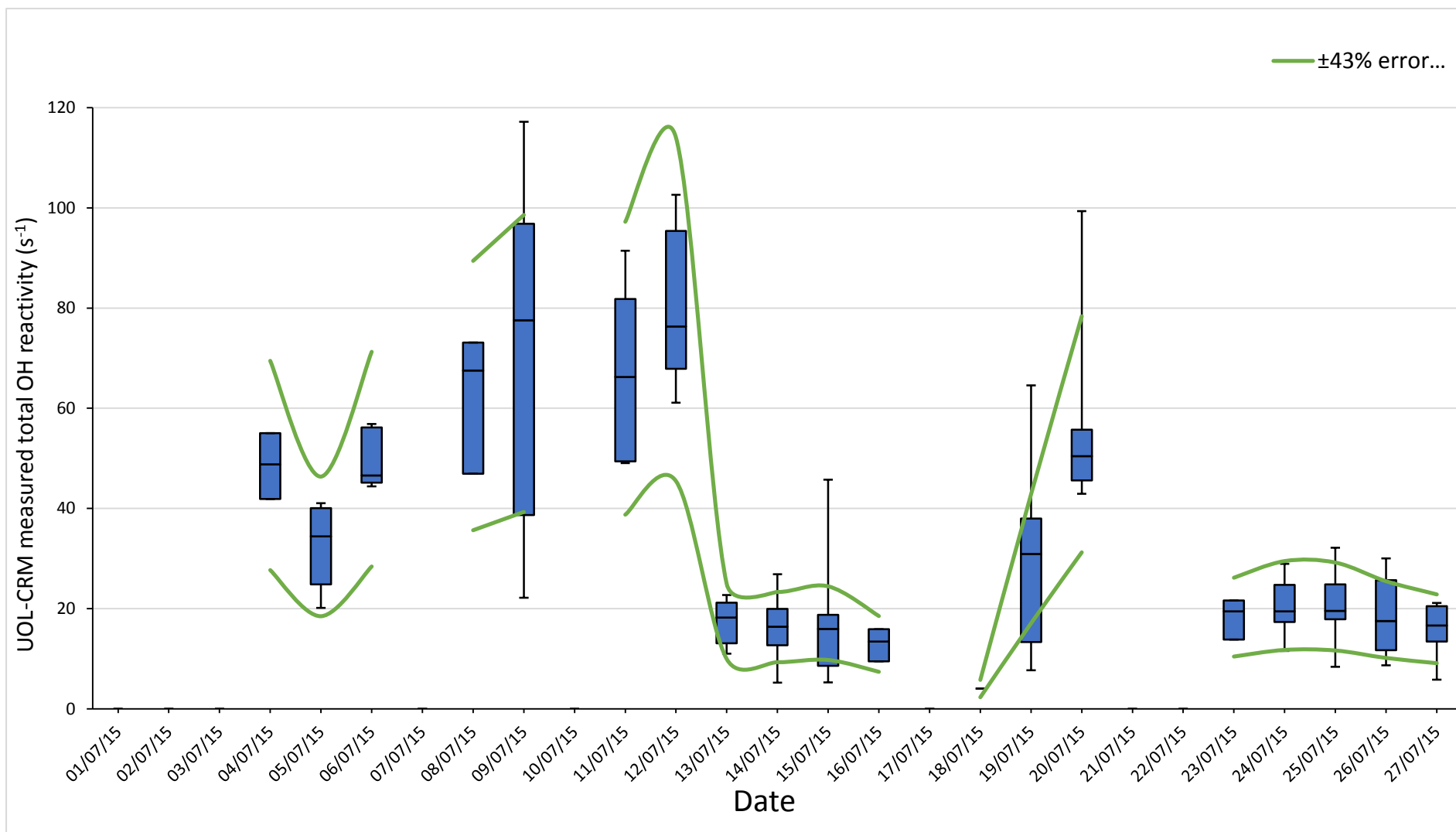
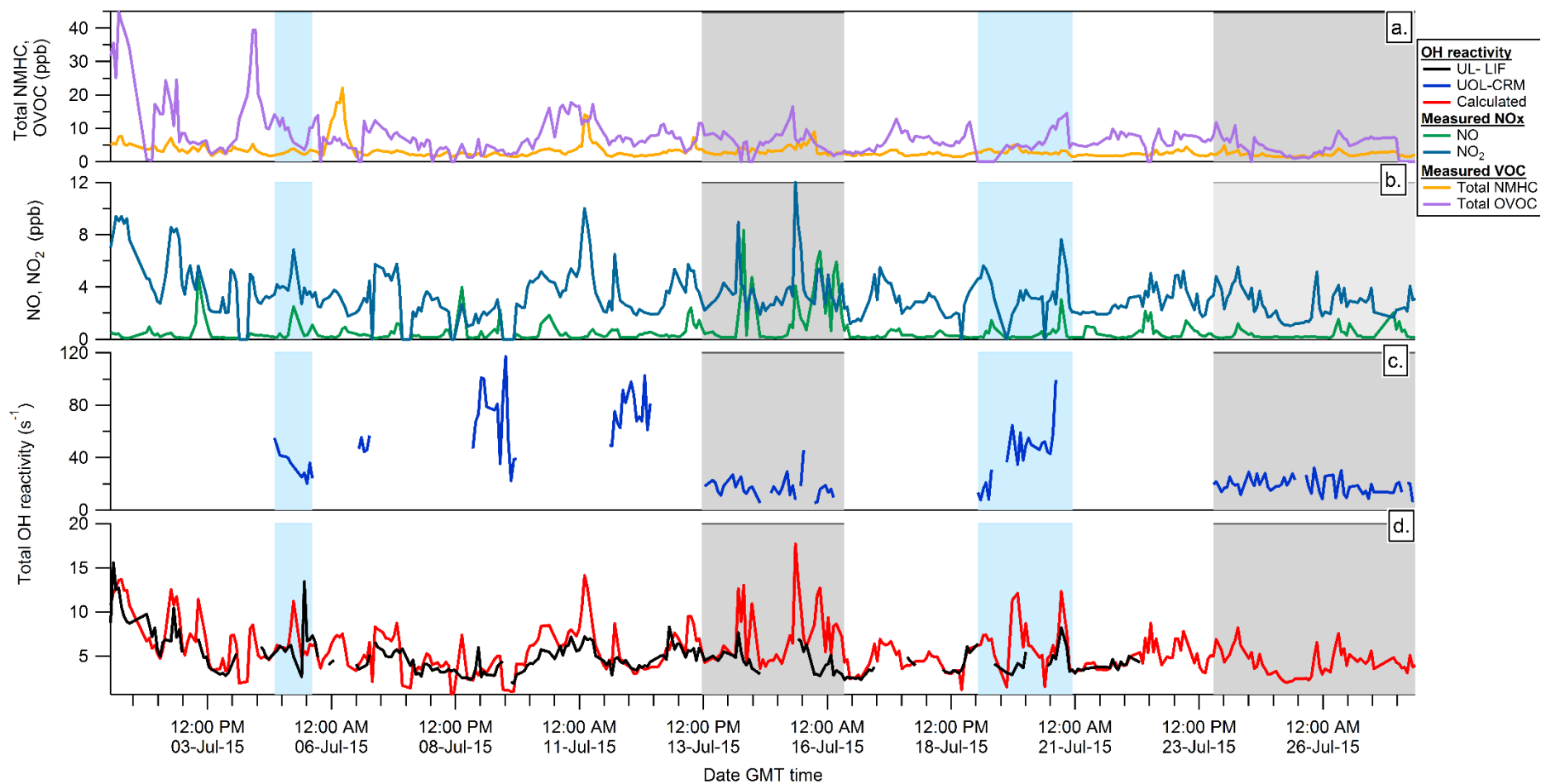


Figure 5:15 Box and whisker plot showing UOL-CRM data measured during the ICOZA campaign and the corresponding error within the mean



**Figure 5:16** Measurements made of VOC concentrations throughout the ICOZA campaign (a.) (total OVOC, total NMHC), NO<sub>x</sub>(b.) along with total OH reactivity measured using both the UL-LIF and UOL-CRM and calculated total OH reactivity (c. and d.). Areas shaded in grey are regions of high instrument and calculated agreement and regions in blue are periods where there is little agreement, discussed, (the same regions are also highlighted in the figures below).

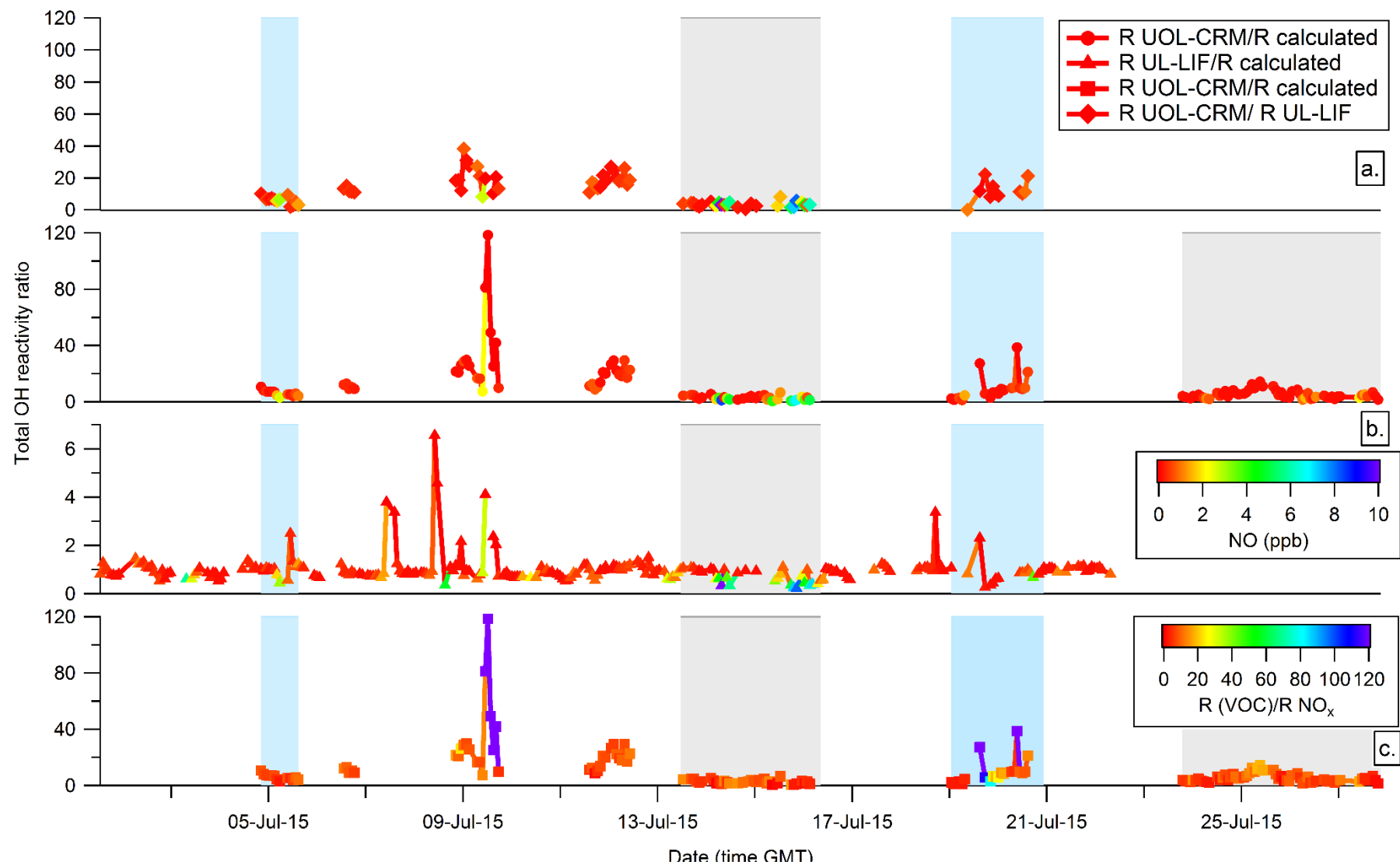


Figure 5:17 (a). Calculated ratios of total OH reactivity measurements and calculations, UOL-CRM/Calculated reactivity, UOL-CRM/UL-LIF reactivity. (b). Ratio of UL-LIF/calculated OH reactivity. Colour scale applied to both a. and b. show the concentrations of NO during the field campaign And (c). Ratios of UOL-CRM/UL-LIF reactivity, colour scales show the ratio of the VOC and inorganic species contribution to OH reactivity to the contribution of NO<sub>x</sub> to total reactivity

Added to the box and whisker plot of the UOL-CRM measurements are calculated error bars (Figure 5:15). These bars are calculated by adding or subtracting an error of 43% from the mean (uncertainty calculated in section 3.8).

A large degree of error is observed within the measurements during the campaign, and there are periods at which some of the measurements exist outside of the error. However it is observed that, during periods 2 and 4 of the campaign, when the measurements made by the UOL-CRM agree to a higher degree (than periods 1 and 3) with the calculated measurements and the UL-LIF data, the range in error is lower than periods 1 and 3. This is owing to a larger standard deviation in UOL-CRM measurements made during periods 1 and 3 in comparison to periods 2 and 4.

Figure 5:16 shows measurements of: total VOCs made by the PTR-QMS and the GC-FID, NO<sub>x</sub>, wind direction, calculated OH reactivity and measured OH reactivity (UOL-CRM and UL-LIF). The data presented within this figure, is used to determine what the ambient conditions were when the UOL-CRM agreed with the calculation of OH reactivity. As stated previously, periods of agreement are highlighted in grey, periods of disagreement are highlighted in blue.

As no correlation could be found between UOL-CRM measurements and calculated reactivity, ratios were calculated for each day of the field campaign (where the ratio of measured to calculated reactivity is termed as 'R UOL-CRM/R Calculated', and 'R UL-LIF/ R Calculated' and the ratio between measured data is termed as 'R UOL-CRM/ R UL-LIF' respectively). Figure 5:17 shows the calculations of these ratios along with the concentrations of NO measured during the campaign (colour scale) and the fraction of VOC dependant OH reactivity to NO<sub>x</sub> dependant reactivity. This fraction is calculated by separating the calculated NO<sub>x</sub> based contribution to OH reactivity from the VOC and inorganic species based contribution to OH reactivity.

### 5.5.1 Period 1 04/07/15 to 05/07/15

Large spikes OH reactivity due to a sudden increase in total OVOC and NMHC concentrations are observed during this period of measurement. An example of this is 20:21 on 04/07/15 (Figure 5:16), in which a spike in OVOC concentrations are observed, (13 ppb), the concentration then proceeds to decrease to 5 ppb on 5<sup>th</sup> July at 12:09 pm.

During this time period, the corresponding OH reactivity that results from the sudden spike and the subsequent decrease in OVOC concentration is observed and tracked within the UOL-CRM measurements. As OH reactivity is measured at  $55 \text{ s}^{-1}$  within the UOL-CRM, when the OVOC concentration is 13 ppb, which then decreases to  $20 \text{ s}^{-1}$  as the OVOC concentration falls.

The species contributing to this sudden increase and slow decrease in total OVOC concentrations are: methanol, acetone, acetaldehyde, acetic acid MVK, MEK and formaldehyde. This was determined from the concentrations changes of individual species within Figure 5:2, and the corresponding fluctuations in species based OH reactivity within Figure 5:9.

When the UOL-CRM measured OH reactivity reaches its peak on this day ( $55 \text{ s}^{-1}$  on 4<sup>th</sup> July), it is ten times higher than the calculated OH reactivity, (Figure 5:17). Figure 5:17 shows that the R UOL-CRM/ R calculated ratios have a possible dependence on the concentration of NO, as the ratio between the measurements and calculations decrease with NO concentration.

When the ratio R UOL-CRM/ R calculated is 10:1, the NO concentration is 0.17 ppb, as the ratio decreases, the NO concentration increases as seen when the ratio is at its minimum, 2.9:1, the NO concentration is 2.5 ppb (Figure 5:18). The same trend is observed in period two and discussed in further detail in the following sections.

It is likely then that the UOL-CRM is able to follow the same trends and fluctuations in OVOC and NMHC concentrations, and the resulting OH reactivity, however the absolute value differs from the calculated value. And for the measured OH reactivity to match the calculated OH reactivity, higher

concentrations of NO are needed. These observations are seen in the following periods of measurement.

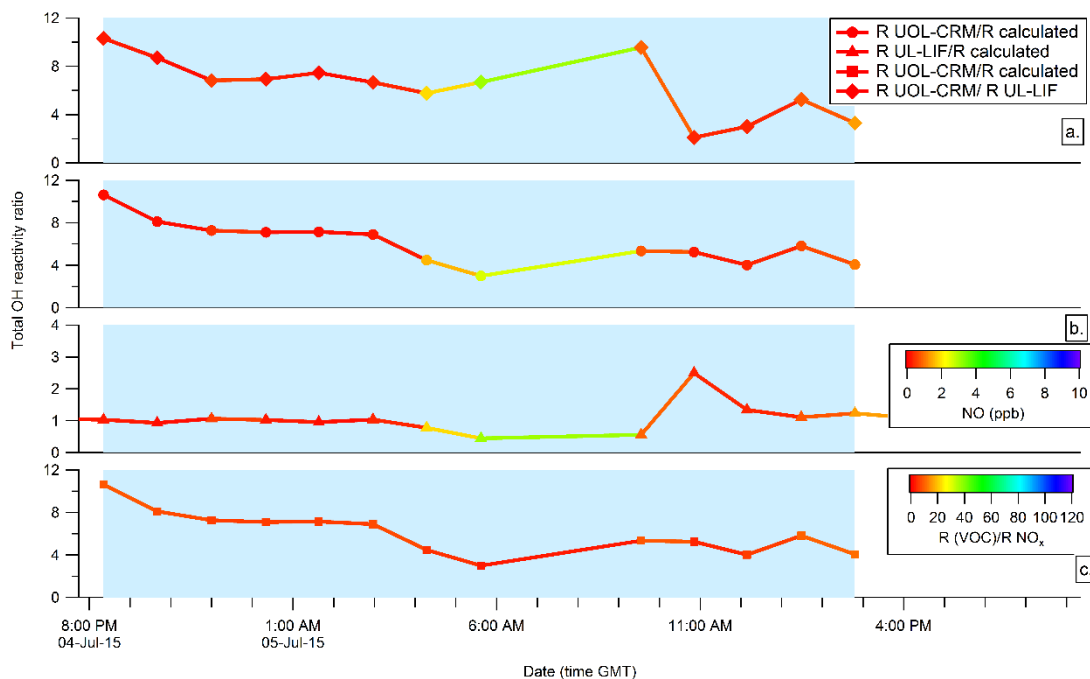


Figure 5:18 Magnification of Period 1 shown in Figure 5:17

## 5.5.2 Periods 2 13/07/15 to 16/07/15

From 13<sup>th</sup> to 16<sup>th</sup> July, the UOL-CRM measurements reached a minimum. Ranging from 11 s<sup>-1</sup> to 5 s<sup>-1</sup> on 15<sup>th</sup> July. With maximum measurements ranging from 15.9 s<sup>-1</sup> to 45.7 s<sup>-1</sup>. The degree of overlap between the calculated and measured OH reactivity is higher during this period in comparison to the rest of the campaign, as the calculated reactivity ranged from an average minimum of 3.5 s<sup>-1</sup> to an average maximum of 12.3 s<sup>-1</sup> as shown in Figure 5:14 and Table 5:6. On average the UOL-CRM measurements was 57% higher than the calculated reactivity.

In comparison to Periods 1, 3 and 4, the concentration of NO<sub>x</sub> was elevated above the average (8 ppb of NO and 10 ppb of NO<sub>2</sub> from 13<sup>th</sup> to 16<sup>th</sup> July) and just as with the Period 1, the ratio R UOL-CRM/ R calculated reaches a minimum when the concentration of NO is at its highest (Figure 5:19). The ratio of

UOL-CRM measured to calculated OH reactivity is 1.1:1 when the concentration of NO is 8.3 ppb (the highest measured during the campaign) and 1.2:1 when NO was measured at 6.7 ppb, (Figures 5:15, 5:16 and 5:18). When the concentration of NO was less than 2 ppb during this period, the UOL-CRM/calculated R ratio ranged from 1.5:1 to 4:1.

There are two conditions to this conclusion that when the NO concentration is elevated the UOL-CRM measured reactivity is low. That the measurements made by the UOL- CRM is generally high in comparison to the calculated reactivity but is affected by the concentrations of NO and at high concentrations of NO, the measurements made by the UOL-CRM will decrease. The second conclusion is that the measurements made by the UOL-CRM is higher in general in comparison to the calculated OH reactivity, regardless of the concentration of NO. And that high concentrations of NO only affects the calculated OH reactivity.

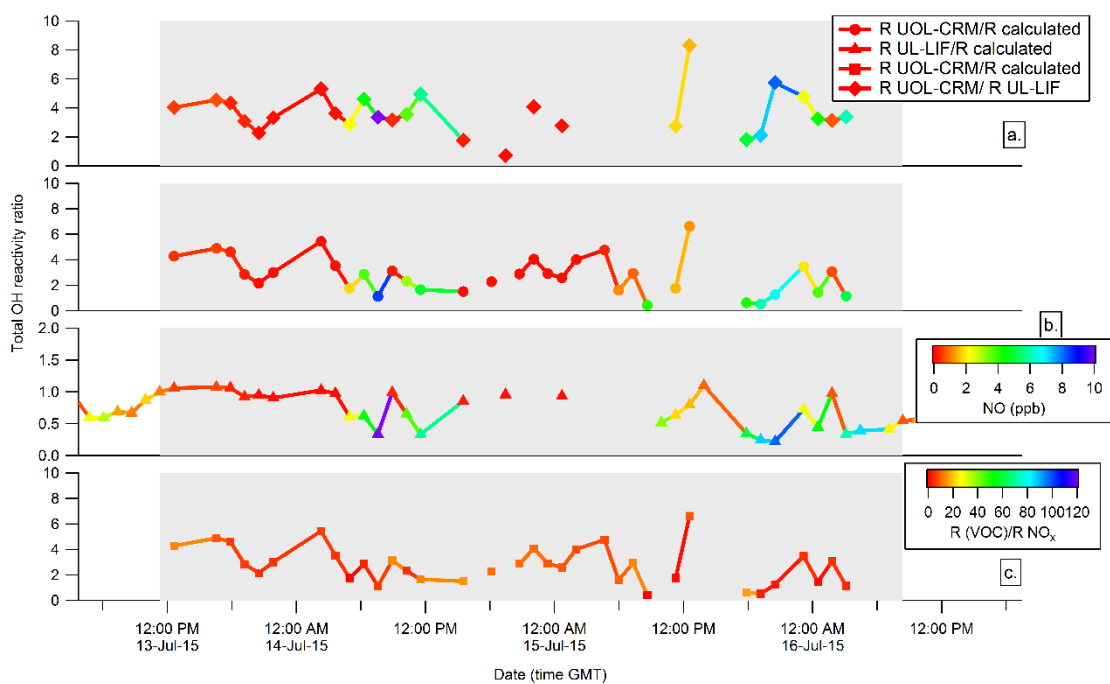


**Figure 5:19 Magnified view of Period 2 from Figure 5:17**

Figures 5:16 and 5:17 (and 5:19) show that the former is the case, as there are periods of the field campaign when the concentration of NO is low, but the measured OH reactivity is higher than the calculated reactivity. More specifically, Period 1 which follows the calculated trend in OH reactivity, but is ten times

higher the calculated reactivity, the R UOL- CRM/ R calculated ratio then decreases as the concentration of NO increases. The same is seen from 6<sup>th</sup> July to 13<sup>th</sup> July and during period 3 (23<sup>rd</sup> to 27<sup>th</sup> July) as the UOL-CRM measured OH reactivity is higher than the calculated reactivity when the concentration of NO is low.

### **5.5.3 Period 3 19/07/15 to 20/07/15**

At the start of period 3, (from 00:58 to 07:32 on 19<sup>th</sup> July), there is a high degree of agreement between the measurements made by the UOL-CRM and the calculated OH reactivity, as the UOL- CRM/ R calculated ratio ranged from a maximum of 4.5:1 (30 s<sup>-1</sup> measured by the UOL-CRM) to a minimum of 1.2:1 (7.6 s<sup>-1</sup> as measured by the UOL-CRM) (Figures 5:16 and 5:17). The minimum measurement of the UOL-CRM shown in Figure 5:14, and Table 5:6 is 6.3 s<sup>-1</sup> higher than the minimum calculated OH reactivity.

In contrast to the Period 2, when the UOL- CRM/ R calculated ratio was low whenever the concentration of NO was high, over this period of time, the concentration of NO was minimal and ranged from 0.14 ppb to 0.9 ppb. The agreement between the calculated and measured reactivity is so high (the measurements made by the UOL-CRM is close to the calculated reactivity) during this period because the measured concentrations of OVOCs is at a minimum (less than the LOD), (from measurements shown in Figure 5:16). This is because the reactivity measured by the UOL-CRM depends upon the difference in pyrrole concentration measured during C2 and C3 modes. This difference between C2 mode and C3 mode therefore only depends upon the concentration of VOCs when sampling ambient air (if any fluctuation in humidity and the presence of NO within the ambient air has been corrected for). If the concentration of VOCs within the ambient air is minimal during C3 mode, the difference between C2 and C3 pyrrole concentration is also minimal, and therefore, so is the measured OH reactivity. As shown when correcting the UOL-CRM measurements due to deviations from pseudo first order conditions within section 3.4.1, and Figure 3:6 and Equation 1:14.

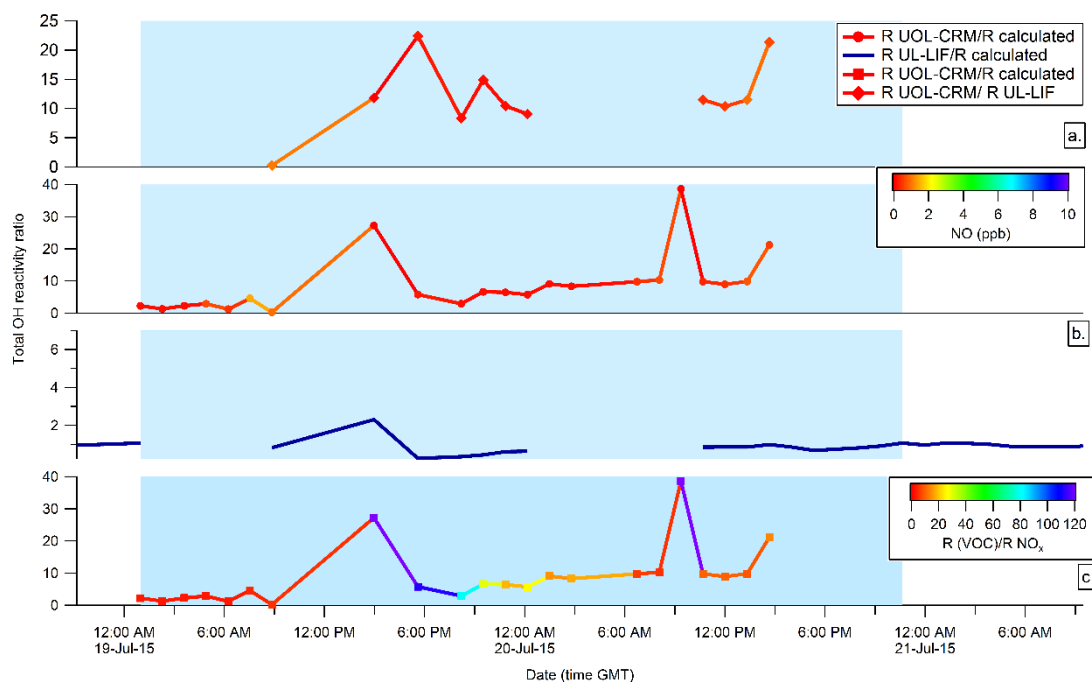


Figure 5:20 Magnified view of Period 3

After this point the UOL- CRM/ R calculated ratio increases to 27:1 at 14:58 on 19<sup>th</sup> July. This is because at this point, the concentration of both NO and NO<sub>2</sub> was less than their LOD respectively. This resulted in a calculated reactivity of 1.4 s<sup>-1</sup>. The same is seen at 09:22 on 20<sup>th</sup> July when the NO<sub>x</sub> concentration again decreased below the LOD and OH reactivity was calculated as 1.5 s<sup>-1</sup>, corresponding to a UOL- CRM/ R calculated ratio of 38:1. As a comparison, when examining the UL-LIF data, a similar response is observed when the NO<sub>x</sub> concentration falls to below its LOD, and the ratio of UL-LIF to calculated OH increases to 2:1 (at 14:58 19<sup>th</sup> July) as OH reactivity is dominated by OVOCs and NMHCs (Figures 5:9 and 5:17). The same trend is observed within the UOL- CRM/ R calculated ratio at 09:22 on 20<sup>th</sup> July as the NO<sub>x</sub> concentrations decrease below its LOD, the ratio of UOL-CRM measured OH reactivity to calculated reactivity is 38:1.

The UOL-CRM measurements are higher than the calculated reactivity because some OH reactivity is detected due to the concentrations of VOCs within the ambient air sample, but just like the measurement within the R previous periods,

this is out of scale and higher than the calculated data. This is possibly owing to calibration errors, and is discussed within section 5.7.

For example, following a decrease in  $\text{NO}_x$ , a large increase in isoprene is observed on 19<sup>th</sup> July at 17:36. As seen within the GC-FID measurements (Figure 5:2 a), the concentration of isoprene increase from an average of approximately 0.01 ppb to 3.1 ppb, over this time period, isoprene becomes the dominant species that contributes to OH reactivity, shown by the change in the fraction of VOC to  $\text{NO}_x$  reactivity in Figure 5:9 and Figure 5:20.

Before the spike, the calculated OH reactivity corresponding to the concentrations of isoprene was on average  $0.06 \text{ s}^{-1}$ , this then increased to  $8.1 \text{ s}^{-1}$  (at 3.1 ppb of isoprene) (Figure 5:9) when the increase in isoprene concentration occurred. Total terpene based OH reactivity increased from on average  $0.08 \text{ s}^{-1}$  to  $8.1 \text{ s}^{-1}$  as isoprene was the only terpene based VOC to increase in concentration at the time, (increasing the contribution to total OH reactivity to 73%).

Calculated total OH reactivity and UOL-CRM OH reactivity increases from  $1.4 \text{ s}^{-1}$  to  $11.3 \text{ s}^{-1}$  and  $36.5 \text{ s}^{-1}$  to  $64 \text{ s}^{-1}$  respectively during this time. As the UOL-CRM/R calculated ratio is 5:1 (UOL-CRM measurements was 82% higher than the calculated reactivity). This follows on from the pattern stated previously, in which the UOL-CRM is able to observe the resulting changes in OH reactivity as the concentrations of VOCs change, but the absolute value is higher in comparison to the calculated value.

A second spike in OH reactivity at 17:20 on 20<sup>th</sup> July, corresponding to an increase in  $\text{NO}_x$  and total OVOC concentrations, more specifically: acetic acid, DMS, methanol, acetaldehyde, ketones and terpenes, is seen in Figures 5:2 and 5:9. Whilst the peak in OH reactivity at this point is not observed by the UOL-CRM (due to the UOL-CRM reaching the end of its sampling cycle), the increase in reactivity beforehand is detected, as the measurement increases from  $44 \text{ s}^{-1}$  to  $99 \text{ s}^{-1}$ . This fluctuation in  $\text{NO}_x$  and OVOC concentrations is observed in both the calculated and measured OH reactivity, but the

UOL- CRM/ R calculated ratio is 21:1 as the measured OH reactivity is on average 95% higher than the calculated reactivity.

#### **5.5.4 Period 4 23/07/15 to 27/07/15**

The fourth period of the campaign is characterised by low concentrations of both NO<sub>x</sub> and VOCs, ranging from 11 to 0.7 ppb of OVOCs, 4.9 to 1.4 ppb of NMHCs and NO<sub>x</sub> ranging from 5 to 1 ppb of NO<sub>2</sub> and 1.5 to 0.1 ppb of NO.

On average, UOL-CRM measurements were 76% higher than the calculated measurements, with the UOL- CRM/ R calculated ratio ranging from 14:1 to 1.4:1. On average the minimum measurements of reactivity was 4 s<sup>-1</sup> higher than the minimum calculated reactivity, (shown in Figure 5:14 and Table 5:6).

Just like the previous periods, the agreement between the calculated and measured reactivity is high when the concentrations of VOCs and NO is low. However, the agreement is higher than in the previous period because the concentrations of OVOCs is higher than the previous period. The concentration of VOCs needs to be at a minimum for the UOL-CRM to completely agree with the calculated OH reactivity.

### **5.6 Comparisons between UOL-CRM and UL-LIF measurements**

Figure 5:21 shows a box and whisker plot comparing the data collected by the UL-LIF and the UOL-CRM, and the corresponding data from the box and whisker plot is shown in Table 5:6. When comparing the average measurements for the entire campaign, the UOL-CRM measurements was 89% higher than the UL-LIF measured reactivity, (42 s<sup>-1</sup> in comparison to 4 s<sup>-1</sup>). With the highest degree of overlap within the measurements occurring during Period 2.

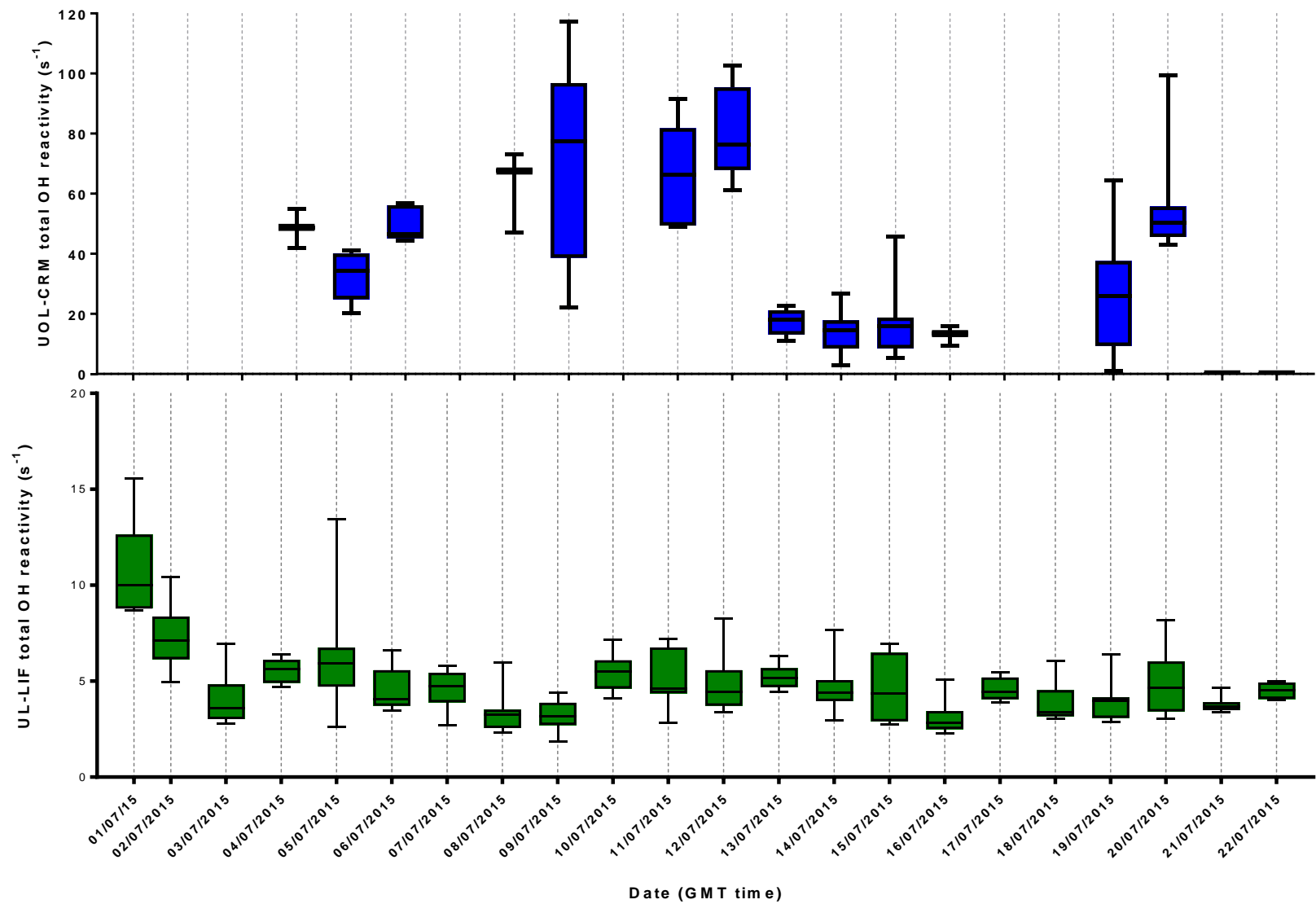


Figure 5:21 Box and whisker plot of the OH reactivity measurements made by the UL-LIF and the UOL-CRM during the ICOZA campaign

**Total OH reactivity (s-1)**

	Minimum		Mean		Maximum		25% Percentile		75% Percentile		Std. Deviation (1 $\sigma$ )	
	UL-LIF	UOL-CRM	UL-LIF	UOL-CRM	UL-LIF	UOL-CRM	UL-LIF	UOL-CRM	UL-LIF	UOL-CRM	UL-LIF	UOL-CRM
04/07	4.68	41.89	5.58	48.58	6.4	55.05	4.91	41.89	6.11	55.05	0.62	6.58
05/07	2.62	20.15	6.08	32.42	13.43	41.07	4.71	24.84	6.74	40.08	2.47	7.57
06/07	3.48	44.43	4.58	49.84	6.61	56.88	3.72	45.16	5.57	56.17	1.10	5.84
08/07	2.3	46.93	3.30	62.54	5.98	73.12	2.55	46.93	3.52	73.12	0.88	13.8
09/07	1.87	22.18	3.16	68.95	4.4	117.2	2.71	38.67	3.87	96.86	0.76	30.76
11/07	2.83	49.05	5.15	68	7.19	91.47	4.37	49.41	6.76	81.82	1.31	15.97
12/07	3.37	61.11	4.82	79.74	8.28	102.6	3.72	67.89	5.57	95.39	1.40	15.21
13/07	4.46	11.02	5.21	17.43	6.3	22.7	4.693	13.08	5.68	21.19	0.59	4.338
14/07	2.96	2.93	4.63	14.54	7.65	26.86	3.96	8.44	5.06	17.89	1.21	7.327
15/07	2.74	5.25	4.69	17.1	6.95	45.73	2.905	8.56	6.48	18.76	1.70	11.24
16/07	2.29	9.49	3.06	12.95	5.07	15.91	2.5	9.49	3.44	15.91	0.78	3.236
19/07	2.88	7.67	4.03	29.95	6.38	64.55	3.09	13.34	4.16	37.99	1.14	19.25
20/07	3.03	42.92	4.86	54.8	8.18	99.34	3.42	45.57	6.03	55.73	1.57	16.34
<b>Average</b>	3.03	28.25	4.55	42.83	7.14	62.49	3.63	31.79	5.30	51.22	1.19	12.11

**Table 5:7 summary of the statistics collected from the box and whisker plot comparing the data collected by the UOL-CRM and the UL-LIF**

Figure 5:22 shows a scatter plot comparing the UL-LIF measured OH reactivity to the calculated reactivity for the entirety of the field campaign, (scatter plots comparing the UOL-CRM measurements and calculated reactivity for periods 2 and 4 of the campaign are shown in section 5.7, Figure 5:23). The UL-LIF measurements shows good agreement with the calculated OH reactivity, but there is some discrepancy between the measured and calculated data as seen within Figure 5:21. Both Figures 5:17 and 5:22 show that the UL-LIF underestimates total OH reactivity in comparison to the calculated reactivity at higher NO concentrations. The average UL-LIF to calculated OH ratio during the campaign was 0.9:1, however, during periods of the campaign, when the concentration of NO was above the average (0.4 ppb) the UL-LIF/ R calculated ratio decreased below the average.

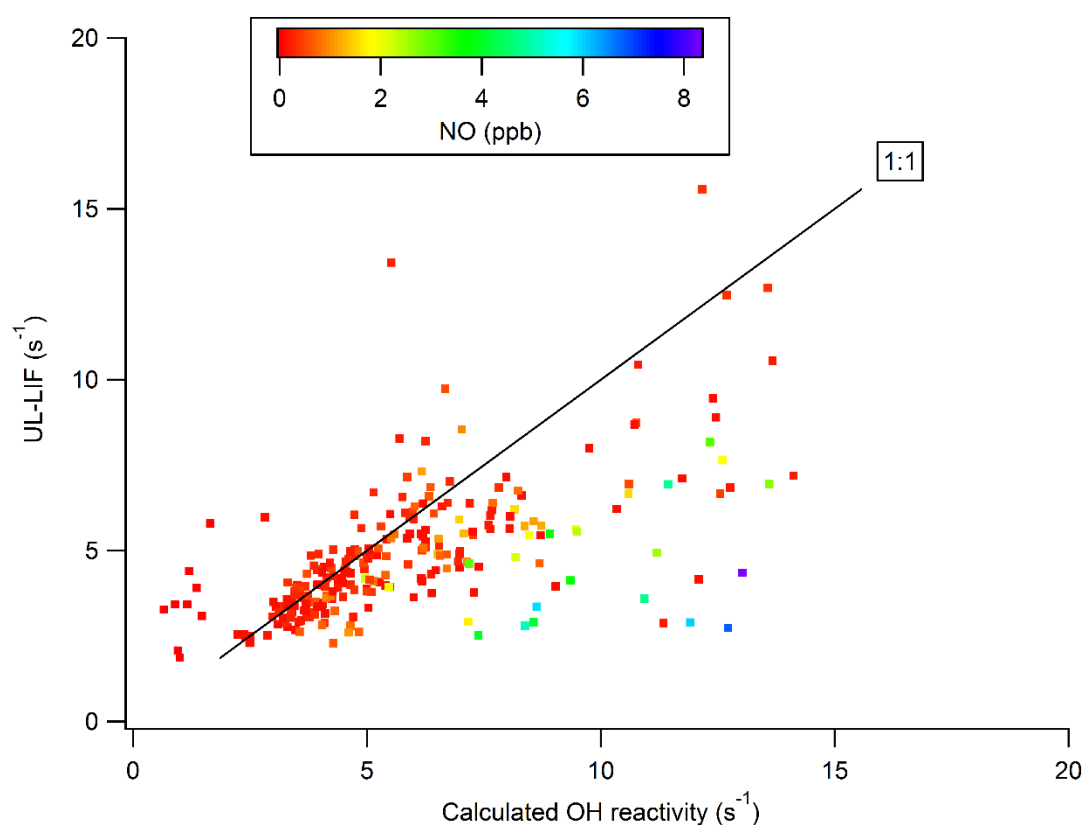


**Figure 5:22** Scatter plot comparing the UL-LIF measured OH reactivity to the calculated reactivity. Red line shows a 1:1 ratio between calculated and measured reactivity. The colour scale shows concentrations of NO measured during the campaign

For example, during period 1 when a spike in NO concentration was observed, the UL-LIF to calculated OH ratio decreased to 0.4:1 from the average, and during period 2 when the concentrations of NO was at its highest, the UL-LIF to calculated reactivity decreased to 0.3:1 and 0.2:1 from the average when the concentrations of NO was 8.3 ppb and 6.7 ppb respectively (shown in Figure 5:17).

Because of degree at which the UL-LIF and calculated OH reactivity agree, on average, the ratio between the UOL-CRM and the UL-LIF measurements is the same as the UOL- CRM to calculated reactivity ratio, (on average the calculated OH reactivity is 13% higher than the UL-LIF measured reactivity). However, as the UL-LIF underestimates OH reactivity when the concentration of NO is high, the disagreement between UOL- CRM and UL-LIF measurements is higher than that of the UOL-CRM to calculated reactivity when the concentration of NO is high.

Table 5:8 summarises the comparisons made between the UOL-CRM, the calculated reactivity and the UL-LIF. As can be seen from the table, the percentage difference between the UOL-CRM and the UL-LIF for period 1 is very similar to the percentage difference between the UOL-CRM and the calculated OH reactivity.

	<b>R UOL-CRM/ R Calculated</b>		<b>R UOL-CRM/ R UL-LIF</b>	
	<b>Average ratio</b>	<b>Average % difference</b>	<b>Average ratio</b>	<b>Average % difference</b>
Period 1	6.0:1	86	6.3:1	85
Period 2	2.5:1	57	3.4:1	71
Period 3	8.8:1	84	11.1:1	89

**Table 5:8 Summary of measurements comparing the average UOL-CRM/ calculated R, UOL-CRM/ UL-LIF ratios for periods 1, 2 and 3, along with the percentage difference between measurements and calculated reactivity for the three periods**

The percentage difference between the UOL-CRM and UL-LIF measured reactivity is higher than the difference between UOL-CRM and calculated

reactivity during periods 2 and 3 because a higher concentration of NO was measured during periods 2 and 3.

This is because the measurements made by the UL-LIF is so similar to the calculated reactivity during period 1, that it is not discussed below when comparing the UL-LIF to UOL-CRM measurements. Period 4 is also not discussed below because the UL-LIF collected measurements only until the 22<sup>nd</sup> July.

During period 2, when the concentration of NO was less than 2 ppb, the UOL- CRM/ R Calculated ratio ranged from 0.6:1 to 5:4, and the UOL-CRM/ UL-LIF ratio ranged from 0.7:1 to 5.3:1. However, when the concentration of NO was above 2 ppb, the range of ratios differed, (from 2:1 to 1.1:1 UOL- CRM/ R Calculated and 4.6:1 to 3.3:1 for the UOL-CRM/ UL-LIF ratio). This difference in measurements is due to the discrepancy within the UL-LIF measurements and calculated reactivity at high NO concentrations.

Over period 3, the same discrepancy between calculated and measured OH reactivity is observed when the concentration of NO is above 2 ppb. However one notable feature of this period is the isoprene spike that is observed within the measured VOC concentrations and the calculated OH reactivity (discussed within sections 5.2). The UL-LIF underestimates OH reactivity in comparison to calculated reactivity, as OH reactivity is measured at  $2.8 \text{ s}^{-1}$  by the UL-LIF and calculated at  $11.3 \text{ s}^{-1}$ .

However, the UOL-CRM is able to observe and measure this fluctuation in OH reactivity whilst overestimating the reactivity in comparison to the calculated OH reactivity. The ratio of UOL-CRM to calculated reactivity here is 5:1 compared to a UL-LIF to calculated reactivity ratio of 22:1.

## **5.7 Possible calibration and instrumentation errors**

Based on the comparisons of the measurements made by the UOL-CRM with the calculated reactivity and the measurements made by the UL-LIF, a number of conclusions can be made:

1. When the concentrations of VOCs are at a minimum, the measurements made by the UOL-CRM agrees well with the calculated OH reactivity. As shown by the ratios calculated during periods 1 and 3. When the concentration of VOCs increase and fluctuate, the UOL-CRM is able to track the corresponding change in OH reactivity, but the measurement differs in absolute value in comparison to the calculated OH reactivity. An example of this is during period 3 when there is an increase in isoprene based OH reactivity, the UOL-CRM is able to monitor this change in reactivity, but the measurements is higher than the calculated reactivity. The same is true
2. The agreement between the UOL-CRM and the calculated reactivity is higher when the concentration of NO is more than 2 ppb. It is likely that this is owing to calibration errors, and is discussed below.

The first point can partly be explained by the degree of noise within the OH reactivity measurements. Both Tables 5:6 and Table 5:7 show that the standard deviation within the UOL-CRM measurements is lower during periods 2 and 4, as the agreement between calculated and measured reactivity is higher during these periods, and there is a higher degree of overlap in measurements during these periods. Unfortunately, the reasons as to why the standard deviations is differs through the entire campaign is likely due to fluctuations in PTR–ToF-MS sensitivity and temperature variations within the shipping container resulting in variations within the hydronium ion count (section 4.5), but these days have been removed from the data shown within this section.

The measurements made by the UOL-CRM have to be corrected due to deviations from pseudo- first order kinetics, this is done by calculating a true reactivity from known concentration of a standard. It is likely then that these deviations have not been fully characterised, and that the correction factor used on the raw data should be higher as a wide range of VOCs and pyrrole to OH ratios need to be tested. As the calibration was conducted using propyne, and mixture of hydrocarbons as a test gas, (section 3.4) it does not cater for all of the VOCs measured during the campaign with the PTR-QMS and GC-FID.

Although the UOL-CRM operates at pseudo-first order conditions, these conditions, it does not account for the kinetics of other VOC.

By rearranging Equation 3:7 (and taking  $R_{\text{true}}$  as the calculated reactivity), the difference in the correction factor used within the raw campaign data and the true correction factor can be determined based on the calculated OH reactivity. As a result, it was determined that the correction factor used through the calibration procedure discussed within section 3.4 was 62% higher, 47% higher, 33% higher, 78% higher than compared to that using the calculated reactivity as a basis of true reactivity for each period of the campaign respectively, this is also likely owing to varying PTR-ToF-MS sensitivity towards pyrrole throughout the field campaign.

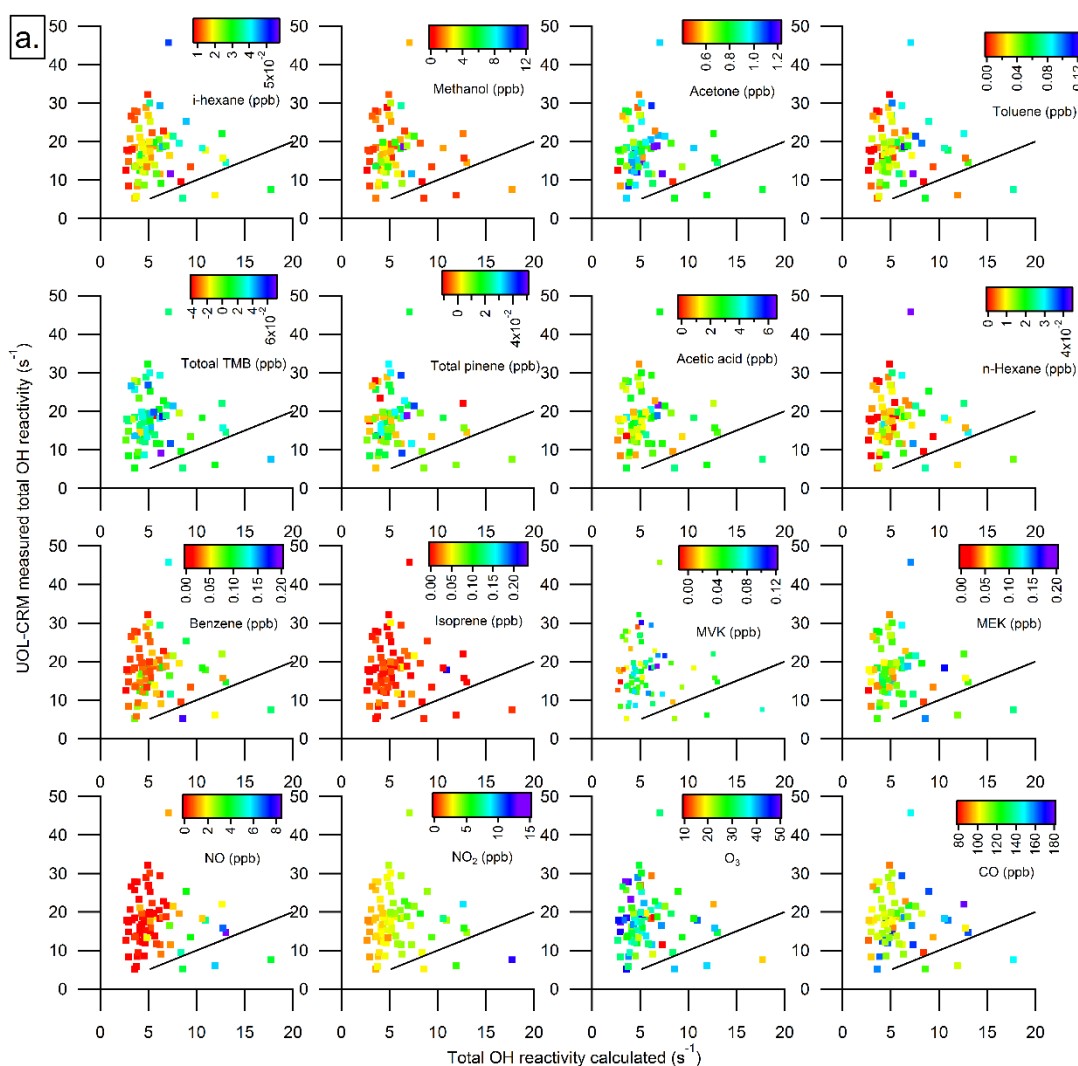


**Figure 5:23 a. and b. Correlations of the total OH reactivity measured by the UOL-CRM to the calculated total OH reactivity for periods 1 and 2. Colour scales depict concentrations of OVOCs and NMHCs. Lines in black show a 1:1 ratio**

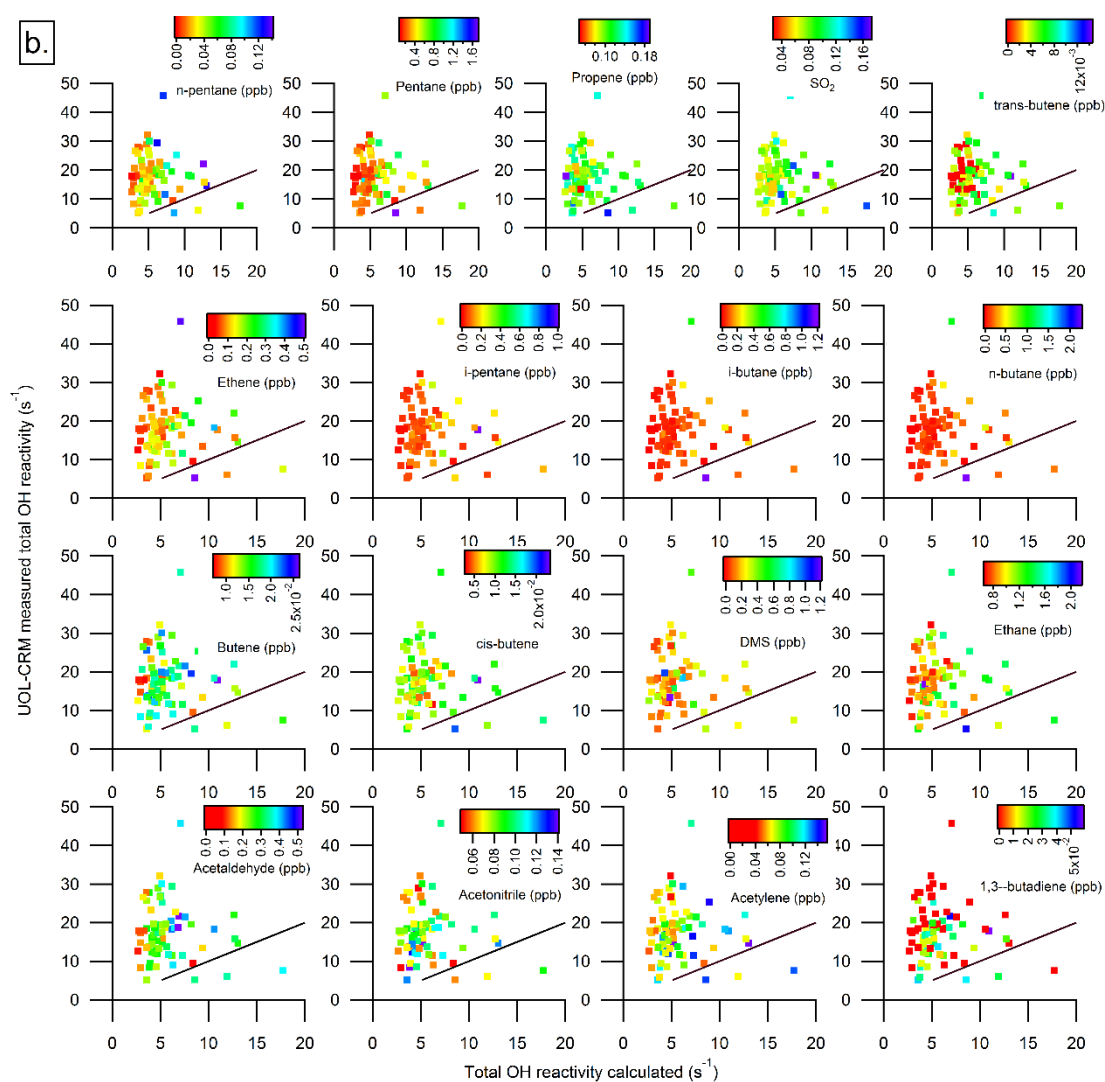


Figure 5:23 continued

Figure 5:23 depicts correlations of the measurements made by the UOL-CRM and the calculated total OH reactivity during periods 3 and 4 of the campaign. Colour scales within the correlation plots show the concentrations of OVOs, NMHCs and inorganic species during this time frame.

These scatter plots were created in order to determine whether there is a pattern to the disagreement between the calculated and measured OH reactivity. It shows that overall, no individual VOC contributes to the measured or calculated OH reactivity during the better periods of agreement. However it does confirm that the agreement is better when during periods of high NO concentrations,

confirming the statements made about the measurements during periods 1, 2, 3 and 4.

Two factors play a role in producing a better agreement when the concentration of NO is high:

1. In general, the measurements made by the UOL-CRM is higher than the calculated reactivity, (as seen in Figure 5:17 when calculating ratio of measurements when discussing various periods of the field campaign). The use of a calibration to correct for deviation from pseudo first order corrects for this. However, as mentioned above, this correction factor does not fully correct the measured reactivity (leaving the measurements still higher than the calculated reactivity).
2. The addition of NO within the UOL-CRM system recycles OH, this will therefore decrease the difference between C2 and C3 pyrrole concentrations (as discussed in section 3.5) thereby decreasing the measured OH reactivity, in addition to the decrease in measured reactivity after applying the calibration due to deviations from pseudo first order kinetics.

The effect of OH recycling due to high NO concentrations was characterised using a calibration discussed within section 3.5. High concentrations of NO will recycle OH within the UOL-CRM reaction vessel, this will decrease the measured C3 pyrrole concentrations in comparison to the expected C3 pyrrole concentrations, and therefore, during the C3 mode of measurements, the concentration of OH within the reaction vessel will vary in comparison to that generated during C2. The difference between C2 and C3 should only depend on the concentrations of VOC and any other OH reactive species entering the UOL-CRM. The larger the concentration of VOCs during C3, the greater the difference between C2 and C3, and therefore the greater the measured reactivity.

Through this calibration to determine the degree at which C3 will decrease based on the concentration of NO entering the UOL-CRM reaction vessel, it was determined that a minimum of 10 ppb NO was enough to cause a 1 ppb change

in pyrrole concentration, by rearranging Equation 3:10. As a result, the NO calibration was not applied to the UOL-CRM data, as the concentrations of NO during the campaign did not reach this threshold, (the maximum concentration observed was 8 ppb NO during period 2). Though these calibrations were conducted using NO concentrations ranging from 20 ppb to 120 ppb, and the calibrations shows good linearity, the range of NO concentrations measured during the campaign was lower than that used within in the calibration, and it is likely that the difference in C3 measured during the campaign, due to the addition of NO is outside of the uncertainty calculated during the calibration.

## 5.8 Conclusions

The calculation of total OH reactivity based on the measured concentrations of VOCs, and inorganic species show that the reactivity during the campaign is driven by NO<sub>2</sub> as it contributes up to 64% of the total OH reactivity (Table 5:4). This was observed within air masses arriving at the measurement site from a south to westerly direction for the first and final third of the campaign, and within air arriving from a northerly direction over the midpoint of the campaign.

Over the entire campaign, on average the UOL-CRM measurements was higher than the calculated reactivity by 80%. Four periods of the campaign show interesting regions when the disagreement between the measured reactivity and the calculated reactivity is high or low. Periods 2 and 4 show better agreement between the calculated and measured OH reactivity. Over which the UOL-CRM measurements was higher than the calculated by 57% over period 2 and 76% during period 4.

Over the entire campaign, it was observed that the UOL-CRM is able to monitor fluctuations in OVOC and NMHC based OH reactivity, as seen in periods 1 and 3. When there was a sudden fluctuation in methanol, acetone, acetaldehyde, acetic acid MVK, MEK and formaldehyde based reactivity during period 1, the UOL-CRM was able to monitor the change, all be it overestimating the calculated OH reactivity. The same is true during period 3, in which a large increase in isoprene based reactivity was observed, the UOL-CRM was able to monitor this

change, but the measured reactivity was overestimated, being 82% higher than the calculated OH reactivity.

At the start of period 3, the concentration of OVOCs was 0 ppb, and the ratio of UOL-CRM measured reactivity to calculated reactivity ranged from 4.5:1 to 0.2:1 before the spike in isoprene concentration. From this it can be concluded that the measurements made by the UOL-CRM overestimates the true reactivity, but any fluctuations in OH reactivity will be recorded by the UOL-CRM.

This disagreement is reduced during periods of the campaign when the concentration of NO is above 2 ppb, as period 2 shows that when the concentration of NO is less than 2 ppb, the UOL-CRM/ calculated R ratio ranged from 0.7: 1 to 4:1. However when the NO concentration was increased to 8.3 ppb, when the concentration measured to calculated reactivity ratio was 1.1:1.

The UL-LIF measurements of OH reactivity correlates well with the calculated reactivity, however, during periods of high NO concentrations, the UL-LIF underestimated reactivity in comparison to the calculated reactivity. This therefore leads to further overestimation of the UOL-CRM reactivity when comparing to the UL-LIF measured reactivity during high NO periods (above 2 ppb NO).

This finally leads to two conclusions, that in general, the UOL-CRM overestimates OH reactivity. This overestimation is reduced when correcting for deviations from pseudo first order kinetics. However, as the UOL-CRM overestimates reactivity after the application of the calibration discussed within section 3.4, it is likely that this deviation needs to be characterised further with the use of numerous gas standards that have varying rates of reaction with OH.

The second conclusion is that high concentrations of NO will reduce this overestimation further as OH is recycled when the concentration of NO is above 2 ppb, resulting in a better agreement between measured and calculated reactivity. This needs to be further characterised by repeating the calibrations discussed within section 3.5 at a wider range of NO concentrations and pyrrole to OH ratios.

## Chapter 6. Conclusions and future work

The work presented in this thesis describes the development, characterisation and deployment of an instrument that is used to measure total OH reactivity by implementing the Comparative Reactivity Method (UOL-CRM). The primary aim of this work was to compare total OH reactivity measurements made by the UOL-CRM with calculations of reactivity and measurements made by an additional technique (the University of Leeds LIF instrument). The secondary aim of this work was to explore the application of utilising the PTR-ToF-MS to simultaneously measure OH reactivity and VOC concentrations.

The use of a PTR-ToF-MS presented a novel aspect in its use to simultaneously measure concentrations of VOCs and total OH reactivity. This method was first proposed by Kumar and Sinha (2014) and first implemented within the frame of this work, in order to conduct measurements at a coastal region. This method, however proved unsuccessful as no variations in VOC concentrations were observed during the field campaign. It was therefore observed, that the PTR-ToF-MS used must be optimised in order to strike a balance between obtaining a suitable sensitivity towards pyrrole for total OH reactivity measurements, and a large sensitivity towards detectable atmospheric VOCs (discussed within section 4.4), with the implementation of the improvements discussed within section 6.5 and Table 6:1 and an improvement of the sampling strategy.

Previous measurements of total OH reactivity using the CRM technique are shown in Table 1:5. When comparing these measurements, a wider range in OH reactivity is observed with the UOL-CRM, however on average the UOL-CRM measured total OH reactivity was lower in comparison to that measured in previous work (an average of  $14 \text{ s}^{-1}$  determined from one minute measurements).

For example, Sinha et al. (2012) have measured total OH reactivity ranging from 3.6 - 85 s<sup>-1</sup> in El Arenisillo, Spain. A coastal location approximately 300 m north of the Atlantic Ocean, whereas the UOL-CRM measured total OH reactivity ranging from 11.4 - 83.7 s<sup>-1</sup> at the Weybourne Atmospheric Observatory (approximately 200 m from the North Sea) a smaller range in measurements at two coastal locations.

Comparing CRM measurements at different locations, the UOL-CRM at a coastal location recorded a lower range of reactivity than that measured in urban locations. For example, the UOL-CRM on average, measured total OH reactivity at 14.4 s<sup>-1</sup> (one minute measurement), whereas measurements made by Hansen et al. (2015), Williams et al. (2016) and Dolgorouky et al. (2012) in Lille, Beijing and Paris have recorded OH reactivity at levels of 70 s<sup>-1</sup>, 19.98 s<sup>-1</sup> and 10-130 s<sup>-1</sup> respectively. These measurements were made in major cities during large pollution regimes during which large concentrations of NO<sub>x</sub>.

The measurements made by the CRM instrument during the above mentioned field campaigns was corrected for OH recycling through the same method discussed in section 3.5. For example, Williams et al. (2016) corrected their measurements based on measured concentrations of 2 ppb NO and Dolgorouky et al. (2012) measured average concentrations of 10 ppb NO which was used to correct their measurements. Contrast this with the UOL- CRM where these measured concentrations of NO (2 ppb and 10 ppb) would not be large enough to cause significant recycling of OH (at a minimum, 10 ppb of NO would could 1 ppb change in pyrrole concentration).

Previously, Lee et al. (2009) have conducted total OH reactivity measurements at the Weybourne Atmospheric Observatory using a LIF instrument. In contrast to the measurements made by the UOL-CRM at the same location, the measured concentrations of NO was more than 10 ppb (maximum measured NO concentration during the ICOZA campaign was 8.3 ppb). However, on average a lower value of total OH reactivity was measured by Lee et al. (2009) in comparison to the UOL-CRM (4.8 s<sup>-1</sup> to 14 s<sup>-1</sup>), where the contribution to OH reactivity is dominated by firstly NO<sub>2</sub> and secondly by CO, in contrast the

calculations conducted within section 5.2 for the ICOZA campaign show that the contribution to OH reactivity comes from firstly NO<sub>2</sub> and secondly NO.

This contribution to OH reactivity originated from air masses travelling from three different locations, the North Sea, the Atlantic Ocean and from mainland Europe, over different periods of the TORCH-2 campaign. Whereas from the wind roses and back trajectories seen in seen in Figures 5:4, 5:5 and 5:6 for the ICOZA campaign show air arriving at the measurement site from primarily the North Sea, and from mainland England (likely also over the Atlantic) with the exception being the large spike in measured ozone concentration at the start of the field campaign shown in Figure 5:8.

## **6.1 The UOL-CRM and the PTR-ToF-MS**

The CRM technique was first developed at the Max Planck Institute, Mainz (Sinha et al., 2008). Chapter 2 discusses the development of the UOL-CRM and the PTR-ToF-MS coupled to the UOL-CRM. The UOL-CRM is similar to that described in Sinha et al. (2008), however in comparison to the original CRM design, the UOL-CRM uses a heated catalyst to ensure that the relative humidity of sampled ambient air is consistent during measurement.

Measurements of total OH reactivity using the UOL-CRM consists of two primary phases, dry air mode (C1) in which the concentration of pyrrole is determined without OH radicals, and humid air modes (C2 and C3), in which the concentration of pyrrole is measured in the presence of OH radicals in two phases, with clean air free of VOCs present (C2 mode) and after the introduction of ambient air into the UOL-CRM reaction vessel (C3 mode).

The PTR-ToF-MS is used as a detector and is tuned and optimised in order to detect the changes in pyrrole concentrations during each mode of measurement. The PTR-ToF-MS can also be used to track changes in relative humidity within the reaction vessel during C2 and C3 modes which can be used to correct for changes in OH concentrations when sampling ambient air.

## 6.2 Interferences

The CRM technique is subject to a number of interferences. The influence of these interferences on pyrrole and OH concentrations can be characterised through a number of experiments. These interferences include:

1. Variation in OH concentrations owing to fluctuations in ambient air humidity. This can be corrected for by determining the dependence of C2 mode pyrrole concentrations with relative humidity.
2. Deviations from pseudo first order kinetics regime as the concentration of pyrrole is on the same order of magnitude as the concentration of OH. In order to derive the correction factor of this interference, a series of experiments were conducted in which a number of gas standards were introduced into the UOL-CRM reaction vessel. The relationship between measured OH reactivity and calculated reactivity (based on the concentration of standards introduced) is determined, and the dependence of this relationship on pyrrole to OH ratio is also determined in order to derive a correction factor.
3. NO driven recycling of OH through the use of a mercury UV lamp to generate OH radicals. HO<sub>2</sub> formed within the UOL-CRM glass vessel will react with NO introduced when sampling ambient air. This will result in a linear decrease in C3 pyrrole concentration with increasing NO concentration. This linear relationship can be used to correct C3 mode pyrrole concentrations based on measurements of ambient NO concentrations made alongside the UOL-CRM.
4. VOCs sampled during C3 mode are diluted owing to the use of humidified nitrogen and pyrrole. This can be corrected for by calculating a correction factor based on the flow rates of all species during C3 mode.

## 6.3 Instability and noise within the UOL-CRM measurements

The UOL-CRM was deployed at the ICOZA field campaign throughout July 2015. A large degree of fluctuation was observed within the measured total OH reactivity as a standard deviation of 29.09 (1 $\sigma$ ) was calculated.

The source of noise within the measurements is owing to fluctuations within the hydronium signal within the PTR-ToF-MS which fluctuates with temperature within the shipping container. It was observed that an increase of 5°C results in an increase of 6000 counts per minute within the hydronium signal, this fluctuation also propagates into the pyrrole signal. Improvements that can be made to the PTR-ToF-MS in order to prevent variations in the hydronium signal are discussed within section 6.5 and Table 6:1.

## **6.4 Discrepancies between measured and calculated OH reactivity**

On average, over the entire campaign, measurements made by the UOL-CRM was higher than the calculated reactivity by 80%. With four periods of the campaign showing interesting regions when the disagreement between the measured reactivity and the calculated reactivity is high or low.

Periods 2 and 4 show better agreement between the calculated and measured OH reactivity than periods 1 and 3. In comparison to period 1, large concentrations of NO was measured (8 ppb) during period 2 as the ratio of measured to calculated reactivity was 1.1:1. Based on the patterns observed during the field campaign and the scatter plots created within Figure 5:22, it was determined that as the concentration of NO decreased, the ratio between the UOL-CRM measured OH reactivity and the calculated reactivity increased and the disagreement was worse off.

Whilst this is the case for the duration of the field campaign, it was observed that the measured ambient concentrations of NO was not large enough to cause significant recycling of OH, as a result the correction determined within section 3.5.1 was not applied to the collected data as seen within Figures 4:16 and 4:17.

Experiments conducted within section 3.4 show that UOL-CRM overestimates calculated OH reactivity, by applying the correction factor discussed within 3.4.1, this overestimation is reduced. However it was determined that there is a large degree of error within these experiments resulting in a smaller correction factor

than that based on the calculated reactivity as seen within section 5.7. This is likely owing to PTR-ToF-MS sensitivity changes throughout the campaign and a need to further test a wider range of VOCs at a number of pyrrole to OH ratios.

The UL-LIF shows a large amount of agreement with the calculated reactivity, therefore the comparisons between the UOL-CRM with the UL-LIF is similar to the comparison of the UOL-RM with calculated reactivity. However there is some degree of underestimation with regards to UL-LIF measurements in OH reactivity during high NO regimes as seen within Figure 5:22. As a result the disagreement between the UOL-CRM and UL-LIF is larger than that of the UOL-CRM and calculated reactivity when the concentration of NO is high.

Regardless of the disagreement between the measured and calculated reactivity, it was observed that the UOL-CRM is able to monitor fluctuations in OVOC and NMHC based OH reactivity. As shown in periods 1 and 3, when there are fluctuations in ambient VOC concentrations, the UOL-CRM detects changes in total OH reactivity.

## **6.5 Future work**

The difficulties encountered during the development and deployment of the UOL-CRM are shown in Table 6:1. It is clear that the interferences regarding OH recycling and deviations from pseudo first order kinetics needs to be further characterised. The measurements made within section 3.4.1 were conducted using propyne and a mixture of hydrocarbons, it is recommended that these experiments be expanded with the use of a wider range of VOCs with differing rate of reaction with OH and pyrrole to OH ratios to improve the accuracy of this correction.

These experiments can also be modelled with the use of the Maser Chemical Mechanism (MCM). Michoud et al. (2015), for example, have used the MCM (v3.2) to conduct an analysis of the chemistry occurring within the CRM reaction vessel, these tests can also be conducted for the UOL-CRM and compared to

the experimentally determined correction factors in order to constrain and improve the accuracy of the various correction factors.

<b>Error source</b>	<b>Improvement recommendation</b>
Temperature fluctuations	Heated ion and water source
Power fluctuations	PTR-ToF-MS powered through Universal Power Supply (UPS)
Variations within the measured PTR-ToF-MS sensitivity towards pyrrole	Increase the number of calibrations. Depending on the rate at which the sensitivity towards pyrrole changes within laboratory experiments, the number of calibrations during field campaigns have to be changed
Error within OH recycling corrections	Further experiments needed at a wider range of pyrrole to OH ratios
Error within kinetics corrections	Further experiments conducted with a wider range of fast and slow reacting VOCs and pyrrole to OH ratios. Experiments can be modelled using the Master Chemical Mechanism (MCM)
Unable to determine VOC concentration profiles	Improve the balance between sampling ambient air and CRM measurements using the PTR-ToF-MS by increasing both the ambient air and C3 sampling time, whilst also reducing the C2 sampling time

**Table 6:1 A list of problems determined during the development and deployment of the UOL-CRM and recommended improvements**

Hydronium signal fluctuations owing to variations in temperature within the shipping container, can be reduced by insulating and heating both the ion source and water vapour source.

Variations in voltage and the current supplied to the mass spectrometer have been observed to change the generated hydronium signal, a Universal Power Supply (UPS) for the mass spectrometer can be used in future work to ensure a constant and stable power supply to the instrument and therefore a stable hydronium signal.

The use of the PTR-ToF-MS to simultaneously detect VOC concentrations and measure total OH reactivity should also be explored further. The PTR-ToF-MS in this thesis was configured in order to improve the sensitivity and detection toward pyrrole. However the caveat to this approach is that the sensitivity towards VOCs is decreased.

Ideally a middle ground is needed in which the detection of pyrrole is optimised, whilst minor changes in ambient VOC concentrations are detected. This can be done through fragmentation tests, in which the PTR-ToF-MS detects a mixture of standard, including pyrrole, the E/N of the mass spectrometer is changed in order to determine the optimal in conditions in which there is little fragmentation of VOCs whilst also achieving a high pyrrole sensitivity.

A better sampling strategy can improve on this difficulty, in which the length of ambient air sampling time can be increased (ambient air was sampled for a maximum time of two minutes per cycle for each day of the field campaign), whilst also increasing length of time at which C3 is employed and whilst reducing the C2 measurement time. This can be achieved by changing the rate at which the Solenoid valves used by the UOL-CRM switch on and off.

However, this requires extensive testing, Sonderfeld et al. (2016), for example have determined that for the PARADE and ClearfLo campaigns, the discrepancy between OH reactivity calculated from 5 minute data and hourly values was 2 - 26% and 0 - 44% respectively therefore a balance is needed in order to measure the full extent of OH reactivity within an environment and to detect VOCs which may have a short lifetime.

Optimisation of the system can be tested by introducing a flow of a detectable VOC into the PTR-ToF-MS during the ambient air sampling mode. By measuring the changes in concentration of this VOC during ambient air mode, any variation

in the measured signal due to pressure changes or wall losses be can be determined, allowing for the verification of the optimum sampling time (Kumar and Sinha, 2014).

It is also important to note that the relative humidity of the sampled ambient air may be different in comparison to the air sampled during OH reactivity modes. For example, if the UOL-CRM is used within a dry environment, the humidity of the air entering the PTR-ToF-MS during ambient air mode will be lower than the humidity introduced into the mass spectrometer from the UOL-CRM (due to the use of humidified nitrogen to generate OH radicals) therefore, the sensitivity towards numerous VOCs will vary. And so in order to determine, a calculated OH reactivity via the VOC concentrations measured during ambient air mode, calibrations need to be conducted for all detectable VOCs in order to determine their PTR-ToF-MS sensitivity at all humidity levels.

As shown in section 3.2 and Figure 3:1, a large degree of variation was observed within the measured PTR-ToF-MS sensitivity towards pyrrole over a period of one year. Whilst the pyrrole sensitivity was measured at the start and end of the field campaign it is likely that the sensitivity can change over the duration of the campaign, it is therefore possible that the discrepancy between the calculated and measured total OH reactivity is owing to sensitivity changes during the field campaign.

Intern, it is recommended that the sensitivity towards pyrrole and a calibration be measured on a regular basis, due to the fact that the sensitivity has changed on such a large degree over the period of one year, it is recommended that the sensitivity be measured on a weekly basis during the field campaign.

## References

- ALICKE, B., GEYER, A., HOFZUMAHAUS, A., HOLLAND, F., KONRAD, S., PÄTZ, H. W., SCHÄFER, J., STUTZ, J., VOLZ-THOMAS, A. & PLATT, U. 2003. OH formation by HONO photolysis during the BERLIOZ experiment. *Journal of Geophysical Research: Atmospheres*, 108, PHO 3-1-PHO 3-17.
- AMEDRO, D., MIYAZAKI, K., PARKER, A., SCHOEMAECCKER, C. & FITTSCHEN, C. 2012. Atmospheric and kinetic studies of OH and HO<sub>2</sub> by the FAGE technique. *Journal of Environmental Sciences*, 24, 78-86.
- ATKINSON, R. 1986. Kinetics and mechanisms of the gas-phase reactions of the hydroxyl radical with organic compounds under atmospheric conditions. *Chemical Reviews*, 86, 69-201.
- ATKINSON, R. 2003. Kinetics of the gas-phase reactions of OH radicals with alkanes and cycloalkanes. *Atmos. Chem. Phys.*, 3, 2233-2307.
- ATKINSON, R. 2007. Gas-phase tropospheric chemistry of organic compounds: a review. *Atmospheric Environment*, 41, Supplement, 200-240.
- ATKINSON, R., ASCHMANN, S. M., WINER, A. M. & CARTER, W. P. L. 1984. Rate constants for the gas phase reactions of OH radicals and O<sub>3</sub> with pyrrole at 295 ± 1 K and atmospheric pressure. *Atmospheric Environment (1967)*, 18, 2105-2107.
- ATKINSON, R., BAULCH, D. L., COX, R. A., CROWLEY, J. N., HAMPSON, R. F., HYNES, R. G., JENKIN, M. E., ROSSI, M. J. & TROE, J. 2004. Evaluated kinetic and photochemical data for atmospheric chemistry: Volume I - gas phase reactions of Ox, HOx, NOx and SOx species. *Atmos. Chem. Phys.*, 4, 1461-1738.
- BAASANDORJ, M., MILLET, D. B., HU, L., MITROO, D. & WILLIAMS, B. J. 2015. Measuring acetic and formic acid by proton-transfer-reaction mass spectrometry: sensitivity, humidity dependence, and quantifying interferences. *Atmos. Meas. Tech.*, 8, 1303-1321.
- BELL, N., HEARD, D. E., PILLING, M. J. & TOMLIN, A. S. 2003. Atmospheric lifetime as a probe of radical chemistry in the boundary layer. *Atmospheric Environment*, 37, 2193-2205.
- BLAKE, R. S, MONKS, P. S & M, E. A. 2009. Proton-Transfer Reaction Mass Spectrometry. *Chem. Rev.*, 109, 861–896.
- BLOSS, W. J., GRAVESTOCK, T. J., HEARD, D. E., INGHAM, T., JOHNSON, G. P. & LEE, J. D. 2003. Application of a compact all solid-state laser system to the in situ detection of atmospheric OH, HO<sub>2</sub>, NO and IO by laser-induced fluorescence. *Journal of Environmental Monitoring*, 5, 21-28.

- BRASSEUR, G. P. & SOLOMON, S. 2005. *Aeronomy of the Middle Atmosphere: Chemistry and Physics of the Stratosphere and Mesosphere*, Springer Netherlands.
- BREHAM, B., GROSSER, J., RUSCHEINSKI, T. & ZIMMER, M. 1995. Absolute detection efficiencies of a microchannel plate detector for ions. *Meas. Sci. Technol.*, 6, 953-958.
- BROOKS, B. 2016. Weybourne Atmospheric Observatory – Annual Report of AMF Long-term measurements. In: FORSTER, G., REEVES, C., ORAM, D., MANNING, A., BANDY, B., PICKERS, P. & BARNINGHAM, T. (eds.). <https://www.ncas.ac.uk/index.php/en/documents/amf/1260-wao-annual-report-2014-1/file>.
- CALLENDAR, G. S. 1940. Variations of the amount of carbon dioxide in different air currents. *Quarterly Journal of the Royal Meteorological Society*, 66, 395-400.
- CHATANI, S., SHIMO, N., MATSUNAGA, S., KAJII, Y., KATO, S., NAKASHIMA, Y., MIYAZAKI, K., ISHII, K. & UENO, H. 2009. Sensitivity analyses of OH missing sinks over Tokyo metropolitan area in the summer of 2007. *Atmos. Chem. Phys.*, 9, 8975-8986.
- CHIN, J.-Y. & BATTERMAN, S. A. 2012. VOC composition of current motor vehicle fuels and vapors, and collinearity analyses for receptor modeling. *Chemosphere*, 86, 951-958.
- CREASEY, D. J., HEARD, D. E. & LEE, J. D. 2000. Absorption cross-section measurements of water vapour and oxygen at 185 nm. Implications for the calibration of field instruments to measure OH, HO<sub>2</sub> and RO<sub>2</sub> radicals. *Geophysical Research Letters*, 27, 1651-1654.
- DE GOUW, J. & WARNEKE, C. 2007. Measurements of volatile organic compounds in the earth's atmosphere using proton-transfer-reaction mass spectrometry. *Mass Spectrometry Reviews*, 26, 223-257.
- DE GOUW, J., WARNEKE, C., KARL, T., EERDEKENS, G., VAN DER VEEN, C. & FALL, R. 2003. Sensitivity and specificity of atmospheric trace gas detection by proton-transfer-reaction mass spectrometry. *International Journal of Mass Spectrometry*, 223–224, 365-382.
- DERWENT, R. G. 2001. Chemistry of the natural atmosphere. By Peter Warneck. Academic Press. Second edition 2000. pp. xvii + 927. Price \$149.95 (hardback). ISBN 0 12 735632 0. *Quarterly Journal of the Royal Meteorological Society*, 127, 2205-2205.
- DI CARLO, P., BRUNE, W. H., MARTINEZ, M., HARDER, H., LESHER, R., REN, X., THORNBERRY, T., CARROLL, M. A., YOUNG, V., SHEPSON, P. B., RIEMER, D., APEL, E. & CAMPBELL, C. 2004. Missing OH reactivity in a forest: evidence for unknown reactive biogenic VOCs. *Science*, 304, 722-5.

- DILLON, T. J., TUCCERI, M. E., DULITZ, K., HOROWITZ, A., VEREECKEN, L. & CROWLEY, J. N. 2012. Reaction of Hydroxyl Radicals with C<sub>4</sub>H<sub>5</sub>N (Pyrrole): Temperature and Pressure Dependent Rate Coefficients. *The Journal of Physical Chemistry A*, 116, 6051-6058.
- DOLGOROUKY, C., GROS, V., SARDA-ESTEVE, R., SINHA, V., WILLIAMS, J., MARCHAND, N., SAUVAGE, S., POULAIN, L., SCIARE, J. & BONSANG, B. 2012. Total OH reactivity measurements in Paris during the 2010 MEGAPOLI winter campaign. *Atmos. Chem. Phys.*, 12, 9593-9612.
- EDWARDS, P. M., EVANS, M. J., FURNEAUX, K. L., HOPKINS, J., INGHAM, T., JONES, C., LEE, J. D., LEWIS, A. C., MOLLER, S. J., STONE, D., WHALLEY, L. K. & HEARD, D. E. 2013. OH reactivity in a South East Asian tropical rainforest during the Oxidant and Particle Photochemical Processes (OP3) project. *Atmos. Chem. Phys.*, 13, 9497-9514.
- ELLIS, A. & MAYHEW, C. 2014a. *Proton Transfer Reaction Mass Spectrometry Principles and Applications*, Wiley.
- ELLIS, A. M. & MAYHEW, C. A. 2014b. Background. *Proton Transfer Reaction Mass Spectrometry*. John Wiley & Sons, Ltd.
- ELLIS, A. M. & MAYHEW, C. A. 2014c. Chemical Ionization: Chemistry, Thermodynamics and Kinetics. *Proton Transfer Reaction Mass Spectrometry*. John Wiley & Sons, Ltd.
- ELLIS, A. M. & MAYHEW, C. A. 2014d. Experimental: Components and Principles. *Proton Transfer Reaction Mass Spectrometry*. John Wiley & Sons, Ltd.
- ELLIS, A. M. & MAYHEW, C. A. 2014e. Quantitative Analysis. *Proton Transfer Reaction Mass Spectrometry*. John Wiley & Sons, Ltd.
- ELSHORBANY, Y. F., KLEFFMANN, J., HOFZUMAHAUS, A., KURTENBACH, R., WIESEN, P., BRAUERS, T., BOHN, B., DORN, H. P., FUCHS, H., HOLLAND, F., ROHRER, F., TILLMANN, R., WEGENER, R., WAHNER, A., KANAYA, Y., YOSHINO, A., NISHIDA, S., KAJII, Y., MARTINEZ, M., KUBISTIN, D., HARDER, H., LELIEVELD, J., ELSTE, T., PLASS-DÜLMER, C., STANGE, G., BERRESHEIM, H. & SCHURATH, U. 2012. HO<sub>x</sub> budgets during HO<sub>x</sub>Comp: A case study of HO<sub>x</sub> chemistry under NO<sub>x</sub>-limited conditions. *Journal of Geophysical Research: Atmospheres*, 117, n/a-n/a.
- ENNIS, C. J., REYNOLDS, J. C., KEELY, B. J. & CARPENTER, L. J. 2005. A hollow cathode proton transfer reaction time of flight mass spectrometer. *International Journal of Mass Spectrometry*, 247, 72-80.
- FINLAYSON-PITTS, B. J. & PITTS JR, J. N. 2000a. CHAPTER 5 - Kinetics and Atmospheric Chemistry. *Chemistry of the Upper and Lower Atmosphere*. San Diego: Academic Press.

- FINLAYSON-PITTS, B. J. & PITTS JR, J. N. 2000b. CHAPTER 6 - Rates and Mechanisms of Gas-Phase Reactions in Irradiated Organic – NO<sub>x</sub> – Air Mixtures. *Chemistry of the Upper and Lower Atmosphere*. San Diego: Academic Press.
- FINLAYSON-PITTS, B. J. & PITTS JR, J. N. 2000c. CHAPTER 7 - Chemistry of Inorganic Nitrogen Compounds. *Chemistry of the Upper and Lower Atmosphere*. San Diego: Academic Press.
- GLUECKAUF, E. 1951. The Composition of Atmospheric Air. In: MALONE, T. F. (ed.) *Compendium of Meteorology: Prepared under the Direction of the Committee on the Compendium of Meteorology*. Boston, MA: American Meteorological Society.
- H. EHHALT, D. 1999. Photooxidation of trace gases in the troposphere Plenary Lecture. *Physical Chemistry Chemical Physics*, 1, 5401-5408.
- HANSEN, R. F., BLOCQUET, M., SCHOEMAECKER, C., LÉONARDIS, T., LOCOGE, N., FITTSCHEN, C., HANOUNE, B., STEVENS, P. S., SINHA, V. & DUSANTER, S. 2015. Intercomparison of the comparative reactivity method (CRM) and pump–probe technique for measuring total OH reactivity in an urban environment. *Atmos. Meas. Tech.*, 8, 4243-4264.
- HANSEN, R. F., GRIFFITH, S. M., DUSANTER, S., RICKLY, P. S., STEVENS, P. S., BERTMAN, S. B., CARROLL, M. A., ERICKSON, M. H., FLYNN, J. H., GROSSBERG, N., JOBSON, B. T., LEFER, B. L. & WALLACE, H. W. 2014a. Measurements of total hydroxyl radical reactivity during CABINEX 2009 – Part 1: field measurements. *Atmos. Chem. Phys.*, 14, 2923-2937.
- HANSEN, R. F., GRIFFITH, S. M., DUSANTER, S., RICKLY, P. S., STEVENS, P. S., BERTMAN, S. B., CARROLL, M. A., ERICKSON, M. H., FLYNN, J. H., GROSSBERG, N., JOBSON, B. T., LEFER, B. L. & WALLACE, H. W. 2014b. Measurements of total hydroxyl radical reactivity during CABINEX 2009 &ndash; Part 1: field measurements. *Atmos. Chem. Phys.*, 14, 2923-2937.
- HARRISON, R. M. 2007. *Principles of Environmental Chemistry*, RSC Publishing.
- HEARD, D. E. & PILLING, M. J. 2003. Measurement of OH and HO<sub>2</sub> in the Troposphere. *Chemical Reviews*, 103, 5163-5198.
- INGHAM, T., GODDARD, A., WHALLEY, L. K., FURNEAUX, K. L., EDWARDS, P. M., SEAL, C. P., SELF, D. E., JOHNSON, G. P., READ, K. A., LEE, J. D. & HEARD, D. E. 2009. A flow-tube based laser-induced fluorescence instrument to measure OH reactivity in the troposphere. *Atmos. Meas. Tech.*, 2, 465-477.
- INOMATA, S., TANIMOTO, H., KAMEYAMA, S., TSUNOGAI, U., IRIE, H., KANAYA, Y. & WANG, Z. 2008. Technical Note: Determination of formaldehyde mixing ratios in air with PTR-MS: laboratory experiments and field measurements. *Atmos. Chem. Phys.*, 8, 273-284.

- KARL, T. G., CHRISTIAN, T. J., YOKELSON, R. J., ARTAXO, P., HAO, W. M. & GUENTHER, A. 2007. The Tropical Forest and Fire Emissions Experiment: method evaluation of volatile organic compound emissions measured by PTR-MS, FTIR, and GC from tropical biomass burning. *Atmos. Chem. Phys.*, 7, 5883-5897.
- KESEL, S., NOLSCHER, A. & WILLIAMS, J. 2014. Comparative Reactivity Method (CRM)-Setup, Measurement and Data Evaluation. Organic Reactivity Species Understanding and Measurement (ORSUM) Conference.
- KIM, S., GUENTHER, A., KARL, T. & GREENBERG, J. 2011. Contributions of primary and secondary biogenic VOC total OH reactivity during the CABINEX (Community Atmosphere-Biosphere Interactions Experiments)-09 field campaign. *Atmos. Chem. Phys.*, 11, 8613-8623.
- KORE-TECHNOLOGY-LTD. 2010. *Ststem Overview PTR-ToF Mass Spectrometer*.
- KOVACS, T. A. & BRUNE, W. H. 2001. Total OH Loss Rate Measurement. *Journal of Atmospheric Chemistry*, 39, 105-122.
- KOVACS, T. A., BRUNE, W. H., HARDER, H., MARTINEZ, M., SIMPAS, J. B., FROST, G. J., WILLIAMS, E., JOBSON, T., STROUD, C., YOUNG, V., FRIED, A. & WERT, B. 2003. Direct measurements of urban OH reactivity during Nashville SOS in summer 1999. *Journal of Environmental Monitoring*, 5, 68-74.
- KUMAR, V. & SINHA, V. 2014. VOC-OHM: A new technique for rapid measurements of ambient total OH reactivity and volatile organic compounds using a single proton transfer reaction mass spectrometer. *International Journal of Mass Spectrometry*, 374, 55-63.
- LEE, J. D., WHALLEY, L. K., HEARD, D. E., STONE, D., DUNMORE, R. E., HAMILTON, J. F., YOUNG, D. E., ALLAN, J. D., LAUFS, S. & KLEFFMANN, J. 2016. Detailed budget analysis of HONO in central London reveals a missing daytime source. *Atmos. Chem. Phys.*, 16, 2747-2764.
- LEE, J. D. Y., JENNIFER C., READ, K. A., HAMILTON, J. F., HOPKINS, J. R., LEWIS, A. C., BANDY, B. J., DAVEY, J., EDWARDS, P., INGHAM, T., SELF, D. E., SMITH, S. C., PILLING, M. J. & HEARD, D. E. 2009. Measurement and calculation of OH reactivity at a United Kingdom coastal site. *Journal of Atmospheric Chemistry*, 64, 1573-0662.
- LINDINGER, W., FALL, R. & KARL, T. 2001. *Environmental, food and medical applications of Proton- Transfer- Reaction Mass Spectrometry (PTR-MS)*, Elsevier.
- LINDINGER, W., HANSEL, A. & JORDAN, A. 1998. On-line monitoring of volatile organic compounds at pptv levels by means of proton-transfer-reaction mass spectrometry (PTR-MS) medical applications, food control and environmental research. *International Journal of Mass Spectrometry and Ion Processes*, 173, 191-241.

- LOCKHART, J., BLITZ, M. A., HEARD, D. E., SEAKINS, P. W. & SHANNON, R. J. 2013. Mechanism of the Reaction of OH with Alkynes in the Presence of Oxygen. *The Journal of Physical Chemistry A*, 117, 5407-5418.
- LOU, S., HOLLAND, F., ROHRER, F., LU, K., BOHN, B., BRAUERS, T., CHANG, C. C., FUCHS, H., HÄSELER, R., KITA, K., KONDO, Y., LI, X., SHAO, M., ZENG, L., WAHNER, A., ZHANG, Y., WANG, W. & HOFZUMAHAUS, A. 2010. Atmospheric OH reactivities in the Pearl River Delta – China in summer 2006: measurement and model results. *Atmos. Chem. Phys.*, 10, 11243-11260.
- LU, K., ZHANG, Y., SU, H., BRAUERS, T., CHOU, C. C., HOFZUMAHAUS, A., LIU, S. C., KITA, K., KONDO, Y., SHAO, M., WAHNER, A., WANG, J., WANG, X. & ZHU, T. 2010. Oxidant (O<sub>3</sub> + NO<sub>2</sub>) production processes and formation regimes in Beijing. *Journal of Geophysical Research: Atmospheres*, 115, n/a-n/a.
- LU, K. D., HOFZUMAHAUS, A., HOLLAND, F., BOHN, B., BRAUERS, T., FUCHS, H., HU, M., HÄSELER, R., KITA, K., KONDO, Y., LI, X., LOU, S. R., OEBEL, A., SHAO, M., ZENG, L. M., WAHNER, A., ZHU, T., ZHANG, Y. H. & ROHRER, F. 2013. Missing OH source in a suburban environment near Beijing: observed and modelled OH and HO<sub>2</sub> concentrations in summer 2006. *Atmos. Chem. Phys.*, 13, 1057-1080.
- MAO, J., REN, X., BRUNE, W. H., OLSON, J. R., CRAWFORD, J. H., FRIED, A., HUEY, L. G., COHEN, R. C., HEIKES, B., SINGH, H. B., BLAKE, D. R., SACHSE, G. W., DISKIN, G. S., HALL, S. R. & SHETTER, R. E. 2009. Airborne measurement of OH reactivity during INTEX-B. *Atmos. Chem. Phys.*, 9, 163-173.
- MAO, J., REN, X., CHEN, S., BRUNE, W. H., CHEN, Z., MARTINEZ, M., HARDER, H., LEFER, B., RAPPENGLÜCK, B., FLYNN, J. & LEUCHNER, M. 2010. Atmospheric oxidation capacity in the summer of Houston 2006: Comparison with summer measurements in other metropolitan studies. *Atmospheric Environment*, 44, 4107-4115.
- MAO, J., REN, X., ZHANG, L., VAN DUIN, D. M., COHEN, R. C., PARK, J. H., GOLDSTEIN, A. H., PAULOT, F., BEAVER, M. R., CROUNSE, J. D., WENNBERG, P. O., DIGANGI, J. P., HENRY, S. B., KEUTSCH, F. N., PARK, C., SCHADE, G. W., WOLFE, G. M., THORNTON, J. A. & BRUNE, W. H. 2012. Insights into hydroxyl measurements and atmospheric oxidation in a California forest. *Atmos. Chem. Phys.*, 12, 8009-8020.
- MCLAREN, R., WOJTAL, P., HALLA, J. D., MIHELE, C. & BROOK, J. R. 2012. A survey of NO<sub>2</sub>:SO<sub>2</sub> emission ratios measured in marine vessel plumes in the Strait of Georgia. *Atmospheric Environment*, 46, 655-658.
- MICHOUD, V., HANSEN, R. F., LOCOGE, N., STEVENS, P. S. & DUSANTER, S. 2015. Detailed characterizations of the new Mines Douai comparative reactivity method instrument via laboratory experiments and modeling. *Atmospheric Measurement Techniques*, 8, 3537-3553.

- MONKS, P. S. 2005. Gas-phase radical chemistry in the troposphere. *Chemical Society Reviews*, 34, 376-395.
- MONKS, P. S. 2007. Tropospheric Photochemistry. *Handbook of Atmospheric Science*. Blackwell Science Ltd.
- MONKS, P. S., GRANIER, C., FUZZI, S., STOHL, A., WILLIAMS, M. L., AKIMOTO, H., AMANN, M., BAKLANOV, A., BALTENSPERGER, U., BEY, I., BLAKE, N., BLAKE, R. S., CARSLAW, K., COOPER, O. R., DENTENER, F., FOWLER, D., FRAGKOU, E., FROST, G. J., GENEROSO, S., GINOUX, P., GREWE, V., GUENTHER, A., HANSSON, H. C., HENNE, S., HJORTH, J., HOFZUMAHAUS, A., HUNTRIESER, H., ISAKSEN, I. S. A., JENKIN, M. E., KAISER, J., KANAKIDOU, M., KLIMONT, Z., KULMALA, M., LAJ, P., LAWRENCE, M. G., LEE, J. D., LIOUSSE, C., MAIONE, M., MCFIGGANS, G., METZGER, A., MIEVILLE, A., MOUSSIOPOULOS, N., ORLANDO, J. J., O'DOWD, C. D., PALMER, P. I., PARRISH, D. D., PETZOLD, A., PLATT, U., PÖSCHL, U., PRÉVÔT, A. S. H., REEVES, C. E., REIMANN, S., RUDICH, Y., SELLEGRI, K., STEINBRECHER, R., SIMPSON, D., TEN BRINK, H., THELOKE, J., VAN DER WERF, G. R., VAUTARD, R., VESTRENG, V., VLACHOKOSTAS, C. & VON GLASOW, R. 2009. Atmospheric composition change – global and regional air quality. *Atmospheric Environment*, 43, 5268-5350.
- MOORE, J. H., CHRISTOPHER C. DAVIS, & COPLAN., M. A. 2009. *Building Scientific Apparatus*, Cambridge University Press.
- MÜLLER, M., MIKOVINY, T., FEIL, S., HAIDACHER, S., HANEL, G., HARTUNGEN, E., JORDAN, A., MÄRK, L., MUTSCHLECHNER, P., SCHOTTKOWSKY, R., SULZER, P., CRAWFORD, J. H. & WISTHALER, A. 2014. A compact PTR-ToF-MS instrument for airborne measurements of volatile organic compounds at high spatiotemporal resolution. *Atmos. Meas. Tech.*, 7, 3763-3772.
- MURPHY, J. G., ORAM, D. E. & REEVES, C. E. 2010. Measurements of volatile organic compounds over West Africa. *Atmos. Chem. Phys.*, 10, 5281-5294.
- NAKASHIMA, Y., KATO, S., GREENBERG, J., HARLEY, P., KARL, T., TURNIPSEED, A., APEL, E., GUENTHER, A., SMITH, J. & KAJII, Y. 2014. Total OH reactivity measurements in ambient air in a southern Rocky mountain ponderosa pine forest during BEACHON-SRM08 summer campaign. *Atmospheric Environment*, 85, 1-8.
- NÖLSCHER, A. C., SINHA, V., BOCKISCH, S., KLÜPFEL, T. & WILLIAMS, J. 2012a. Total OH reactivity measurements using a new fast Gas Chromatographic Photoionization Detector (GC-PID). *Atmos. Meas. Tech.*, 5, 2981-2992.
- NÖLSCHER, A. C., WILLIAMS, J., SINHA, V., CUSTER, T., SONG, W., JOHNSON, A. M., AXINTE, R., BOZEM, H., FISCHER, H., POUVESLE, N., PHILLIPS, G., CROWLEY, J. N., RANTALA, P., RINNE, J., KULMALA, M., GONZALES, D., VALVERDE-CANOSSA, J., VOGEL, A., HOFFMANN, T., OUWERSLOOT, H. G., VILÀ-GUERAU DE ARELLANO, J. & LELIEVELD, J. 2012b. Summertime total OH reactivity measurements from boreal forest during HUMPPA-COPEC 2010. *Atmos. Chem. Phys.*, 12, 8257-8270.

- NOLSCHER, A. C., YANEZ-SERRANO, A. M., WOLFF, S., DE ARAUJO, A. C., LAVRIC, J. V., KESSELMEIER, J. & WILLIAMS, J. 2016. Unexpected seasonality in quantity and composition of Amazon rainforest air reactivity. *Nat Commun*, 7, 10383.
- PRINN, R. G. 2003. THE CLEANSING CAPACITY OF THE ATMOSPHERE. *Annual Review of Environment and Resources*, 28, 29-57.
- PUSEDE, S. E., GENTNER, D. R., WOOLDRIDGE, P. J., BROWNE, E. C., ROLLINS, A. W., MIN, K. E., RUSSELL, A. R., THOMAS, J., ZHANG, L., BRUNE, W. H., HENRY, S. B., DIGANGI, J. P., KEUTSCH, F. N., HARROLD, S. A., THORNTON, J. A., BEAVER, M. R., ST. CLAIR, J. M., WENNBERG, P. O., SANDERS, J., REN, X., VANDENBOER, T. C., MARKOVIC, M. Z., GUHA, A., WEBER, R., GOLDSTEIN, A. H. & COHEN, R. C. 2014. On the temperature dependence of organic reactivity, nitrogen oxides, ozone production, and the impact of emission controls in San Joaquin Valley, California. *Atmos. Chem. Phys.*, 14, 3373-3395.
- REN, X., BRUNE, W. H., CANTRELL, C. A., EDWARDS, G. D., SHIRLEY, T., METCALF, A. R. & LESHER, R. L. 2005. Hydroxyl and Peroxy Radical Chemistry in a Rural Area of Central Pennsylvania: Observations and Model Comparisons. *Journal of Atmospheric Chemistry*, 52, 1573-0662.
- REN, X., BRUNE, W. H., MAO, J., MITCHELL, M. J., LESHER, R. L., SIMPAS, J. B., METCALF, A. R., SCHWAB, J. J., CAI, C., LI, Y., DEMERJIAN, K. L., FELTON, H. D., BOYNTON, G., ADAMS, A., PERRY, J., HE, Y., ZHOU, X. & HOU, J. 2006. Behavior of OH and HO<sub>2</sub> in the winter atmosphere in New York City. *Atmospheric Environment*, 40, Supplement 2, 252-263.
- REN, X., HARDER, H., MARTINEZ, M., LESHER, R. L., OLIGER, A., SIMPAS, J. B., BRUNE, W. H., SCHWAB, J. J., DEMERJIAN, K. L., HE, Y., ZHOU, X. & GAO, H. 2003. OH and HO<sub>2</sub> Chemistry in the urban atmosphere of New York City. *Atmospheric Environment*, 37, 3639-3651.
- RENNIE, E. E., JOHNSON, C. A. F., PARKER, J. E., FERGUSON, R., HOLLAND, D. M. P. & SHAW, D. A. 1999. A photoabsorption and mass spectrometry study of pyrrole. *Chemical Physics*, 250, 217-236.
- SADANAGA, Y., YOSHINO, A., KATO, S., YOSHIOKA, A., WATANABE, K., MIYAKAWA, Y., HAYASHI, I., ICHIKAWA, M., MATSUMOTO, J., NISHIYAMA, A., AKIYAMA, N., KANAYA, Y. & KAJII, Y. 2004a. The importance of NO<sub>2</sub> and volatile organic compounds in the urban air from the viewpoint of the OH reactivity. *Geophysical Research Letters*, 31, n/a-n/a.
- SADANAGA, Y., YOSHINO, A., WATANABE, K., YOSHIOKA, A., WAKAZONO, Y., KANAYA, Y. & KAJII, Y. 2004b. Development of a measurement system of OH reactivity in the atmosphere by using a laser-induced pump and probe technique. *Review of Scientific Instruments*, 75, 2648-2655.
- SEELEY, I., TIPLER, A. & GROSSER, Z. Ozone Precursor Analysis Using the TurboMatrix Thermal Desorption GC System Operating Manual.

- SGHAIER, L., VIAL, J., SASSIAT, P., THIEBAUT, D., WATIEZ, M., BRETON, S., RUTLEDGE, D. N. & CORDELLA, C. B. Y. 2016. An overview of recent developments in volatile compounds analysis from edible oils: Technique-oriented perspectives. *European Journal of Lipid Science and Technology*, 118, 1853-1879.
- SHIRLEY, T. R., BRUNE, W. H., REN, X., MAO, J., LESHER, R., CARDENAS, B., VOLKAMER, R., MOLINA, L. T., MOLINA, M. J., LAMB, B., VELASCO, E., JOBSON, T. & ALEXANDER, M. 2006. Atmospheric oxidation in the Mexico City Metropolitan Area (MCMA) during April 2003. *Atmos. Chem. Phys.*, 6, 2753-2765.
- SINHA, V., CUSTER, T. G., KLUEPFEL, T. & WILLIAMS, J. 2009. The effect of relative humidity on the detection of pyrrole by PTR-MS for OH reactivity measurements. *International Journal of Mass Spectrometry*, 282, 108-111.
- SINHA, V., WILLIAMS, J., CROWLEY, J. N. & LELIEVELD, J. 2008. The Comparative Reactivity Method – a new tool to measure total OH reactivity in ambient air. *Atmospheric Chemistry and Physics*, 8, 2229-2242.
- SINHA, V., WILLIAMS, J., DIESCH, J. M., DREWNICK, F., MARTINEZ, M., HARDER, H., REGELIN, E., KUBISTIN, D., BOZEM, H., HOSAYNALI-BEYGI, Z., FISCHER, H., ANDRÉS-HERNÁNDEZ, M. D., KARTAL, D., ADAME, J. A. & LELIEVELD, J. 2012. Constraints on instantaneous ozone production rates and regimes during DOMINO derived using in-situ OH reactivity measurements. *Atmospheric Chemistry and Physics*, 12, 7269-7283.
- SINHA, V., WILLIAMS, J., LELIEVELD, J., RUUSKANEN, T. M., KAJOS, M. K., PATOKOSKI, J., HELLEN, H., HAKOLA, H., MOGENSEN, D., BOY, M., RINNE, J. & KULMALA, M. 2010. OH Reactivity Measurements within a Boreal Forest: Evidence for Unknown Reactive Emissions. *Environmental Science & Technology*, 44, 6614-6620.
- SONDERFELD, H., WHITE, I. R., GOODALL, I. C. A., HOPKINS, J. R., LEWIS, A. C., KOPPMANN, R. & MONKS, P. S. 2016. What effect does VOC sampling time have on derived OH reactivity? *Atmos. Chem. Phys.*, 16, 6303-6318.
- STONE, D., WHALLEY, L. K. & HEARD, D. E. 2012. Tropospheric OH and HO<sub>2</sub> radicals: field measurements and model comparisons. *Chemical Society Reviews*, 41, 6348-6404.
- STONE, D., WHALLEY, L. K., INGHAM, T., EDWARDS, P. M., CRYER, D. R., BRUMBY, C. A., SEAKINS, P. W. & HEARD, D. E. 2016. Measurement of OH reactivity by laser flash photolysis coupled with laser-induced fluorescence spectroscopy. *Atmos. Meas. Tech.*, 9, 2827-2844.
- TAIPALE, R., RUUSKANEN, T. M., RINNE, J., KAJOS, M. K., HAKOLA, H., POHJA, T. & KULMALA, M. 2008. Technical Note: Quantitative long-term measurements of VOC concentrations by PTR-MS measurement, calibration, and volume mixing ratio calculation methods. *Atmos. Chem. Phys.*, 8, 6681-6698.

- TRANS, P. & KEELING, R. *Trends in Atmospheric Carbon Dioxide* [Online]. NOAA/ESRL, Scripps Institution of Oceanography. Available: <http://www.esrl.noaa.gov/gmd/ccgg/trends/data.html>.
- TUCK, A. F. 1992. *Chemistry of Atmospheres*. By Richard P. Wayne. Clarendon Press, Oxford, 1991, 2nd Edition. Pp. 447. Price £19.50 (Paperback). *Quarterly Journal of the Royal Meteorological Society*, 118, 413-413.
- WEBB, A. R. & COE, H. 2007. *Atmospheric Energy and the Structure of the Atmosphere. Handbook of Atmospheric Science*. Blackwell Science Ltd.
- WHALLEY, L. K., FURNEAUX, K. L., GODDARD, A., LEE, J. D., MAHAJAN, A., OETJEN, H., READ, K. A., KAADEN, N., CARPENTER, L. J., LEWIS, A. C., PLANE, J. M. C., SALTZMAN, E. S., WIEDENSOHLER, A. & HEARD, D. E. 2010. The chemistry of OH and HO<sub>2</sub> radicals in the boundary layer over the tropical Atlantic Ocean. *Atmos. Chem. Phys.*, 10, 1555-1576.
- WHALLEY, L. K., STONE, D., BANDY, B., DUNMORE, R., HAMILTON, J. F., HOPKINS, J., LEE, J. D., LEWIS, A. C. & HEARD, D. E. 2016. Atmospheric OH reactivity in central London: observations, model predictions and estimates of in situ ozone production. *Atmos. Chem. Phys.*, 16, 2109-2122.
- WILLIAMS, J., KEBEL, S. U., NÖLSCHER, A. C., YANG, Y., LEE, Y., YÁÑEZ-SERRANO, A. M., WOLFF, S., KESSELMEIER, J., KLÜPFEL, T., LELIEVELD, J. & SHAO, M. 2016. Opposite OH reactivity and ozone cycles in the Amazon rainforest and megacity Beijing: Subversion of biospheric oxidant control by anthropogenic emissions. *Atmospheric Environment*, 125, Part A, 112-118.
- WINER, A. M. & BIERMANN, H. W. 1994. Long pathlength differential optical absorption spectroscopy (DOAS) measurements of gaseous HONO, NO<sub>2</sub> and HCNO in the California South Coast Air Basin. *Research on Chemical Intermediates*, 20, 423-445.
- YANG, Y., SHAO, M., WANG, X., NÖLSCHER, A. C., KESSEL, S., GUENTHER, A. & WILLIAMS, J. 2016. Towards a quantitative understanding of total OH reactivity: A review. *Atmospheric Environment*, 134, 147-161.
- YOKELSON, R. J., KARL, T., ARTAXO, P., BLAKE, D. R., CHRISTIAN, T. J., GRIFFITH, D. W. T., GUENTHER, A. & HAO, W. M. 2007. The Tropical Forest and Fire Emissions Experiment: overview and airborne fire emission factor measurements. *Atmos. Chem. Phys.*, 7, 5175-5196.
- YOSHINO, A., SADANAGA, Y., WATANABE, K., KATO, S., MIYAKAWA, Y., MATSUMOTO, J. & KAJII, Y. 2006. Measurement of total OH reactivity by laser-induced pump and probe technique—comprehensive observations in the urban atmosphere of Tokyo. *Atmospheric Environment*, 40, 7869-7881.
- ZANNONI, N., DUSANTER, S., GROS, V., SARDA ESTEVE, R., MICHOU, V., SINHA, V., LOCOGE, N. & BONSANG, B. 2015. Intercomparison of two comparative

reactivity method instruments in the Mediterranean basin during summer 2013. *Atmos. Meas. Tech.*, 8, 3851-3865.

ZANNONI, N., GROS, V., LANZA, M., SARDA, R., BONSANG, B., KALOGRIDIS, C., PREUNKERT, S., LEGRAND, M., JAMBERT, C., BOISSARD, C. & LATHIERE, J. 2016. OH reactivity and concentrations of biogenic volatile organic compounds in a Mediterranean forest of downy oak trees. *Atmos. Chem. Phys.*, 16, 1619-1636.